Strål
säkerhets
myndigheten
Swedish Radiation Safety Authority

Redaktörer: Ninos Garis,
Henrik Glänneskog,
Lennart Agrenius

Forskning

2015:27

APRI-8: Accident Phenomena of Risk Importance

En lägesrapport om forskningen inom området svåra haverier under åren 2012-2014

Rapportnummer: 2015:27 **ISSN:** 2000-0456
Tillgänglig på www.stralsakerhetsmyndigheten.se

Strål
säkerhets
myndigheten
Swedish Radiation Safety Authority

Redaktörer: Ninos Garis [1)], Henrik Glänneskog [2)], Lennart Agrenius [3)]
[1)] SSM, [2)] Vattenfall, [3)] Ingenjörsbyrå AB

2015:27

APRI-8: Accident Phenomena of Risk Importance

En lägesrapport om forskningen inom området svåra haverier under åren 2012-2014

Datum: Juni 2015
Rapportnummer: 2015:27 **ISSN:** 2000-0456
Tillgänglig på www.stralsakerhetsmyndigheten.se

Denna rapport har tagits fram på uppdrag av Strålsäkerhetsmyndigheten, SSM. De slutsatser och synpunkter som presenteras i rapporten är författarens/författarnas och överensstämmer inte nödvändigtvis med SSM:s.

Forskningsprojektet APRI-8 har genomförts i samarbete mellan följande organisationer:

- Strålsäkerhetsmyndigheten (SSM)
- Ringhals AB (RAB)
- OKG Aktiebolag (OKG)
- Forsmarks Kraftgrupp AB (FKA)
- Vattenfall

Projektet har varit underställd en styrgrupp med representanter från SSM och kraftbolagen enligt följande:

Mauritz Gärdinge, OKG (ordförande)
Ninos Garis, SSM
Patrick Isaksson, SSM
Anders Henoch, RAB
Staffan Dittmer, RAB
Margareta Tanse Larsson, FKA
Henrik Glänneskog, Vattenfall
Lennart Agrenius, Agrenius Ingenjörsbyrå AB (projektledare)

Arbetet har genomförts i projektform med deltagande från parterna och andra svenska och utländska uppdragstagare och samarbetspartners.

Redaktörer:

Ninos Garis, SSM
Henrik Glänneskog, Vattenfall Research and Development
Lennart Agrenius, Agrenius Ingenjörsbyrå AB

Personer som har bidragit till olika avsnitt:

Wiktor Frid, SSM
Patrick Isaksson,SSM
Oddbjörn Sandervåg, SSM
Johan Ljung, RAB
Pavel Kudinov, KTH
Weimin Ma, KTH
Sergey Yakush, IPM RAS
Dmitry Grishchenko, KTH
Walter Villanueva, KTH
Alexander Konovalenko, KTH
Simone Basso, KTH
Mikhail Davydov, EREC
Sergey Galushin, KTH
Viet-Anh Phung, KTH
Sachin Thakre, KTH
Henrik Glänneskog, Vattenfall
Christian Ekberg, Chalmers
Ivan Kajan, Chalmers
Sabrina Tietze, Chalmers
Mark Foreman, Chalmers

SAMMANFATTNING

Kunskap om de fenomen som kan uppträda vid svåra haverier i en kärnkraftanläggning är en viktig förutsättning för att kunna förutse anläggningens beteende, för att kunna utforma rutiner och instruktioner för haverihantering, för beredskapsplaneringen samt för att få god kvalitet på haverianalyser och riskstudier.

Sedan början på 80-talet har kärnkraftföretagen och myndigheten i Sverige samarbetat inom forskningsområdet svåra reaktorhaverier. Samarbetet i början var framför allt knutet till att förstärka skyddet mot omgivningskonsekvenser efter ett svårt reaktorhaveri genom att bl.a. ta fram system för filtrerad tryckavlastning av reaktorinneslutningen. Sedan början på 90-talet har samarbetet delvis ändrat karaktär och inriktats mer på fenomenologiska frågor av riskdominerande betydelse.

Under åren 2012-2014 har samarbetet fortsatt inom forskningsprogrammet APRI-8. Syftet har varit att visa om de lösningar som har valts i den svenska strategin för haverihantering ger ett tillräckligt skydd för omgivningen. Detta sker genom att få fördjupad kunskap om dels viktiga fenomen vid härdsmälteförlopp, dels mängden radioaktivitet som kan släppas ut till omgivningen vid ett svårt haveri.

För att nå syftet har forskningsprogrammet omfattat dels uppföljning av den internationella forskningen inom svåra haverier och utvärdering av resultaten, dels fortsatt stöd till forskningen på KTH och Chalmers om svåra haverier.

Uppföljningen av den internationella forskningen har främjat utbyte av kunskap och erfarenheter samt har gett tillgång till en mängd information om olika fenomen av betydelse för händelseförlopp vid svåra haverier. Detta är viktigt för att erhålla en god bedömningsgrund av de utsläppsbegränsande åtgärderna i svenska kärnkraftsreaktorer.

Det fortsatta stödet till KTH har gett ökade kunskaper om möjligheterna och förutsättningarna för att kyla härdrester i reaktortanken och om de identifierade processerna i samband med tankgenomträngning samt kylbarheten av härdrester i inneslutningen. Utvecklingen av ROAAM+ vid KTH har resulterat av en stor mängd resultat och data för känslighets- och osäkerhetsstudier av de ingående fenomenen och förloppen. Även verktyg för analys av dessa fenomen har utvecklats.

Stödet till Chalmers har resulterat i ökade kunskaper om jod interagerar med olika färger och andra material i inneslutningen. Det har också visats att infångningen av organisk jod i skrubbern kan ökas genom att tillsätta organiska fosfiner.

INNEHÅLLSFÖRTECKNING

1. INLEDNING

Kunskap om de fenomen som kan uppträda vid svåra haverier i en kärnkraftanläggning är en viktig förutsättning för att kunna förutse anläggningens beteende, för att kunna utforma rutiner och instruktioner för haverihantering, för beredskapsplaneringen samt för att få god kvalitet på haverianalyser och riskstudier.

De svenska parterna, SSM (tidigare SKI) och kraftföretagen i Sverige har under en följd av år samarbetat inom forskningsområdet svåra reaktorhaverier. Detta har skett inom projekten FILTRA, RAMA, RAMA II, RAMA III, HAFOS, APRI, APRI 2, APRI 3, APRI 4, APRI 5, APRI 6 och APRI 7. TVO har deltagit i projekten APRI, APRI 3 och APRI 4.

FILTRA- och RAMA-projekten var knutna till processen att utforma, genomföra och verifiera de haveriförebyggande och konsekvenslindrande åtgärder som 1989 införts vid samtliga kärnkraftverk.

I projekten HAFOS, APRI, APRI 2, APRI 3, APRI 4, APRI 5, APRI 6 och APRI 7 var en viktig uppgift att följa internationell forskning rörande svåra härdhaverier. En annan uppgift var att stödja eget arbete inom Sverige där forskningen på härdsmälteförlopp genomförts vid KTH och kemiska förhållanden i inneslutningen har undersökts vid Chalmers.

APRI 8-projektet har i stora drag haft samma inriktning som tidigare APRI.

1.1 Kort historik

Sedan början på 80-talet har kärnkraftföretagen i Sverige och myndigheten samarbetat inom forskningsområdet svåra reaktorhaverier. Samarbetet i början var framför allt knutet till att förstärka skyddet mot omgivningskonsekvenser efter ett svårt reaktorhaveri genom att bl.a. ta fram system för filtrerad tryckavlastning av reaktorinneslutningen. Sedan början på 90-talet, har samarbetet delvis ändrat karaktär och inriktats mer på fenomenologiska frågor av riskdominerande betydelse.

I början av 1986 beslutade regeringen att som villkor för fortsatt drift skulle utsläppsbegränsande åtgärder vidtas vid reaktorerna i Forsmark, Oskarshamn och Ringhals. Åtgärderna skulle vara genomförda senast vid utgången av 1988. I anslutning till dessa regeringsbeslut[1] uppdrog regeringen åt dåvarande Statens kärnkraftinspektion (SKI) att utöver redovisning av beslut som myndigheten fattat med anledning av regeringens nya driftvillkor även redovisa en bedömning av behovet av fortsatta insatser inom området svåra haveriförlopp.

Efter myndighetens granskning av de åtgärder som vidtagits vid berörda anläggningar konstaterades i ett beslut[2] av den 19 december 1988 att de mål som regeringen angivit som villkor för fortsatt drift hade uppfyllts. I myndighetens beslut peka-

[1] Regeringsbeslut 14 ”Uppdrag att redovisa det fortsatta arbetet att begränsa utsläpp vid svåra reaktorhaverier”. Industridepartementet 1986-02-27.
[2] SKI-beslut ”Utsläppsbegränsande åtgärder vid kärnkraftverken i Forsmark, Oskarshamn och Ringhals”. SKI 1988-12-19.

des emellertid också på att tillståndshavarna även fortsättningsvis behövde följa de forsknings- och utvecklingsinsatser som bedrevs och dra slutsatser om vilka ytterligare säkerhetshöjande åtgärder som bör komma ifråga vid de egna anläggningarna.

I slutet av 1990-talet förtydligades myndighetens allmänna krav på utsläppsbegränsande åtgärder genom föreskrifterna SSMFS 2008:1 (tidigare SKIFS 1998:1 och SKIFS 2004:1) om säkerhet i kärntekniska anläggningar. I föreskrifterna ställdes krav på att radiologiska olyckor skall förebyggas genom en för varje anläggning anpassad grundkonstruktion med flera barriärer och ett anpassat djupförsvar. Bestämmelserna om djupförsvar innehåller bl.a. krav på att utsläpp av radioaktiva ämnen till omgivningen skall förhindras och begränsas genom anordningar och förberedda åtgärder. I föreskrifterna infördes även krav på att säkerheten vid en anläggning fortlöpande skall analyseras och bedömas på ett systematiskt sätt, och i allmänna råd pekades på att bl.a. forskningsresultat särskilt bör beaktas vid sådan fortlöpande analys och bedömning.

Genom föreskrifterna SSMFS 2008:17 (tidigare SKIFS 2004:2) om konstruktion och utförande av kärnkraftsreaktorer har myndigheten sedan ytterligare förtydligat och skärpt kraven i vissa avseenden. Även svåra haverier med större härdskador skall beaktas när det gäller konstruktionen av inneslutningsfunktionen, instrumentering för övervakning av anläggningens tillstånd, samt för att kunna uppnå ett stabilt sluttillstånd med reaktorn så att den inte utgör ett hot mot omgivningen på lång sikt. I konsekvensutredningen[3] av föreskrifterna konstaterades att dessa krav, som inte fanns då reaktorerna konstruerades, tillkom i viss omfattning genom regeringsbeslutet om utsläppsbegränsande åtgärder 1986.

Den svenska strategin för haverihantering innebär att inneslutningarna försetts med förstärkt inneslutningskylning, tryckavlastning och filtrering av utsläpp. Den svenska strategin för att hantera en härdsmälta - att låta en härdsmälta falla i djupt vatten i inneslutningen – har visat sig vara ovanlig. Endast i ett fåtal andra reaktorer i världen tillämpas denna strategi aktivt. Eftersom den svenska strategin är ovanlig, finns det mycket lite internationell forskning som direkt belyser denna. Dock bedrivs internationell forskning om fenomen som även kan inträffa under ett svårt haveri i ett svenskt verk.

Det finns kvarvarande osäkerheter förknippade med den svenska strategin som behöver belysas ytterligare genom forskning. Genom den svenska strategin undviks troligen en stor inledande interaktion mellan betong och smälta. Å andra sidan kan ångexplosioner inträffa när smältan faller i djupt vatten. Forskningen på svåra haverier inriktas nu på att visa om de lösningar som har valts ger ett tillräckligt skydd för omgivningen, vilket vi idag håller för troligt med vissa osäkerheter som nämnts ovan.

Utgående från regeringens och myndighetens beslut i slutet av 1980-talet har myndigheten och tillståndshavarna tillsammans fortsatt att bedriva forskning om svåra haverier samt följa upp internationell forskning.

---

[3] Konsekvensutredning av Statens kärnkraftinspektions förslag till föreskrifter (SKIFS 2004:2) om konstruktion och utförande av kärnkraftsreaktorer, Statens kärnkraftinspektion 2004-10-07.

1.2 Projektets syfte

Projektet syftar till att visa om de lösningar som har valts i den svenska strategin för haverihantering ger ett tillräckligt skydd för omgivningen. Detta sker genom att få fördjupad kunskap om dels viktiga fenomen vid härdsmälteförlopp, dels mängden radioaktivitet som kan släppas ut till omgivningen vid ett svårt haveri.

För att nå syftet och i enlighet med rekommendationerna från APRI-7 (SSM rapport 2012:12) har projektet arbetat med följande uppgifter:

- att följa den internationella forskningen inom svåra haverier och utvärdera resultaten för att erhålla en god bedömningsgrund av de utsläppsbegränsande åtgärderna i svenska kärnkraftsreaktorer.
- att fortsätta att stödja forskningen på KTH och Chalmers om svåra haverier.
- att speciellt studera vissa fenomen som t ex smältans kylbarhet i reaktortanken och i reaktorinneslutningen samt haverikemi.

1.3 Organisation och arbetsformer

Projektet har bedrivits under åren 2012 - 2014 med en total kostnadsram på 21,6 MSEK. SSM och kraftföretagen har bidragit med ungefär hälften var till denna budget. Arbetet inom projektet har varit uppdelat i 9 delprojekt med var sin delprojektledare.

Deltagande i CSARP - NRC:s forskningsprogram

Delprojektledare har varit Wiktor Frid, SSM. En redogörelse för denna verksamhet ges i avsnitt 2.1

Deltagande i SARNET – Integration av EU:s forskning inom svåra haverier

Delprojektledare har varit Ninos Garis, SSM. En redogörelse för denna verksamhet ges i avsnitt 2.2

Deltagande i ISTP – International Source Term Programme

Delprojektledare har varit Henrik Glänneskog, Vattenfall. En redogörelse för denna verksamhet ges i avsnitt 2.3.

Deltagande i THAI 2 – Studier av hur vätgas, jod och aerosoler uppför sig i inneslutningen

Delprojektledare har varit Wiktor Frid. En redogörelse för denna verksamhet ges i avsnitt 2.4.

Deltagande i BIP 2 – Jodkemi i reaktorinneslutningen

Delprojektledare har varit Prof. Christian Ekberg. En redogörelse för denna verksamhet ges i avsnitt 2.5.

Uppföljning av Fukushima-händelsen

Delprojektledare har varit Oddbjörn Sandervåg. En redogörelse för denna verksamhet ges i avsnitt 2.6.

KTH:s forskning inom svåra haverier

Forskningen vid KTH beskrivs i kap. 3 och har följts upp av styrgruppen genom två möten per år.

Under tidigare APRI-projekt har betydande framsteg av förståelse av de fysikaliska fenomen som inträffar i samband med svårt härdhaveri gjorts. Dessa insikter har resulterat i bedömningen att endast deterministisk analys av fenomen såsom kylbarhet och ångexplosioner ej är tillräckligt för att få adekvat kunskap om hur fenomenen påverkar haveriförloppet. Därför har inom APRI 8 en så kallad Risk Oriented Accident Analysis Methodology (ROAAM) utvecklats som kombinerar probabilistiska metoder med deterministiska. Denna metod bedöms kunna ge relevanta verktyg för att analysera härdsmälteförlopp i anläggningarna. Detta projekt löper över fem år och i denna APRI 8 rapport redovisas forskningsresultaten efter tre år.

Chalmers forskning inom svåra haverier

Forskningen vid Chalmers beskrivs i kap. 4 och har följts upp av styrgruppen genom ett möte per år. Forskningen under perioden har behandlat jod- och ruteniumkemi.

Forskningen rörande jodkemi har bl.a. omfattat hur organisk jod bildas i inneslutningen, hur organisk jod fångas i vatten och hur jod reagerar med färgytor. Denna forskning redovisas i avsnitt 4.1.

Ruteniumforskningen var inriktad på kemiförhållanden i vattenfas, växelverkan mellan rutenium och ytor i inneslutningen, återförångning och växelverkan med jod. Denna forskning redovisas i avsnitt 4.2.

Handbok i haverikemi

Arbetet med att ta fram en handbok i haverikemi har pågått under APRI 8 - perioden. Haverikemihandboken finns i dagsläget i en remissversion. Ytterligare bearbetning behövs dock innan den kan ges ut.

1.4 Erfarenhetsutbyte och seminarier

Ett slutseminarium med ca 60 deltagare arrangerades i APRI:s regi den 4 - 5 februari 2015 på Steningeviks konferens, Märsta. Seminariets syfte var att presentera det arbete som utförts och de resultat som erhållits inom projektet APRI 8. Ett annat syfte med seminariet var också att ge möjlighet till diskussioner mellan representanter för kraftverken och de som deltagit i APRI:s arbete.

1.5 Ekonomi och rapportering

Ekonomiskt har en viss omfördelning skett mellan olika delprojekt och några nya delprojekt har tillkommit men den totala budgetramen har innehållits.

De olika delprojekten har genererat publicerade artiklar, reserapporter och dylikt vilket framgår av referenslistan i varje kapitel.

2. INTERNATIONELL FORSKNING INOM SVÅRA HAVERIER

2.1 CSARP – NRC:s Forskningsprogram

CSARP står för ”Cooperative Severe Accident Research Programme” och var från början den amerikanska kärnsäkerhetsmyndigheten NRC:s (Nuclear Regulatory Commissions) forskningsprogram om svåra haverier. Numera deltar de flesta kärnkraftsländer, inklusive Sverige och Finland, i CSARP-programmet där man utbyter forskningsresultat och erfarenheter samt gemensamt diskuterar inriktning och prioriteringar av fortsatt forskning inom området svåra haverier. CSARP-möten hålls årligen i september månad i USA.

I direktanslutning till ett CSARP-möte hålls ett MCAP-möte (MELCOR Cooperative Assessment Program) om applikationer av MELCOR-koden. MELCOR har blivit ett väletablerat verktyg för analys av svåra haverier och antalet användare världen över växer. MELCOR används mer och mer för beräkningar på nya reaktorkoncept och för haveriscenarier med stora härdskador.

Under CSARP-mötena redovisas forskning om olika haverifenomen och detta gäller speciellt de internationella projekt som pågår inom området, som t ex OECD MCCI 2, OECD SERENA, OECD BIP 2, PHEBUS, SARNET, etc. En annan punkt på dagordningen är utveckling och validering av olika programkoder. En tredje punkt berör kodutveckling för nya reaktorkoncept. Under CSARP-mötet för år 2011 hölls även en session om händelsen i Fukushima.

2.2 SARNET2 - Integration av EU:s forskning inom svåra haverier

I april 2004 bildades nätverket SARNET (Severe Accident Research – NETwork of excellence) för att bl.a. samordna forskningen inom svåra haverier inom EU. Avsikten var att SARNET efter en 4-års period skulle leva vidare av egen kraft. Så blev dock inte fallet, utan i början av 2009 bestämdes att projektet skulle fortsätta, dvs. SARNET 2, och pågå under fyra år (2009-2013) med fortsatt stöd från EU.

De huvudsakliga målen med SARNET 2 var att:

- Öka kunskapen om svåra haverier for att minska osäkerheten för kvarstående frågor för att öka reaktorsäkerheten genom experiment och analysarbete,
- Koordinera forskningsinsatser och expertis i Europa,
- Ta hand om forskningsdata och sprida kunskap.

I SARNET 2 medverkade 22 länder inom EU samt Schweiz, Kanada, USA, Rep. Korea och Indien med totalt 43 organisationer. Från svensk sida har KTH och Chalmers medverkat.

Forskningen i SARNET har redovisats och diskuterats på konferenser, den senaste var i oktober 2013 och ytterligare en planeras till mars 2015.

Arbetet i SARNET kommer i framtiden att bedrivas inom ramen för projektet NUGENIA, som är en icke vinstdrivande organisation som ska hantera forskning och utveckling av fissionsreaktorer med fokus på generation II och generation III.

2.3 ISTP - International Source Term Programme

Mellan 1988 och 2012 pågick PHEBUS-projektet i Cadarache i södra Frankrike. I detta projekt genomfördes kontrollerade härdsmältor i en specialkonstruerad anläggning med avsikten att studera härdsmältans beteende vid ett antaget reaktorhaveri. Dessutom studerades hur fissionsprodukter frigjordes från en överhettad reaktorhärd och deponerades i reaktorns primärsystem och dess inneslutning. Resultaten från dessa experiment har redovisats i tidigare APRI-projekt.

Under de senaste cirka tio åren har det pågått ett uppföljande forskningsprogram, ISTP (International Source Term Programme), som kom till eftersom alla observerade fenomen i PHEBUS inte fullt ut kunde förklaras. I viss mån har ISTP också haft som syfte att försöka behålla kritisk kompetens i flera forskningsorganisationer efter PHEBUS-projektets avslutande. Till skillnad från de storskaliga PHEBUS-experimenten har alla experiment i ISTP genomförts i laboratorie-skala där avgränsade system studerats, för att på en detaljerad och mekanistisk nivå kunna förstå varför vissa förlopp ser ut som de gör. Denna typ av experiment brukar få den engelska benämningen *Separate Effects Tests*.

Eftersom en mindre del av finansieringen av ISTP kommer från EU har Sverige kunnat ta del av resultaten under tiden programmet pågått. Under 2014 avslutades även ISTP och fortsatta aktiviteter med avsikt att förklara observerade fenomen i PHEBUS sker på nationell nivå.

Innehållet i ISTP har varierat något under åren men under APRI 8-perioden har det bestått av tre delprojekt:

1. CHIP
2. EPICUR
3. VERDON

I samtliga delprojekt är avsikten att använda resultaten till modellutveckling och/eller verifiering av enskilda moduler i programkoder för simulering av svåra haverier. Nedan följer en sammanfattning av varje delprojekt i ISTP under APRI 8-perioden.

2.3.1. CHIP

Experimenten i CHIP genomförs av Institut de Radioprotection et de Sûrité Nucléaire (IRSN) i Frankrike och har som syfte att studera reaktioner och reaktionskinetik för fissionsprodukter vid hög temperatur i primärsystemet. Den centrala fissionsprodukten i detta sammanhang är jod, och avsikten är att förstå och mekanistiskt kunna modellera reaktioner mellan jod och ämnen som kan interagera med jod i primärsystemet. Detta åstadkoms genom att var för sig studera systemen [I, O, H], [Cs, I, O, H], [Mo, Cs, I, O, H] och [B, Cs, I, O, H]. Experimenten har genomförts både i den stora CHIP-anläggningen och i två mindre anläggningar benämnda GAEC och CHIPINIO. Projektet har pågått i många år och brottades initialt med

stora utmaningar vad gäller experimentutrustning och kvalificering av analysinstrument. De senaste åren har dessa praktiska frågor lösts och under APRI 8 har flera lyckade experiment genomförts inom projektet.

Experimenten genomförs på så sätt att de aktuella fissionsprodukter som ska studeras tillförs tillsammans med ånga och ett bärgasflöde av argon (Ar) till en rörugn indelad i olika temperturzoner. Fissionsprodukterna får reagera vid hög temperatur och därefter analyseras reaktionsprodukterna vid de lägre temperaturer som råder nedströms i ugnen. Stor vikt har lagts vid att injiceringen av de olika fissionsprodukterna ger en homogen blandning så att anläggningsspecifika fenomen kan uteslutas i så hög grad som möjligt. En förenklad skiss av experimentanläggningen visas i Figur 2.1.

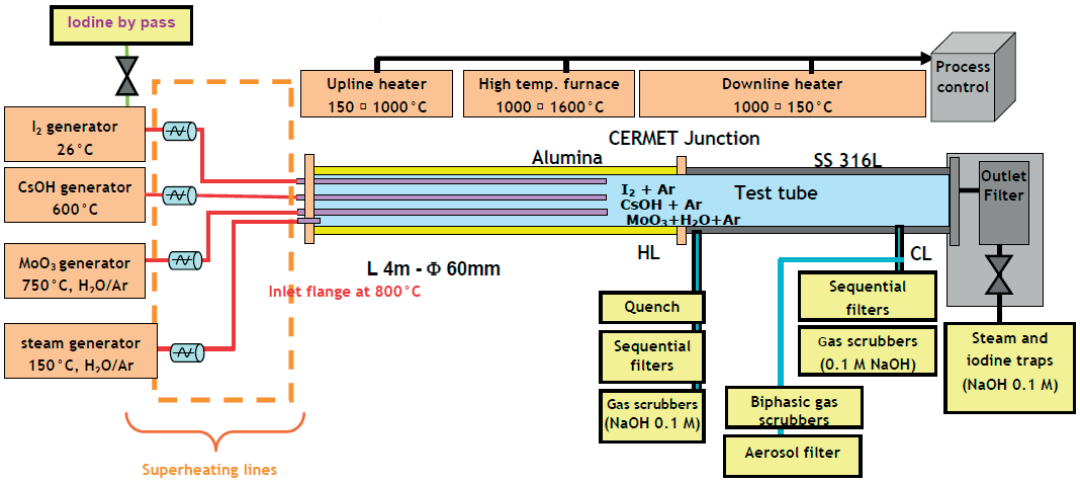

Figur 2.1. *Skiss av experimentanläggningen CHIP. Reaktanterna injiceras från speciella generatorer in i en rörugn där de reagerar. Reaktionsprodukterna analyseras med olika metoder i olika temperaturzoner nedströms rörugnen.*

De viktigaste resultaten från CHIP sammanfattas kort nedan:

- En observation som gjordes relativt tidigt var att molybden (Mo) effektivt konsumerar cesium (Cs) och bildar cesiummolybdater ($Cs_2Mo_xO_y$). Därigenom undertrycks reaktioner mellan jod (I) och cesium så att jod kan transporteras genom ”primärsystemet” som gasformig elementär jod (I_2) istället för som cesiumjodid (CsI). Effekten är mycket tydlig under oxiderande förhållanden (god tillgång på ånga) och vid måttliga temperaturer - något som i CHIP brukar betecknas som ”cold leg conditions”. Under reducerande förhållanden (mycket vätgas och lite ånga) observerades dock inte någon påverkan från Mo på jodkemin.
- Termodynamiska jämviktsberäkningar visar att nästan all jod bör existera som vätejodid (HI) i ett primärsystem med en oxiderande atmosfär. I CHIP observerades dock att mer än 50 % av all jod förelåg som I_2. För att förklara denna skillnad mellan beräkningar och experiment framkastades hypotesen att det råder kinetiska begränsningar som gör att en del reaktioner som involverar jod inte hinner att gå till jämvikt. Orsaken till detta är att vissa re-

aktioner tar lång tid och temperaturen snabbt sjunker vilket tillsammans gör att den kemiska sammansättningen ”fryser” i ett visst läge, vilket i detta fall innebär att I_2 blir en dominerande jodform. Efterhand som fler experiment har genomförts i CHIP har hypotesen stärkts och man har därför implementerat en ny kinetisk modell i modulen SOPHAEROS i ASTEC-koden som på ett bra sätt kan förutse experimentella resultat vad gäller frigörelse av gasformig jod (I_2 och HI).

- Vid reducerande förhållanden kunde ingen I_2 detekteras. Vid dessa förhållanden kunde dock en viss förekomst av CsI observeras.
- Inverkan av bor på jodkemin vid höga temperaturer är fortfarande oklar. Detta undersöks närmare i framtida experiment som dock inte lyder under ISTP. I dessa experiment kommer också betydelsen av styrstavsmaterial (Ag, In, Cd) att studeras.

Det är viktigt att komma ihåg att CHIP-experimenten inte representerar en hel sekvens vid ett svårt haveri utan bara det skede då Mo och Cs existerar samtidigt. I verkligheten kommer en stor mängd Cs att frigöras tidigare än Mo och denna mängd Cs kommer inte att kunna bilda cesiummolybdater. I PHEBUS-experimenten studerades hela haverisekvensen, och en del av denna sekvens utgjordes av den situation som studeras i CHIP.

2.3.2. EPICUR

EPICUR-anläggningen i Cadarache konstruerades med syftet att studera bildning och frigörelse av organisk jod från målade prov-bitar, s.k. ”kuponger”, på vilka det i förväg deponerats elementär jod (I_2). De målade kupongerna bestrålas under olika långa tider i olika sorters atmosfärer och dessutom varieras temperaturen, doshastigheten och den initiala jodkoncentrationen på kupongen. Genom åren har närmare 30 experiment utförts i anläggningen. Under APRI 8 har framför allt betydelsen av långa bestrålningstider (>30 h) undersökts i EPICUR. Generellt samlar EPICUR en stor mängd observationer för bestrålade system med olika miljömässiga förutsättningar. Avsikten är inte att förklara mekanismer i detalj utan istället att se trender, t.ex. hur andelen frigjord organisk jod förändras med ökad initial jodkoncentration på kupongen.

De viktigaste resultaten från EPICUR under APRI 8 sammanfattas kort nedan:

- Frigörelsegraden av organisk jod förändras inte när den initiala jodkoncentrationen på kupongen är $\leq 9{,}5\times10^{-4}$ mol(I)·m^{-2}. Om den initiala jodkoncentrationen är högre än detta värde minskar dock frigörelsegraden av organisk jod. En hypotes har framkastats inom projektet att detta skulle bero på olika sorters kemiska säten för organisk jod och I_2.
- Frigörelsegraden av organisk jod minskar med ökande luftfuktighet.
- En temperaturökning från 80°C – 120°C påverkar inte frigörelsegraden av organisk jod.
- Frigörelsegraden av organisk jod ökar med ökande doshastighet.

Mekanistiska förklaringar till observationerna försöker man hitta genom arbeten som utförs separat av IRSN och som inte rapporteras inom ISTP. Vissa insikter därifrån har dock redovisats för ISTP. Bland annat har en viktig hypotes som det verkar finnas starkt stöd för lagts fram, avseende att det ska finnas olika sorters kemiska säten för elementär jod och organisk jod när de fastnar på epoxy-färger. Elementär jod skulle då vara bundet till reversibla säten medan organisk jod skulle vara bundet till irreversibla säten.

2.3.3. VERDON

Experimentprogrammet VERDON genomförs i det franska atomenergiorganet CEA:s (Commissariat à l'Energie Atomique) regi och experimenten utförs i deras anläggningar i Cadarache i södra Frankrike. Det övergripande syfte är att studera frigörelsen av fissionsprodukter från högutbränt bränsle då tidigare studier främst har använt sig av medelutbränt bränsle. Under APRI 8 har fyra experiment genomförts i anläggningen där överhettning och ibland smältning av enskilda kutsar har framkallats under kontrollerade former. Experimenten har skiljt sig åt vad gäller typ av bränsle (MOX eller UO_2-bränsle), oxiderande respektive reducerande miljö och i viss mån också graden av upphettning. Vid varje experiment har smälttemperatur, identifiering av gasformiga fissionsprodukter och hastigheter för frigörelsen noga följts och efteråt har också deponerade fissionsprodukter på ytor i experimentutrustningen analyserats.

VERDON använder sig av mycket avancerad utrustning både för experiment- och analysdelen. Ett laboratorium har specialinretts för att kunna utföra alla experimenten där bland annat extra förstärkning av golvet har varit nödvändig för att klara lasterna från den tunga utrustningen. En förenklad skiss av experimentanläggningen visas i Figur 2.2.

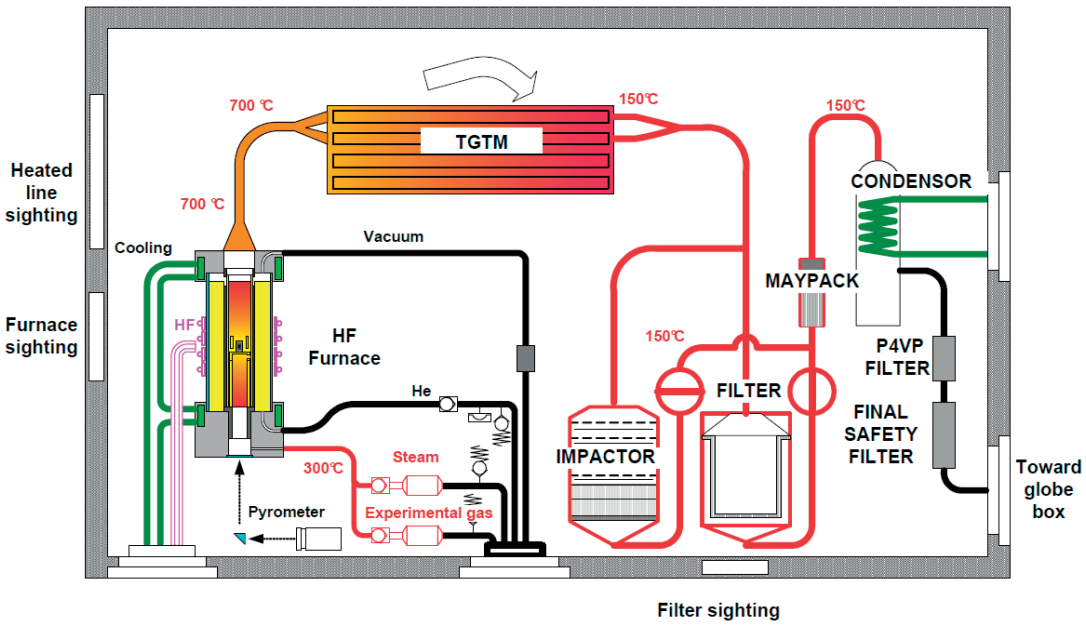

Figur 2.2. *Skiss av experimentanläggningen VERDON. Bränsleprovet upphettas i en ugnsdel och sedan analyseras frigjorda fissionsprodukter i och efter ett termogradientrör vid ugnens utlopp.*

Varje bränsleprov som ska testas består av två stycken högutbrända UO_2- eller MOX-kutsar vilka placeras mellan två kutshalvor av utarmad UO_2. De två hela provkutsarna härstammar från en av energibolaget EDF:s (Électricité de France) reaktorer och har inför experimentet neutronbestrålats i en forskningsreaktor för att få en lämplig fördelning av lång- och kortlivade fissionsprodukter. Kutsarna omges av en liten bit kapsling av materialet M5 (ett nyutvecklat kapslingsmaterial som är mer resistent mot korrosion än tidigare material). När ett experiment genomförs sker uppvärmning enligt en noga bestämd temperaturramp med vissa platåer där provtagning på gasfasen utförs. Ett exempel på temperaturramp och tidpunkter för provtagning ges i Figur 2.3.

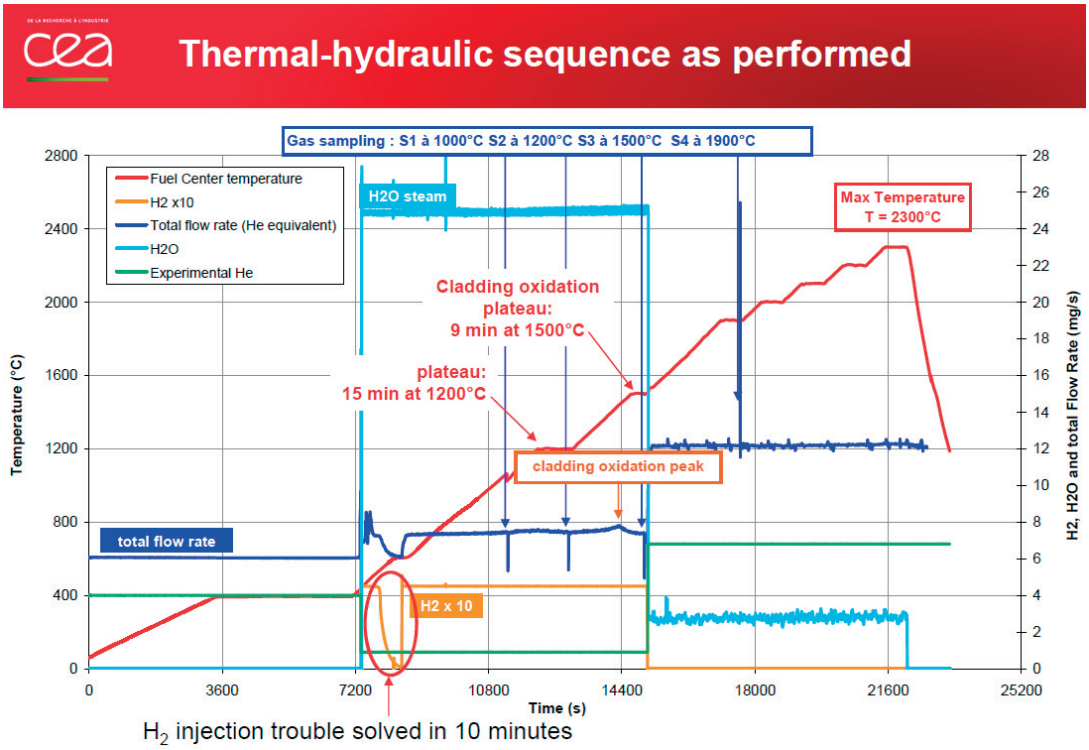

Figur 2.3. *Temperaturprofilen för ett av experimenten i VERDON. Provtagning på gasfasen görs vid de temperaturplatåer som bestämts i förväg. I diagrammet syns också de tidpunkter då injicering av ånga och vätgas görs för att simulera oxiderande och reducerande atmosfärsförhållanden.*

De viktigaste resultaten från VERDON sammanfattas kort nedan:

- Det frigörs mer rutenium (Ru) från en UO_2-kuts jämfört med en MOX-kuts. Vid oxiderande förhållanden med god tillgång på ånga frigjordes ~65 % av innehållet av Ru från en UO_2-kuts, att jämföra med några få procent från en MOX-kuts. Det är de oxiderade formerna av Ru, framför allt rutenium-tetroxid (RuO_4), som är flyktiga. Idag finns det ingen mekanistisk förklaring till denna observation, men det är sedan tidigare känt att en MOX-matris generellt är svårare att oxidera än en UO_2-matris. En annan bidragande faktor kan vara att inventariet av Ru är högre i MOX-bränsle än i UO_2-bränsle, och därmed kan det ta längre tid att oxidera detta.

- Jod frigörs som väntat ganska tidigt när bränslet överhettas och deponerar sedan på ytor i termogradientröret med gradvis sjunkande temperatur. Om luft därefter tillförs systemet kommer en mycket stor andel av denna deponerade jod att återförångas och transporteras vidare.
- Frigörelse av Cs var snabb och startade tidigt vid uppvärmningen. Redan vid ~1200°C frigjordes ~10 % av det initala Cs-innehållet i kutsarna. När temperaturen ökade till 1500°C frigjordes ~40 % av det initiala Cs-innehållet i kutsarna, och när temperaturen ökade ytterligare var frigörelsen av Cs total. Temperaturplatån vid 1200°C var avsiktligt vald för att simulera LOCA-förhållanden, och observationen av Cs-frigörelse vid så låga temperaturer var inte väntad.
- Vid oxiderande förhållanden var frigörelsen av halvflyktiga element som barium (Ba) och molybden (Mo) i princip lika omfattande som för flyktiga element. Mo frigjordes mycket snabbt och vid experimentets slut var frigörelsen fullständig. Ba frigjordes något långsammare och vid experimentets slut hade ~80 % av den initiala mängden i kutsen frigjorts.
- Frigörelsen av lättflyktiga element som ädelgaserna xenon (Xn), krypton (Kr), halogenen jod (I) och alkalimetallen cesium (Cs) var fullständing. Frigörelsen av ädelgaserna skedde som en serie skurar vid olika temperaturer i temperaturområdet 700°C och uppåt, se Figur 2.4.

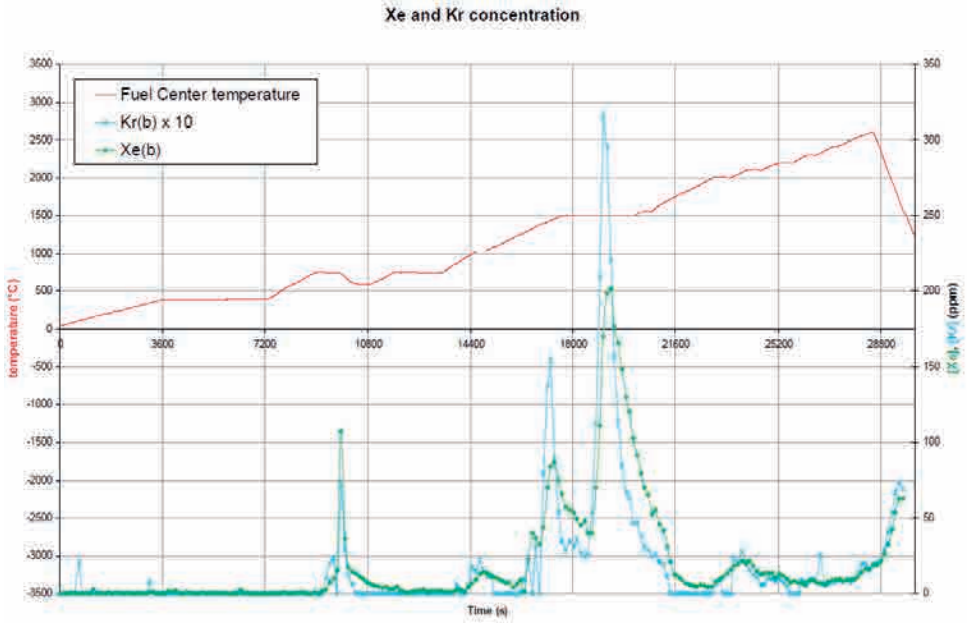

Figur 2.4. *Frigörelse av Kr och Xe från bränslekutsar i VERDON. Frigörelsen sker i form av olika skurar vid olika temperaturer i området 700 °C och uppåt. Notera att skalan för Kr är förstorad 10 gånger för att få en tydligare utformning av trender i diagrammet.*

Inom SARNET har en speciell arbetsgrupp bildats för att analysera resultaten från VERDON. Ungefär tio organisationer är representerade i denna arbetsgrupp vilka undersöker hur olika koder (MELCOR, ASTEC, MAAP, ATHLET-CD m.fl.) kan simulera och återskapa observationerna i VERDON. Sverige finns dessvärre inte representerat i arbetsgruppen.

2.4 THAI2 - Thermal-hydraulics, Hydrogen, Aerosols and Iodine project

2.4.1. Bakgrund

THAI-anläggningen som ligger i Eschborn utanför Frankfurt har använts av det nationella, tyska THAI-projektet sedan 1998 för att undersöka frågeställningar kring bl.a. strömning och transport i inneslutningen, vätgasförbränning, jodkemi och aerosoler under svåra haveriförhållanden.

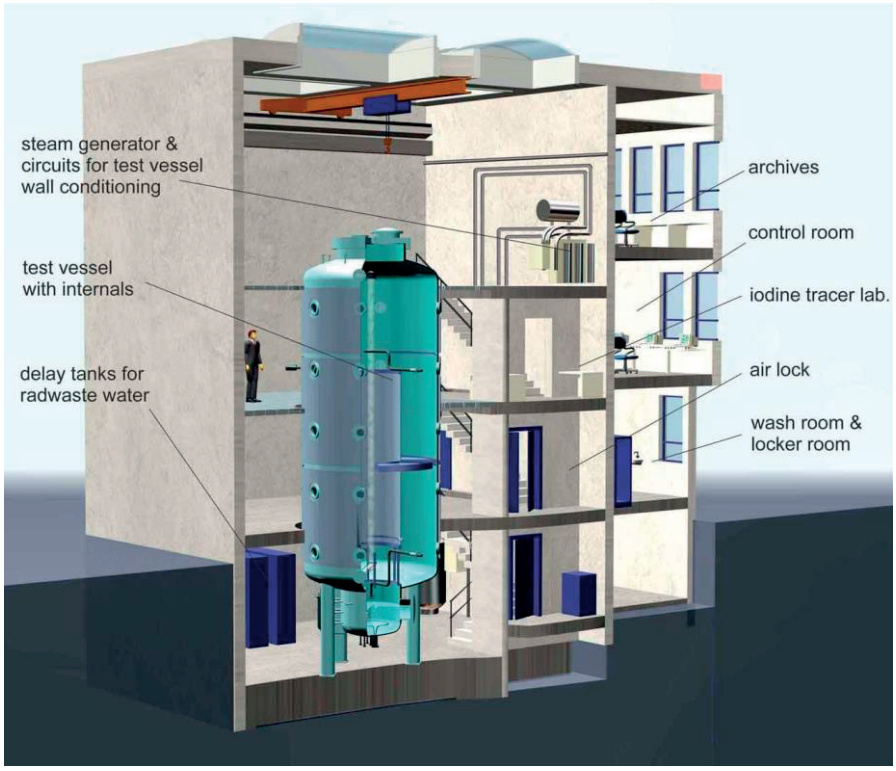

Figur 2.5 *THAI-anläggningen vid Becker Technologies i Eschborn, Tyskland.*

2.4.2. Kort beskrivning av första etappen (THAI-1)

En första etapp av projektet, OECD-THAI, pågick under åren 2007-2009. Totalt genomfördes över 70 försök. Nedan redovisas projektets olika testområden med huvudsakliga slutsatser för respektive område:

- *Helium/hydrogen Material scaling (HM1-5)*
  Testerna bekräftade att helium kan användas istället för vätgas vid undersökningar av flödesdynamiska fenomen i inneslutningsatmosfären. Beräkningar med olika beräkningskoder (både av LP- och CFD-typ) visade att stora framsteg skett i modelleringen av stratifiering och omblandning.

- *Hydrogen Deflagration (HD1-29)*
  Genom att variera olika parametrar såsom initialtryck och -temperatur, ånghalt, förbränningsriktning och gasernas spatiala fördelning kunde deras inflytande på tryck- och temperaturförlopp, flamfrontspropagering och förbränningens fullständighet bestämmas.
- *Hydrogen Recombiner (HR1-30)*
  Kunskapsbasen kring olika PAR (Passive Autocatalytic Recombiner)-typers prestanda under typiska svåra haveriförhållanden ökade markant som ett resultat av HR-testerna. Detta gäller både PAR-enheternas förmåga att komma igång, deras rekombineringshastighet och potentialen för PAR-inducerad antändning. En särskilt viktig slutsats var att PAR-inducerad antändning bara är möjlig i ett relativt begränsat område i Shapirodiagrammet, som visar zoner för självantändning.och explosion i en gasblandning som innehåller vätgas, luft och vattenånga i olika relativa koncentrationer.
- *Interaction of metal iodides with passive autocatalytic recombiner (HR-31)*
  Testet visade att cesiumjodid kan brytas ner och omvandlas till gasformig jod i en omfattning som kan påverka källtermen till inneslutningen.
- *Passive autocatalytic recombiner poisoning (HR-32)*
  Testet visade att förgiftning av PAR-enheterna i form av aerosoler och jod inte förefaller påverka prestandan i någon större utsträckning.
- *Aerosol wash-down (scoping test)*
  Testet visade att svagt lutande ytor utsätts för nedtvättning av CsI-partiklar med en tidskala som varierar från minuter till timmar. Tidsskalan och även omfattningen/effektiviteten beror på vattenflödet och ytans egenskaper.

Det experimentella arbetet kompletterades med analysverksamhet genom att en analytisk arbetsgrupp etablerades med målsättningen att utvärdera testresultaten för att validera och vidareutveckla modeller och analysverktyg såsom ASTEC CPA, COCOSYS, MELCOR, REKO-DIREKT, SPARK och ANSYS CFX-13.

Projektet redovisades i en slutrapport, se ref. [1].

2.4.3. Beskrivning av andra etappen (THAI-2)

Projektets andra etapp, OECD-THAI2, påbörjades 2011 och avslutades hösten 2014. Projektet undersökte följande fyra frågeställningar:

I. *Release of gaseous iodine from a flashing jet (Iod29)*
Försöket syftade till att undersöka hur gasformig jod kan frigöras vid flashflödet efter ett ånggeneratortubbrott.

II. *Deposition of molecular iodine on aerosol particles (Iod25-26)*
Deponering av jod på aerosoler kan konkurrera med t.ex. jods interaktion med färg och en förståelse för fenomenet behövs för att kunna bestämma källtermen.

III. *Hydrogen combustion during spray operation (HD33-35)*
Syftet var att undersöka hur vätgasförbränning påverkas av sprinkling, dvs. om förloppet lindras pga. kylning eller förvärras pga. ökad turbulens.

IV. *Onset of PAR operation in case of extremely low oxygen content (HR33-42)* Försöken syftade till att undersöka om/hur rekombineringen kommer igång vid låga eller mycket låga syrgashalter, vilka kan förekomma t.ex. i ett sent skede av ett haveri i samband med betong/smälta-interaktion (MCCI).

2.4.4. Resultat och slutsatser

Resultat och slutsatser från respektive område sammanfattas nedan:

I. Testet verkar tyvärr ha blivit misslyckat då man trots ansträngningar med förberedande analyser inte fick rätt kemiska förhållanden för att kunna dra relevanta slutsatser. Ingen gasformig jod detekterades i THAI-behållaren (halterna hamnade under detektionsgränsen för instrumenteringen).

II. Experimenten visade tydligt skillnaden mellan reaktiva (Ag) och icke-reaktiva (SnO_2) aerosolers förmåga att påverka inventariet av gasformig jod. Jod var främst bundet till aerosoler i försöken med Ag-aerosoler som möjliggör s.k. kemisorption, medan främst i gasform i försöken med SnO_2 som endast tillåter svagare s.k. fysisorption. Minskningen av gasformig jod var betydligt effektivare med Ag-aerosoler (40 gånger snabbare än med SnO_2).

III. De genomförda försöken har gett kunskap om sprinklingens inverkan på flampropagering, såsom inverkan från droppstorlek (mindre droppar ger mer kylning, större droppar ger mer omblandning men mindre kylning), förbränningens riktning (uppåt/nedåt) samt sprinklingens varaktighet innan antändning. Testerna bekräftade också reproducerbarheten i testerna.

IV. Försöken har ytterligare utökat databasen för rekombinatorernas prestanda med nya förhållanden. Testerna visar att rekombineringen startar snabbt när O_2 frigörs i en inert atmosfär. För $\Phi>2$ (där $\Phi = 2c(O_2)/c(H_2)$) blir ökningen i verkningsgrad väldigt liten för ökande syrgashalt.

Arbetet som genomförts inom THAI2 presenterades och diskuterades på det avslutande seminariet i november 2014 i Frankfurt. Den allmänna slutsatsen från slutseminariet var att projektet har levererat värdefulla och högkvalitativa data för validering av koder och förbättrad förståelse av haverifenomen rörande jod, vätgas och aerosoler. Projektet kommer att slutrapporteras under 2015.

2.4.5. Analytiskt arbete

Även i THAI2 har en analytisk arbetsgrupp etablerats för att samla den analytiska verksamhet som bedrivits av deltagarna (kodutveckling, validering, pre- och post-test-beräkningar m.m.). Deltagarna har varit mest aktiva inom de vätgasrelaterade områdena III och IV där man bl.a. tagit fram en förbättrad modell för vätgasrekombinering under substökiometriska syrgasförhållanden (oxygen starvation). Exempel på koder som använts är följande:

- CFX (FZJ, GRS, KAERI)
- FLUENT (VTT)
- ASTEC (IRSN)
- SPARK (IRSN)
- GASFLOW (KIT)

- GOTHIC (AECL)
- MELCOR (UJV)

Inom område I och II har främst IRSN och GRS varit aktiva, men även JAEA har gjort beräkningar på jodkemi/aerosoler (med koden ART/THALES2). Vissa framsteg har nåtts med att skapa en modell som beskriver jods uppförande i en flashande jetstråle, där en termohydraulisk modell beskriver flashningshastighet och droppar-nas storleksfördelning och en mekanistisk modell utvecklats för att beskriva kemin.

2.4.6. Planerad fortsättning (THAI-3)

En eventuell fortsättning på projektet har diskuterats och de områden som identifierats som intressanta är följande:

1. PAR-prestanda under motströmsflöde
2. Vätgasdeflagration och flamfrontspropagering i ett system med två sammankopplade utrymmen
3. Frigörelse av fissionsprodukter från en bassäng vid förhöjda temperaturer
4. PAR-prestanda och antändningspotential vid sprinkling

Några av idéerna bygger på att man planerar att utveckla THAI-anläggningen med en andra tank under år 2015. Varje ämnesområde kommer att kunna rymma flera försök (3–5 st).

Projektförslagen diskuterades vidare på ett expertmöte i anslutning till slut-seminariet i november 2014. Förslag nummer 4 kommer eventuellt att ersättas med en mer komplex, integral studie av vätgasdeflagration och flampropagering ovanför en vattenbassäng under samtidig frigörelse av fissionsprodukter.

Generellt verkade det finnas ett tydligt intresse för att delta i THAI3, varför utsik-terna för en fortsättning bedöms som goda.

2.4.7. Referenser

[1]. OECD/NEA THAI Project – Hydrogen and Fission Product Issues Relevant for Containment Safety Assessment under Severe Accident Conditions, Final Report, NEA/CSNI/R(2010)3, https://www.oecd-nea.org/nsd/docs/2010/csni-r2010-3.pdf.

2.5 BIP 2 - Behaviour of Iodine Project

The Behavior of Iodine project 2 (BIP-2) was ending in September 2014 after a 6 months extension. A six month extension could be realized due to that South Korea decided to join BIP-2 in the last year of the 3 year project.

The objectives of the BIP-2 project were

- Improvement of the mechanistic understanding of iodine absorption
- Understanding of the formation of organic iodides
- Comparison of results being obtained within BIP-1 and EPICUR

The program and results of BIP-1 were published in 2011 and described in the previous APRI-7 report. The program content of BIP-2 was very similar to the studies

performed at Chalmers. At Chalmers the main focus was on the in Sweden used epoxy paint (Teknopox Aqua VA ^{TM}) and zinc primer (Interzinc 315^{TM}). The outcome of BIP-2 is summarized in an OECD-NEA publication which will enter the public domain at the beginning of 2015.

A main focus of the studies at AECL (the hosting organization) during BIP- 2 was on the sorption of iodine on polymers behavior from both aqueous and gaseous phase. Iodine was found to be primarily adsorbed on paint, followed by Nylon and TETA cured DOW DER 332 resin. Significant lower absorption from aqueous phase was found for polypropylene (PP) and non-cured DOW DER 661 resin. Compared to the studied paint products, Ripolin and Amerlock, Nylon-66 was the only polymer found to show a significant gas phase absorption of elemental iodine which was corresponding to 1/5 of that of the studied paints. An effect of humidity on the sorption behavior could be found only for Nylon-66.

Similar to the studies at Chalmers, the effects on the sorption behavior on different paint surfaces of chlorine and nitrogen dioxide were investigated. In AECL studies no apparent effect was detected for the iodine absorption after exposure of their paint films for 1 h with 5 ppm of the gases.

Additionally, to the epoxy paint films discussed within BIP-2 zinc primer surfaces were included in the experimental matrix and iodide ions were found to irreversibly bound to the zinc containing surfaces. For solution of pH > 8 a higher loading with iodide ions was observed.

In order to better understand how the water content in the paint films affects the sorption behavior, the water adsorption behavior with and without presence of gamma irradiation (160 h; 2 kGy/h) was studied. No measureable effect of the irradiation was detected and the water absorption and desorption behavior was found to follow atmospheric trends and no conclusions were drawn.

Attempts were made to detect possibly formed chemical bonds resulting from iodine absorption using Raman spectroscopy and FTIR. However, no conclusive results were obtained for C-I or O-I bond formation. Using UV/Vis a possible charge transfer complex of iodine which absorbs at 371 nm was detected.

SEM-EDX studies of the Ripolin samples revealed that they mainly consist of C, O, Si, Ti and in the primer layer additionally Mg and Pb were detected. The iodine was predominately in the surface layer.

Studies of the formation of organics iodides were part of the BIP-2 program. It was found by AECL that all studied polymers and paints formed organic iodides. From polymer coupons that were manufactured without any solvents it was concluded that the formation of organic iodides is a surface phenomenon and not related to water or solvents. The effects of heating up to 80 ^{o}C and pre-exposure to nitrogen dioxide or chlorine were investigated but no effects were detected. GEHOPON epoxy paint, a paint used in German nuclear installations and which is studied in the German THAI test facility, was studied for comparison and was found to form more organic iodides than the Ripolin and Amerlock paint coupons. GEHOPON paint

coupons were also investigated at Chalmers University of Technology for comparison to paint products used in Sweden (see Section 4.1).

The irradiation of commercial available iodine containing organic compounds such as iodophenol, iodobutane and iodoethane showed to form methyl iodide. It was concluded that the amount of formed methyl iodide is dependent on the volatility of the original iodine species. In preliminary tests it was found that methyl iodide can be formed from iodine pentoxide aerosols and iodic acid but in lower yields than from elemental iodine. It needs to be noted that no aerosol production facility was used for the experiments. The commercial available powder of iodine pentoxide was applied as powder on a paint surface.

Water was found to increase the methyl iodide formation from paint coupons leading to the conclusion that the formation of methyl iodide is an aqueous phase process. Chalmers suggest this conclusion to be considered with care as water could promote the formation of elemental iodine.

As of the 13th of October 2014 it has not been decided yet if BIP-2 will be continued further. The proposals written by the partners have been sent for review. Attempts are made to continue the work in a joint project, which would be a continuation of ISTP, which would start with the end of ISTP-1 in spring 2014. The partners have an interest in the modelling of the data and to combine their results with those from other programs such as EPICURE. For this purpose an OECD workshop on iodine behavior modeling is planned for March 2014 in Marseille in connection with the ERMSAR 2014 meeting. Currently partners such as the USA, France and Canada are working on their own national models and consider different phenomena and sources of experimental and theoretical data.

2.6 SERENA – Ångexplosioner i reaktorinneslutningen

Under januari 2002 startades ett OECD/NEA-projekt kallat SERENA – Steam Explosion REsolution for Nuclear Applications. Det övergripande målet med projektet var att få en tillräckligt bra förståelse för ångexplosioner för att kunna göra riskbedömningar av reaktoranläggningar. När projektet avslutades i december 2005 kunde man konkludera dels att reaktortanken skulle motstå postulerade ”in-vessel” ångexplosioner, dels att ”in-vessel” ångexplosioner inte utgör något hot mot inneslutningens integritet. Beträffande ”ex-vessel” explosioner var slutsatsen att det inte gick att utesluta att en ångexplosion skulle kunna hota inneslutningens integritet.

Ett annan slutsats var att olika datamodeller som beräknar förloppen vid ångexplosioner, gav mycket stor spridning i resultaten. Detta kunde tyda på att det finns brister i förståelsen av fenomen relaterade till ångexplosioner i reaktorinneslutningen.

Utvärderingen av resultaten från SERENA-projektet ledde till en rekommendation för fortsatt forskning med syfte att minska osäkerheter och därigenom uppnå större tillförlitlighet i beräkningar av säkerhetsmarginalerna, i synnerhet vad gäller inneslutningsbelastningar.

Fas 2 av SERENA-projektet startade i oktober 2007 och 18 organisationer från 11 länder har deltagit. Huvudsyftet med fas 2 av projektet har varit att bringa klarhet i

ångexplosionsfenomen för prototypiska smältor genom att genomföra ett begränsat antal väl designade experiment med avancerad mätutrustning. Ett annat syfte har varit att tillhandahålla experimentella data för vidareutveckling och validering av ångexplosionskoder. Som stöd till den experimentella delen fanns en grupp vars uppdrag har varit att genomföra för- och efterberäkningar med olika koder samt beräkningar för realistiska ex-vessel BWR- och PWR-haveriscenarier.

Experimenten har genomförts i två testfaciliteter, nämligen TROI vid KAERI (Korean Atomic Energy Research Institute) i Daejon i Korea och KROTOS vid CEA (Commissariat l'Energie Atomique des aux Energies Alternatives) i Cadarache i Frankrike. I TROI har 20 kg prototypisk smälta använts i 3-D geometri medan i KROTOS har 5 kg prototypisk smälta använts i huvudsakligen 1-D geometri.

En serie med sex kompletterande tester vardera i TROI och KROTOS har genomförts, dvs. totalt 12 tester. Grundkompositionen har varit en eutektisk blandning av UO_2 och ZrO_2, dvs. 70 % UO_2 och 30 % ZrO_2, eftersom tidigare TROI-experiment visade att denna sammansättning kan ge spontana explosioner med större verkningsgrad än andra kompositioner. I tabell 2.6.1 visas fyra smältkompositioner som har använts i TROI och KROTOS tester. Smältans temperatur har legat nära den temperatur som ges av realistiska bedömningar av haveriförloppet, med en överhettning mellan 40 och 270 K. För att säkerställa en reproducerbar initiering av potentiella ångexplosionsförlopp, har en trigger använts i alla tester. Testmatrisen för TROI och KROTOS tester visas i Tabell 2.6.2.

Tabell 2.6.1: Fyra kompositioner av smälta i TROI och KROTOS tester.

Material [wt%]	Composition	Situation / Related effect
Mat 1	Oxide corium :70%UO_2-30%ZrO_2	Prototypical material -Reference material/Reactor case
Mat 2	Oxide corium :80%UO_2-20%ZrO_2	Prototypical material, also used in FARO and KROTOS/Reactor case
Mat 3	Sub-oxide corium: 70%UO_2-15%ZrO_2 + 15%Zr	Metal content representative of a reactor situation
Mat 4	Oxide corium : 73%UO_2-20,4%ZrO_2 Structural material: 4.1% Fe_2O_3 1.3% Cr_2O_3 Low volatile Fission Products: 0.3% BaO; 0.8% LaO; 0.2% SrO	Focus on role of large liquidus-solidus large interval Other composition representative of a reactor situation

Tabell 2.6.2: Testmatris för anläggningarna KROTOS och TROI.

Test n°	Conditions (wt. %)	KROTOS	TROI
1	Challenging conditions **Mat 1: 70%UO_2-30%ZrO_2** Vessel: 0.4 MPa- 273K Corium melt: overheating	**KS-1** Jet diameter: 30 mm	**TS-1** Jet diameter: 50 mm
2	Geometry effect **Mat 1: 70%UO_2-30%ZrO_2** Vessel: 0.2 MPa- 333K Corium melt: overheating	**KS-2** 1D Jet diameter: 30 mm	**TS-2** 2 D Jet diameter: 50 mm
3	Reproducibility test-Idem test 2	**KS-3**	**TS-3**
4	Material effect/oxide composition **Mat 2: 80%UO_2-20%ZrO_2** Vessel: 0.2 MPa- 333K Corium melt: overheating	**KS-4** Jet diameter: 30 mm	**TS-4** Jet diameter: 50 mm
5	Material effect/sub-oxide composition/oxidation process **Mat 3: 70%UO_2-30%ZrO_2** Vessel: 0.2 MPa- 333K Corium melt: overheating	**KS-5** Jet diameter: 30 mm	**TS-5** Jet diameter: 50 mm
6	Material effect/oxide composition/large interval of solidification **Mat 4: 70%UO_2-30%ZrO_2+Fe_2O_3+Low volatile Fission Products** Vessel: 0.2 MPa- 333K Corium melt: overheating	**KS-6** Jet diameter: 30 mm	**TS-6** Jet diameter: 50 mm

Följande viktiga observationer har gjorts från experimentella resultat och från analyser:

- Prototypiska smältor är mindre explosiva än icke-prototypiska, som t.ex. aluminiumoxid.

- Verkningsgrad av explosioner, dvs. andel av smältans termiska energi som omvandlas till mekaniskt arbete, har varit mindre än 1 %.

- Explosioner med icke-eutektisk smältkomposition 80 % UO_2-20 % ZrO_2 var något kraftigare jämfört med explosioner med eutektisk sammansättning av smältan, vilket var ett oväntat resultat.

- Oxidationsprocessen under pre-mixing fasen, som föregår själva explosionen, verkar vara viktig för explosionens styrka, sannolikt på grund av vätgasgenerering som stabiliserar ångfilmen som omger smältdroppar.

- Modellering av smältstrålens fragmentering behöver förbättras.

- Kunskapen om, och modellering av, den begränsande effekten av smältdropparnas stelnande för explosionens triggering och styrkan behöver förbättrats. Den viktiga frågan här är inverkan av smältas sammansätning.

- Resultat från KROTOS och TROI tester var tillräckligt konsistenta för att kunna extrapoleras till reaktorförhållanden under förutsättning att osäkerheter hanteras på lämpligt sätt.

Beträffande beräkningskoder har man konstaterat att koderna har förbättrats sedan SERENA 1-projektet. Dock har experimentella data inte kunnat utnyttjas till fullo under projektperioden i vidarutveckling och validering av koder på grund av resursbrist hos organisationer som ansvarar för kodutveckling, och fortsatt arbete krävs. Av den anledningen har projektets Management Board beslutat att förlänga sekretess perioden för experimentella data med två år, till september 2016.

Beräkningar med flera koder för typiska ex-vessel haveriscenarier i BWR- och PWR inneslutningsgeometrier har visat att spridning av resultat (tryck och impulser) är mindre jämfört med motsvarande resultat i SERENA 1-projektet. Man förväntar sig att situationen kommer att förbättrats ytterligare när alla experimentella resultat har bearbetats av kodutvecklarna. I tabell 2.6.3 visas vilka beräkningskoder som har tillämpats i projektet.

Tabell 2.6.3. Beräkningskoder som har använts i reaktoranalyser.

Code	Organisation
MC3D	AECL, CEA + Tractabel, IKE, IRSN, JSI, KAERI, KINS, VTT
TEXAS-V	UWM, VTT, SSM
JEMI (IKEMIX/IKEJET) + IDEMO	IKE
JASMINE	JNES
TRACER-II	KMU

Resultaten visar att beräknade belastningar är något mindre jämfört med resultat från SERENA 1-analyser men spridningen av beräkningsresultat är fortfarande för stor för att man skall kunna göra tillförlitlig bedömning av säkerhetsmarginaler. Samtidigt har man konstaterat att ett specifikt beräkningsprogram kan vara ett adekvat verktyg för riskbedömningar, till exempel i myndighetens tillsynsarbete, men att fortsatt validering och utveckling av koder är önskvärd för att minska osäkerheter och för att öka förtroende för beräkningsverktyg.

SERENA 2-projektet har sammanfattas i en rapport (Integrated report), som beskriver alla experiment i TROI och KROTOS samt redovisar alla analyser och drar slutsatser från projektet. Vidare har beräkningsresultat från reaktoranalyser redovisats i detalj i en separat rapport (Reactor excercise - Synthesis of calculations).

Ett slutseminarium hölls den 13 – 15 november 2012 på CEA i Cadarache (Frankrike).

2.6.1. Referenser

OECD/SERENA Project Report, Summary and Conclusions, 16-Feb-2015, NEA/CSNI/R(2014)15. http://www.oecd-nea.org/nsd/docs/2014/csni-r2014-15.pdf

2.7 Uppföljning av kärnkraftsolyckan i Fukushima-Daiichi

En preliminär sammanställning av erfarenheterna från kärnkraftsolyckan i Fukushima-Daiichi gjordes under APRI-seminariet 2012 [7]. Som det framgick av denna var det inte så mycket av nya fenomen att adressera. Det är snarare på andra områden som konstruktionsförutsättningar, drift och organisation som nya viktiga erfarenheter har gjorts. Dessa områden har behandlats i stresstester, rapporter av olika organisationer och japanska haveriutredningar. Slutsatserna på dessa områden är väl kända och repeteras endast översiktligt här.

Beskrivningen här reflekterar över analysläget vid utgången av november 2014 med fokus på de fenomen som i huvudsak uppträdde i tidsrymden mellan tsunamin och härdsmältorna. Det som är intressant att notera under denna tidsrymd är den varierande tillgången på elkraft och de stora skillnaderna som inträffade i förloppen mellan reaktorerna. En övergripande reflektion är att skydden för olika komponenter kan ha haft stor betydelse. Noterbart är att i de reaktorer som hade viss tillgång till elkraft, och där komponentskydden därför åtminstone delvis var aktiva, inträffade härdsmältorna snabbare än i de reaktorer som inte hade tillgång till el.

Det kan konstateras att antagna scenarier direkt efter kärnkraftsolyckan har utvecklats och ändrats baserat på gjorda analyser och de sparsamma och i vissa fall osäkra data som finns från förloppen. Eftersom analyserna kommer att pågå under avsevärd tid är ytterligare kompletteringar troliga. Det måste konstateras att det än så länge inte finns några slutsatser när det gäller konfiguration och slutläge för härdsmältorna. När sådan information kommer fram kan det finnas anledning att revidera och utvidga denna beskrivning och möjligen kunna dra ytterligare slutsatser.

Viktigt underlag vid reflektion av analysläget har varit Hatamuras rapport, både interrimsversionen [2] och slutversionen [1], Diet-rapporten [3] och INPO-rapporten [5]. Speciellt har de slutsatser som beskrivs i TEPCO:s rapport [8] där vissa slutsatser direkt har kunnat genomgås i gemensam sittning av APRI och TEPCO [6] haft betydelse. Det finns emellertid motstridigheter i materialet där slutsatserna har baserats på en rimlighetsvärdering.

De områden som det kan finnas lärdomar att dra från kärnkraftsolyckan är följande:

- Skydd mot externa händelser,
- Skydd mot svåra haverier,
- Beredskap för olyckor och förmåga att hantera svåra haverier,
- Olyckstolerant instrumentering för att kunna bestämma anläggningens status,
- Bättre förståelse av fenomen som uppträder under svåra haverier.

2.7.1. Utredningar om kärnkraftsolyckan i Fukushima-Daiichi

INPO-rapporten [5], som gjordes på uppdrag av TEPCO, tar upp några övergripande aspekter vid kärnkraftsolyckan. Det var klart att varken TEPCO eller övrig kärnkraftsindustri har varit beredd på att upprätthålla kritiska säkerhetsfunktioner under de extrema villkor som rådde vid Fukushima. Det är troligt att beredskapen för att hantera ett svårt haveri vid andra organisationer inte är så olik den som fanns i Fukushima. Översyn i olika länder har därför identifierat behov för förbättringar på ett flertal områden.

För svenskt vidkommande publicerades den nationella rapporten [10], som svar på de europeiska stress-proven. I denna diskuteras jordbävning, översvämning, extrema väderförhållanden, förlust av elkraft och förlust av den ultimata värmesänkan. Det kunde konstateras att det finns områden som behöver ses över efter erfarenheterna från Fukushima. Detta gäller till exempel utrustning och bemanning för att kunna hantera samtidiga haverier vid flera block på samma kärnkraftverk och sekvenser med att tillföra vatten och etablera värmesänka för härdens kylning vid bortfall av elektrisk kraft.

I INPO-rapporten [5] diskuteras speciellt kraven när det gäller beredskap och haveribekämpning. Det framhålls även positiva lärdomar genom att ha tillgång till skyddad byggnad för ledning av haverihanteringen och att personalen visade stort engagemang och stora insatser för att försöka återställa elkraft och kylning.

INPO efterlyser i sin rapport oberoende utvärdering av säkerheten genom en process för periodisk översyn av anläggningen och värdering av ny information. När det finns indikationer som tyder på en försvagning av säkerhetsmarginaler eller att konstruktionsgränser kan överskridas, ska processer finnas att rätta till sådana svagheter. Speciellt bör möjliga fel med gemensam orsak beaktas och snabbt åtgärdas.

INPO framhåller att haverihantering och strategier för respons mot olyckor inledningsvis måste ge härdens kylning högsta prioritet. I ledningscentret måste medvetande om status för härdens kylning finnas och ändringar i metoden att kyla härden måste övervägas med det övergripande målet att etablera en alternativ hållbar kylmetodik.

INPO understryker vikten av att det finns planer för bemanning för att ta hand om olyckor och utrustning på plats som åtminstone i det korta perspektivet kan sättas in. Det är också viktigt med regelmässiga övningar som är tillräckligt utmanande och realistiska för att förbereda personalen för att möta situationer som kan inträffa. Eftersom olyckor utanför konstruktionsförutsättningarna per definition är okända, är det viktigt att ha robusta rutiner som ger möjlighet för flexibel respons på en haverisituation. INPO tar också upp nödvändigheten av att ha och underhålla en säkerhetskultur som främjar säkerheten.

I Diet-rapporten [3], som togs fram av en oberoende kommission som det japanska parlamentet tillsatte, lades grundorsaken för kärnkraftsolyckan på organisationsmässiga faktorer. I denna pekas det på bristande oberoende i samspelet mellan departement, TEPCO och myndigheterna som ska övervaka säkerheten. Speciellt kritiseras myndigheternas ovilja att anamma kunskap och teknologi som utvecklats utomlands. Rapporten pekar på att det hade funnits många tillfällen att vidta åtgär-

der för att förhindra kärnkraftsolyckan och att TEPCO, med myndigheternas stöd, hade försummat dessa möjligheter. Motivet för att TEPCO aggressivt motsatte sig och fördröjde nya föreskrifter var att det skulle påverka driften vid anläggningarna och försvaga företagets position i eventuella rättsliga tvister.

I Diet-utredningen dras slutsatsen att det fanns organisationsmässiga problem inom TEPCO. Detta gäller mer ingående kunskap, övningar och granskning av utrusning för att hantera svåra haverier. Hade det funnits instruktioner för hur personalen på verken skulle agera vid ett svårt haveri hade en mer effektiv respons på kärnkraftsolyckan varit möjlig. Mer specifikt kritiseras att kontrollen av funktionen för hjälpkondensorn i Block 1 inte gjordes. Rapporten hävdar att TEPCO inte hade någon plan för eller organiserade övningar i att driva hjälpkondensorn. I stället för en planerat aktion kom utvecklingen att präglas av mer av improvisation.

Hatamuras utredning, [1] och [2], som togs fram av en oberoende kommission som den japanska regeringen tillsatte, omfattade 772 intervjuer med involverade parter vilket ledde till en omfattande dokumentation. Notera att det som finns i interrimsrapporten endast översiktligt behandlas i slutrapporten. Utredningen innehåller kraftig kritik av organisationer som var involverade, både säkerhetsmyndigheter och TEPCO. Det pekas på att det var oklarheter i samspelet mellan den lokala och den centrala räddningsorganisationen. Detta kunde leda till dåligt underbyggda beslut eller inga beslut alls. En nyckelfaktor är tillgång till korrekt information. En rekommendation var att räddningsorganisationen bör ledas av de som sitter närmast kärnkraftsolyckan eftersom de har tillgång till bättre information. Det riktas kraftig kritik mot TEPCO som hade brustit i att identifiera möjligheten för ett svårt haveri och ge personalen utbildning för att ta hand om en sådan kärnkraftsolycka.

Hatamuras utredning kritiserar också reaktoroperatörerna för att de slog av säkerhetssystem utan att ha någon uppbackning vilket ledde till att reaktorhärdarna var utan kylning under långa perioder. Utredningen pekar på de svåra förhållanden som operatörerna arbetade under men framhåller, med ledning av hur man agerade i Daiichi Blocken 5 och 6, ändå att detta var ett grundläggande felaktigt beteende.

Hatamuras utredning innehåller rekommendationer inom följande områden:

1. Åtgärder for att förbättra säkerheten och beredskapen genom att ta hand om komplexa händelser, få ändrade attityder till risker, analysera brister och att använda ny kunskap för att förhindra olyckor.
2. Säkerhetsmålen för kärnkraften som innefattar införande av säkerhetsförbättringar, omfattande riskanalyser och hantering av svåra olyckor.
3. Organisationers respons på kärnkraftsolyckor som innebär omfattande reformering av organisationen för krishantering, och att ansvarsförhållanden i krisorganisationen för kärnkraftsolyckor klarläggs och speciellt förhållandet mellan den lokala och den centrala delen. Det rekommenderas att länsstyrelsen (”prefectural government”) ges en tydligare roll vid kärnkraftsolyckor.
4. Förhindra skador och lindra konsekvenser genom information och riskkommunikation, förbättring av strålningsmonitorer för att kunna ge snabb och korrekt information till omkringboende och beslut när det gäller evakuering. Det ges rekommendationer när det gäller jodtabletter, medicinsk nödhjälp när det gäller

strålning och information om strålningsrisker. Det påpekas att det finns ett behov för att dela med sig och ta emot information från utlandet.

5. Harmonisering med internationell praxis med speciellt fokus på IAEA:s säkerhetsstandarder.
6. Ansvariga organisationer där bland annat säkerhetsmyndighetens roll kommenteras och vikten av oberoende och transparens understryks. Det rekommenderas att myndigheten ska ha planer för att kunna ge respons i en olyckssituation och att även myndigheten bör öva på detta. Myndigheten bör ha tillgång till specialistkunskap och ha förmågan att etablera en klar bild av en haverisituation. Man bör verka aktivt för att främja samarbetet med myndigheter utomlands. För TEPCO ges det ett stort antal rekommendationer. Det understryks speciellt att organisationen mer aggressivt måste arbete för en företagskultur som främjar säkerheten.
7. Fortsatta analyser med fokus på att klarlägga vad som hände, orsakerna och omfattningen av skadorna. Det förordas en bredare utredning för att kunna lära av erfarenheterna.

2.7.2. Översiktlig beskrivning av händelseförloppen i de mest drabbade kärnkraftsreaktorerna i Fukushima-Daiichi

Figur 2.7.a visar en översikt över kärnkraftverket vid Fukushima med sina 6 block.

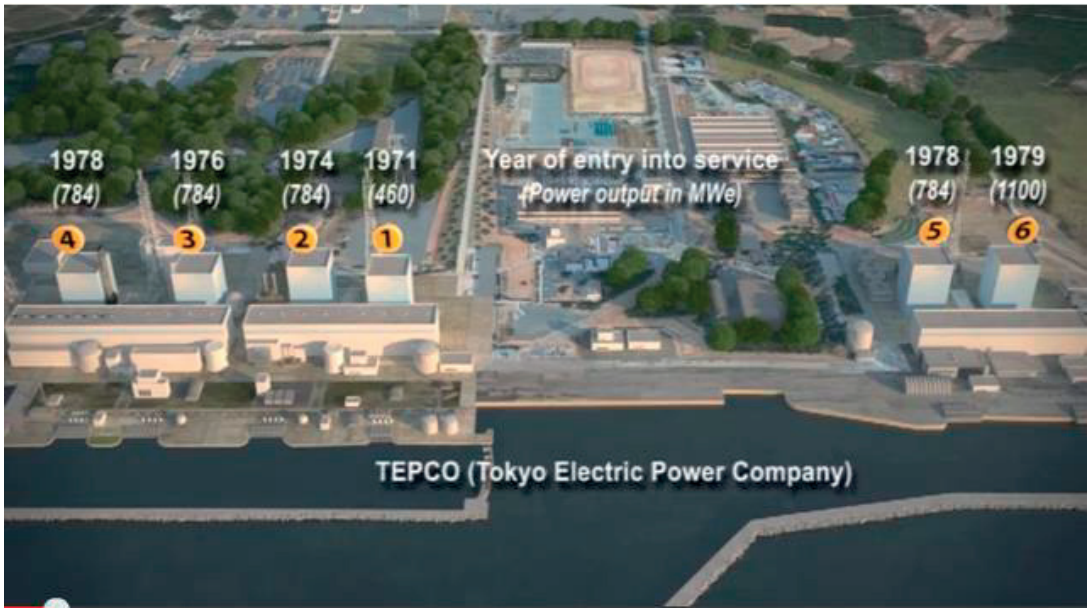

Figur 2.7.a: En översikt över kärnkraftverket vid Fukushima med sina 6 kärnkraftsreaktorer (reaktorblock). Årtalet anger när kärnkraftsreaktorn togs i drift och talet inom parentes anger dess elektriska effekt. Bilden är hämtad från Youtube där IRSN har analyserat kärnkraftsolyckan, se https://www.youtube.com/watch?v=ZJwg_McDGSI&list=PLEF556D9768017698&index=4.

Figur 2.7.b visar händelseförloppet för de mest drabbade blocken, Block 1-3. En detaljerad beskrivning av händelseförloppet för dessa finns i avsnitten 2.7.3-2.7.5. Noggrannare tidsangivelser finns i tabellerna 2.7.1 till 2.7.3.

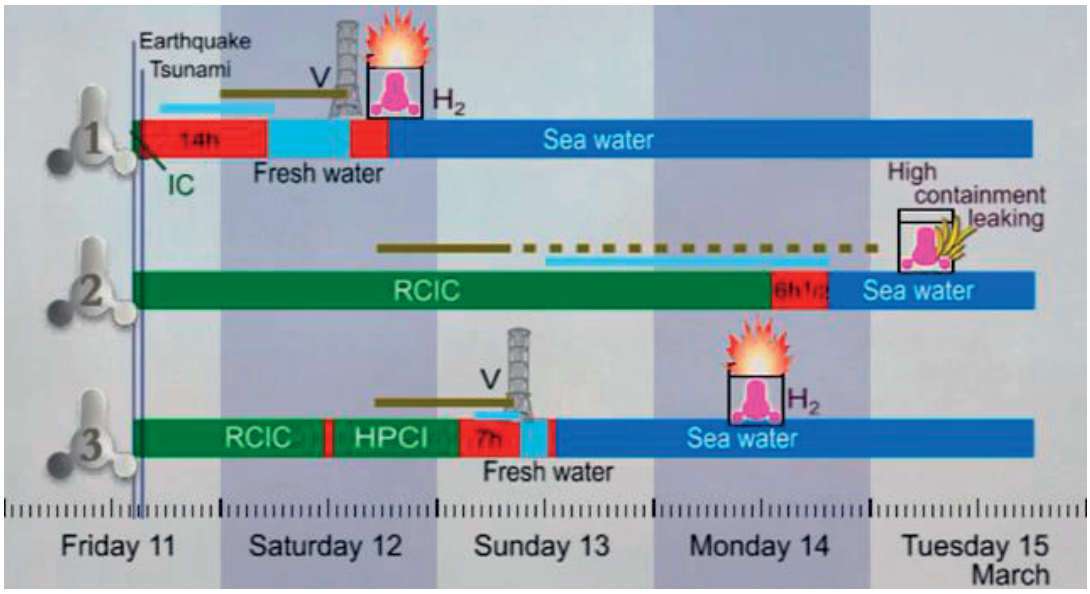

Figur 2.7.b: Översikt över händelseförloppet för de mest drabbade kärnkraftsreaktorer (blocken) i Fukushima Daiichi. Bilden är hämtad från Youtube där IRSN har analyserat kärnkraftsolyckan, se https://www.youtube.com/watch?v=ZJwg_McDGSI&list=PLEF556D9768017698&index=4.

De drabbade japanska anläggningarna har den första generationens BWR-inneslutningar där inga speciella åtgärder hade vidtagits. Inneslutningen är konstruerad för att ta hand om ett stort rörbrott enligt PS-principen där ångan kondenseras i en vattenbassäng. Konstruktionen togs fram av General Electric med beteckningen Mark-1 och består av ett päronformat skal av stål som vilar på en bädd av betong. Utrymmet med kondensationsbassängen där ångan kondenseras är i form av en ringformad volym (torus) runt nedre del av inneslutningen förbundet med 8 rör till utrymmet under reaktorn. Denna konstruktion finns också i andra länder, bland annat i ungefär hälften av USA:s kokvattenreaktorer.

Inneslutningen var därför inte konstruerad för att kunna ta hand om en härdsmälta och heller inte för höga övertryck. I de flesta länder med denna typ av inneslutningar har det gjorts omfattande utredningar och anläggningsändringar för att förbättra hanteringen av svåra olyckor. Med ett par undantag har de flesta av sådana ändringar inte införts i Japan vilket har skarpt kritiserats i flera utredningar.

2.7.3. Beskrivning av händelseförloppet i Block 1

Förloppen av vattennivån i reaktortanken, trycket i reaktortanken och trycket i inneslutningen för Block 1 presenteras i Figurerna 2.7.1 till 2.7.3. Dessa är reproducerade från TEPCO:s andra rapport [8] publicerad 6 augusti 2014.

Det var i Block 1 som den första härdsmältan ägde rum. Denna reaktor har den så kallade hjälpkondensorn som ett säkerhetssystem. Syftet med denna är att kunna kyla reaktorn och leda bort restvärmen efter bortfall av elektrisk kraft vid anläggningen. Efter kärnkraftsolyckan riktades kritik mot operatörer och kraftföretag för driften av hjälpkondensorn. Det verifierades inte att den fungerade som avsett. Det restes kraftig kritik mot att reaktoroperatörerna inte hade utbildning i att driva systemet. Systemet simulerades inte i den fullskalesimulatorn som användes för ope-

ratörsträning och en operatör med 25 års erfarenhet av driften vid reaktorn vittnade att han aldrig hade sett systemet i drift.

Block 1 är en så kallad 2-stråks-anläggning (stråken betecknas A och B) och det finns därför två hjälpkondensorer. Kravet är att hjälpkondensorerna var för sig ska ge tillräckligt med kylning. Varje kondensor har en egen kylkrets med egna anslutningar till reaktortanken och en egen värmeväxlare. I varje kylkrets finns fyra skalventiler; två innanför och två utanför inneslutningen. I normalfallet står tre av dessa ventiler öppna, två innanför och en utanför inneslutningen, och en stängd utanför inneslutningen. Endast en ventil behöver således öppna för att systemet ska börja föra bort värmen från reaktorn. I USA, till exempel, tränar operatörerna att kunna öppna denna ventil manuellt om det skulle behövas.

När det gäller hjälpkondensorn så är det väsentliga osäkerheter i förloppet. Efter jordbävningen men innan tsunamin kopplades systemet i stråk B bort och man slog av hjälpkondensorn i stråk A. Den direkta orsaken till detta var att trycket hastigt sjönk i reaktorn. I [2] anges att operatörerna ville bromsa temperaturnedtagningen till 55 grader per timme vilket anges som maxvärde i de säkerhetstekniska driftförutsättningarna för reaktorn. I [3] anges att operatörerna misstänkte att det var läckage i hjälpkondensorsystemet som gjorde att trycket sjönk. De slog därför av systemet för att se om trycket återhämtade sig; vilket det gjorde; något som indikerade att systemet inte hade skadats. Därefter kontrollerades trycket i reaktorn genom att slå av och på hjälpkondensorn.

När tsunamin kom försvann den dieseldrivna växelströmmen och även likströmmen var endast tidvis tillgänglig på grund av översvämning och kortslutning. Vid elbortfallet i Block 1 fick man en ”fail-safe” signal som ska göra att berörda komponenter går till säkert läge. För hjälpkondensorn innebär detta att ventilerna i systemet fick stängasignal. Det var tveksamt om dessa ventiler verkligen stängde eftersom de kräver växelström som genereras från batterierna som endast delvis fungerade. När man efter ungefär en timme efter tsunamin en stund fick tillbaka likspänningen i kontrollrummet visade ventilen stängd. Nivåmätningen visade sjunkande tendens men nivån hade inte nått överkant av härden.

Operatörerna försökte därefter att öppna ventilerna till hjälpkondensor A lokaliserade utanför inneslutningen. De fick öppensignal och uppger också att ljud av utströmmande ånga till att börja med kunde höras. Funktionen av hjälpkondensorn kunde dock inte säkerställas. Det befarades att vattnet på sekundärsidan i värmeväxlaren skulle ta slut och ventilen i krets A stängdes. Att man stängde av ett system utan att ha uppbackning har kritiserats i efterföljande utredning [3].

I Block 1 började härden överhettas redan drygt tre timmar efter tsunamin och produktionen av vätgas tog fart. Efter drygt fyra timmar var härden avtäckt. En strategi för härdkylning var att pumpa in vatten från brandfordon. Problemet var att en stor del av vattnet som pumpades in från brandfordonen inte kom fram till reaktorn men i stället hamnade bland annat i kondensattanken. Upp till 10 alternativa vägar för vattnet hade identifierats. Bland dem fanns läckande backventiler och felaktigt monterade ventiler. Man uppskattade att endast 20-50 % av externt vatten nådde reaktorn. Meddelande hade gått till Kashiwazaki-Kariwa som redan hade modifierat systemen.

Det finns indikationer på smältans relokering till nedre plenum efter ungefär 6 timmar och efter ungefär 10 timmar sker tryckutjämning med inneslutningen. Strategin därefter är att förse reaktorn med kylvatten från brandbekämpningsutrustning.

En sammanfattning av händelseförloppet ges i Tabell 2.7.1.

Tabell 2.7.1. Sammanfattning av händelseförloppet i Block 1. Huvudsakligt underlag för tabellen är ref. [8]-[9] och [6].

Datum	Tid	Tid efter tsunami	Händelse
11 mars 2011	14:46	-00:51	Jordbävning
	14:48	-00:49	Snabbstopp
	14:48	-00:49	Stängning av ångventiler
	14:52	-00:45	IC (Isolation Condenser) A och B startas automatiskt
	15:03	-00:34	IC A och B stoppas manuellt
	15:05	-00:32	Krets A för kylning av torus startas
	15:10	-00:27	Krets B för kylning av torus startas
	15:17-15:35	-00:20--00:02	IC krets A körs intermittent
	15:37	0	Totalt elbortfall
	16:42-17:00	01:04-01:23	DC delvis återställd, IC ventil (i krets A) visade stängd
	18:10	02:33	Vattennivån passerar toppen av härden, kylning med ånga
	18:18	02:41	Operatörerna försökte öppna ventilerna utanför inneslutningen i IC-krets A. Fick öppen-signal men oviss funktion.
	18:25	02:48	Operatörerna stänger ventilen i IC krets A.
	18:50	03:13	Härden överhettad, metall-vattenreaktion förekommer
	19.40	04:03	Vattennivån passerar botten av härden (baserat på analyser)
	20:50	05:13	Vatteninpumpning med brandpump. Vattnet kom troligen inte fram till reaktorn.
	21:19	05:42	Temporär DC tillgängligt, Nivåmätningen fungerade troligen inte
	21:30	05:53	Ventilen i IC krets A öppnas. Funktionen oviss
	22:00	06:23	Analyser visar plötslig tryckhöjning i tanken, möjligen orsakad av härdens relokering till nedre plenum, dock inga mätningar
12 mars	01:48	10:11	Brandvattensinpumpning avstannar
	02:00	10:23	Reaktortanken skadad, tryckutjämning med inneslutning, ung 0,8 MPa
	04:00	12:23	Färskvattensinpumpning startar
	04:02	12:25	Färskvattensinpumpning stannar
	05:46	14:09	Färskvattensinpumpning återstartas
	10:17-10:23	18:20-18:25	Försök att ventilera inneslutningen. Ingen reaktion på trycket, dosraten vid porten ökade.

	14:30-14:50	22:53-23:13	Ventilering av inneslutning, trycket i inneslutningen sjunker
	14:53	23:16	Färskvattensinpumpning avslutas
	15:36	23:59	Reaktorbyggnaden exploderar
	19:04	27:27	Inpumpning av sjövatten med brandutrustning startas
	21:45	30:08	Inpumpning av sjövatten med brandutrustning stannar
	23:50	32:13	Inpumpning av sjövatten med brandutrustning återstartas
13 mars	01:10	33:33	Inpumpning av sjövatten med brandutrustning stannar
	20:00	52:23	Inpumpning av sjövatten med brandutrustning återstartas

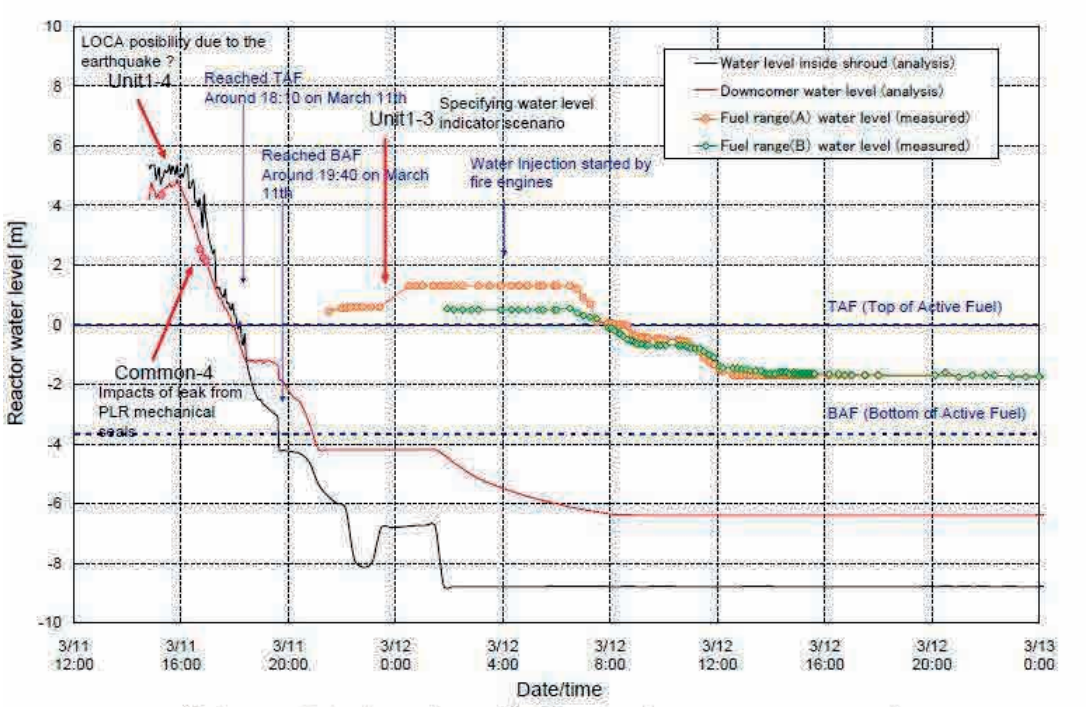

Figur 2.6.1 Nivåförloppet i Block 1 (Reproducerat från [8], Tokyo Electric Power Company, Inc)

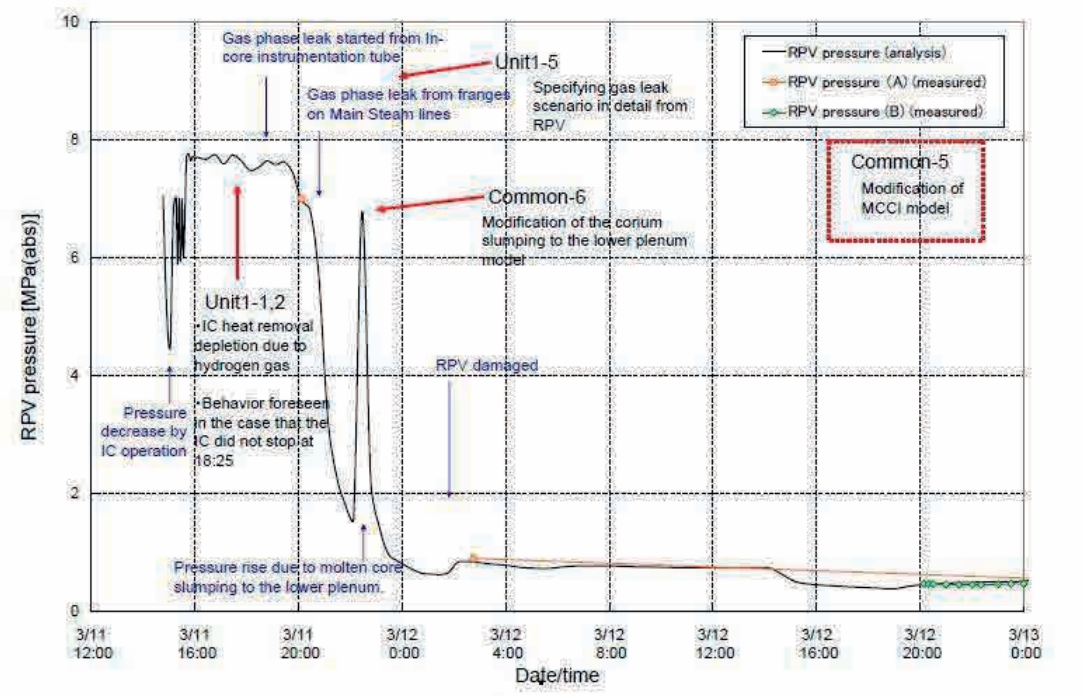

Figur 2.6.2 Tryckförloppet i Block 1 (Reproducerat från [8], Tokyo Electric Power Company, Inc)

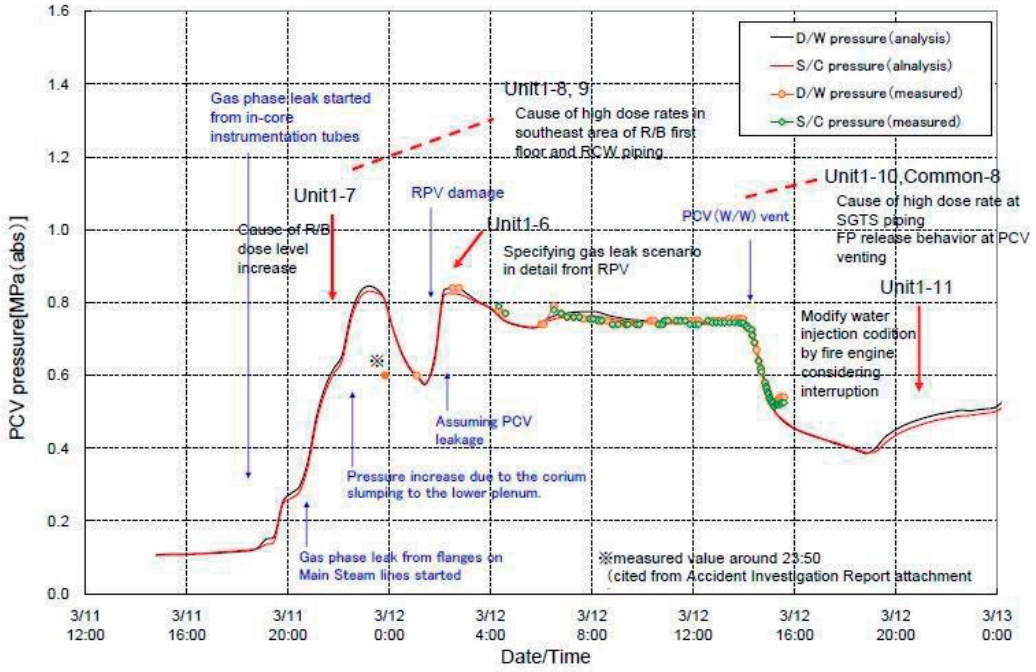

Figur 2.6.3 Inneslutningstrycket i Block 1 (Reproducerat från [8], Tokyo Electric Power Company, Inc)

2.7.4. Beskrivning av händelseförloppet i Block 2

Förloppen av vattennivån i reaktortanken, trycket i reaktortanken och trycket i inneslutningen för Block 2 presenteras i Figurerna 2.7.4 till 2.7.6. Dessa är reproducerade från TEPCO:s andra rapport [8] publicerad 6 augusti 2014.

Efter jordbävningen startades säkerhetssystemen. RCIC (Reactor Core Isolation Cooling) som är ett högtrycksinpumpningssystem men stoppade automatiskt på hög nivå i reaktortanken [9]. RCIC startades manuellt flera gånger med samma resultat. Strax innan tsunamin startades RCIC manuellt. Tsunamin orsakade bortfall av både växelspänning och likspänning. TEPCO:s huvudhypotes är att RCIC med ångdrivna pumpar fortsatta att gå men kunde inte regleras på grund av bortfallet av likspänning. TEPCO har analyserat de ventiler som använts i systemet och har konkluderat att bortfallet av el medför att ventilerna gradvis öppnas till fullt öppet läge. Detta medförde att RCIC pumpade in vatten i reaktortanken tills vattennivån nådde ångledningarna. Uppmätt nivå pekar på att vattennivån har överstigit mätområdet. Det är oklart vad som var den direkta orsaken till att de ångdrivna pumparna slutade att fungera. En hypotes är att funktionen kan ha degraderats när de matades med tvåfasflöde från ångledningarna i stället för med ånga.

Under hela förloppet var det lägre tryck i reaktortanken än nominellt vilket kan stödja hypotesen om att stora mängder kallt vatten pumpades in som kondenserade ångan eftersom det inte skedde någon tryckavlastning. Mot slutet av perioden med drift av RCIC visade trycket i reaktortanken en sjunkande trend vilket orsakades av sjunkande restvärme och att RCIC fungerade och kunde leda bort restvärmen.

Trycket i inneslutningen ökade långsamt under inpumpningen med RCIC vilket kan ha orsakats av att ångan från RCIC kondenserade i bassängen. TEPCO hävdar med stöd av temperaturmätningar i torusen att den troligen var en god värmesänka. Stratifiering med stora temperaturdifferenser observerades och det stod sannolikt kallt vatten utanför torusen något som kan ha bidragit till värmesänkan. Det antas att när RCIC stoppade började vattennivån i reaktortanken att sjunka och trycket i reaktortanken att stiga till nominellt värde, och manuell tryckavlastning genom avblåsningsventilen skedde. Observationer i kondensationsbassängen tyder på att man kan ha blåst vatten genom tryckavlastningsventilerna.

Den manuella tryckavlastningen av reaktortanken ledde inte till att inneslutningstrycket steg. En tänkbar orsak är att avblåsningen till wetwell kan ha orsakat omblandning av bassängen och en utjämning av temperaturerna där.

TEPCO arbetar vidare med en hypotes om att man försökte återstarta RCIC efter att funktionen hade degraderats. Det är dock klart att RCIC inte kom igång som den skulle. En möjlig orsak är ett trippvillkor som mekaniskt stoppade den ångdrivna pumpen.

Det skedde flera tryckavlastningar från reaktortanken och en stund efter varje avlastning började trycket öka igen. Detta förknippades med inpumpning av vatten från brandfordon. Enligt TEPCO:s hypotes var i detta läge härden avtäckt och när vatten pumpades in blev det kokning och ångproduktion nära botten av bränslet. Detta fick trycket att stiga och inpumpningen från brandfordonen att minska eftersom denna var begränsad till ett maxtryck på 1 MPa. Analyserna pekar på att även partialtryck av vätgas kan ha bidragit till tryckökningen.

När det gäller skador på inneslutningen i Block 2 har det tidigare rapporterats att det hördes en smäll och att inneslutningens övertryck försvann. TEPCO:s huvudhypotes

nu är att det var smällen från explosionen i Block 4 som hördes och att tryckmätningen i inneslutningen var felaktig. Stöd för denna uppfattning finns i data från seismiska mätinstrument vilka indikerar att det är samma smäll det är fråga om. Det visas också till att tryckmätningen senare återkom och då visade övertryck i inneslutningen.

En möjlig förklaring TEPCO har till att Block 2 inte utsattes för någon vätgasexplosion är att när Block 1 exploderade så öppnades blåsluckorna på Block 2 och att den vätgas som senare kom till reaktorbyggnaden kunde vädras ut.

Det är sannolikt att det är en skada på torusen eftersom vattennivån nu är den samma utanför och innanför. TEPCO:s hypotes är att den har skadats i ett senare läge; möjligen på grund av smältans angrepp på betongen. Det råder således osäkerhet om när skadan skedde. En annan hypotes är att en ledning i RCIC som går ut från torusen kan ha blivit skadad och att läckaget sker ut från denna. Skadan kan då ha uppkommit genom att RCIC kördes mycket länge under förhållanden som systemet inte var konstruerat för.

Tabell 2.7.2 Händelseförloppet i Block 2. Huvudsakligt underlag för tabellen är [8], [9] och [6]

Datum	Tid	Tid efter tsunami	Händelse
11 mars 2011	14:46	-0:55	Jordbävning och snabbstopp
	14:50	-0:51	RCIC startas manuellt men trippas direkt på indikation om hög nivå i reaktortanken, upprepas flera gånger
	15:07-15:25	-0:34-0:16	Kylning av inneslutning och kondensationsbassäng med RHR startas
	15:39	-0:02	RCIC startas manuellt
	15:41	0	Tsunami kommer. Totalt elbortfall. Kallt vatten pumpas in med RCIC. Nivån i reaktortanken ökar. Reaktortrycket sjunker.
12 mars	01:30	09:49	Minimum tryck (5.4 MPa)i reaktortanken, trycket börjar öka igen
	04:20-5:00	12:39-13:19	Vattenintaget för RCIC ändras från kondensattanken till kondensationsbassängen
	18:00	26:19	Maxtryck på ung 6,4 MPa i reaktortanken, trycket börjar långsamt sjunka på grund av minskande restvärme
14 mars	09:00	65:19	RCIC-funktionen började sannolikt degraderas, trycket i reaktorankenen börjar öka och ökar till nominellt värde
	11:30	67:49	Försök att återstarta RCIC
	12:00	68:19	RCIC troligen borta
	13:25	69:44	RCIC-funktionen definitivt borta
	16:34	72:53	Förberedelse för inpumpning av sjövatten genom brandvattensystemet
	18:00	74:19	Avblåsningsventiler från tanken öppnas, trycket sjunker snabbt
	18:10	74:29	Vattennivån i reaktorn passerar toppen av härden
	18:55	75:14	Vattennivån i härden passerar botten av härden
	19:20	75:39	Härden börjar smälta
	19:20	75:39	Inpumpning med sjövatten upphör på grund av dieselbrist
	19:55	76:14	Återstart inpumpning av sjövatten, vatten kommer troligen till nedre del av härden där kokning troligen sker
	20:30	76:49	Reaktortrycket ökar troligen orsakat av ånga och vätgas från härden
	21:20	77:39	Tryckavlastning genom avblåsningsventiler
	22:40	78:59	Reaktortrycket ökar igen

	23:20	79:39	Tryckavlastning, troligen genom avblåsningsventiler
	23:25	79:44	Läckage mellan reaktortank och inneslutning, tryckökning i inneslutningen
15 mars	00:10	80:29	Trycket i reaktortanken ökar
	01:10	81:29	Tryckavlastning genom avblåsningsventil
	6:00-6:10	86:19- 86:29	Kraftigt ljud observerades och inneslutningstrycket föll till noll. Det var troligen explosionen i Block 4 som hördes och trycket kan ha varit en felmätning eftersom det uppmätta inneslutningstrycket efteråt steg igen.

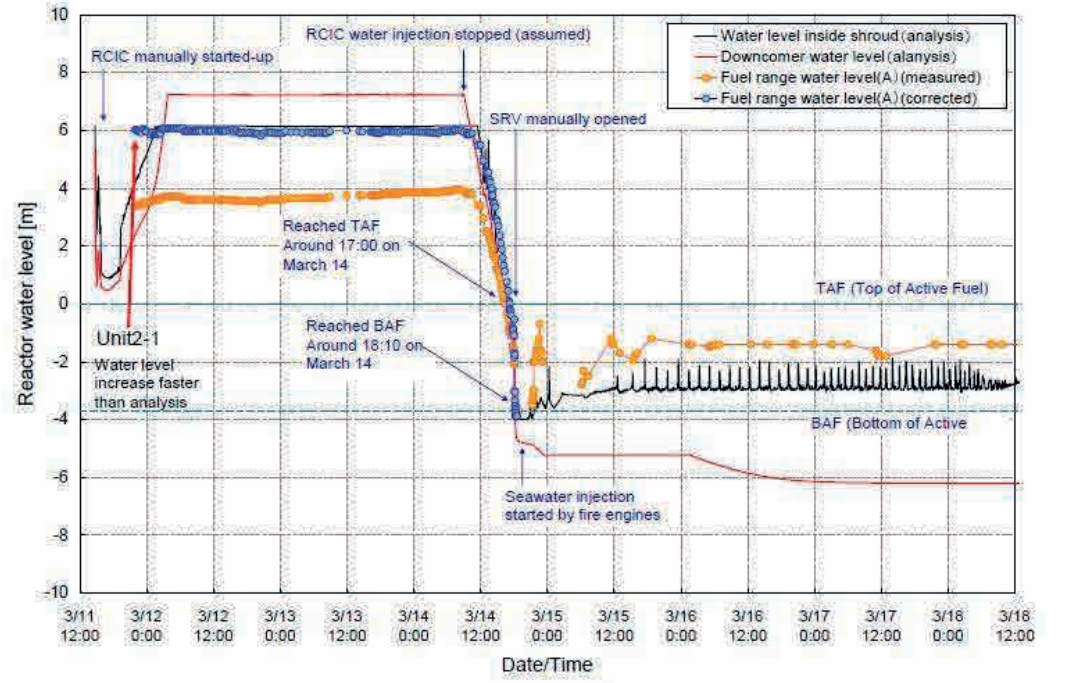

Figur 2.6.4 Nivåförloppet I Block 2 (Reproducerat från [8], Tokyo Electric Power Company, Inc)

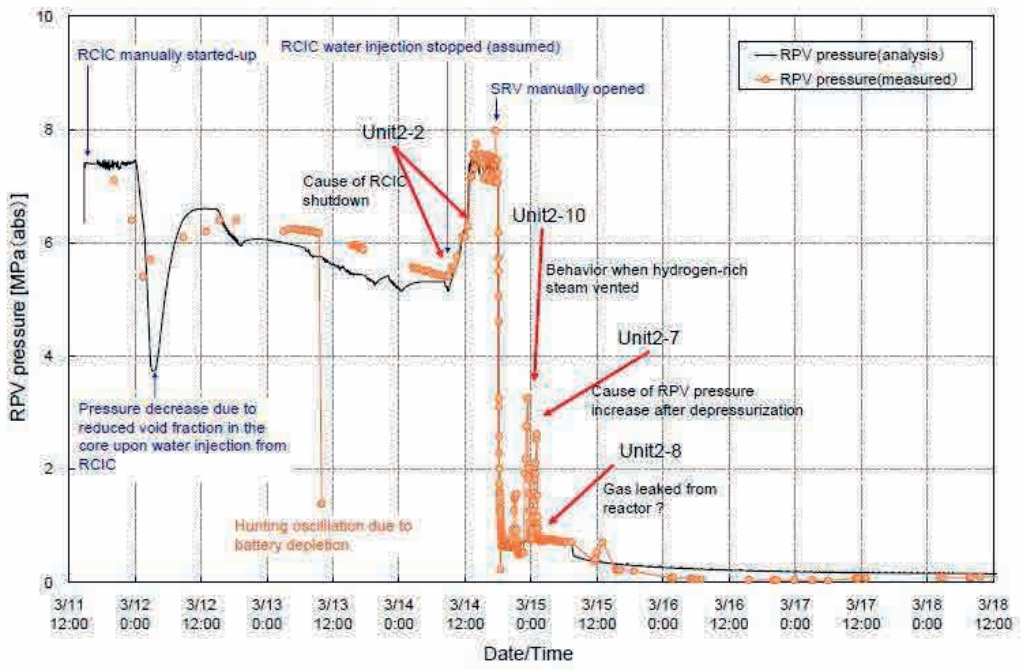

Figur 2.6.5 Tryckförloppet i Block 2 (Reproducerat från [8], Tokyo Electric Power Company, Inc)

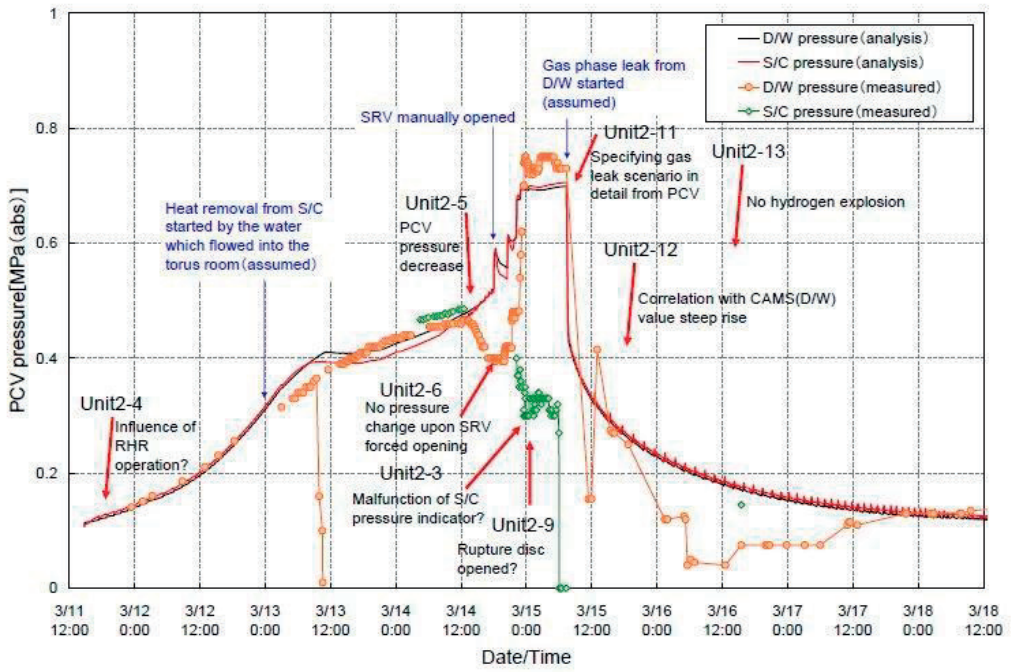

Figur 2.6.6 Inneslutningstrycket i Block 2 (Reproducerat från [8], Tokyo Electric Power Company, Inc)

2.7.5. Beskrivning av händelseförloppet i Block 3

Förloppen av vattennivån i reaktortanken, trycket i reaktortanken och trycket i inneslutningen för Block 3 presenteras i Figurerna 2.7.7 till 2.7.9. Dessa är reproducerade från TEPCO:s andra rapport [8] publicerad 6 augusti 2014.

Reaktorsnabbstopp inträffade efter jordbävningen och RCIC startade automatiskt och stannade sedan på grund av hög nivå i tanken. Efter tsunamin fanns likspänning tillgängligt och RCIC startades manuellt. Med RCIC i drift med ångdrivna pumpar kunde nivån i reaktortanken hållas konstant. Man kunde upprätthålla cirkulation i RCIC via kondensattanken. Reaktortrycket reglerades genom avblåsningsventilerna. Systemen fungerade sannolikt som avsedd under denna period.

Driften av RCIC fortsatte i nästan 20 timmar. Under perioden fram till ungefär 12:00 12 mars 2011 steg trycket i inneslutningen snabbare än det skulle ha gjort jämfört med ett förlopp där hela bassängen medverkar som värmesänka. Detta är en indikation på degraderad PS-funktion. Degraderingen kan antingen förklaras av en ångläcka mellan drywell och wetwell eller stratifiering av vattnet i bassängen. En sådan stratifiering skulle kunna åstadkommas genom att kondensation av ånga från den ångdrivna pumpen i RCIC lokalt värmer upp bassängen till mättnadstemperatur. Analyser av detta måste slutföras för att identifiera orsaken till detta eftersom systemet annars troligen fungerade som avsedd.

RCIC slutade fungera 12 mars 11:36. Orsaken till stoppet är inte helt klarlagt och möjliga alternativ utreds. En hypotes är att skyddet mot högt utloppstryck hade aktiverats. Det konstateras att man var nära trippvillkoret och att stoppet kan ha utlösts genom att både utloppstrycket från RCIC och trycket i wetwell ökade. Kashiwazaki-Kariwa har informerats och enligt deras nuvarande instruktioner ska sådana komponentskydd kunna överridas eller tas bort.

Elkraft var tillgänglig och det gjordes upprepade försök att återstarta RCIC. Vid varje försök stängde ångventilen direkt troligen på grund av en inbyggd trippfunktion. Operatörerna kontrollerade ventilerna utan att hitta några fel och kunde verifiera att till exempel det mekaniska skyddet mot hög hastighet inte hade lösts. Det borde ha varit möjligt att återställa trippvillkoren från kontrollrummet, men detta fungerade inte. Efter ungefär en timme efter bortfallet av RCIC (12:35) startade högtrycksinpumpningen (HPCI) automatiskt på låg nivå i tanken, och samma kylväg som för RCIC etablerades. Trycket i reaktortanken sjönk kraftig på grund av ökande konsumtion av ånga till den ångdrivna pumpen. Trycket stabiliserades en stund kring 1 MPa men sjönk sedan så att drivtrycket för HPCI blev för litet, och systemet slogs av manuellt (13 mars 2:42).

Mätningar av vattennivån i reaktortanken är osäkra. Följande scenario har uppskattas baserat på analyser. Vattennivån nådde toppen av härden ungefär 13 mars 02:30 13. Vattennivån nådde botten av härden ungefär 09:10.

Upprepade försök gjordes att starta HPCI och RCIC. HPCI startade inte på grund av låg batterispänning och RCIC på grund av trippvillkoret på pådragsventilen som inte kunde hävas.

När HPCI kopplades bort skedde en snabb tryckökning i reaktortanken. Trycket stabiliserades kring 7,3 MPa. Det provades att länka om flödet till spray av wetwell från den dieseldrivna brandpumpen till reaktortanken men detta fungerade inte på grund av för högt tryck i tanken. Man försökte att öppna avblåsningsventilerna för att få ned trycket men detta fungerade inte. En snabb tryckavlastning skedde dock 09:08. TEPCO:s känslighetsanalyser tycks peka på att den automatiska tryckned-

tagningen (ADS) hade löst ut. Villkoren för utlösning av ADS är förhöjd inneslutningstryck tillsammans med låg nivå i reaktortanken.

Efter trycknedtagningen blev det problem med nivåmätningarna. Under denna period visade troligen nivån för höga värden på grund av ånga i referensbenet. Kort efter kl. 09:00 den 13 mars har man fått härdavtäckning och härden överhettas och skadas. Det är troligt att endast en del av det inpumpade vattnet från brandfordonen nådde fram till härden och att det i stället tog andra vägar.

Tabell 2.7.3 Händelseförloppet i block 3. Huvudsakligt underlag för tabellen är [8], [9] och [6]

Datum	Tid	Tid efter tsunami	Händelse
11 mars 2011	14:46	-00:52	Jordbävning
	14:47	-00:51	Snabbstopp
	15:05	-00:33	RCIC (Reactor Core Isolation Cooling) startas manuellt
	15:25	-00:13	RCIC trippas på högt vattennivå i tanken
	15:38	0	Förlust av AC, DC var tillgänglig
	16:03	00:25	RCIC startas manuellt, Reglerar på normal vattennivå i reaktortanken, Stor tryckuppbyggnad i inneslutningen, PS-funktionen degraderad
12 mars	11:36	19:58	RCIC trippas automatiskt, pådragsventilen för pumpen troligen stängd
	12:06	20:28	Spray av wetwell startas med dieseldrivna brandpumpar
	12:35	20:57	Automatisk start av HPCI (High Pressure Coolant Injection) på låg nivå i reaktortanken. Trycket i reaktortanken börjar sjunka.
	19:00	27:22	Trycket i tanken stabiliseras på 1 MPa,
13 mars	02:00	34:22	Trycket i tanken börjar sjunka igen. Tveksamt drivtryck till HPCI
	~02:30	34:52	Nivån når toppen av härden (baserat på analys)
	02:42	35:04	HPCI stoppas manuellt, Trycket i reaktortanken börjar öka
	03:05	35:27	Spray av wetwell med dieseldrivna brandpumpar stoppas. Omkoppling till reaktortank provades. Vatten kommer troligen inte in på grund av högt reaktortryck
	04:30	36:52	Trycket 7 MPa i reaktortanken, stabiliseras
	05:08	37:30	Spray med dieseldrivna brandpumpar omlänkas till wetwell
	07:39	40:01	Spray med dieseldrivna brandpumpar omlänkas till drywell
	07:43	40:05	Spray av wetwell stoppas
	08:40-9:10	41:02- 41:32	Spray av drywell stoppas. Troligen ungefär 08:55 eftersom trycket i inneslutningen börja öka. Flödet omlänkas till reaktortanken
	09:08	41:00	Snabb tryckavlastning av reaktortanken
	09:10	41:32	Nivån i tanken når botten av härden
	09:20	41:42	Tryckavlastning av inneslutningen, inneslutningstrycket sjunker
	09:25	41:47	Färskvattensinpumpning till reaktortanken med brandfordon startas
	10:00	42:22	Tryckökning i tanken, öppning avblåsningsventiler
	11:17	43:39	Stängning av avblåsningsventilen från wetwell
	12:00	44:22	Tryckökning i tanken, öppning avblåsningsventiler
	12.20	44:42	Färskvattensinpumpningen stoppar. Förberedelse för omkoppling till saltvatteninpumpning påbörjas
	12:30	44:52	Ventilering av inneslutning börjar
	13:12	45:35	Saltvattensinpumpning med brandfordon startas
	14:10	46:32	Troligt stopp av ventilering av inneslutning, inneslutningstrycket börjar stiga
	21:10	53:32	Ventilering av inneslutning startas
14 mars	00:50	57:12	Ventilering av inneslutning stoppas
	01:10	57:32	Saltvattensinpumpningen stoppas, slut på vattnet
	03:20	59:42	Saltvattensinpumpningen återupptas

	05:20	61:42	Liten avlastningsventil från wetwell börjar öppnas
	06:10	62:32	Liten avlastningsventil från wetwell öppen
	07:10	63:32	Genomsmältning av reaktortanken
	11:01	67:22	Reaktorbyggnaden exploderar
	11:01	67:22	Saltvattensinpumpningen stoppas
	12:00	68:22	Ventilering av wetwell troligen stoppad
	15:30	71:52	Saltvattensinpumpningen återupptas
	16:00	71:22	Ventilering av wetwell börjar öppnas
	19:20	75:42	Det upptäcks att brandutrusningen inte har fungerat under 30 min till 1 timme
	21:04	77:26	Troligen stängning av ventilering av inneslutning, trycket ökar
	21:14	77:36	Saltvattensinpumpning stängs
15 mars	02:30	82:52	Saltvattensinpumpning återupptas
	Följande dagar		Reglering av inneslutningstrycket med periodisk avlastning från wetwell

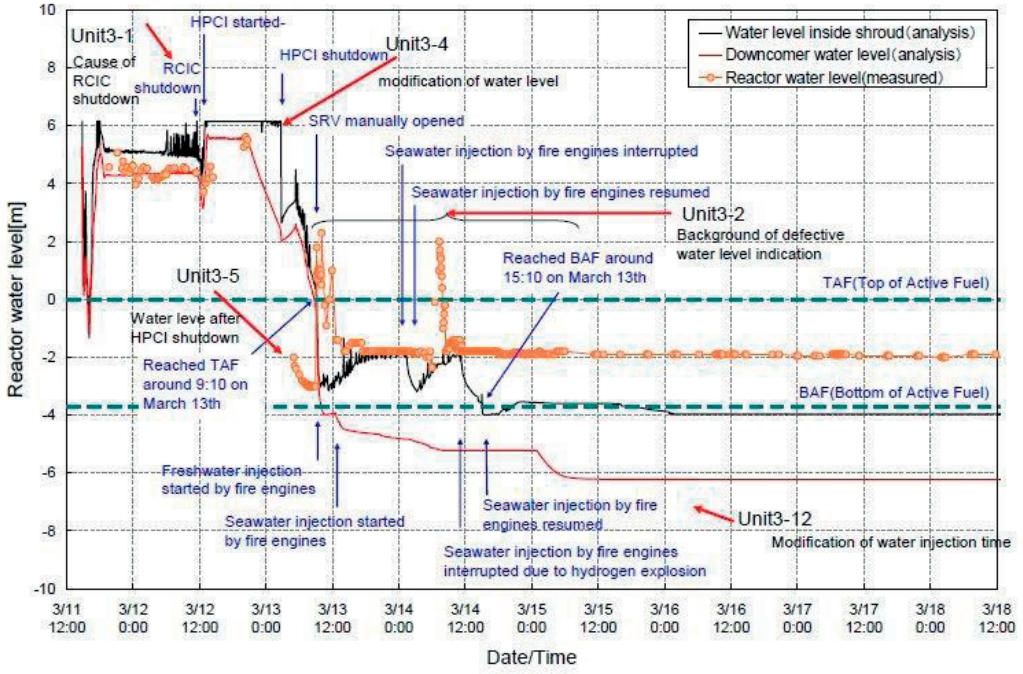

Figur 2.6.7 Nivåförloppet i Block 3 (Reproducerat från [8], Tokyo Electric Power Company, Inc)

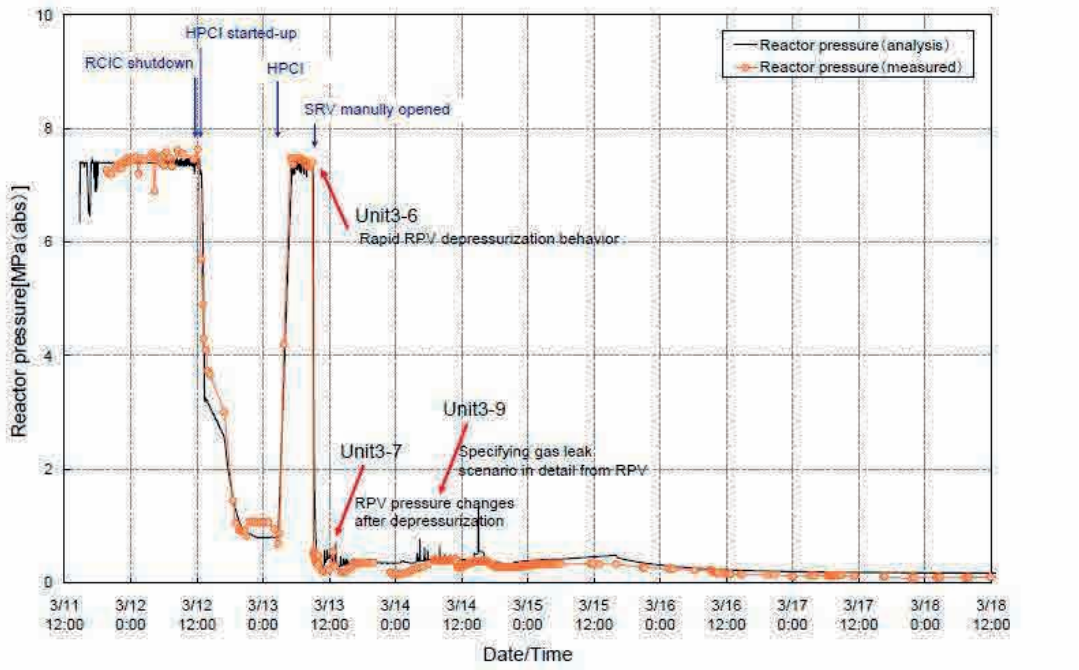

Figur 2.6.8 Tryckförloppet i Block 3 (Reproducerat från [8], Tokyo Electric Power Company, Inc)

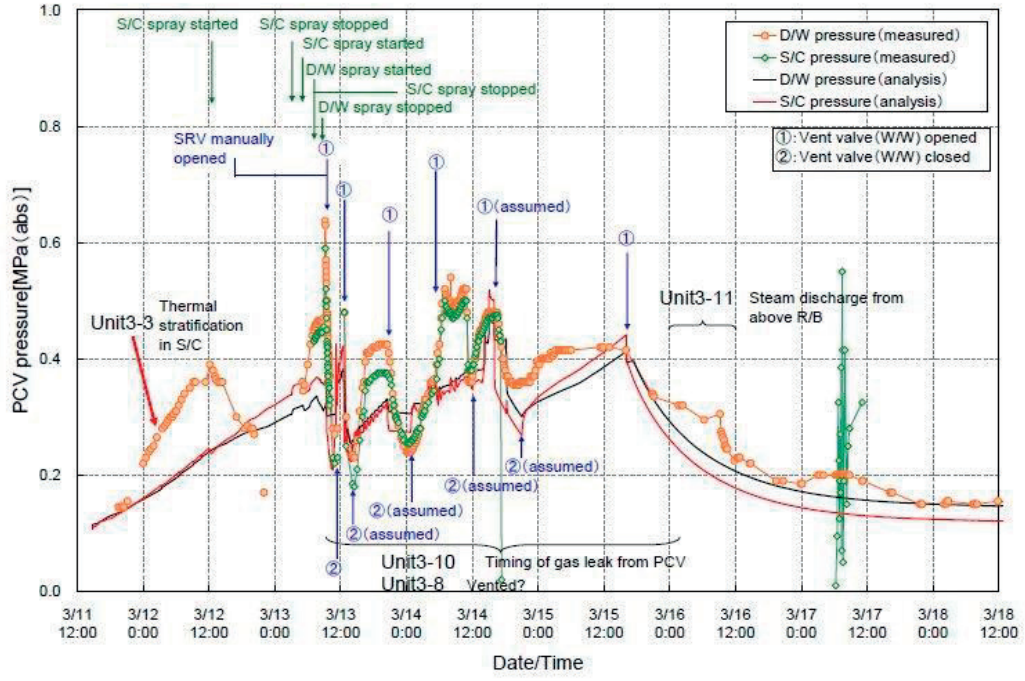

Figur 2.6.9 Inneslutningstrycket i Block 3 (Reproducerat från [8], Tokyo Electric Power Company, Inc)

2.7.6. Beskrivning av händelseförloppet i Block 4

TEPCO är övertygad om att det var vätgas från Block 3 som tog sig över och exploderade.

2.7.7. Studiebesök i Japan med APRI:s styrgrupp

Ett studiebesök arrangerades av APRI-projektet [6] i oktober 2014 där utgångspunkten var att få en bättre förståelse av de fenomen som inträffade under kärnkraftsolyckan i Fukushima-Daiichi och bedöma om det finns potential för att även kunna förbättra säkerheten i svenska reaktorer. Eftersom den svenska reaktorflottan har sju kokvattenreaktorer med PS-inneslutningar av typ Mark 2 är sådan förståelse extra viktig.

Fokus vid besöket var på förståelse av de tekniska faktorer som kan ha bidragit till härdsmältorna. I slutändan är målet att identifiera möjliga faktorer som kunde ha stoppat kärnkraftsolyckan eller begränsat konsekvenserna. Erhållna kunskaper kan bidra till underlag för översyn av om sådana faktorer även är tillämpliga för att värdera säkerheten i svenska reaktorer.

Den metodik som används är att etablera hypoteser om förloppet som kan utvärderas i ljuset av de data som finns från kärnkraftsolyckan. Från svenskt håll var det viktigt att ta del av de analytiska aspekter som kan ha en betydelse även för andra reaktorer. En viktig aspekt var också att etablera personliga kontakter som senare kan bilda ett underlag för utbyte av information. Det var därför viktigt att besöka kärnkraftsföretaget TEPCO och den nyetablerade säkerhetsmyndigheten NRA (Nuclear Regulation Authority) och ta del av och ställa frågor kring deras analysarbete. Viktigt var givetvis också att på plats få direkt intryck av de stora svårigheter som måste hanteras vid Fukushima-Daiichi efter kärnkraftsolyckan. Likaledes var det värdefullt att ta del av det intensiva arbetet som pågår vid en relativt modern reaktor i Kashiwazaki-Kariwa för att ta hand om erfarenheter, förstärka säkerheten och uppfylla de nya säkerhetsbestämmelserna. TEPCO:s mål här är att i första hand kvalificera reaktorerna 6 och 7 för fortsatt drift.

2.7.8. Jämförelse mellan haverihantering i Japan och Sverige

Före kärnkraftsolyckan i Fukushima Daiichi, var det ganska stora skillnader mellan Japan och Sverige i hantering av ett svårt haveri. Detta gällde speciellt frågorna kring hantering av en smält härd och tryckavlastning av inneslutningen. Efter kärnkraftsolyckan har det blivit större likheter i hanteringen. I Japan införs filtrerad tryckavlastning och åtgärder för att stärka möjligheterna att kyla en smält härd i inneslutningen. I Japan krävs även aktiva åtgärder för att begränsa utsläpp efter en härdsmälta med en läckande inneslutning.

Svensk haverihantering

En grundläggande tanke i den svenska strategin för att ta hand om ett svårt haveri är att skydda inneslutningens integritet. En nyckelfaktor när det gäller att begränsa utsläppet under ett haveri med härdsmälta i svenska verk är den filtrerade tryckavlastningen. Tanken är att genom tryckavlastning kunna begränsa belastningarna på inneslutningen så att den kan behålla sin utsläppshindrande funktion när det behövs. Den filtrerade ventileringen ska skilja av radioaktiva ämnen som kan finnas i inneslutningen under en härdsmälta. En viktig del av den svenska strategin är att en härdsmälta ska falla i vatten efter genomsmältning av reaktortanken.

En fundamental säkerhetsstrategi är att även om härden inte kan kylas i tanken så ska den vara kylbar på inneslutningens botten genom att förstärka inneslutningsstri-

len och fylla vatten under tanken. Denna strategi kan förstärkas genom att analysera och införa åtgärder för att öka sannolikheten för i första hand att förhindra härdskador och vidare att kunna kvarhålla en delvis smälthärd i reaktortanken.

Som utgångspunkt för den svenska haverihanteringen har det antagits ett par paraplyhändelser som ska klaras av. Instruktioner utvecklades för hur dessa haverier ska tas om hand.

För kokvattenreaktorerna var en konstruktionsstyrande händelse att det under ett rörbrott uppstår en stor läcka mellan primärutrymmet (drywell), där reaktorn är placerad, och sekundärutrymmet (wetwell), där kondensationsbassängen finns som kondenserar den ånga som kommer ut från brottet. En sådan läcka skulle kunna leda till övertryckning och skador på inneslutningen. Inneslutningarna utrustades därför med avlastningsledningar försedda med sprängbleck och ventiler där ångan kan blåsas av till omgivningen innan radioaktiva ämnen har frigjorts. Avlastningsledningarna stängs automatiskt efter en viss tid.

Den andra konstruktionsstyrande händelsen var fullständigt bortfall av växelström (Station Black Out, SBO). Under detta händelseförlopp har man ingen nödkylning och endast batterispänning är tillgänglig för att till exempel kunna manövrera vissa ventiler och övervaka viss viktig instrumentering. I detta läge kommer man att försöka förse reaktorinneslutningen med vatten genom förberedda anslutningar mot brandvattensystem och via mobila system, samt att fylla utrymmet under tanken med vatten som en förberedelse för en möjlig genomsmältning av reaktortanken i fall kylning av härden i tanken misslyckas. I långtidsförloppet är strategin därför att kyla inneslutningen genom att fylla på vatten och avlasta denna genom att avbörda gaserna via ett filter som tar bort radioaktiva ämnen som långsiktigt kan påverka människors hälsa.

Japansk haverihantering före kärnkraftsolyckan i Fukushima-Daiichi

Japansk strategi för haverihantering kritiserades skarpt i ett flertal utredningar efter kärnkraftsolyckan. Kritiken har inte varit lika hård när det gäller förutsättningar och strategi för haverihanteringen. Det stod dock klart att de åtgärder som vidtas för att få starta äldre anläggningar vittnar [6] om att strategierna i grunden omvärderas.

Inneslutningarna var varken konstruerade för att kunna ta hand om en härdsmälta eller höga övertryck. Detta hänger samman med de säkerhetsmål som tillämpades i Japan, som i motsats till i Sverige, var kvantifierade reaktorsäkerhetsmål baserade på probabilistiska analyser. Dessa uttrycktes som att det ska vara en sannolikhet lägre än 10^{-5} per reaktorår för en härdskada och en sannolikhet lägre än 10^{-6} per reaktorår för brott på inneslutningen. Kraftföretagen har, med stöd av tillsynsmyndigheterna, bedömt potentiella säkerhetshöjande anläggningsändringar så att när man kan räkna hem dessa värden med rimliga antaganden, är anläggningen säker och det förordats därför att ändringen inte behöver genomföras. Det är endast när dessa siffror överskrids som det anses motiverat med speciella åtgärder för haverihantering.

Argumentationen till stöd för denna metodik är att man tillämpar minutiösa procedurer för underhåll och kontroll av anläggningarna. För anläggningar av den typ som finns i Fukushima tillämpades en lagstadgad avställning på 3 månader varje år.

Detta gör att det var mycket ovanligt med störningar eller oplanerade avbrott genom till exempel snabbstopp av anläggningarna under driftsäsongen. Eftersom en kärnkraftsolycka normalt föregås av en störning, gör den låga störningsfrekvensen det än svårare att motivera säkerhetsförbättringar. Denna grundläggande säkerhetsfilosofi har givetvis mindre betydelse när en kärnkraftsolycka sker på grund av en yttre händelse som i Fukushima.

Några ändringar har dock införts. Då diskussionen om hantering av svåra haverier pågick på åttiotalet, föreslog GE en ändring i konstruktionen som medger avlastning av inneslutningstrycket till omgivande reaktorbyggnad genom så kallade ”hardened vents”. Denna ändring infördes även i japanska verk för att göra det enkelt för operatörerna att starta upp en procedur med att fylla på vatten och avlasta inneslutningen. Det var tänkt att denna procedur skulle kunna användas om härdnödkylningen med lågtrycksinpumpning inte skulle fungera.

De japanska kriterierna för tryckavlastning av inneslutningen fick viss betydelse under kärnkraftsolyckan i Fukushima. Tryckavlastningen initieras genom ett sprängbleck och kan bara utlösas om trycket väsentligt överstiger konstruktionstrycket för inneslutningen. Finns det radioaktivitet i inneslutningen aktiveras tryckavlastningen när trycket når dubbla konstruktionstrycket. Dessa värden var baserade på experiment i Sandia som visade att inneslutningen tål belastningar av denna storleksordning. I Block 2 finns det osäkerheter i fall sprängblecket verkligt öppnade, i stället kunde tryckavlastningen av inneslutningen ske genom läckage via andra vägar.

I stället för speciella åtgärder förberedda för att ta hand om en svår kärnkraftsolycka skulle i första hand den utrustning som finns tillgängligt på stationen för andra ändamål användas. Det fanns således anslutningar förberedda för att tillföra vatten till reaktor och inneslutning genom att ansluta från kondensatpumpar och brandsläckningssystem i fall lågtrycksinpumpningen skulle misslyckas.

För att hantera situationer med bortfall av hjälpkraft har ångdrivna pumpar installerats. Dessa fick stor betydelse under kärnkraftsolyckan. Vid bortfall av hjälpkraft på ett block har det installerats möjligheter för överkoppling från de andra blocken på samma ställe. Detta synsätt kan givetvis ifrågasättas när flera anläggningar slås ut av en gemensam orsak som det skedde i Fukushima.

Innan kärnkraftsolyckan hade det gjorts ganska lite för hantering av svåra haverier. Det riktas kritik mot att det inte fanns instruktioner framtagna och att de övningar som genomfördes en gång per år inte baserades på realistiska förlopp. Det kritiserades också att viktiga säkerhetssystem inte simulerades vid övningarna.

Japansk haverihantering efter kärnkraftsolyckan i Fukushima-Daiichi

Detta underlag bygger på en presentation av NRA och ett besök vid TEPCO:s anläggning i Kashiwazaki-Kariwa där blocken 6 och 7 (båda ABWR av GE-typ) byggs om för att uppfylla de nya säkerhetskraven [6].

I de nya kraven läggs det stor vikt vid eliminering av möjligheterna för fel med gemensam orsak och att kunna hantera händelser utanför ursprungliga konstruktionsförutsättningar och skydd mot yttre händelser.

Ett mycket förbättrat skydd mot tsunami ska införas. Man bygger vågbrytarväggar och tsunami-portar för att skydda anläggningarna. Brandskydden ska förbättras väsentligt både när det gäller skydd, upptäckt och släckning av brand samt att begränsa konsekvenserna av en brand.

Skyddet mot svåra haverier innebär att utslagning av hela system för hög och lågtrycksinjektion ska klaras av. Fenomen som förlust av högtrycksinjektion och trycknedtagning, station blackout, ATWS och förlust av slutlig värmesänka ska tas om hand. För inneslutningen ska det som utgångspunkt antas en härdsmälta som ska kunna kylas i inneslutningen. System ska finnas för att reducera aktivitetsmängderna i inneslutningen, att ta ned trycket i inneslutningen och förhindra vätgasexplosioner. För inneslutningen ska det finnas filtrerad tryckavlastning. Vatten ska kunna tillföras inneslutningen både från fasta och mobila system. Den filtrerade avlastningen ska kunna bortföra hela resteffekten och därmed ensamt kunna ta ned trycket i inneslutningen. Systemet ska således användas som ett ”bleed” system.

Ett krav är att minimera utsläppet i fall där inneslutningens integritet har förlorats. Reaktorinneslutningen kommer att spolas på utsidan med vatten genom stora vattenkanoner för att reducera utsläppet.

När det gäller skydd mot terrorister och avsiktliga flygplanskrascher kommer man i första hand att kräva mobila system. Inom 5 år ska speciella bunkrade säkerhetskonstruktioner installeras. Dessa ska förse inneslutningen med vatten och elektricitet för att reducera utsläpp efter ett avsiktligt flygplanskrasch.

Vid genomgången av säkerhetsmoderniseringer i Kashiwazaki-Kariwa kunde det konstateras att konstruktionsförutsättningarna hade fundamentalt ändrats för säkerhetssystemen.

Det har byggts skyddsvallar och portar för att kunna ta hand om stora tsunamier. En jordbävningssäkrad kommandocentral hade byggts redan innan kärnkraftsolyckan. En sådan fanns även i Daiichi, något som fick betydelse för haverihanteringen där.

Satsningen på mobila system är mycket tydlig vid anläggningen. Det finns ett stort antal brandbekämpningsfordon som kan anslutas till och förse säkerhetssystemen med vatten. Det finns även ett antal mobila dieseldrivna elverk. Utrustning finns även för att kunna spola reaktorbyggnader och inneslutning utifrån. Betongpumpar finns för att förse bränslebassängerna med vatten ovanifrån. Tung utrustning finns för att rensa vägar från bråte.

Det installeras reservsystem med värmeväxlare för att kunna kyla reaktorerna och bränslebassängerna med havsvatten i fall ordinarie system inte är tillgängliga. Det finns även vattenreservoarer på olika ställen inom området.

Det installeras filtrerad tryckavlastning av inneslutningarna baserad på skrubbning och metallfilter. Tryckavlastningen ansluts till sekundärutrymmets gasvolym för att kunna dra nytta av extra skrubbning i kondensationsbassängen. Kravet är att den ska kunna avskilja 99,9 % av radioaktiva partiklar. Det finns ett sprängbleck på utloppet från skrubbern för att förhindra nedsmutsning av filtret. Detta sprängbleck

öppnas vid mycket låga tryck. Meningen är att filtersystemen ska aktiveras manuellt från en skyddad plats på utsidan.

Högtrycksinpumpningssystem, RCIC, modifieras så att flödet kan regleras manuellt med en ventil utan hjälp av el.

Vid anläggningen installeras alternativ högtrycksinpumpning av vatten som är oberoende av existerade elförsörjning för kylning av härden. Detta senare är en frivillig åtgärd som införs utan att det krävs i de nya reglerna. De ska installera bunkrade system för att skydda mot avsiktliga flygplanskrascher enligt de nya kraven.

Autokatalytiska rekombinatorer för vätgas installeras i reaktorbyggnaden för att ta hand om läckande vätgas från inneslutningen.

Skyddet mot svåra haverier förbättras genom att batterikapaciteten utökas och tryckluftssystemet modifieras för att kunna ändra ventillägen på ett säkrare sätt. Modifikationer görs på systemen för inpumpning av brandvatten så det inte blir som i Daiichi Block 1 att vattnet inte kommer in dit det ska.

I tillägg till modernisering av hårdvaran uppgavs att nya instruktioner för hantering av olyckor har tagits fram och att det pågår många övningar för att implementera dessa. Instruktionerna är baserade på djupförsvarstänkande och det läggs betydande vikt vid förmågan att möta okända situationer. Instruktioner från BWROG har varit förebild. Haveriövningar genomförs en gång i månaden, och ofta innefattar dessa också fältövningar där ingrepp i anläggningen simuleras rent praktiskt. Stora organisationsändringar hade genomförts efter analyser av arbetsbelastningen under en kärnkraftsolycka. I den nya organisationen införs att en chef ska ha maximum 5 underställda enheter.

En brist som fick viss betydelse under kärnkraftsolyckan gällde övergången från ”EOP” till ”SAMG”. I de gamla kraven saknades kriterier för detta och målen för verksamheten blev oklara. Man har nu tagit fram ett helt eget koncept för att definiera när övergång ska ske baserade på mätningar av gammastrålning vid reaktortanken.

2.7.9. Preliminära slutsatser

Det kan konstateras att det är mycket som återstår innan man har en klar bild av det inträffade. Bland annat saknas information om hur sluttillståndet ser ur i de drabbade reaktorerna. Något som kan ge ledtrådar på flera osäkra områden och speciellt när det gäller de senare delarna av härdsmältförloppen. Analyser som jämförs med data som finns från förloppen börjar peka på viktiga faktorer som tycks ha lett fram till härdsmältorna.

Grundorsaken till kärnkraftsolyckan är att man inte korrekt hade identifierat vilka händelser som kunde inträffa vid anläggningen vilket ledde till helt oförutsedda konsekvenser.

Det har i olika sammanhang rests kritik mot att operatörerna inte var utbildade för att kunna ta hand om allvarliga förlopp. Speciellt tycks detta vara tydligt i hanteringen på Block 1 där det verkade som om det var grundläggande brister i kunskap-

en om hur säkerhetssystemen fungerade. Det noteras att fullskalesimulatorn som användes vid träning och utbildning inte hade någon modell av hjälpkondensorn och att det fanns operatörer som aldrig hade sett den i drift.

Det finns åtgärder som vidtogs i förloppen som kan ha haft en avgörande betydelse för den vidare utvecklingen. En sådan händelse kan ha varit stängningen av hjälpkondensorn i Block 1 som skedde enligt gällande instruktioner. Enligt [8] försökte man att säkerställa att det fanns vatten på sekundärsidan i värmeväxlaren. Denna verifikation genomfördes inte på grund av förhöjd strålningsnivå. Resultatet blev att en möjlig kylväg stängdes. Det visade sig sedan att det var tillräckligt med vatten på sekundärsidan av värmeväxlaren.

Bland de tekniska faktorerna som bidrog till härdsmältorna verkar komponentskydden ha spelat en väsentlig roll. Det kan konstateras att det fanns inbyggda trippvillkor som inte på ett enkelt sätt kunde hävas eller överridas. Detta innebar i flera fall att viktiga komponenter av betydelse för säkerheten inte var tillgängliga som förutsatt. Det gjordes flera gånger upprepade försök att få i gång kritisk utrusning, som till exempel RCIC och HPCI utan att lyckas. I Block 2 som var mest utsatt för elbortfall och som därmed inte hade skydden och trippvillkoren aktiverade tog det längst tid innan härden smälte. Orsakerna till att viss utrustning stannade eller inte var tillgänglig utreds fortfarande. Det noteras att TEPCO inför möjlighet för manuell reglering av RCIC i reaktorerna i Kashiwazaki-Kariwa.

Strategin under haveribekämpningen var att använda brandutrustning för att förse reaktorerna med vatten. Det visade sig att denna strategi innebar olika typer av problem. När inpumpningen kom igång kom bara en mindre del av att vattnet dit det skulle. I stället fanns det alternativa flödesvägar på grund av felmonterade eller läckande ventiler. Analyser pekar på att endast 20-50 % av det inpumpade vattnet i Block 1 nådde reaktorn. En hel del vatten samlades till exempel i kondensattanken. De andra anläggningarna har informerats om detta och ändringar införs. Enligt TEPCO är det troligt att man hade kunnat kyla härden om allt vatten hade gått dit det skulle.

Ett annat problem med brandvattnet var att trycket inte var tillräckligt för att pumpa in vatten mot reaktortrycket. När trycket var tillräckligt lågt pumpades vatten in. Detta vatten förångades nära botten av den överhettade härden och bidrog även till bildande av vätgas vilket i sin tur ledde till ökande tryck och svårigheter att pumpa in mer vatten.

Tryckavlastning av inneslutningen kunde aktiveras med extraordinära åtgärder först när trycket i inneslutningen väsentligt översteg konstruktionstrycket. Denna tryckavlastning krävde manuella åtgärder. Detta ledde till att avlastning skedde ganska sent i förloppen när det var hög aktivitetsnivå i inneslutningen. I de nya säkerhetsföreskrifterna krävs att filtrerad tryckavlastning ska finnas. I TEPCO:s anläggning i Kashiwazaki-Kariwa satsar man på ett system med avblåsning från ”wetwell” som kan öppnas manuellt från en skyddad plats även vid mycket låga inneslutningstryck.

2.7.10. Referenser

[1] Investigation Committee on the Accident at Fukushima Nuclear Power Stations of Tokyo Electric Power Company (Hatamuras rapport) Final Report, July 23,2012.

[2] Investigation Committee on the Accident at Fukushima Nuclear Power Stations of Tokyo Electric Power Company (Hatamuras rapport) Interim Report, December 26,2011

[3] The National Diet of Japan Fukushima Nuclear Accident Independent Investigation Commission (NAIIC) (Diet-rapporten). July 2012

[4] Fukushima Nuclear Accident Analysis Report, June 20, 2012.Tokyo Electric Power Company, Inc.

[5] Special Report: Lessons Learned from the Nuclear Accident at the Fukushima Daiichi Nuclear Power Station. INPO 11-005 Addendum. August 2012.

[6] Reserapport från APRI:s studierese till Japan 14-17 Oktober, 2014. Dokument SSM 014-3514.

[7] Fukushima accident - Challenges for Swedish accident management! Can extremes be managed? APRI Seminar Johannesberg slott, January 25-26, 2012

[8] Evaluation of the situation of cores and containment vessels of Fukushima Daiichi nuclear Power StationUnits-1 to 3 and examination into unsolved issues in the accident progression Progress Report No. 2August 6, 2014. Tokyo Electric Power Company, Inc.

[9] Evaluation of the situation of cores and containment vessels of Fukushima Daiichi Nuclear Power StationUnits-1 to 3 and examination into unsolved issues in the accident progression Progress Report No. 2August 6, 2014. Tokyo Electric Power Company, Inc. Attachment 3. Findings from the latest analyses using MAAP5.

[10] European stress tests. The Swedish National Report for nuclear power plants December 29, 2011.

3. KTH RESEARCH ON SEVERE ACCIDENTS

3.1 Research Goals, Approach and Activities

The severe accident management (SAM) in Nordic boiling water reactors (BWRs) relies on ex-vessel core debris coolability. In the case of core meltdown and vessel failure, melt is poured into a deep pool of water located under the reactor. The melt is expected to fragment, quench, and form a debris bed that is coolable by natural circulation of water. Success of the SAM strategy is contingent upon melt release conditions from the vessel which determine (i) properties of the debris bed and thus the coolability of the bed, as well as (ii) potential for energetic interactions between hot liquid melt and volatile coolant (steam explosion). Both non-coolable debris bed and steam explosion pose credible threats to containment integrity.

While conceptually simple, this strategy involves extremely complex physical phenomena which are sensitive to the conditions of transient accident scenarios. For instance, late recovery actions might affect core degradation and relocation processes, formation of the in-vessel debris bed, heat-up and re-melting, thermo-mechanical interactions between melt and vessel structures and penetrations, vessel failure, melt release and jet fragmentation, debris solidification, energetic melt-coolant interactions, two-phase flow in porous media, spreading of debris in the pool, spreading of particulate debris bed, etc. (Figure 3.1). These phenomena have been a subject of extensive investigations in a large-scale research program on Melt-Structure-Water Interactions (MSWI) at the Royal Institute of Technology (KTH) over the past few decades. A significant progress has been made in understanding and predicting MSWI physical phenomena.

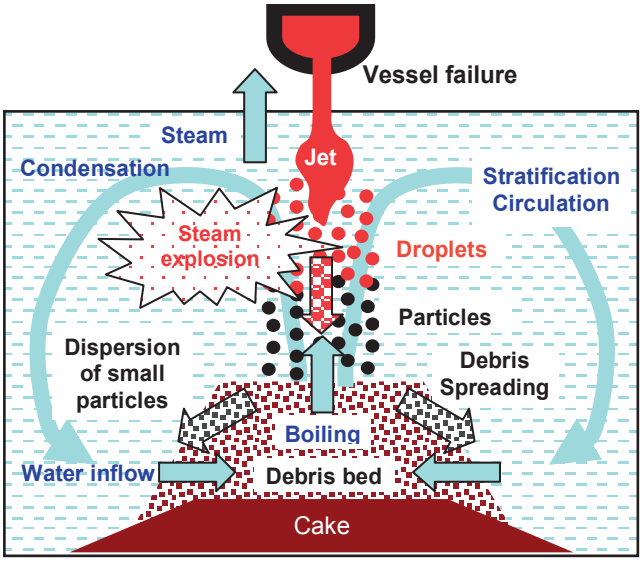

Figure 3.1. Severe accident phenomena in Nordic BWR.

However, the complex interactions and feedbacks between (i) scenarios of accident progression, and (ii) phenomenological processes, have hampered a comprehensive assessment of the SAM effectiveness in the Nordic BWRs. Presently, the issues of ex-vessel debris coolability and steam explosion are considered as intractable by only probabilistic or only deterministic approaches.

The Risk Oriented Accident Analysis Methodology (ROAAM) marries probabilistic and deterministic approaches. This methodology developed by Professor Theofanous [57] has been applied to successfully resolve different severe accident issues in LWR plants, and severe accident treatments in advanced LWR designs e.g., ESBWR [58]. When applied to the Nordic BWR plants, the tight coupling between severe accident threats (steam explosion and basemat melt-through due to debris un-coolability) and high sensitivity of the SAM effectiveness to timing of event (e.g., vessel failure) and characteristics (e.g., melt release conditions), present new challenges to the ROAAM in decomposition, analysis and integration.

APRI-8 project goal is to develop risk oriented accident analysis frameworks for quantifying conditional threats to containment integrity for a reference plant design of Nordic type BWRs. The reference BWR design is not an exact copy of any specific reactor. However, important common features of the existing reactors are preserved for assessment of effectiveness of different severe accident mitigation strategies.

In order to achieve the goal, following tasks were identified to be accomplished in APRI-8:

1. Develop deterministic and probabilistic parts of the ROAAM frameworks connecting plant damage states and respective containment failure modes for the reference Nordic BWR plant design.
2. Further develop necessary deterministic tools (experiments, deterministic codes and simplified surrogate models (maps)) for quantification of loads and fragilities in: vessel-melt interactions and melt release modes; debris bed formation and coolability; impact of ex-vessel steam explosion.
3. In collaboration with APRI reference group: to identify plant data necessary for closure of the ROAAM frameworks; to define the reference Nordic BWR plant design data for closure of the frameworks; to utilize ROAAM frameworks in issue resolution for existing plants by development of integrated Risk Assessment and Risk Management strategy; to perform scoping feasibility studies on application of ROAAM to resolution of severe accident issues specific to other types of Nordic plant designs.
4. Retain and develop national expertise in analysis of severe accident phenomena in order to: support unique experimental infrastructure and team of reactor safety experts knowledgeable and prepared to address complex reactor safety issues in the Nordic plants; contribute to development of general capabilities in simulation of complex severe accident scenarios and quantification of reactor-scale phenomena by further development and validation of the models and codes; participate in international activities (EU, OECD, etc.) related to severe accident analysis to bring and adapt the international efforts and knowledge to Nordic context.

The work is formally divided into four sub-tasks, tightly interconnected with each other: Risk Evaluation and Synthesis (RES); Melt Ejection Mode (MEM); Debris Coolability Map (DECO); Steam Explosion Impact Map (SEIM).

3.2 Risk Evaluation and Synthesis (RES)

The goals of RES are (i) to develop a robust integrated risk assessment approach for the reference Nordic type BWR plant design by developing ROAAM frameworks and synthesizing phenomenological models, and probabilistic frameworks; (ii) to prioritize research objectives for resolution of severe accident issues specific to other types of Nordic plants designs.

Respective strategic tasks for RES are: (i) to implement ROAAM approach for resolution of severe accident issues in Nordic BWRs; (ii) to guide, align and optimize development of deterministic phenomenological models and probabilistic frameworks in MEM, DECO and SEIM subprojects; (iii) to develop integrated risk assessment tool based on data and methods developed in MEM, DECO and SEIM.

3.2.1. Background: Quantitative Definition of Risk and ROAAM Basics

According to quantitative definition of risk, proposed by Kaplan and Garrick [16], the risk R_i associated with specific scenario s_i can be characterized by its frequency f_i and consequences c_i. Consequences are obtained from predictions that are subject to epistemic uncertainty due to incomplete knowledge. The degree of uncertainty in the prediction of the future course of events can be quantified as "probability" P_i or "likelihood" of c_i. Such probability is evaluated by an expert based on the available evidences (data and experience with similar courses of action in the past). Therefore, two rational beings given the identical evidence must assess the probability identically [16]. "Frequency" is the outcome of an experiment involving repeated trials. Aleatory uncertainty is expressed in terms of frequency.

$$R_i = \{s_i, f_i, P_i(c_i)\} \tag{1}$$

Consequences can be presented as joint probability density function $\mathrm{pdf}_{C_iL_i}(L_i, C_i)$ of the loads (L_i) on the system and its capacity (C_i) to withstand the loads. Failure probability P_{Fi} for scenario s_i can be evaluated as

$$P_{Fi} = P(L_i \geq C_i) = P(C_i - L_i = Z_i \leq 0) = \iint_{Z_i \leq 0} \mathrm{pdf}_{C_iL_i}(c, l)dcdl \tag{2}$$

Unacceptability of containment failure is equivalent to requirement that all P_{Fi} should be below "physically unreasonable" level P_s.

ROAAM [57] provides guidelines for development of frameworks for bounding the epistemic (modeling), and aleatory (scenario) uncertainties in a transparent and verifiable manner in order to enable convergence of experts' opinions in the review process. Principal ingredients of ROAAM are: (i) identification, separate treatment, and maintenance of separation (to the end results) of aleatory and epistemic uncertainties; (ii) identification and bounding/conservative treatment of uncertainties (in parameters and scenarios, respectively) that are beyond the reach of any reasonably verifiable quantification; and (iii) the use of external experts in a review, rather than in a primary quantification capacity. Separate treatment of screening frequency for aleatory, and the physically unreasonable concept for epistemic uncertainties is a must for clarity and consistency of the ROAAM result. An arbitrary scale for probability is introduced in ROAAM, which defines a physically unreasonable process

as one involving the independent combination of a process that is within known trends but obtainable only at the edge-of-spectrum parameters and the process that is outside the spectrum of reason but cannot be positively excluded [57].

3.2.2. Nordic BWR challenges for ROAAM: Phenomenology and Scenarios

While ROAAM is logically sound and has been successfully applied in several practical cases to resolve severe accident issues, there are some challenges for application of ROAAM to Nordic BWR case. Typical phenomenological stages of severe accident progression in Nordic BWR are shown in [23].

The multistage path from the initial plant damage state to the containment threats is an important source of complexity and uncertainty. Phenomena and scenarios including operator actions are tightly coupled in their mutual interactions and eventual impact on the possibility of different containment failure modes. Conditions created at the earlier stages can significantly affect configurations and problem statements at later stages. For instance, if there is no activation of lower drywell flooding, then steam explosion risk is eliminated, but hot corium melt will attack cable penetrations in the containment floor leading to containment failure. Timing of transition between different stages is also important. Different time-dependent trajectories of the accident scenarios with the same logical sequence of the stages can result in different outcomes. For instance, decay heat is decreasing with time providing much better chances for coolability of the debris bed if melt is released from the vessel later [70]. However, if melt is released from the vessel later, it will have higher temperature, which could increase the risk of debris agglomeration [26], [20], [21] hindering coolability of the debris bed [71], and creating a potential for an energetic steam explosion which can threaten containment integrity. Combination of (at least) two threats (non-coolable debris and steam explosion) is another source of uncertainty. On one hand, it is not clear if steam explosion might contribute to spreading of the debris over containment floor. On the other hand, even a mild steam explosion might negatively affect debris bed cooling, e.g. by destroying protective covers for cable penetrations in the containment floor and exposing them to hot debris, or by creating a leak of coolant from the lower drywell, or by activating filtered containment venting, releasing fraction of nitrogen which can potentially lead to drop of containment pressure below atmospheric level [11], etc.

The major challenge for application of ROAAM to Nordic BWR is the complexity of tightly coupled transient phenomena and scenarios which limit the effectiveness of heuristic approaches (based on expert judgment) to (i) to a priori identification of the key physics; (ii) judgment about importance and impact of timing and coupling of the phenomena and scenarios on the accident progression and outcome; and (iii) problem decomposition. If inherent safety margins are large, containment failure being physically unreasonable can be demonstrated through consistent conservative treatment of uncertainties. However, for complex systems, such as SAM of Nordic BWR, uncertainty can create a space for “hope” that the system is safe due to some incompletely understood phenomena or interactions. In this case assessment should focus on the necessity of containment failure using “optimistic” treatment of uncertainty. If such necessity is too large, then a modification of the SAM is wanted. A difficulty arises when neither failure nor success can be demonstrated with a sufficient confidence, e.g. when bounding (“conservative” or “opti-

mistic") approaches fail to characterize system risks because only an "optimal" course of events leads to transition from failure to success. This is often the case when there are competing phenomena or threats, when positive or negative effect of some parameters or events on the failure probability changes depending on other parameters or events. Risk quantification can be polluted with uncertainty to the point where "everything is possible" due to combinatorial explosion of possibilities. If "everything is possible", it is a clear sign that the system is complex. In other words, understanding and control of the system is beyond our reach and changes in the system are necessary in order to make its behavior predictable with sufficient confidence. A structured process is necessary for robust assessment of either "possibility" or "necessity" of containment failure. In the next section some aspects of development of such process for Nordic BWR SAM are discussed.

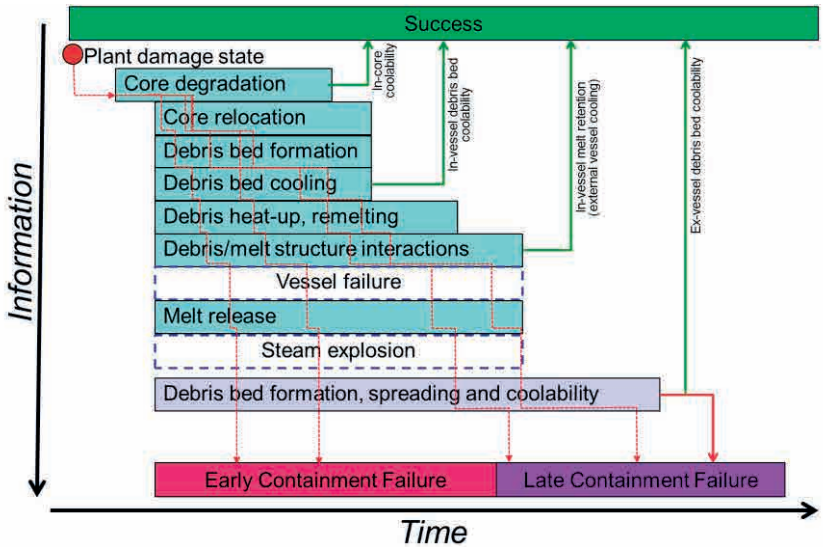

Figure 3.2. Severe accident progression in Nordic BWR.

3.2.3. ROAAM+ Probabilistic Framework for Nordic BWR

It is clear that key ingredients of ROAAM such as: (i) separation of aleatory and epistemic uncertainties through consideration of risk as a set of the triplets (scenario, its frequency, and probability of consequences), and decomposition of the problem into stochastic "scenarios" and deterministic "frameworks"; (ii) arbitrary scale of probability for epistemic uncertainty; and (iii) qualitative definition of safety goal, are critical for consistency of assessment and transparency of review and must be preserved. The challenges presented by Nordic BWR SAM strategy require further development of the approach. In this section we discuss the basic ideas and examples of development of such an approach which we call ROAAM+. The goal of the ROAAM+ approach is to provide sufficient information for a decision to:

I. Either keep the SAM strategy: "Possibility" of containment failure is low even with "conservative" treatment of uncertainty, thus current strategy is reliable.
II. Or modify the SAM strategy: "Necessity" of containment failure in the course of accident is high (i.e., "possibility" that containment doesn't fail is low) even with "optimistic" treatment of uncertainty, thus the current strategy is unreliable and changes should be considered.

In order to achieve the goal, ROAAM+ process is developed for coherent construction and adaptive refinement of (i) risk assessment framework, and (ii) necessary data and knowledge. This process is guided by extensive sensitivity and uncertainty analysis. The process is aiming to refine the resolution of the framework in order to bound the influence of the largest contributors to the uncertainty in risk assessment.

Iterative Adaptive Refinement Process for Development of Risk Assessment Framework

Since system complexity limits effectiveness of heuristic approach (based on expert judgment), there is a need for an iterative research process which can help in identifying and evaluating importance of different factors for the ultimate risk assessment. A framework for risk assessment is needed as a platform that provides means for sensitivity and uncertainty analysis. Based on the analysis results, activities on improvement of the framework and data are undertaken in order to provide more reliable estimates for "possibility" and "necessity" of containment failure with each new iteration. The framework is designed to carry out three different types of analysis (1) conservative assessment of containment failure possibility; (2) optimistic assessment of containment failure necessity; and (3) sensitivity and uncertainty analysis as an instrument for guiding construction and refinement of the risk assessment framework itself. In practice, different analysis types are implemented through consistent use of assumptions on uncertainty in (i) scenarios and (ii) ranges and probability distributions of the uncertain parameters. Sensitivity and uncertainty analysis is employed for both (a) optimal refinement of the data, knowledge and risk analysis framework, and (b) optimization and assessment of effectiveness of potential system modifications.

Full and Surrogate Models, "Coarse-Fine", "Forward" and "Reverse" Analyses

Complex phenomena and feedbacks require adequate complexity of the models. Such "full models" (FMs) are implemented for each stage of the accident progression in multidimensional severe accident, thermal hydraulics, and structural analysis codes. Applications of such FMs for extensive sensitivity and especially uncertainty analysis are often unaffordable. Therefore, a two-level coarse-fine modeling approach is proposed. At the first (bottom) level we use loosely coupled FMs and experimental evidences in order to generate relevant data and develop understanding of key physics. The data are used to develop and validate coarse-resolution computationally efficient "surrogate models" (SMs) which approximate the most important parameters of the FM solutions. The SMs are used at the second (top) level of the framework for sensitivity, uncertainty analysis and risk quantification. We call this process "forward" analysis.

There is a need for iterative refinement process of the FMs, SMs, experimental data and structure of the framework. Criteria for the need of refinement can be established based on consideration of the failure domain. Failure domain (FD) is a domain in the space of the uncertain parameters where probability of containment failure is larger than a "physically unreasonable" threshold. The main questions that should be addressed are (i) how large is the uncertainty in resolving the boundaries of the failure domain with existing FMs and SMs, and (ii) are there any physical phenomena or scenarios which are not taken into account yet, but can significantly change FD boundaries. Naturally, the FD identification and refinement starts from

the last stages of the accident progression analysis and propagates "upstream" to the earlier stages. We call this process "reverse" analysis. In fact, FMs should be designed according to the requirements which can be inferred from the results of the reverse analysis. The need for new data stems from the model validation. The two-level coarse-fine approach to development and iterative adaptive refinement of the risk assessment frameworks is summarized below:

1) *Development and refinement:* of models, frameworks and data based on the results of the forward and reverse analyses in order to reduce uncertainty in the failure probability and resolution of failure domain boundaries.
   Experimental evidences and fine-resolution but computationally expensive methods (FMs) are used in order to:
   i. Develop hypothesis about key phenomena and provide better understanding of their possible interdependencies,
   ii. Identify transitions between different regimes and failure modes, and
   iii. Generate reference databases for development calibration and verification of coarse-resolution but computationally efficient surrogate models (SMs).
   FMs are run in "exploratory" mode, loosely coupled or independently from each other, assuming bounding ranges for model input parameters. Preliminary scaling analysis is carried out for the experimental evidences.

2) *Forward analysis: quantification* of major contributors to the uncertainty in the failure probability at each stage of the modeling of accident progression.
   A probabilistic framework is developed based on coupled SMs in order to connect the initial plant damage states with respective containment failure modes.
   i. Deterministic processes are treated using the developed and verified SMs preserving importance of scenarios and timing.
   ii. Sensitivity and uncertainty analysis is carried out to (a) identify significant and unimportant parameters, regimes and scenarios, (b) quantify contribution of the most influencing factors to the uncertainty in failure probability.

3) *Reverse analysis:* identification of failure domains and their boundaries at each stage of the modeling of accident progression.
   Failure domains and their boundaries are identified in the spaces of uncertain input parameters for each SM (representing different stages of the accident progression) in order to identify the needs for improvement of: experimental data and scaling; FMs and their validation matrices; SMs, calibration and verification databases (based on FMs and experimental data), interconnections and databases of solutions; overall problem decomposition into scenarios and frameworks.

Such iterative process is designed to develop state of the art knowledge, confidence and transparency in the risk assessment results, to the point when convergence of experts' opinion on the possibility or necessity of containment failure can be achieved. Such convergence is a stopping criterion for the refinement process. Failure probability (P_{Fi}) is used in the process not only as the final outcome of the assessment, but also as a research instrument in the adaptive refinement process. Sensitivity analysis of P_{Fi} to ranges and distributions of the uncertain parameters is used to identify (i) major sources of the uncertainty and possible unreasonable conservatism in the risk assessment, and (ii) the needs for refinement of the evidence database. The primary goal of Failure Domain (FD) analysis is to identify the conditions and explain the reasons of failure in terms of key physics and scenarios. Iden-

tification of the failure domain is a product of the "reverse" analysis which propagates information "backwards" from the end state where failure is determined through the casual relationships (CR) to the spaces of input (scenario and modeling) parameters. By identifying and grouping scenarios and conditions which lead to failure, we can determine and explain the reasons of failure using compact representation of information, amenable for scrutiny. Details of the mathematical approaches developed for quantification of the failure probability and failure domains in the multistage deterministic analysis model are provided in [23].

Development and Implementation of the ROAAM+ Framework

The top layer of the ROAAM+ framework for Nordic BWR (Figure 3.3) decomposes severe accident progression (Figure 3.1) into a set of causal relationships (CR) implemented as respective surrogate models (SM) connected through initial conditions. Initial plant damage states $\{D_j\}$ and their frequencies $\{f_j\}$ are determined based on PSA L1 data [24] aiming at completeness of the analysis. For each plant damage state, a full set of possible events (such as different recovery and mitigation actions) which can affect further accident progression is considered. The events, their order and timing create a space of scenarios $\{s_i\}$. Forward analysis defines conditional containment failure probability for each scenario $\{s_i\}$. Reverse analysis identifies failure domains in the space of scenarios $\{s_i\}$, and "deterministic" $\{d_i\}$ and "intangible" $\{i_i\}$ parameters specific to each model. Grouping and classification of failure scenarios corresponding to specific initial plant damage states help to identify plant vulnerabilities and provide insights into possible efficient mitigation actions by operator. Failure domain in the space of deterministic and intangible modeling parameters identifies the need for improvement of knowledge, modeling and data.

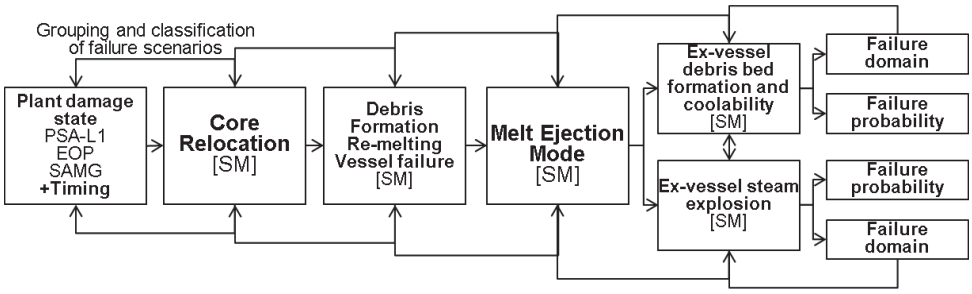

Figure 3.3. ROAAM+ framework for Nordic BWR.

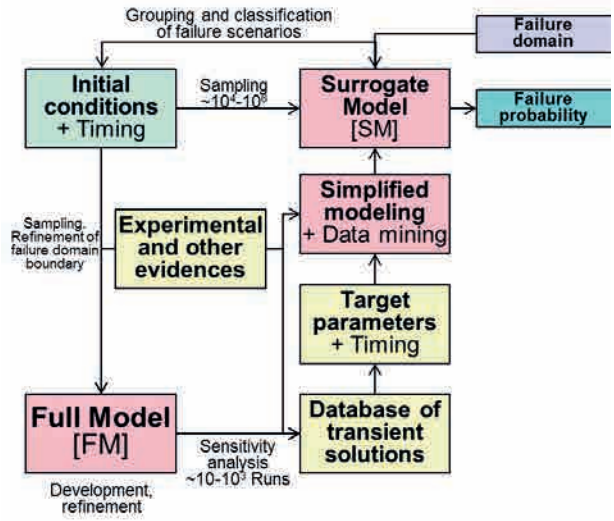

Figure 3.4. Full and surrogate model development, integration with evidences, refinement, prediction of failure probability and failure domain identification.

The process of development and validation of the individual surrogate models is important for completeness, consistency, and transparency of the results. General ideas of the process are illustrated in Figure 3.4. Initial conditions come from the analysis at the previous stages of the framework. Experimental evidences provide a knowledge base for validation of the FMs and calibration of SMs. Full Model (FM) is implemented as detailed fine resolution (computationally expensive) simulation approach. Database of the FM transient solutions is developed in order to provide better understanding of basic physical processes and typical behavior of the target parameters. The target parameters are the input conditions for the next model in the framework. Simplified modeling approaches and data mining techniques are used in order to develop a surrogate model. Surrogate model (SM) is an approximation of the FM model prediction of the target parameters which employ simplified (coarse resolution) physical modeling, calibratable closures, or approximations to the response surface of FM. Lists of input/output parameters are determined for each SM: (i) scenario specific data (e.g. water level and temperature in the lower drywell, possible mitigating actions and their timing, etc.); (ii) initial conditions (p_{ki}), that connects SMs between each other through SM input/output; (iii) deterministic and intangible parameters $\{d_{ki}, i_{ki}\}$. Ranges and respective multidimensional probability density functions are determined for all $\{d_{ki}, i_{ki}\}$. Advanced sampling techniques (e.g. GA-IDPSA [65], Adaptive-Mesh-Refinement (AMR) [39]) are used to increase computational efficiency of failure domain identification in the space of uncertain parameters and accident scenarios. Characterization of the failure domains is carried out using clustering and classification approaches. Decision tree is used for visualization of the failure domain [10] in multidimensional space in order to provide information that can be appreciated by the decision maker.

3.2.4. RES: Summary and Outlook

The focus of RES is on the process of refining the ROAAM+ framework. The aim of the process is to achieve (i) completeness, (ii) consistency, and (iii) transparency in the review of the analysis and its results. A two-level coarse-fine iterative analysis approach is proposed. First, fine-resolution but computationally expensive methods are used in order (a) to provide better understanding of key phenomena

and their interdependencies, (b) to identify transitions between qualitatively different regimes and failure modes, and (c) to generate reference data. The fine-resolution codes are run independently, assuming wider possible ranges of the input parameters. Second, a set of coupled modular frameworks is developed connecting initial plant damage states with respective containment failure modes. Deterministic processes are treated using surrogate models based on the data obtained from the fine-resolution models. The surrogate models are computationally efficient and preserve the importance of scenario and timing. Analysis carried out with the complete frameworks helps to identify risk significant and unimportant regimes and scenarios, as well as ranges of the uncertain parameters where fine-resolution data is missing. This information is used in the next iteration of analysis with fine-resolution models, and then refinement of (1) overall structure of the frameworks, (2) surrogate models, and (3) their interconnections. Such iterative approach helps identifying areas where additional data may significantly reduce uncertainty in the fine- and coarse-resolution methods, and increase confidence and transparency in the risk assessment results. Further experience of practical application of the framework and process will be accumulated in the preliminary risk assessment of the containment failure.

3.3 Melt Ejection Mode (MEM)

The MEM goal is to develop deterministic models in order to establish connection between plant damage states and respective characteristics of (i) core relocation; (ii) vessel failure (timing and mode); and (iii) melt ejection (vessel breach size, melt superheat, composition, flow rate and total amount of ejected melt).

3.3.1. Core Relocation

The work is motivated by the high sensitivity of the vessel failure phenomena to the characteristics of the debris in the lower plenum [64, 14]. The ultimate goal of this work is to develop Core Relocation full and surrogate models that can be used in the ROAAM+ framework [23] for prediction of the effect of core degradation and relocation processes on the debris bed properties in the lower head. General approach to the development of the Core relocation SM is illustrated in Figure 3.5. In order to achieve the goal and develop the SM according to the general approach, following tasks are addressed and discussed in this work: (i) definition of the plant damage states and respective frequencies from PSA-L1; (ii) definition of the scenario space including possible timing of system recovery and operator actions; (iii) development of the database of the core degradation transients using MELCOR code and GA-IDPSA [66, 30, 67, 65] adaptive sampling techniques in the scenario space; (iv) establishing of connections with the other SMs in the ROAAM+ framework; (v) data mining and simplified modeling for development of the SM based on the database of the FM solutions.

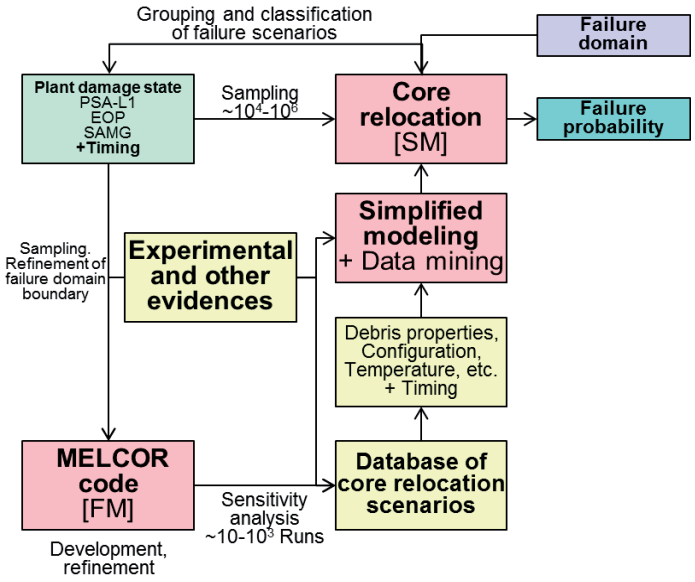

Figure 3.5. Core relocation surrogate model.

Definition of the plant damage states based on PSA-L1 data

This task includes (i) grouping of initial plant damage states based on PSA-L1, EOP and SAMG; (ii) selection of representative plant damage states (based on contribution to total core damage frequency) and scenarios for MELCOR (FM) analysis. It is important to identify (a) possible accident progression scenarios; (b) safety systems that can affect in-vessel/ex-vessel accident progression (e.g. ECCS, RHR, etc.); and (c) conditions for activation of these safety systems (e.g. lower drywell flooding condition – together with ECCS, RHR and depressurization history will identify water pool temperature in the cavity). In PSA L1 for Nordic BWR reference plant design the core damage states are grouped into 4 categories: HS1 (ATWS), HS2 (core damage due to inadequate core cooling), HS3 (core damage due to inadequate residual heat removal) and HS4 (rapid overpressure of the primary system). The categories (HS1, HS2, HS4) correspond to early core damage scenarios, HS3 corresponds to late core damage. In addressing ex-vessel behavior and consequences the following physical phenomena can challenge containment integrity: direct containment heating (DCH), ex-vessel steam explosions (EVE) and basemat penetration (BMP) by non-coolable corium debris. DCH scenario corresponds to high pressure (HP) accident scenario, steam explosion in the containment (EVE) corresponds to low pressure (LP) scenario. Both HP and LP will lead to formation of ex-vessel debris bed and potential corium interaction with containment basemat. The core damage sequences can be grouped together based on the aforementioned challenges to the containment integrity as shown in Figure 3.6. Corresponding frequencies are obtained from PSA L1 data.

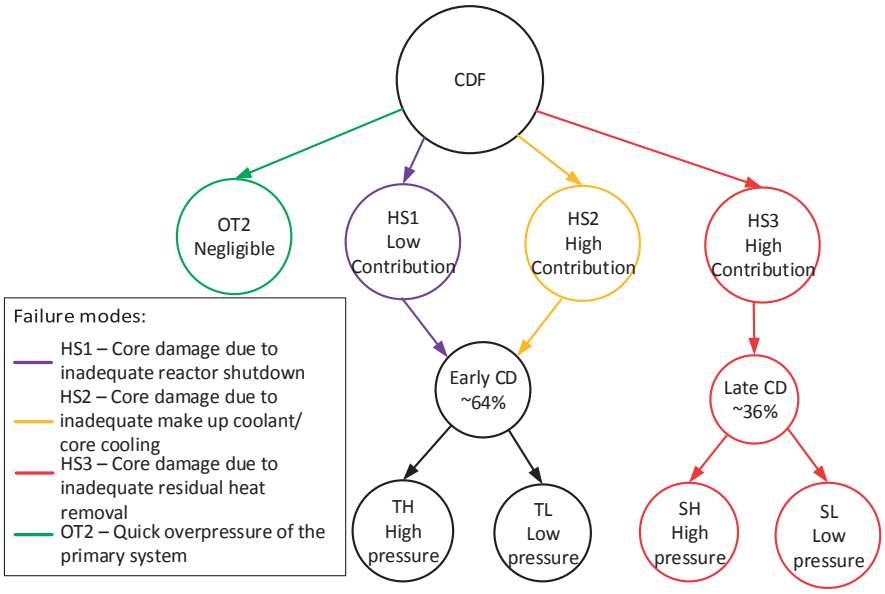

Figure 3.6. Core damage states classification.

Definition of the scenario space with possible recovery and operator actions

The MELCOR code is used (Figure 3.7) to develop the database of the core degradation transients starting from selected plant damage states [12]. The station blackout (SBO) scenarios (with different timing of power recovery) are chosen as the major contributor to the CDF according to PSA-L1. The timing of the safety systems recovery is as part of the accident scenarios space. For instance, we consider a delay in activation of Reactor Pressure Vessel (RPV) depressurization systems which includes battery-powered ADS-Valves (System 314) and Water-Valves (System VX105, FL314 & FL330). Overpressure protection system (FL314) is spring-operated will open stepwise, starting at slightly above 70 bar and opening completely at 75 bar to protect the RPV from failure. The auxiliary Feedwater System (System 327, FL327) is considered non-functional. Other system like the Control Rod Guide Tube (CRGT) Cooling or the Residual Heat Removal (RHR) Systems are also considered non-functional. The capacity and timing of activation of the Emergency Core Cooling System (ECCS System 323, FL323) is another element of the scenario. Necessary condition for activation of the ECCS is low pressure in the RPV. Mass flow begins at pressure of 12.5 bars and will reach its maximum value at 2 bars above the wetwell pressure.

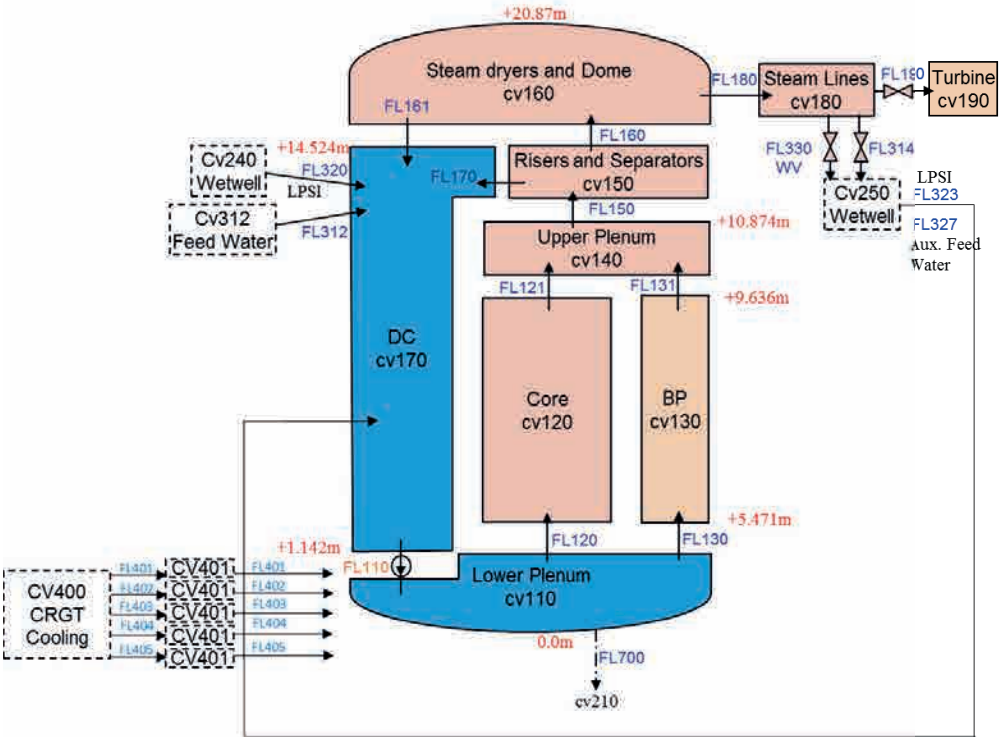

Figure 3.7. MELCOR nodalization of the Nordic BWR.

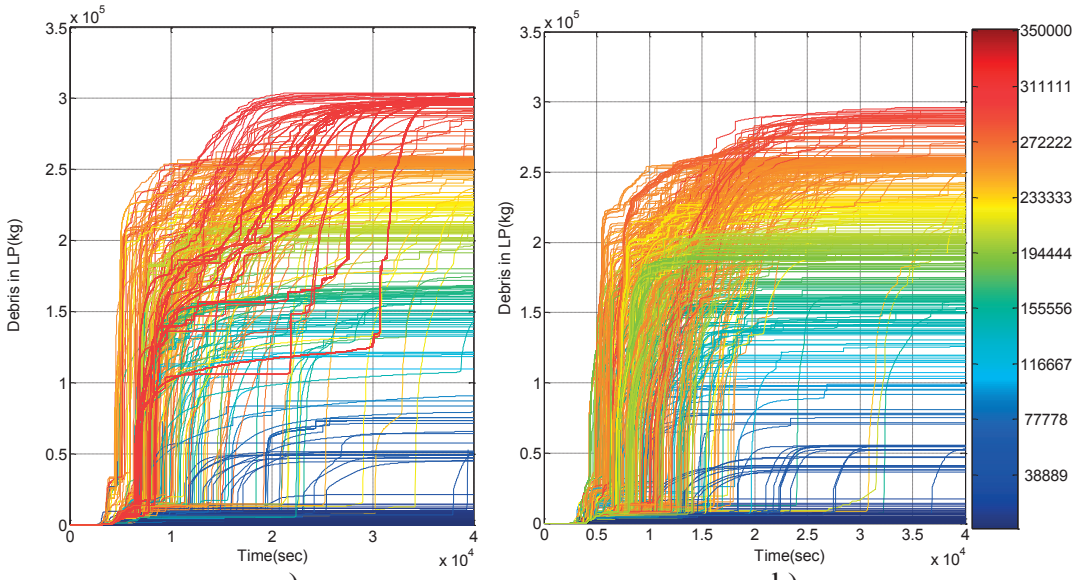

Figure 3.8. Relocated debris mass over time as a function of a) $\boldsymbol{ADS_{\Delta T}, ECCS_{\Delta T}, ECCS_{A}}$, and b) $\boldsymbol{ADS_{\Delta T}, ECCS_{\Delta T}}$, with full ECCS capacity.

We employ the GA-IDPSA [67] to search the space of scenario parameters such as (i) activation time delay of the depressurization of the Reactor Pressure Vessel (affected: Systems 314 and VX105) from 0 to 15 000 seconds; (ii) activation time delay of the low-pressure coolant injection (affected: System 323) from 0 to 15 000 seconds; (iii) maximum mass flowrate delivered by System 323, when working, between 0 and 1120 kg/s (fraction from 0.0 to 1.0 of full ECCS capacity) in order to find combinations which provide specific values of selected fitness function, e.g. mass of the relocated debris. The vessel breach condition was not implemented in

the analysis. Figure 3.8 - Figure 3.9 present summary of obtained results. In total there are more than ~10^3 runs which represent a database for development of the core relocation SM.

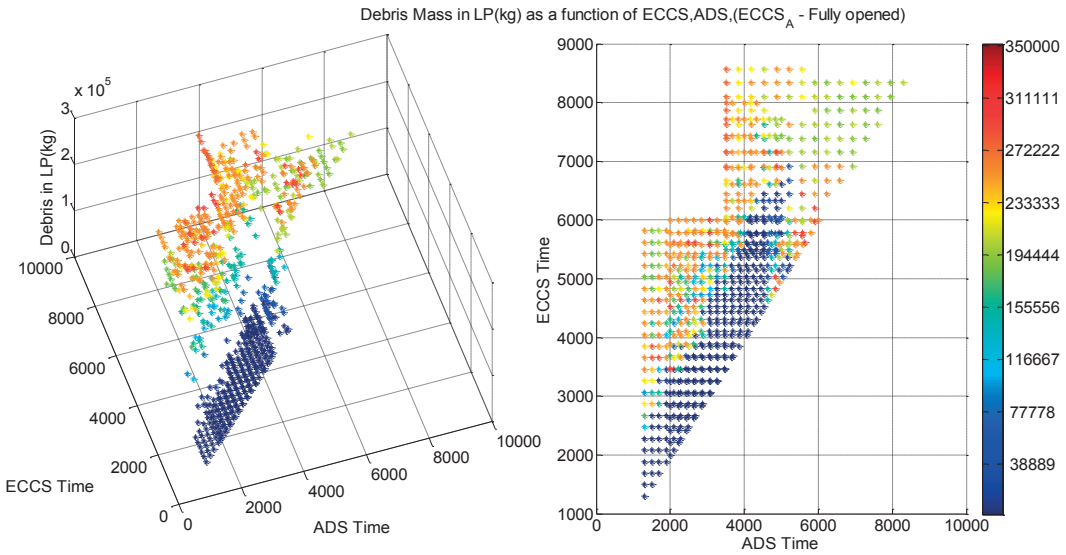

Figure 3.9. Relocated debris mass map depending on recovery time of ADS, ECCS with full capacity of ECCS.

Establishing of connections with the other SMs in ROAAM+ framework

The input to the surrogate model consists of: (1) scenario parameters including initial plant damage states identified in PSA-L1, timing of recovery and capacity of safety systems, and possible operator actions (EOPs, SMAGs); (2) deterministic modeling parameters: candling heat transfer coefficients, component critical minimum thicknesses to maintain intact, in-vessel falling debris quench model parameters and decay heat model; and (3) intangible parameters: loading and failure criteria for support structures. The output of Core relocation SM such as relocation time, debris mass and temperature, debris bed composition, spatial configuration are provided as input parameters in the In-Vessel Debris Coolability and Vessel Failure SMs. Containment pressure, lower drywell pool depth and temperature are treated as scenario parameters in Ex-Vessel Coolability (DECO) and Steam Explosion Impact Map (SEIM) SMs.

Data mining and simplified modeling

Classification and clustering analysis is used in order to group different transients into clusters, whose members have similar characteristics determined by the user. We use principal component analysis (PCA) together with grid based clustering and Adaptive Mesh Refinement (AMR) [10]. In Figure 3.10 the clustering analysis results based on the amount of relocated debris to the lower plenum indicates two characteristic domains of the scenarios space. Green and red domains represent scenarios with small relocations (between 0 and 10 tons) and very large relocations (over 200 tons). The shape of the domains suggests that the activation of ECCS is effective in preventing core relocation only within certain time window. If activation is delayed, then large mass of relocated debris is expected with high likelihood. It is instructive to note that domains of scenarios with intermediate (10-100 tons) and large (100-200 tons) relocation masses are rather small (Figure 3.10b). The fig-

ure shows that the domains of very large, large and intermediate relocations may overlap, especially for the late ADS activation where decay heat is lower. In the overlap domain relatively large variation of the masses of relocated debris (from 10-200 tons) can be obtained with relatively small variations of the input parameters.

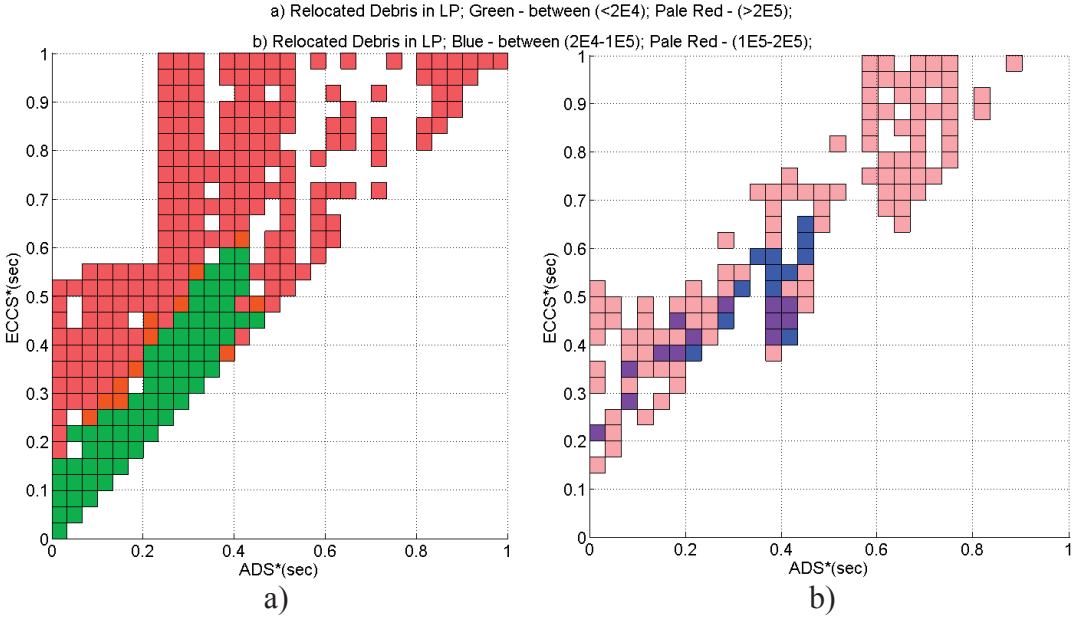

Figure 3.10. Clustering analysis results for the mass of relocated debris.

Development of the SM based on the FM solutions database and neural networks

An approach to development of the SM is shown in Figure 3.11. The SM uses the safety systems' recovery time and capacity as inputs. We use Artificial Neural Networks (ANN) for prediction of the mass and properties of relocated debris. We use Multi-Layer Perceptron (MLP) trained by a back-propagation algorithm [9], and Radial Basis Function (RBF) multilayer architecture which is feed-forward and can be used for strict interpolation in multi-dimensional space [9].

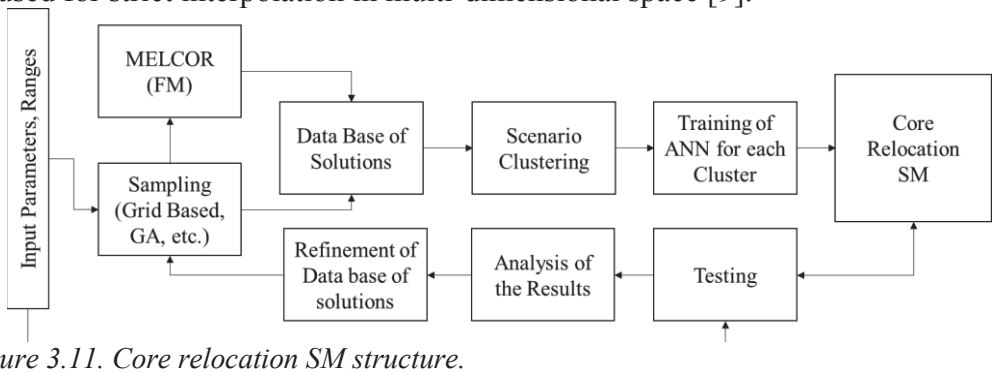

Figure 3.11. Core relocation SM structure.

Currently there are two approaches under development for the core relocation SM. First, scenarios in the database are clustered into different groups. Each group is modeled by a neural network. The neural network is trained using scenarios in the corresponding group. Approach 1 uses MLP method and is based on clustering of the database outputs (e.g. large/small mass of core relocation, early/late large core relocation). It predicts the debris mass and the timing of relocation. Approach 2 can use MLP or RBF methods and is based on clustering of the database inputs (location in the scenario space). It predicts the lower and upper bounds of the output parameters scenario database inputs clustering. The results show that both methods

provide reasonable approximation for the total debris mass in the lower plenum and the time of large core relocation in most of the FM scenarios.

3.3.2. Vessel Failure Mode

Motivation, Goal, Approach and Tasks

Vessel failure mode and timing provides initial conditions and limiting factors for the melt release and ex-vessel accident progression. The ultimate goal of this work is to develop surrogate models (SMs) that can be used in the ROAAM+ framework [23] for prediction of timing, amount, properties and superheat of the melt available for release in different vessel failure modes: instrumentation guide tube (IGT), control rod guide tube (CRGT), pump, vessel wall. In order to achieve the goal, the most important task is to develop deterministic tools to connect core damage and relocation modes and timing with vessel failure modes and timing at given SAM measures. Figure 3.12 shows the schematic framework for the development of the vessel failure mode surrogate model (SM). The switch from core relocation SM to vessel failure SM is carried out at the moment when core relocation has been finished, or when SM is considered as inadequate in resolving further accident progression, i.e. vessel failure. The DECOSIM [73] and PECM [59], [60], [61] codes are employed as complementary FMs which describe respectively two different scenarios with initially (i) porous debris bed and (ii) "solid cake" bed. First, we perform Full Model (FM) calculations (DECOSIM and PECM/ANSYS) and characterize the data as functions of initial debris bed properties. Second, we develop the vessel failure Surrogate Model (SM) as an approximation of the FM solution for output parameters that are needed as input parameters in the next stage of the ROAAM+, that is, melt ejection SM.

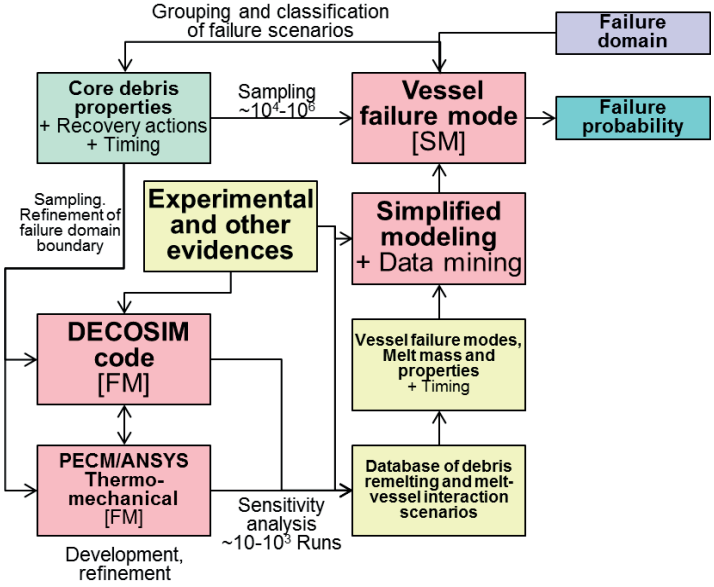

Figure 3.12. Debris re-melting and Vessel failure surrogate model.

PECM/ANSYS Thermo-mechanical Full Model

PECM is a 3D model for prediction of melt pool convection and heat transfer (see [59], [60], [61] for more discussions) in the BWR lower plenum. In scenarios with cooling, CRGTs are cooled from inside by water flow; the water is assumed to be

ejected from the CRGTs providing a water layer atop of the debris bed. Other surfaces are subjected to Neumann boundary conditions. The vessel wall is insulated and therefore a small heat flux (20 W/m^2) is allowed at the external surface. Resulting transient thermal loads on the vessel wall are then used for the thermo-mechanical creep analysis. For full transient analyses, a strong structural-thermal coupling is supported and a modified time hardening (primary) creep model is chosen in ANSYS 14 [63]. Coefficients for the model are generated using the experimental creep data for vessel steel SA533B1 from Rempe et al. [46]. See [64] for complete details along with the validation. A yield or creep limit is not used in this study (see [64] for more discussion). Instead a range of percent strain reliably predicted by the model is identified based on the experimental data. The reliable range is considered to be up to 20 % strain. At this strain the structure is close to its mechanical failure. Therefore time necessary to reach 20 % strain is considered as vessel wall failure timing.

Effective Slice PECM

Previous PECM-ANSYS calculations [64] were done using a 3D slice model of the lower head (see Figure 3.13b). A more detailed 3D quadrant model of the lower head has also been used but it is computationally expensive. To combine the accuracy of the 3D quadrant model and the efficiency of the 3D slice model, an effective 3D slice model was developed by preserving (i) the cooled surface to heated volume ratio, (ii) surface area (in contact with the debris bed) to volume ratio, and (iii) mechanical load to the vessel wall (due to the penetrations) as in the 3D quadrant model.

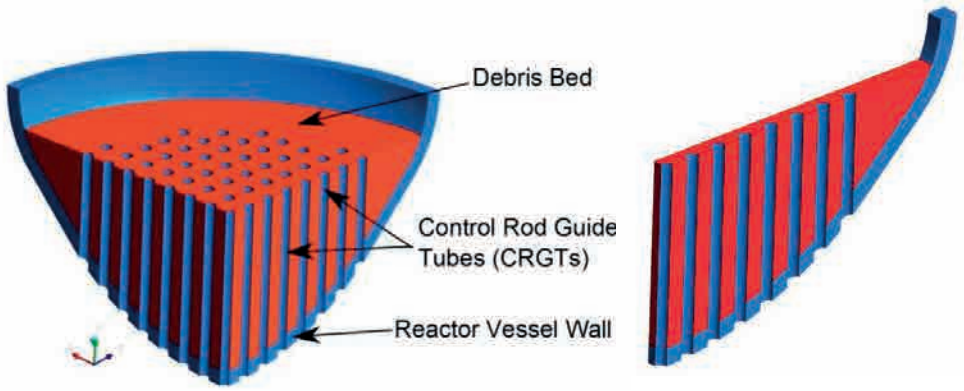

Figure 3.13. Geometry of (a) 3D quadrant and (b) 3D Slice used in PECM.

The debris averaged temperature and melt fraction are presented in Figure 3.14 providing comparison for the (a) 3D quadrant, (b) slice model [64], and (d) effective slice model. Reference time (t = 0) corresponds to the start of PECM simulation, i.e. when core relocation and in-vessel debris bed formation has been finished. This time corresponds to ~2-4 h from reactor trip, according to MELCOR analyses. The debris averaged temperature and melt mass are in excellent agreement between quadrant and effective slice. The vessel is always depressurized. It has been shown that higher pressure has a small effect on vessel failure timing [14]. Cooling of the CRGTs is considered as possible SAM measure. The debris remelting starts around 2.5 hours, and it intensifies between 2.75 – 3.75 hours; during which more than 50 % (~115 tons of 230) of debris bed becomes molten in all the cases. The vessel wall centerline displacement predicted with the structural analysis is presented in

Figure 3.15. It can be seen that displacements in the effective slice model and the 3D quadrant are in excellent agreement until reliably predicted strain is achieved at ~3.7 h. The vessel wall failure time in the effective slice model is ~3 min earlier compared to the 3D quadrant, while the original slice model predicts ~15 min earlier failure.

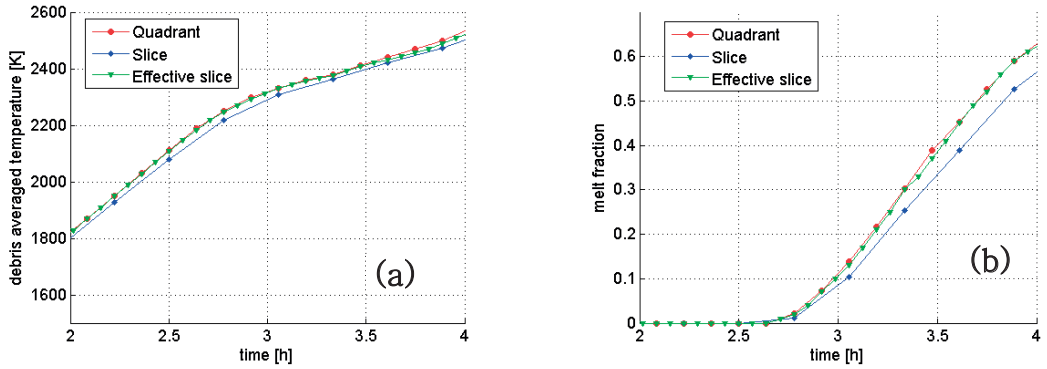

Figure 3.14. (a) Debris averaged temperature and (b) melt fraction as a function of time for both slice and quadrant models.

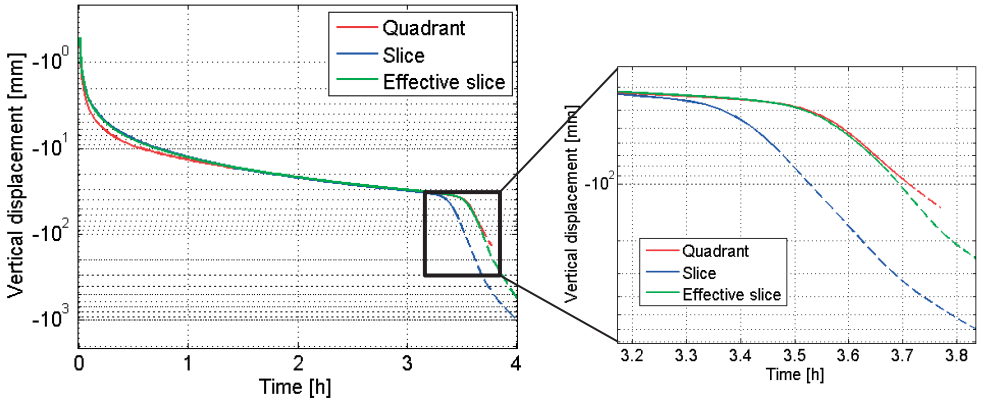

Figure 3.15. Vertical displacement of the vessel bottom centerline for the 3D Quadrant and Effective slice model with axisymmetric 2D mechanical model.

Non-uniformity of debris bed properties and database of PECM-ANSYS calculations

It was found previously [14] that the thermal conductivity is the most influential parameter for timing of the failure and for the mass and superheat of liquid melt available for release. Therefore, it is important to consider different configurations and more realistic properties of the debris bed. MELCOR analysis of Core Relocation is used to determine vertical distributions of the debris bed composition and respective properties. Two debris bed configurations are considered: (i) debris bed with horizontal layers; (ii) debris bed with concave layers aligned along the vessel wall. The first configuration can be formed in scenario with melt pool formation in the core region followed by sudden melt drainage to the lower plenum, while the second configuration can be formed in scenario with gradual core melt relocation in dripping mode when lower head is filled with debris layer by layer. Non-homogeneous properties of the debris are obtained using MELCOR analysis. The volumetric decay heat distribution is modeled proportionally to the fraction of total

UO_2 mass in each debris bed layer. The major difference between the two configurations is the fact that for concave debris bed the whole vessel surface is uniformly covered with this layer, while for flat configuration layers with high UO2 concentration (and therefore low thermal conductivity, high decay heat) are in direct contact with the vessel wall.

The non-dimensional parameters are introduced in order to facilitate generalization of the FM solutions database and the development of the SM. The current database is obtained for cake bed 1.9 m deep with and without activation of CRGTs and top cooling. Different debris bed configurations are also considered: homogenous, flatly and concavely stratified. The non-dimensional time $\tilde{t}$, thermal conductivity $\tilde{k}$, melt mass $\tilde{m}$, and melt temperature $\tilde{T}$, are

$$\tilde{t} = \frac{t \cdot Q^*}{\rho \cdot C_p \cdot T_{solidus}} \cdot \alpha, \; \tilde{k} = \frac{k^* \cdot T_{initial}}{Q^* \cdot L^2}, \tag{3}$$

$$\tilde{m} = \frac{m_{melt}}{m_{total}}, \; \tilde{T} = \frac{T_{melt}}{T_{solidus}}, \tag{4}$$

where $Q^*, k^*, \rho, C_p, T_{solidus}, T_{initial}$, and L are the effective volumetric decay heat [W/m^3], effective thermal conductivity [W/(m·K)]; debris bed density [kg/m^3], debris bed specific heat [J/(kg·K)], debris bed solidus temperature [K], debris bed initial temperature [K], and debris bed height [m], respectively. Debris bed shape coefficient α equals to 1 for homogeneous, 0.85 for concave and 0.73 for flat layer configurations. For the homogeneous debris bed, a constant value of thermal conductivity and volumetric decay heat are used as k^* and Q^* respectively. Effective values of Q^* and k^* are introduced for non-homogeneous configurations to represent observed behavior of the FM solutions. Specifically we observe that debris properties of the 20 cm thick layer near the vessel wall determine failure time for the concave configuration. Therefore mass-averaged thermal conductivity and volumetric decay heat in this layer are used as k^* and Q^* respectively. Vessel failure location in case of the flat layer configuration is near the debris bed region with highest fraction of UO_2 (having maximum decay heat and low thermal conductivity). Therefore, Q^* and k^* are defined as decay heat and thermal conductivity in this region for the flat configuration.

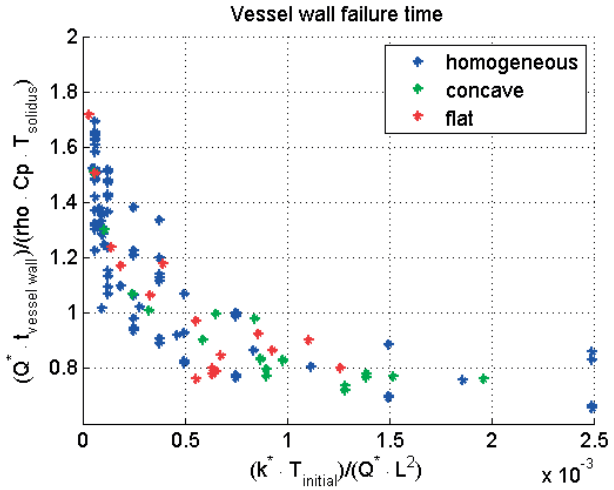

Figure 3.16. Non-dimensional vessel failure time against non-dimensional thermal conductivity.

Figure 3.16 shows that non-dimensional vessel failure time $\tilde{t}$ follows the same trend with respect to the introduced non-dimensional thermal conductivity for all considered debris bed configurations. However, there is still some scattering in the data due to influence of the other parameters. Similar plots have been generated for the corresponding melt masses and superheat, IGT failure time, and onset of debris remelting. Figure 3.17a shows the non-dimensional IGT failure time plotted against the non-dimensional thermal conductivity. It should be noted here that in most of the cases at the time of IGT failure, the oxidic debris bed remains in solid form. Thus the onset of remelting provides the earliest possible time for melt ejection. In addition, the vessel failure SM should also specify for the Melt-Ejection SM if the remelted material will be available for the release or it will be located away from the openings. Figure 3.17b shows the onset of debris remelting for cases with and without CRGT cooling. Figure 3.18a shows the melt mass and superheat with respect to non-dimensional vessel wall failure time and thermal conductivity. Currently, we are using regression analysis to develop surrogate models for prediction of the vessel failure modes.

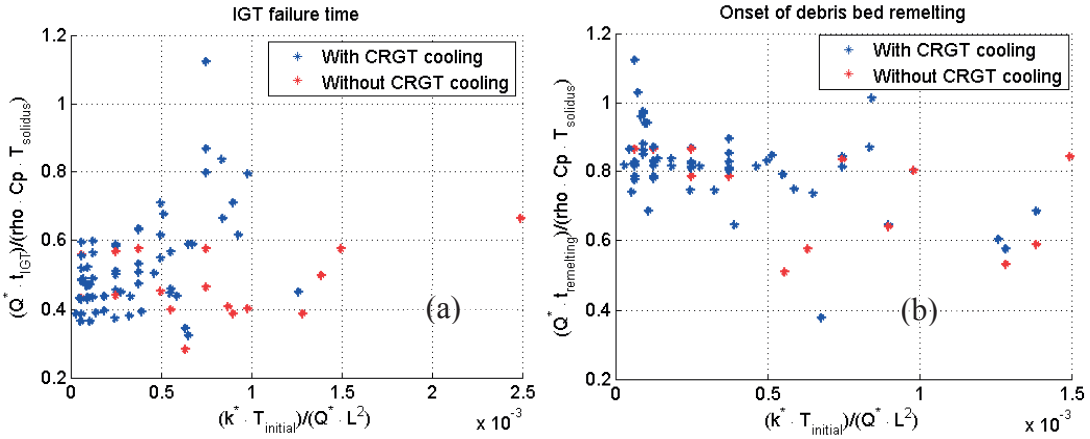

Figure 3.17. (a) IGT failure time and (b) onset of debris bed remelting as a function of the non-dimensional thermal conductivity.

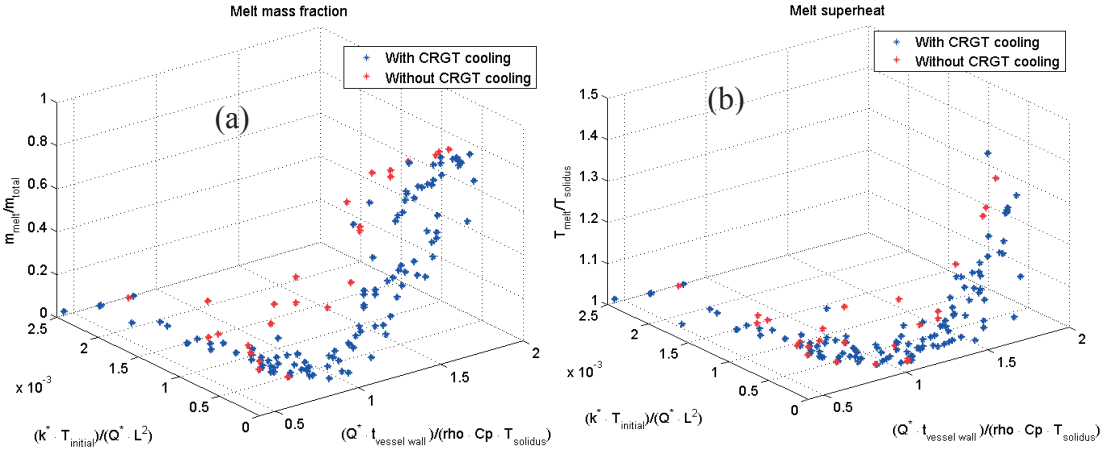

Figure 3.18. (a) Liquid melt mass fraction and (b) corresponding superheat with respect to non-dimensional vessel wall failure time and thermal conductivity.

DECOSIM Full Model

We use DECOSIM (Debris COolability SIMulator) multiphase code being developed at KTH for reactor safety analysis as a full model (see also Section 3.4.2 and

[77]). The vessel geometry of a reference design of Nordic-type BWRs is used in simulations (Figure 3.19). A vertical cylindrical shroud is present in RPV which can restrict the lateral spreading of debris in the case of core meltdown and fragmentation. In the bottom part of the shroud, there are windows for coolant inflow. The assumed shape of the top boundary of debris bed repeats the shape of bottom wall of the lower plenum (shown by solid curves in Figure 3.19). The dashed lines (at the heights of 0.17 and 0.4 m above the vessel bottom) indicate positions of IGTs and CRGTs nozzle welding points. Failure of the welds can result in fallout of CRGTs or IGTs leaving paths for melt to escape the reactor vessel possibly before vessel wall loses its integrity [14].

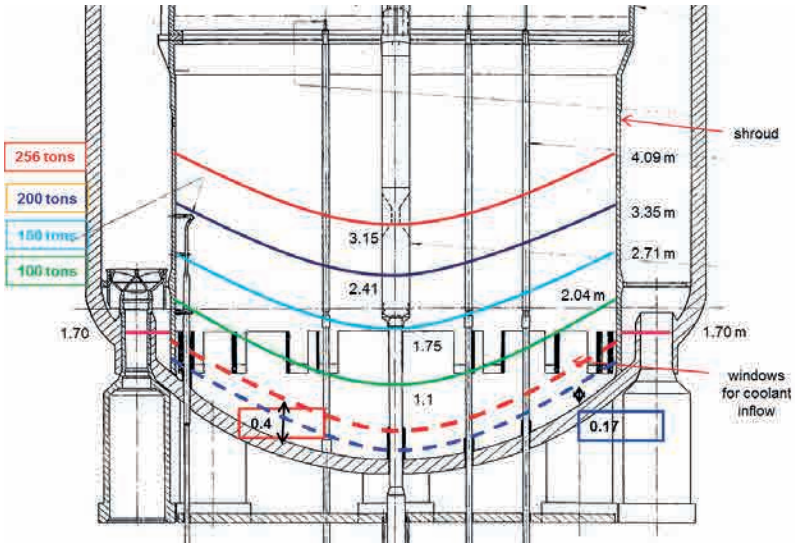

Figure 3.19. Sketch of reactor pressure vessel geometry and assumed debris bed shape.

Database of DECOSIM calculations

The following properties of materials were assumed: i) Corium properties in the solid state: density $\rho_s = 8285.1$ kg/m^3, specific heat capacity $C_s = 566.2$ J/kg K, heat conductivity $\lambda_s = 1$ W/m K; ii) Corium properties in the liquid state: density $\rho_s = 7121.6$ kg/m^3, specific heat capacity $C_s = 680.7$ J/kg K, heat conductivity $\lambda_s = 3.6$ W/m K; iii) Corium melting temperature: $T_m = 2750$ K, melting heat $\Delta H_m = 4.28 \cdot 10^5$ J/kg; iv) Decay heat specific power was calculated according to ANS 5.1 standard curve, with time after SCRAM equal to the sum of core relocation time t_r and simulation time t; the core relocation time was taken to be $t_r = 1.5$ h and 3 h (based on results of MELCOR simulations for the reference design of Nordic-type BWR); v) Properties of steel: density $\rho_s = 7800$ kg/m^3, specific heat capacity $C_s = 500$ J/kg K, heat conductivity $\lambda_s = 15$ W/m K. Simulations were carried out for the following debris bed properties: i) Particle diameter $d = 1-3$ mm; ii) Porosity $\varepsilon = 40\%$; iii) Total mass of debris bed: $M = 100-200$ t. Scenario-dependent parameters: System pressure: 3 bar (was set on the top of the computational domain, 4 m above the RPV bottom point).

Initially Quenched Debris Bed

In its initial state, the debris bed was completely filled with water and the temperature of solid particles was equal to the saturation temperature at the local pressure. Simulations have shown that debris bed coolability is strongly affected by the particle diameter. For 3 mm particles, the debris bed was coolable for all melt masses and relocation times; local dryout did not occur and cooling of the material was provided by water evaporation, the maximum solid particle temperature remained close to the local saturation temperature. For 2 mm particles, local dryout was observed for the largest mass of debris bed $M = 200$ t at the relocation time $t_r = 1.5\ h$, however, in this case the maximum superheat of particles with respect to the saturation temperature was about 50 K, after about 1 hour the dry zone was reflooded again, the solid material temperature remained close to saturation afterwards. For 1 mm particles, debris bed coolability depends on the total mass M and relocation time t_r. Results of simulations are summarized in Figure 3.20(a) where time histories of the maximum temperature of solid material are shown for 1 mm particles; also, one curve (dotted line) is also shown for 2 mm particles in the above-mentioned case where temporary dryout occurred in the debris bed. Dryout occurs for 1 mm particles in all the cases, however, its consequences depend on the debris bed mass and relocation time. For example, debris bed with $M = 100$ t is reflooded after 1.5 hours for $t_r = 3.0\ h$ (i. e., 4.5 hours after SCRAM), while for $t_r = 1.5\ h$ no total reflooding occurs during the whole simulated period (3 h after relocation), however, the maximum temperature remains below 1000K, decreasing gradually after 1.5 h. With the debris bed mass of $M = 150$ t, temperature is stabilized at a level of about 1000 K for the relocation time $t_r = 3.0\ h$. All other cases for 1 mm particles are featured by steady temperature escalation, however, none of the cases was featured by oxidic debris material melting during the first three hours after core relocation. Thus, for 1 mm particles, only for the smallest debris bed mass of $M = 100$ t a stable configuration was obtained.

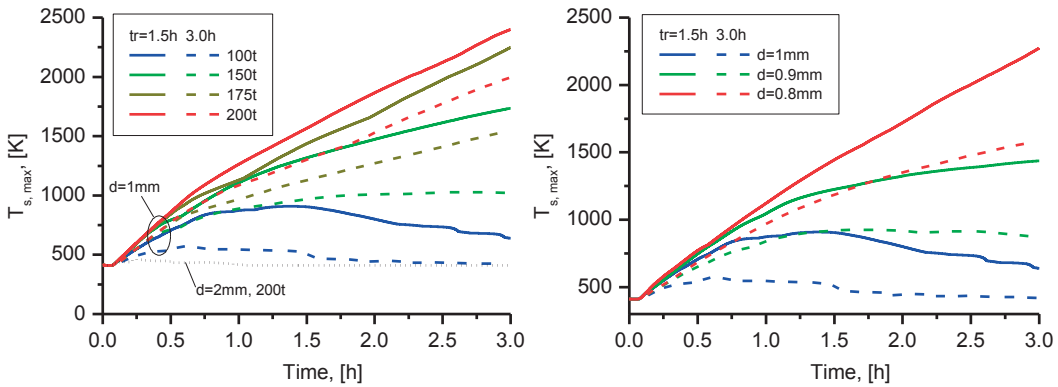

(a) (b)

Figure 3.20. Time histories of maximum temperature of solid material in initially quenched debris bed: 1-2 mm particles (a); sub-mm particles (b).

To estimate the margin to the coolability boundary, additional simulations were carried out with two smaller particle diameters, $d = 0.9$ and 0.8 mm (Figure 3.20(b)) for the debris bed mass of 100 t. Particle diameter 0.9 mm represents approximately the boundary between the cases of temperature stabilization and escalation. It should be kept in mind, however, that in the melt-coolant interaction exper-

iments performed at KTH and results with prototypic corium compositions available in the literature (e.g., FARO experiments) such small mean particle diameter was never observed. Therefore, it is reasonable to conclude that fragmented debris beds with mass below 100 t are going to be coolable in the severe accident conditions, provided that sufficient water inventory is maintained in the reactor pressure vessel. The coolability results obtained for initially quenched debris bed are summarized in Figure 3.21 where color coding is use to mark the cases where temperature escalation (red), temperature stabilization (green), or "no dryout" or "dryout followed by reflooding" (blue) was observed within 3 hours after core relocation.

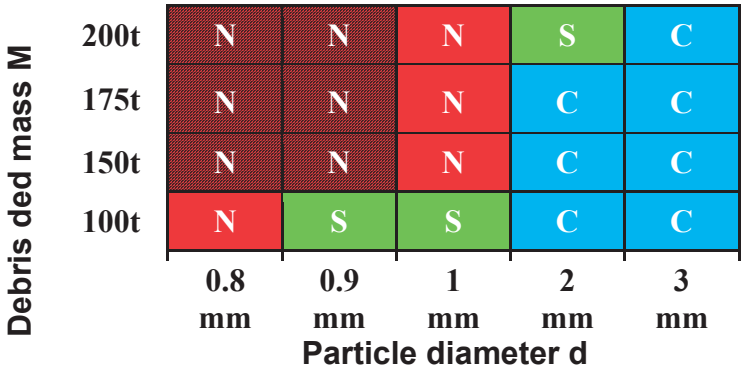

Figure 3.21. Summary of coolability results for initially quenched debris bed. N - non-coolable with temperature escalation, S - dryout with temperature stabilization, C - coolable (no dryout, or dryout followed by reflooding).

To elucidate the development of dry zone in different conditions, spatial distributions of particle temperatures in debris beds are presented in Figure 3.22 for the debris bed masses of 200, 150, and 100 t; the debris bed shape is shown by the white lines. In all cases the particle diameter was d = 1 mm, the relocation time for the smallest and largest debris masses was $t_r = 1.5\ h$, while for the intermediate mass of 150 t results are shown in the case of $t_r = 3.0\ h$ (the latter case was chosen because it corresponds to temperature stabilization, see Figure 3.20). It can be seen in Figure 3.22 (a)–(c) that for the initially quenched debris bed, dryout develops in the upper zone of the debris bed where the vapor flow rate is the highest and, therefore, water penetration into it is more difficult. Water ingress into the debris bed occurs in the bottom part of the debris bed and the vapor flow is directed upwards. Therefore, the water and vapor flows are co-current, rather than counter-current, as is the case in the one-dimensional problem of flat top-flooded debris bed coolability. In the large debris bed (Figure 3.22 (a)) the dry zone extends over the whole top of debris bed. Remelting of the material may occur approximately 4 hours after core relocation (5.5 hours after SCRAM), and a melt pool will be formed in the top part of the debris bed, blocking vapor evacuation and resulting in total dryout. Later on, the molten material can propagate downwards and reach the reactor vessel. In the medium and small-mass debris beds (Figure 3.22 (b), (c)) the, occurrence of dryout is also observed near the top boundary of the debris bed. In the former case, the dryout zone is stabilized by vapor cooling, in the latter case the dryout zone is of small size and is shrinking with time. The decay heat power is gradually decreasing with time, and even when the temperature looks stabilized (namely, the case of 150 t debris bed with 1 mm particles and both cases of 0.9 mm particles in Figure 3.20), it will actually be decreasing slowly later on, and the size of dry zone will be shrinking accordingly.

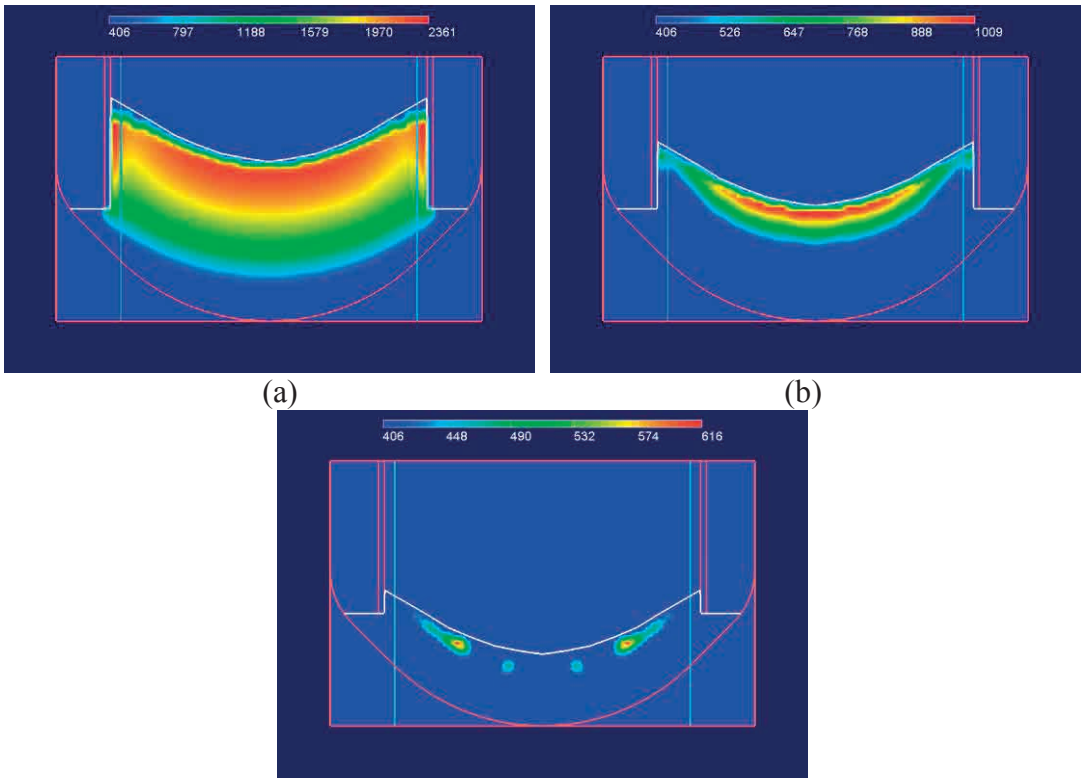

(a) (b)

(c)

Figure 3.22. Particle temperature in initially quenched debris bed at time t=3 h: (a) $\boldsymbol{M = 200\ t}$, $\boldsymbol{d = 1\ mm}$, $\boldsymbol{t_r = 1.5\ h}$; *(b)* $\boldsymbol{M = 150\ t}$, $\boldsymbol{d = 1\ mm}$, $\boldsymbol{t_r = 3.0\ h}$; *(c):* $\boldsymbol{M = 100\ t}$, $\boldsymbol{d = 1\ mm}$, $\boldsymbol{t_r = 1.5\ h}$.

Initially Dry Hot Debris Bed

Six cases are considered: debris beds with masses of M = 100 and 150 t and particle diameters of 1 and 2 mm, as well as debris mass M = 200 t and particle diameters 2 and 3 mm; relocation time $t_r = 1.5\ h$. Also, same simulations were repeated for the relocation time $t_r = 3\ h$. The debris bed had initial temperature of 1000K and was initially filled with vapor at the same temperature. The space above the debris bed is filled with saturated water. In these cases, unlike the initially quenched debris bed, the porous material possesses significant initial sensible heat energy which, together with the decay heat, governs the evolution of debris bed. In Figure 3.23, the time histories of maximum temperature of solid material are presented. Initially, the temperature rise rate is the same in all cases, the maximum temperature rise occurring near the shroud. For larger particles, as can be seen from the dashed lines in Figure 3.23, total reflooding of the debris bed occurs after 1–2 hours, and the maximum temperature of solid material falls down to the saturation temperature. For 1 mm particles, as well as for 2 mm particle and corium mass of 200 t, high drag prevents incoming water from reflooding the whole volume of the debris bed, and steady temperature rise can be observed to the levels where remelting of the material can occur. In the case of 200 t – 2 mm debris bed, reflooding occurred for relocation time of 3 h. The time to reach remelting is approximately 2.5 h after core relocation, or 4 h after SCRAM. To demonstrate the process of heatup of an initially dry debris bed, in Figure 3.24–Figure 3.25 the temperature distributions are shown for three of the cases presented in Figure 3.23 in which remelting of porous material

occurred. In each case, predicted temperature fields at times 1000 and 10800 s are shown.

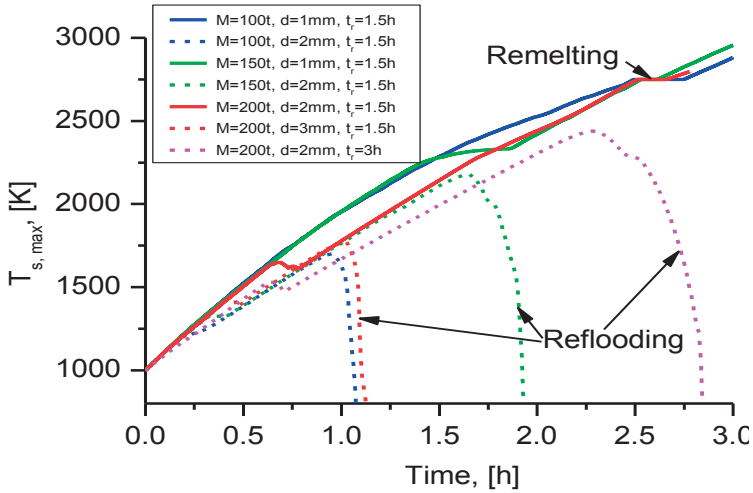

Figure 3.23. Time histories of maximum temperature of solid material in initially dry debris bed with initial temperature 1000 K.

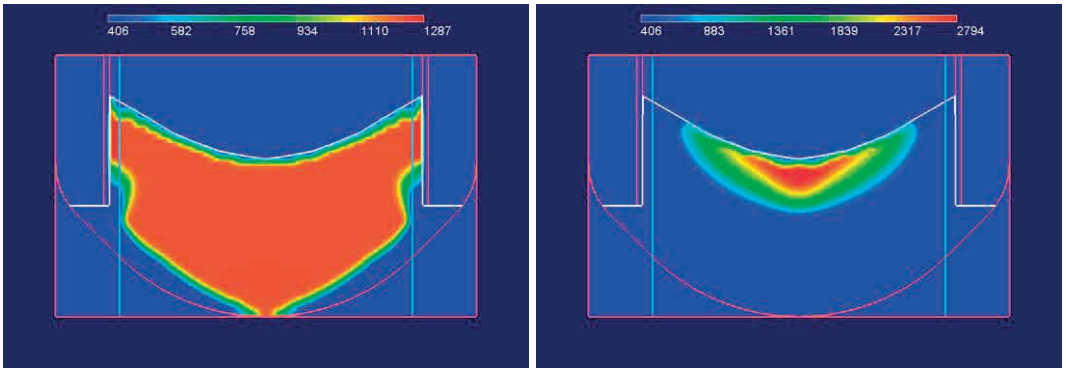

t = 1000 **s** t = 10800 **s**

Figure 3.24. Particle temperature in initially dry debris bed: $\boldsymbol{M = 200\ t}$, $\boldsymbol{d = 2\ mm}$, $\boldsymbol{t_r = 1.5\ h}$.

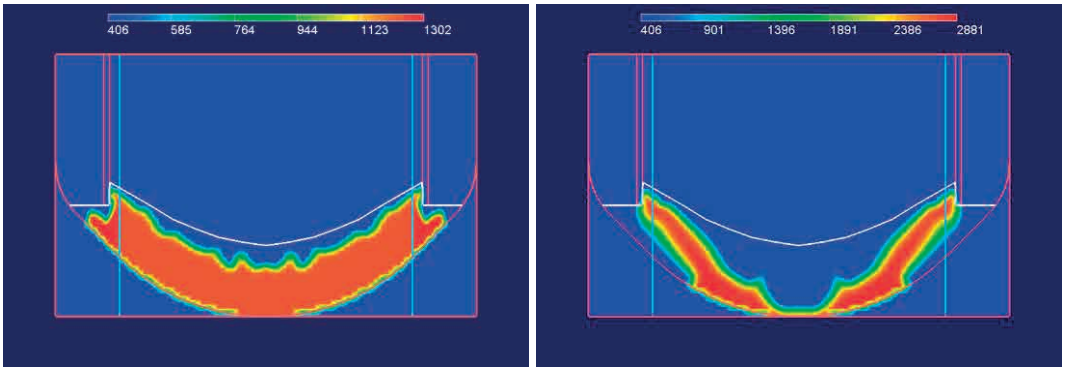

t = 1000 **s** t = 10800 **s**

Figure 3.25. Particle temperature in initially dry debris bed: $\boldsymbol{M = 100\ t}$, $\boldsymbol{d = 1\ mm}$, $\boldsymbol{t_r = 1.5\ h}$.

In Figure 3.24, the case of large debris bed ($M = 200\ t$) and moderately small particles ($d = 2\ mm$) is presented. Water ingress occurs along the reactor vessel bottom wall, quenching hot particles and separating the hot debris from the wall, which

is an important finding for the vessel failure mode. Further ingress of water leads to total detachment of the dry zone from the bottom vessel wall and its shrinking both vertically and horizontally. Eventually, the dry zone becomes localized in the upper part of the debris bed where remelting of the porous material occurs.

For smaller particles ($d = 1\,mm$), high drag in the porous medium significantly hinders water ingress into the debris bed. It can be seen in Figure 3.25 (for debris mass of 100 t) that water front can penetrate along the vessel wall only to approximately half the distance between the water inlet openings and axis of symmetry. Also noticeable is the water ingress through the upper boundary of the debris bed. For the smallest debris bed mass (Figure 3.25), water front reaches the bottom of reactor vessel by the time 3 h after core relocation. Similar processes are observed for the medium mass (150 t), but the top water front propagates downwards to about half of debris bed height near the axis. Thus, in all the cases some part of debris remains dry; the temperature in these zones increases and reaches the melting point. To elucidate this, in Figure 3.26 the mass fractions of molten corium are shown at the final instant $t = 3\,h$ (i. e., 4.5 h after SCRAM). Evidently, in the last two cases remelting and high temperatures are reached in the bottom part of the debris bed in the vicinity of the vessel wall.

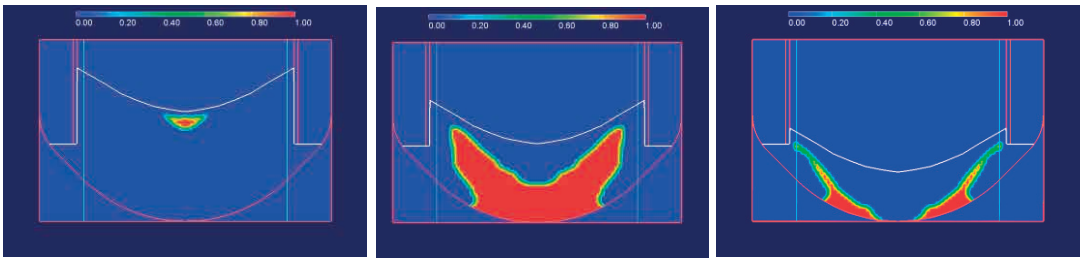

Figure 3.26. Melt fraction at time t=3 hours in the initially dry debris bed.

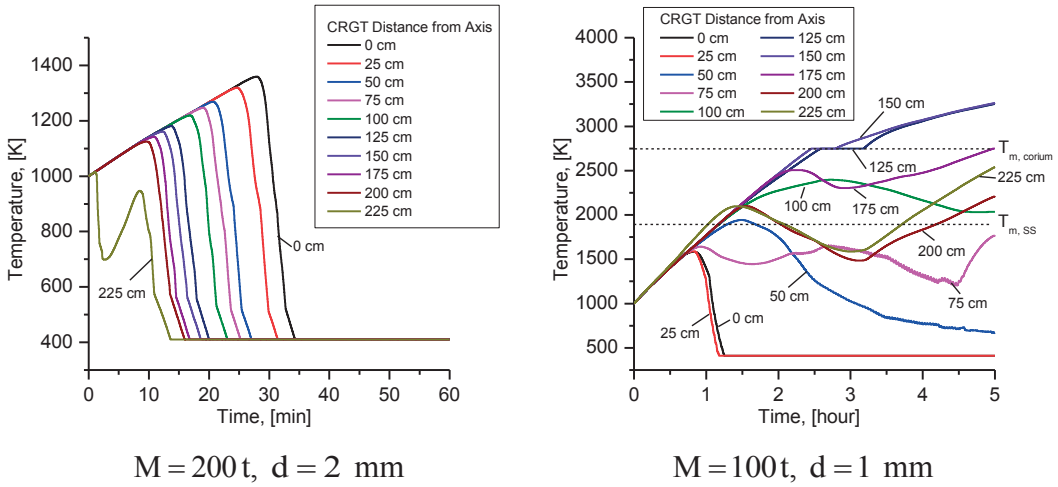

Figure 3.27. Time histories of temperatures at CRGT welding points.

In Figure 3.27, the temperatures at the levels of CRGT welding points are shown, demonstrating rapid quenching of debris bed for M=200 t and d=2mm (the maximum temperature remains below the melting point for stainless steel). However, in the case of small particles (M=100 t, d=1 mm), only the central CGRTs are reflooded completely, while all other CRGTs feature some temporary temperature de-

crease, turning into secondary reheating because of shrinking of the reflooded zone with time.

3.3.3. Melt ejection mode

There are several phenomena that govern melt ejection. Ablation or plugging of the vessel breach can change jet diameter and melt release rate. The remelting of multi-component debris and liquid melt filtration through porous debris bed can slow down melt release rate. The goal of this work is to develop a numerical tool for prediction of the melt ejection mode parameters, i.e. jet diameter, melt superheat and duration of the release that will be used as an input in SEIM and DECO. Following tasks should be addressed: (i) development of the full models for remelting of the debris and ablation / plugging of the breach during melt ejection; (ii) full model sensitivity studies to develop an efficient approach (experimental and analytical) to decreasing the uncertainty and to provide data for development of surrogate models. In this work we report a progress on the development of the full model for ablation/plugging of the vessel breach as the key element of MEM.

Approach to modeling of ablation / plugging of the vessel breach

The aims of the melt-structure interaction model is to predict the evolution of the lower head breach size as a function of melt flow rate and superheat. Two domains are considered (see Figure 3.28).

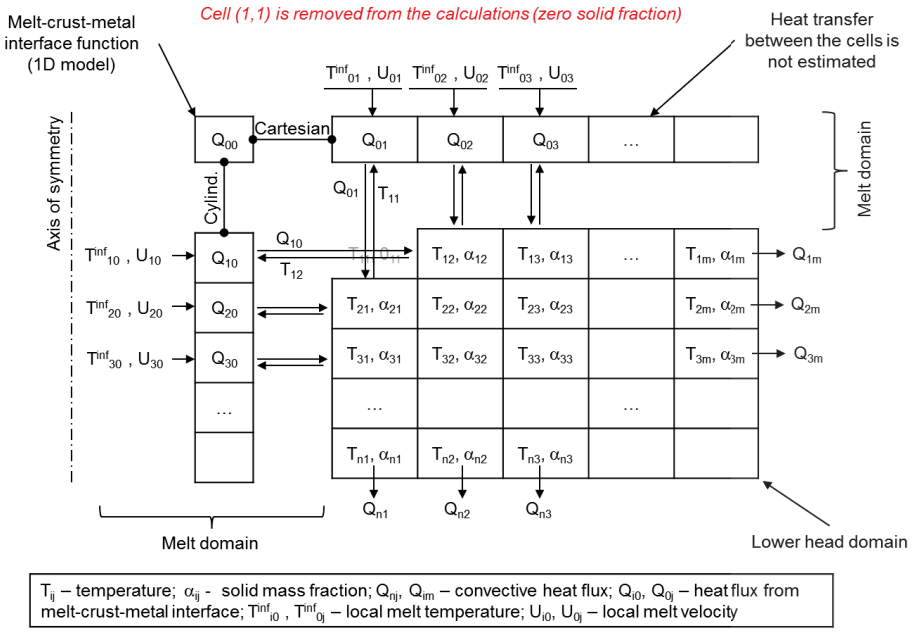

Figure 3.28. Schematics of the melt / structure interaction model.

The lower head wall near the breach is represented as an axisymmetric 2D domain that is subject to Neumann boundary conditions: (i) cooling of the wall outer surface; (ii) heating by the flowing melt. Transient temperature profile and ablation of the wall are resolved. Melt domain is represented as a number of 1D models that describe transient melt-crust-metal interface using local velocity and temperature of the melt. Each 1D model is coupled to the 2D domain using temperature and heat flux at the boundary. Transient thickness of the crust, temperature profile in melt-crust-metal interface and throughout heat flux are resolved. When the vessel wall

material in the boundary cell is completely melted the cell is removed from calculations and melt 1D model is re-coupled to the next adjacent vessel wall cell. Temperature profile and crust thickness in the 1D models are preserved and only the coordinate vector is shifted with respect to the size of the melted cell. This process is illustrated in the Figure 3.28. Instantaneous amount of liquid metal depends on the balance between the rate of ablation and the rate of metal outflow through the breach. We assume that the layer of liquid metal has constant (1-2 mm) thickness. This layer is implemented in the 1D model as a permanent part of a 3-layer system: melt, crust and metal.

3.3.4. MEM: Summary and outlook

Full model (FM) of core relocation has been developed using MELCOR code. GA-IDPSA and MATLAB tools are used for sampling and populating the database of the FM solutions. More than 10^3 accident scenarios have been simulated with MELCOR. The results indicate that depending on the scenario and timing of safety systems recovery, core degradation most likely results in small (less than 10 tons) or very large (more than 200 tons) relocation of debris. The number of scenarios with intermediate (from 10 to 200 tons) mass of relocated debris is relatively small. The domain where such scenarios are located overlaps with the domain of very large relocation, meaning that small variations in the scenario parameters can lead to significant variations of the properties of relocated debris bed in this domain. Two approaches are being developed for the core relocation SM using ANNs and the database of FM solutions. The preliminary results show that the methods can predict core relocation in most of the scenarios. Further development of the FM database and SM is necessary in order to predict other important parameters of core relocation, such as composition of the debris for all initial plant damage states.

Results of Vessel Failure Full Models have been presented. The DECOSIM FM is used for porous debris beds while the PECM-ANSYS FM is implemented for non-porous (cake) debris beds. Extensive analysis with the PECM-ANSYS has been carried out using properties of the bed determined by the input from the previous core relocation SM. The FM analysis data has been generalized to facilitate the development of surrogate sub-models. Output parameters such as (i) failure timing, (ii) melt mass, and (iii) melt superheat has been generated and will be used as input parameters for the next stage of ROAAM+, that is, Melt-Ejection FM. However, the FM database is still not complete and more calculations are needed to cover more scenarios and influences of other parameters. For scenarios and assumptions covered by the current database, the prediction of the FM output parameters has shown to be feasible with relatively simple SM approximations.

The DECOSIM FM can provide information on the coolability of the debris bed as a function of particle size as well as time histories of temperature and melt fraction. DECOSIM results show that, once the mean particle diameter exceeds 1 mm, there are good chances that initially quenched debris bed will be either coolable, or dried out first but followed by reflooding of the dry zone. For initially dry debris bed with particles larger than 1 mm, water ingress along the vessel walls rapidly cuts the hot zone from the walls and CRGT/IGT welding locations; remelting, if at all, is most probable to occur in the upper zone. Debris beds with 1 mm particles are not coolable, whether initially quenched or dry; the drag in the bed is very high, so that water

ingress is hindered or stopped, leading to formation of massive remelting zone in the bottom part of the debris bed. Additional work is needed to couple DECOSIM with vessel wall failure analysis in order to determine mode and timing of failure.

The implementation of the melt ejection model is an ongoing work. Application of the model requires input from vessel failure simulations. Once implementation will be finished, it is planned to perform model verifications by comparison of decoupled calculations with analytical solutions. Validation of the model is envisaged through comparison with available experimental data on ablation obtained in a number tests on melt / structure interactions at KTH. After verification and validation we plan to develop a corresponding surrogate model. This will be performed starting from sensitivity study, following the common approach applied for other SMs.

3.4 Debris Coolability Map (DECO)

3.4.1. Motivation, Goal and Tasks

Non-coolable debris bed presents a credible threat to containment integrity. Coolability of the bed is determined by the properties of the bed, which, in turn, are dependent on the debris bed formation phenomena and conditions of melt ejection from the vessel. Phenomenology of ex-vessel debris bed formation and coolability is quite complex (see Figure 3.1), it includes (i) jet breakup, (ii) melt droplet sedimentation and interaction with water pool; (iii) debris agglomeration; (iv) particle spreading by pool flows; (v) debris bed self-levelling by vapor flows; (vi) debris bed coolability; (vii) post-dryout behavior with possible remelting, etc. The physical phenomena involved are closely coupled. Debris bed cooling is provided by heat transfer to the water that enters the porous bed interior by filtration from the pool. Steam generated inside the debris bed is escaping predominantly upwards, generating two-phase convection flows in the pool and changing conditions for fuel-coolant interaction (FCI). In turn, FCI phenomena affect particle properties (size distribution and morphology). Particle properties, packing, agglomeration and lateral redistribution affect the debris bed coolability phenomena. The large-scale circulation in the pool can spread effectively the falling corium particles over the basemat floor, distributing the sedimentation flux beyond the projection area of particle source (e.g., size of reactor vessel). Debris is gradually spreading under the influence of steam production in the bed, resulting in self-leveling of the settled portion of the debris and changing the shape of debris bed with time. This can serve as an additional physical mechanism that prevents formation of a tall non-coolable debris bed.

The primary goal of DECO part of the project is to develop debris bed formation and coolability map – a tool for assessment of the risk of formation of a non-coolable debris bed. The general approach to the development of DECO framework is presented in Figure 3.29. Obtaining missing and confirmatory experimental data on the debris bed formation and coolability phenomena, is an important DECO task. Another important task is the development of the SMs for debris bed formation and coolability analysis including post-dryout coolability and respective failure criteria. In this work we present a progress on study of relevant phenomena (Figure 3.29), experiments on debris bed and particle properties (DEFOR-S) [28], debris agglom-

eration (DEFOR-A) [26], porous media coolability (POMECO) [31], particulate debris spreading (PDS) [2], [19]. Also we present a set of full and surrogate models that have been developed and validated against produced experimental data for the debris formation [29], agglomeration ([20], [21]), coolability ([75], [68]) and spreading [3] of the debris (Figure 3.29).

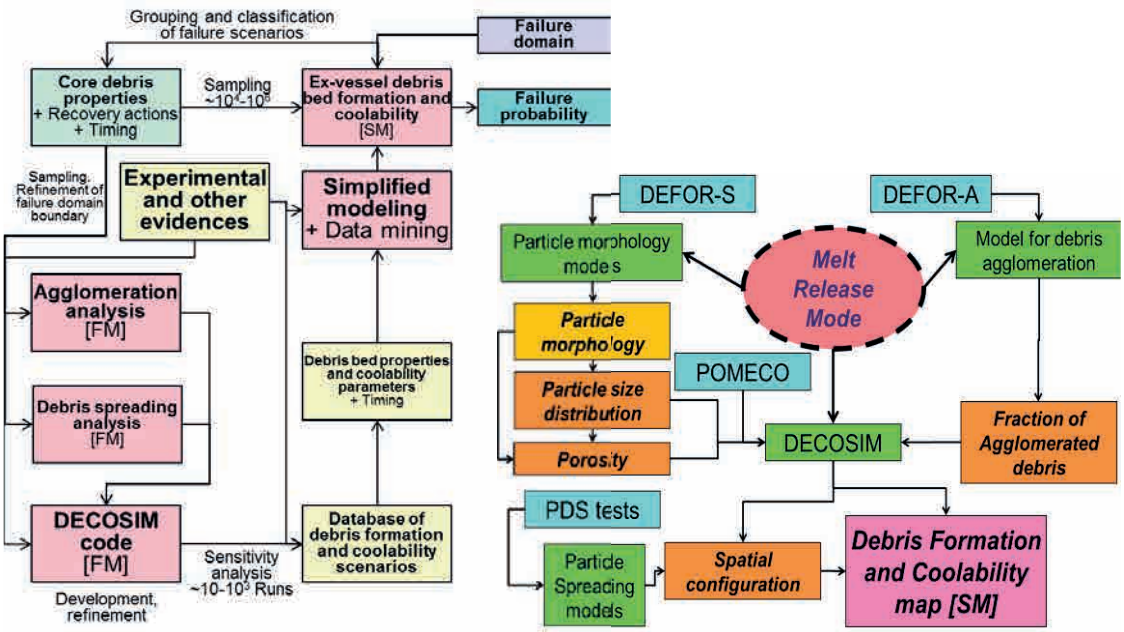

Figure 3.29. Ex-vessel debris bed formation and coolability framework.

3.4.2. DECOSIM Models for Debris Bed Coolability Analysis

DECOSIM is a thermohydraulic code being developed at KTH for simulation of debris bed formation and coolability ([72], [69], [73]). The main code capabilities implemented in the current project are: i) two-phase drag models for the porous medium (modified Tung and Dhir's model [62],[49]) taking into account the inter-phase drag between the liquid and vapor phases; ii) energy equations for the liquid and gas phases; iii) solver for heat transfer in the solid phase; iv) variable-shape debris beds with submodel for lateral particle spreading rate derived from PDS-C experiments performed at KTH. These new capabilities allow us to study for debris bed coolability in subcooled pool, apply DECOSIM to simulation of post-dryout debris bed in which a dry high-temperature zone can develop in the porous material, as well as study effects of particle spreading on debris coolability. Also, an algorithm for automatic finding of the dryout boundary has been developed and implemented, similar to the well-known bisection algorithm for finding the root of a function. To speed up convergence process, empirical rules based on the observations of the behavior of the maximum void fraction in the debris bed are formulated and implemented in the code to decide if dryout is going to occur or not without the need of running complete steady states for all intermediate power levels.

Surrogate model for ex-vessel debris bed coolability

By performing the similarity analysis of the governing equations and by generalization of DECOSIM numerical predictions of ex-vessel debris bed coolability, a computationally inexpensive surrogate model was developed. The surrogate model approximates the dryout conditions for non-flat debris beds and can be used for fast evaluation of the dryout heat flux in extensive sensitivity, uncertainty and risk analysis by evaluating the conditional dryout probabilities [75], [76]. By the analysis of governing equations, a non-dimensional form of the critical condition is obtained for an arbitrary-shaped debris bed. It is shown that the concept of Dryout Heat Flux (DHF), well-known for flat debris beds, can be extended naturally to multidimensional debris beds. On the basis of this analysis, the functional form of a surrogate model for DHF is offered in which the influence of debris bed shape is factored out, while functions describing the influence of porous media properties and system pressure are obtained by the asymptotic interpolation.

The surrogate model was tested first on the classical one-dimensional coolability problem [62], [49], and then extended to the case of a cone-shaped debris bed, where the dryout condition data necessary for fitting the approximating functions are obtained from 2D simulations carried out by DECOSIM code. The surrogate model is validated against the experimental data available for multidimensional debris beds. The data for validation were taken from small-scale experiments performed at VTT on COOLOCE facility [54], [55], [56].

The surrogate model was implemented in Cool1D code and run in the context of probabilistic framework. Monte Carlo simulations were performed with the surrogate model for the dryout heat flux in order to evaluate the influence of uncertainties in the input parameter ranges, as well as in the distribution functions, on the conditional probabilities of debris bed dryout. Since there is no sufficient data for the distribution functions of input parameters, simulations were carried out for three model distribution functions: uniform (U0), clipped Gaussian (CG), and narrower uniform (U1) distribution having the same variance as CG. These set of functions allows us to evaluate the uncertainties in the final results introduced by the shape and width of input distribution functions.

Parameters used in simulations are presented in Table 3.1. Three ranges for the slope angle of the conical bed were studied, corresponding to low, intermediate, and tall debris beds. Also, uniform distributions with narrower ranges for particle diameters, 1–3 mm (denoted U0d1-3) and 2-4 mm (denoted U0d2-4) were considered. Typical probability density functions for the heat flux at the debris bed top point (HF), dryout heat flux (DHF) and their difference (DHF-HF) are presented in Figure 3.30. Conditional dryout probabilities obtained are summarized in Table 3.2, providing quantitative view on the importance of different sources of uncertainty (aleatory and epistemic) in risk assessment of debris bed coolability. The uncertainties in the ranges for (i) particle size and (ii) the slope angle of the debris bed are deemed to be the most important contributors to the uncertainty of the risk. Therefore, research on the clarification of possible ranges of the slope angle and particle sizes would be the most effective, leading to more credible evaluation of severe accident risks.

Table 3.1: Parameter ranges

Parameter	Description		U0, CG		U1	
			Min	Max	Min	Max
P_{sys}	System pressure, [atm]		1	4	1.28	3.72
d	Mean particle diameter, [mm]		1	5	1.37	4.63
ε	Porosity, [–]		0.35	0.5	0.364	0.486
M	Total mass of released melt, [t]		30	256	50.7	233.3
t_r	Time after SCRAM, [h]		3	10	3.65	9.35
θ	Slope angle of the bed, [degr]	**Low**	0	20	1.85	18.5
		Wide	0	35	3.24	31.8
		High	20	35	21.4	33.6

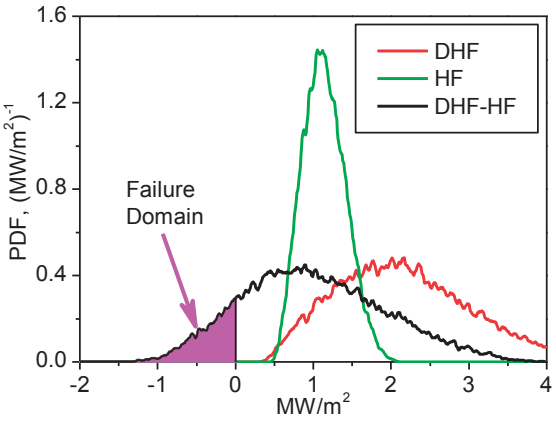

Figure 3.30. Probability density functions for dryout heat flux (DHF), heat flux at the debris bed top (HF) and their difference (DHF-HF); the colored area is equal to conditional dryout probability.

Table 3.2: Parameters of distribution functions, safety coefficient and dryout probabilities.

Distribution	$\overline{HF}$, [MW/m^2]	σ_{HF} [MW/m^2]	$\overline{DHF}$ [MW/m^2]	σ_{DHF} [MW/m^2]	S, [–]	P_{dry}, [%]
Angle range: 0-20° (Low)[a]						
U0	0.55	0.25	1.93	0.77	1.70	2.46
CG	0.55	0.20	2.00	0.65	2.13	0.62
U1	0.55	0.20	2.01	0.64	2.18	0.30
U0d1-3	0.55	0.25	1.46	0.57	1.46	4.85
U0d2-4	0.55	0.25	2.01	0.61	2.21	0.18
Angle range: 0-35° (Wide)[a]						
U0	0.80	0.39	2.00	0.79	1.36	7.34
CG	0.81	0.32	2.08	0.66	1.73	3.30
U1	0.81	0.31	2.10	0.66	1.77	2.84
U0d1-3	0.80	0.39	1.52	0.59	1.02	14.2
U0d2-4	0.80	0.39	2.09	0.63	1.74	2.62
Angle range: 20-35° (High)[a]						
U0	1.14	0.27	2.10	0.80	1.14	13.7
CG	1.14	0.22	2.17	0.67	1.46	7.84
U1	1.14	0.21	2.18	0.68	1.46	7.42
U0d1-3	1.14	0.27	1.61	0.61	0.70	26.7
U0d2-4	1.14	0.27	2.21	0.64	1.54	6.09

[a]The angle range boundaries for the distribution function **U1** are given in Table 3.1.

Another effective way to reduce the uncertainty in risk assessment might be to consider correlations between individual parameters. For example, the combination of

small particle diameters and high slope angles results in an unacceptable 27% probability of dryout, as is shown in Table 3.2. However, experiments and numerical simulations performed in this project indicate that small particles are prone to spreading over the pool basemat by several physical mechanisms, including interaction with the large-scale circulation flows in the pool, and self-leveling of debris bed due to boiling and vapor release in the bulk of porous layer. This means that the probability of having a small particle diameter and a steep slope angle simultaneously would be less than that of having a tall bed with large particles, or a flat bed with small particles, limiting thus the probability of dryout occurrence. Also, there is a fundamental question on what failure criteria we use in our risk evaluation, and whether debris bed dryout necessarily means "failure". These questions are addressed in the following sections.

Post-dryout behavior of debris bed

Once a dry zone occurs in the debris bed dries, the temperature of solid material starts to increase due to the continuing decay heat release. In the absence of water evaporation, solid particles can be cooled by i) heat transfer to the vapor; ii) heat conduction in the particulate debris; iii) radiative heat transfer (at high temperatures). These can stabilize the solid material temperature at some level. Therefore, an important question is whether the dry zone temperature can reach some critical levels at which remelting of debris and thermal attack on the basemat of reactor containment can occur. Post-dryout behavior of debris beds was studied by DECOSIM; also, an analytical model for post-dryout debris bed heat transfer was developed [70]. Two debris bed geometries were studied: mound-shaped debris bed and a conical bed, resting on the basemat of a water pool of 9 m in diameter. The computational domain was 6 m high, on its top boundary a constant system pressure $P_{sys} = 3$ bar was maintained. The conical debris bed was of height $H = 3$ m, the diameter of its base was 6 m. The mound-shaped debris bed was of the height 2.5 m, the diameter of its base was 6 m, and that of the top was 2 m. For each geometry, several cases were calculated, with particle diameter D_p from 1 to 3 mm, and specific decay heat power W from 150 to 250 W/kg. The simulation matrix is summarized in Table 3.3, with the case acronyms comprised of geometry (C is conical, M is mound-shaped debris bed), particle diameter d* (millimeters), and decay heat specific power W* (W/kg).

Numerical grids used in the simulations had 30 cells in the radial direction (uniform grid, 15 cm cells) and 51 cells in the vertical direction (non-uniform, with the minimum cell size of 7 cm near the top boundary of the debris bed). Simulations started from quenched debris bed (temperatures of solid material and pool water equal to local saturation temperature, zero initial void fraction). Calculations were carried out for the period of 5000 s which was sufficient for the establishment of steady-state temperature in the dryout zone in most of the cases where stabilization was observed. In Figure 3.31, the time histories of the maximum temperature of the solid material are shown. The time of dryout (visible as the time at which the temperature curve deviates from the initial saturation temperature) is of the order of few minutes and is determined by the decay heat. In all the cases with particle diameters of 3 mm, temperature stabilization occurred, while for the smallest particles (1 mm) steady temperature rise is observed at a rate proportional to specific power W.

Typical spatial distributions of the void fraction and temperature of the solid material in post-dryout debris beds are shown in Figure 3.32 and Figure 3.33. In Figure 3.34, vertical distributions of void fraction (left) and vapor temperature (right) on the axis of symmetry are shown for all the cases from Table 3.3 in which stabilization of the dry zone was obtained. The temperature distribution in the dry zone is nearly linear, the fact which was used to derive an analytical model for the dry zone. Vertical distributions of void fractions on the axis of symmetry (Figure 3.34) were used to determine the vertical coordinates of the top and bottom boundaries of the dry zone (Z_{top} and Z_{bot}, respectively), as well as the fraction of debris bed height occupied by the dry zone $\xi = \left(Z_{top} - Z_{bot}\right)/H$.

Table 3.3: DECOSIM simulations of post-dryout debris beds.

Case	D_p, mm	W, W/kg	$T_{s,max}$, K	$T_{s,max}$-T_{sat}, K	Z_{bot}/Z_{top}, m	ξ, [–]
Conical, $H = 3$ m						
C-d1-W150	1	150	*1334.0*[a]	*947.0*[a]	0.3/2.8	0.89
C-d2-W150	2		559.8	173.4	1.8/2.8	0.36
C-d1-W200	1	200	*1699.1*[a]	*1311.7*[a]	0.05/2.8	0.89
C-d2-W200	2		781.5	395.0	1.37/2.8	0.51
C-d3-W200	3		512.5	126.1	2.1/2.8	0.25
Mound-shaped, $H = 2.5$ m						
M-d1-W150	1	150	*1300.0*[a]	*912.5*[a]	0.23/2.4	0.90
M-d2-W150	2		476.7	89.9	1.95/2.45	0.20
M-d1-W200	1	200	*1646.5*[a]	*1258.9*[a]	0.05/2.4	0.98
M-d2-W200	2		654.9	268.5	1.4/2.45	0.43
M-d3-W200	3		419.0	32.4	2.30/2.45	0.06
M-d1-W250	1	250	*1978.7*[a]	*1590.3*[a]	0/2.4	1
M-d2-W250	2		994.5	608.1	1.0/2.45	0.59
M-d3-W250	3		546.6	160.2	1.70/2.45	0.31

[a] *Temperature stabilization did not occur, values at time 4000 s are given*

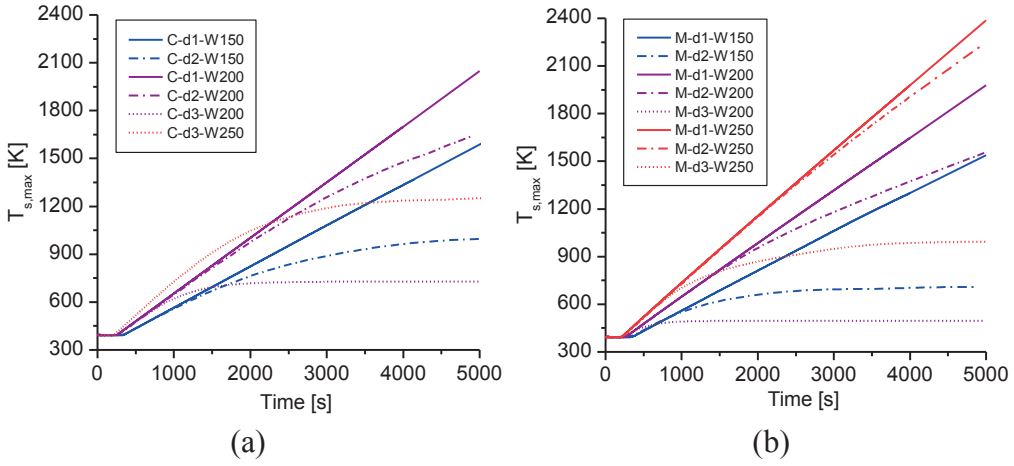

Figure 3.31. Time histories of the maximum temperature of solid particles in conical (a) and mound-shaped (b) debris bed.

The numerical results obtained by DECOSIM indicate that in the cases where dryout occurs in the debris bed: (i) dryout zone is located in the top part of the debris bed, vapor flows through the dry zone vertically; (ii) temperatures of solid par-

ticles and vapor increase in the vertical direction almost linearly, the difference between them being few degrees; maximum temperatures are attained in the top part of the dry zone; (iii) vapor cooling is capable of stabilizing the solid material temperature, provided that its flowrate through the dry zone is sufficient.

An analytical model for the dry zone was developed which provides analytical formulas relating the critical fraction of debris bed height taken by the dry zone ξ_* to the maximum temperature T_*. Function $T_*(\xi_*)$ is plotted in Figure 3.35 by the solid line, with two critical temperatures indicated. Temperature 1500 K at which zirconium oxidation begins can be reached if the dry zone takes at least half the debris bed height. Corium remelting temperature 2800 K can be reached if the dry zone comprises at least 70% of the debris bed height (massive dryout). Temperature in smaller dry zones will be stabilized due to large flowrate of vapor generated under the dry material. The points in Figure 3.35 correspond to the results of numerical simulations carried out by DECOSIM for conical and mound-shaped debris beds (see Table 3.3).

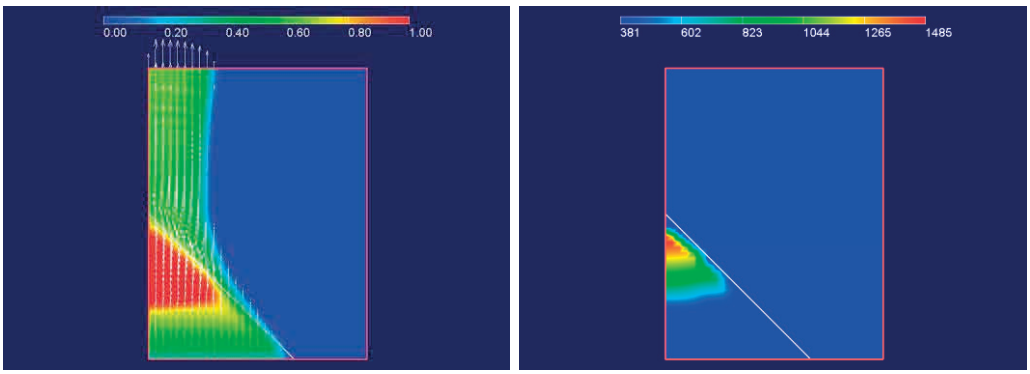

Figure 3.32. Void fraction (left) and solid particle temperature (right) in the post-dryout cone-shaped debris bed ($W = 200$ *W/kg,* $D_p = 2$ *mm) at 4000 s.*

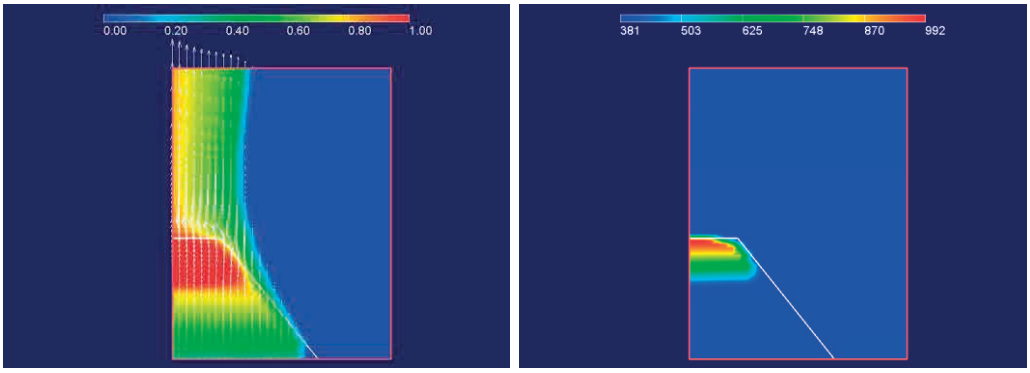

Figure 3.33. Void fraction (left) and solid particle temperature (right) in the post-dryout mound-shaped debris bed ($W = 250$ *W/kg,* $D_p = 3$ *mm) at 4000 s.*

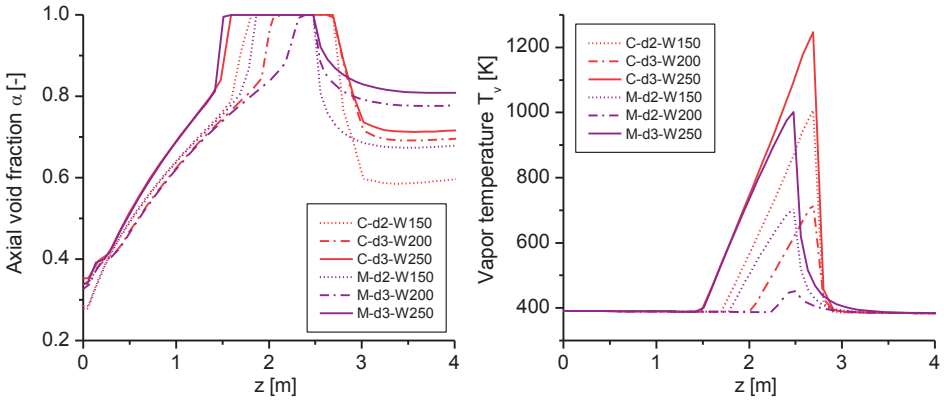

Figure 3.34. Void fraction (left) and vapor temperature (right) distributions along the axis of symmetry for the cases where temperature stabilization was obtained (Table 3.3).

The analytical formula predicts quite well the maximum temperature rise in the debris bed. Importantly, the results in Figure 3.35 are practically independent of debris bed shape and involve only few parameters, which reduces the uncertainties in the estimation of post-dryout behavior of debris beds. In the further work, relationship between the relative size of the dry zone and debris bed properties has to be obtained in order to apply the theory presented in the current work in the context of surrogate model for debris bed coolability and analysis of severe accidents risks.

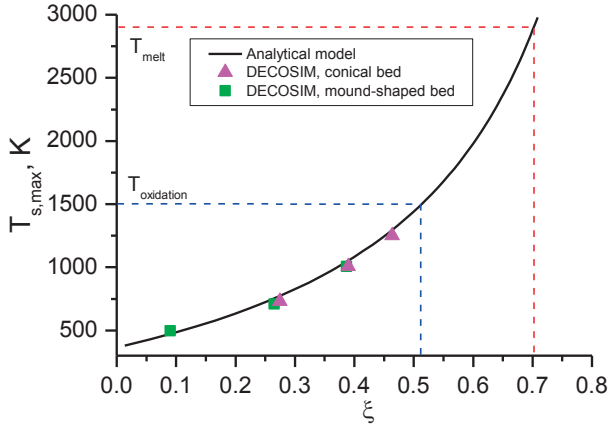

Figure 3.35. Maximum temperature vs relative size of dry zone.

Implementation of particle spreading model

In PDS-C experiments, a correlation for the particle flux as a function of local slope angle, gas flowrate, and debris bed properties was obtained in the non-dimensional form [2], [3]. These correlations were implemented in DECOSIM in order to enable simulations of debris beds with evolving (due to particle spreading) geometry. On each time step, particle fluxes are evaluated at the boundaries between the top surface cells of debris bed, and particulate matter is redistributed along the debris bed top, ensuring proper emptying/filling of top cells and packing to provide the given debris bed porosity ε. In Figure 3.36, the results of DECOSIM simulations of debris bed spreading are presented, demonstrating the change in debris bed shape with time.

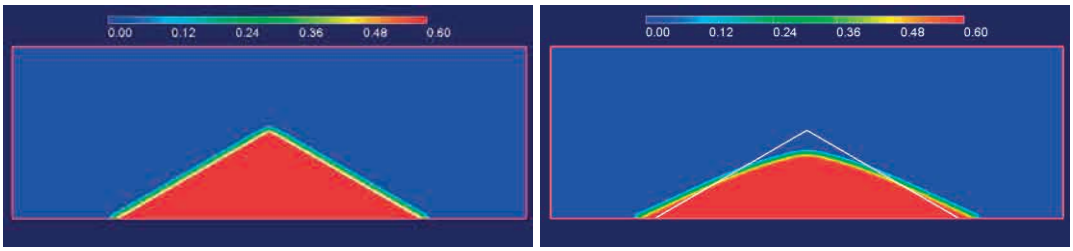

t=0 t=60 min

Figure 3.36. Self-levelling of debris bed (volume fraction of particles, d=1mm, W=160 W/kg).

Full DECOSIM simulations were performed for a conical debris bed with slope angle 30°; total mass of corium 143 t; relocation time 1.5 h and 3 h; porosity 40%; particle diameter of 1, 1.5, and 2.0 mm. Maximum temperatures of solid material were compared in the cases with and without particle spreading, see Figure 3.37. It can be seen that: (i) for 1 mm particles, debris bed is non-coolable, temperature escalation is observed with or without particle spreading; (ii) for 1.5 mm particles temperature stabilization is observed, for spreading debris bed (dashed lines) the maximum temperature is stabilized at a lower level; for 2 mm particles, debris bed is coolable, regardless of particle spreading. It was shown that occurrence of dryout does not deteriorate particle spreading.

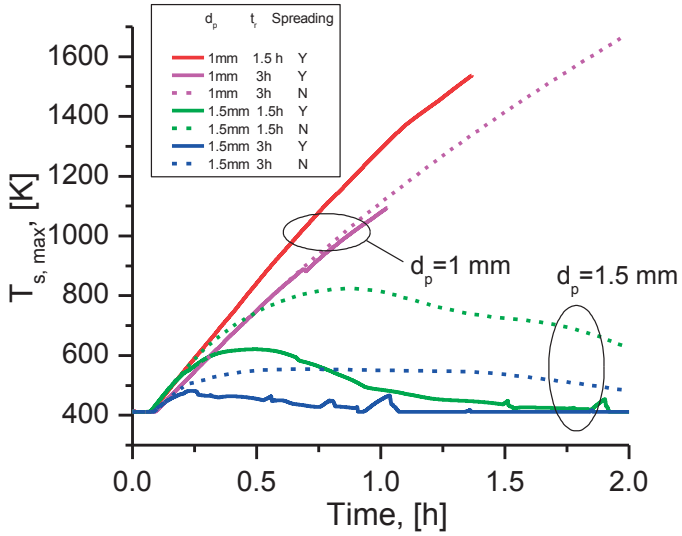

Figure 3.37. Maximum temperatures of solid particles. Solid lines: spreading, dashed lines: no spreading.

3.4.3. Debris Agglomeration Surrogate Model

If melt is not completely solidified prior to settlement on top of the debris bed, agglomeration of the debris and even "cake" formation is possible [27], [20]. Agglomeration of the debris bed can negatively affect the debris bed coolability [71]. The data obtained in DEFOR-A tests [27] was used for development and validation of modeling approaches for prediction of agglomerated debris in various scenarios of melt ejection [20], [22] using FCI code VAPEX-P. Computational costs of running a multidimensional FCI code (such as VAPEX-P) are prohibitive when parametric analysis is needed in order to quantify the influence of uncertainties in the scenarios of melt release from the vessel.

The goal of this work is to develop and validate a surrogate models for prediction of mass fraction of agglomerated debris. Physics based surrogate modeling approach is employed where computational efficiency and numerical stability are achieved by (i) considering only most important physical phenomena, and by (ii) decomposing tightly coupled problem into a set of loosely coupled ones with information exchange through initial and boundary conditions. The merits of physics based SM are (i) reduced number of the full model runs which are necessary for the calibration process; (ii) application of the SM beyond the domain covered with the original model. Physical phenomena and parameters important for assessment of agglomeration fraction are presented in Figure 3.38. The SM predicts mass fraction of liquid particles as a function of the pool depth and then fraction of agglomerates is predicted using developed and validated approaches [20], [22]. The interactions between the models, which describe the phenomena presented in Figure 3.38, can be introduced through the input/output parameters. Thus all models can be implemented and used independently from each other. The development of the surrogate model for prediction of agglomeration fraction consists of the following main steps:

1. To create a database of cooling histories for single droplets of different diameters using models for: drag, film boiling and radiation heat transfer, particle temperature profile, and crust formation.
2. To determine parameters of the melt release scenario such as: (i) melt thermophysical properties: density, solidus, liquidus and initial temperatures, etc.; (ii) melt release conditions: melt flow rate (initial melt velocity), initial jet diameter, jet free fall height, pool depth, etc.
3. To assess the parameters of corium jet at water pool surface according to the jet free fall model and to calculate jet breakup (jet penetration) length.
4. To determine droplet size distribution. For the sake of bounding assessments, particle size distribution can be determined based on the available data from the experiments with prototypic corium mixtures.
5. To predict the fraction of liquid droplets at certain pool depth using the database for single droplet cooling histories and melt release scenario parameters. Particle sedimentation length is determined using scenario data (pool depth) and the jet breakup length. Liquid droplets are determined as particles with crust thickness less than certain value. Mass faction of liquid droplets at certain depth is determined taking into account particle size distribution.
6. To calculate mass fraction of agglomerated debris using the correlation for agglomeration coefficient and predicted mass fraction of liquid droplets.

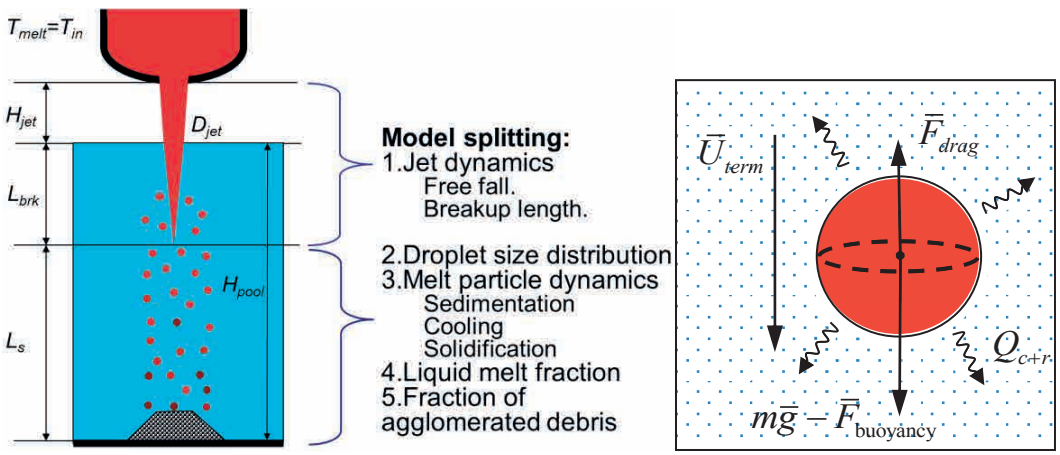

Figure 3.38. Splitting of physical processes for development of the SM.

The most important physical phenomena are modeled in the SM explicitly. However, mutual feedbacks between such parameters as jet breakup length, coolant void fraction and velocity are not modeled directly in the SM. Nevertheless, SM can take these effects into account if such relations are provided as closures. Details of model implementation, calibration and verification are provided in [21]. Quite good agreement between FM and SM solutions is illustrated in Figure 3.39. It is instructive to note that in order to obtain one point on the agglomeration map (single combination of jet size and pool depth) with FM takes ~24 - 168 hours of computational time. Obtaining complete agglomeration map using SM takes about half an hour including post processing of the results.

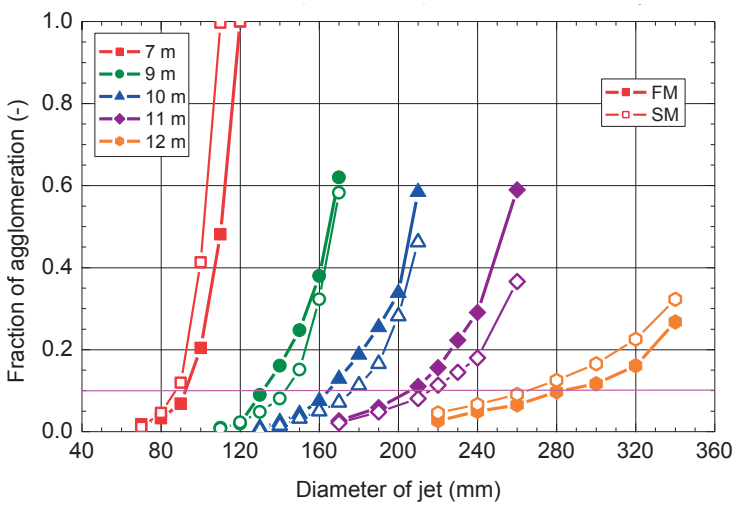

Figure 3.39. Comparison of predictions of mass fraction of agglomerated debris with full model and SM. Solid symbols – FM, half-filled symbols – SM.

3.4.4. Confirmatory Experiment on Debris Formation and Agglomeration

The goal of DEFOR experimental work is to provide data necessary for the development of analytical models and approaches for prediction of debris bed formation and agglomeration phenomena using different melt simulant materials. Liquid melt jet fragmentation and debris bed formation are considered at different conditions such as melt release (jet diameter, free fall height etc.), melt superheat, water subcooling and water pool depth. Experimental methods for investigation of the debris bed formation phenomena in DEFOR test facility (Figure 3.40) are described in detail in [26], [71], [28], [27], [53].

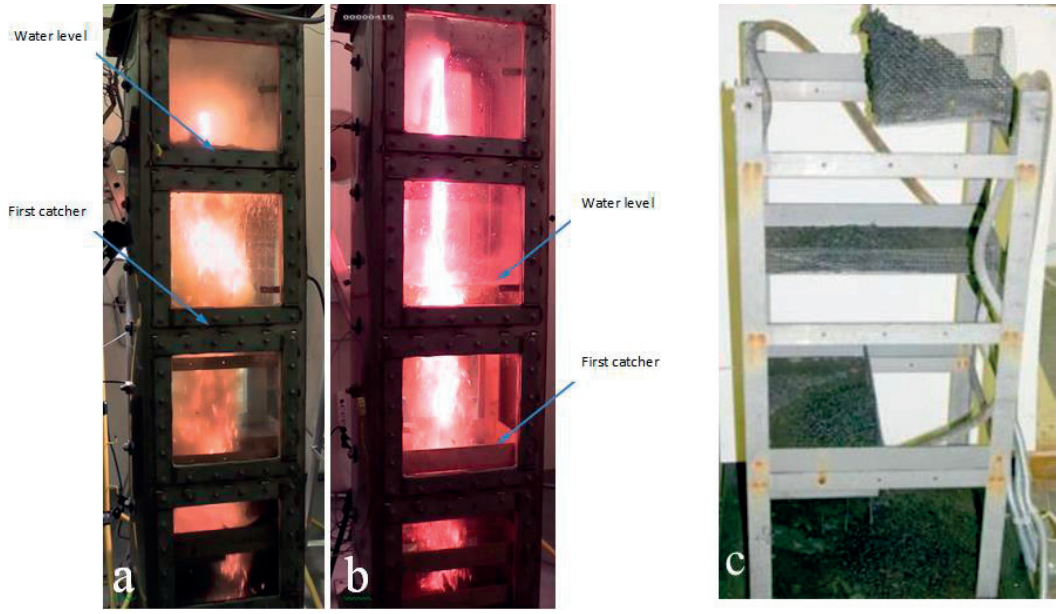

Figure 3.40: Melt pouring in DEFOR-A10 (a) and DEFOR-A11 (b) tests. Catchers for fragmented and agglomerated debris at varying depths (c).

More than 20 DEFOR-A tests have been carried out (Table 3.4). In the first test series (A1-A9 [26], [71], [27], [53]) Bi_2O_3-WO_3 (eutectic) melt with melting temperature 870 °C was used. Second test series (A10-A21) was carried out using ZrO_2-WO_3 (eutectic) melt with melting temperature 1231 °C. Debris bed topology, total porosity, agglomerated mass, and particle size distribution were measured in each test. Melt was released above or below the water surface in order to assess the effect of the jet velocity on the particle size distribution. Analysis of experimental data suggests that fraction of agglomerated debris decreases rapidly with the depth of the coolant as noticeable in Figure 3.41 for the whole set of experiments (A1-A21). Data on fraction of agglomerated debris from the new DEFOR-A tests agrees well with previously obtained results in the DEFOR-A and DEFOR-S experiments where smaller amount of melt (about 1.0 liter) was used [28]. We found that water subcooling is of minor importance until thermal stresses start to induce solid particle fracture.

Table 3.4: Ranges of the experimental parameters in DEFOR-A tests.

Parameters	A1	A2	A3	A4	A5	A6	A7	A8	A9	A10	A11	A12	A13	A14	A15	A16	A17	A18	A19	A20	A21
Melt temperature, K	1253	1246	1483	1221	1245	1279	1349	1255	1343	1371	1333	1345	1293	1467	1330	1348	1462	1420	1545	1518	1517
Melt superheat, K	110	103	-*	78	102	136	206	112	200	150	102	114	62	196	100	117	231	189	314	287	286
Melt jet initial diameter, mm	10	20	20	20	10	12	25	25	20	20	20	20	10	15	20	15	2x20	2x20	30	30	30
Elevation of nozzle outlet, m	1.7	1.7	1.7	1.7	1.7	1.7	1.62	1.62	1.7	1.72	1.8	1.85	1.85	1.75	1.8	1.65	1.65	1.65	1.44	1.65	1.5
Jet free fall height, m	0.18	0.18	0.18	0.2	0.18	0.18	0.2	0.2	0.18	0.2	0.7	0.13	0.13	0.2	0.2	0.2	0	0	0	0	0
Duration of melt release, s	38	11	-	11	38	20	10	10	11	13	12	23	6.3	-	9.6	22	10	13	10	15	13
Melt volume, l	3	3	3	3	3	3	3	3	3	3	3	3	3	3	2	4	5	5	5	5	5

Average flow rate, l/s	0.079	0.273	-	0.273	0.079	0.15	0.3	0.3	0.273	0.19	0.16	0.097	0.155	-	0.208	0.125	0.354	0.254	0.44	0.25	0.333
Initial average melt jet velocity, m/s	1.01	0.87	-	0.87	1.01	1.33	0.61	0.61	0.87	0	0	0	0	-	1.01	-	-	-	-	-	-
Water pool depth, m	1.52	1.52	1.52	1.5	1.52	1.52	1.42	1.42	1.52	1.52	1.1	1.85	1.85	1.75	1.8	1.65	1.65	1.65	1.44	1.65	1.5
Water initial temperature, K	346	366	345	346	364	346	356	355	355	348	348	348	348	354	354	345	355	354	359	353	358
Water subcooling, K	27	7	28	27	9	27	17	18	18	25	25	25	25	19	19	28	18	19	14	20	15

The effect of melt material can be considered by comparing similar tests in the first and second test series. In terms of the melt superheat and jet diameter the A10 and A11 tests can be compared to A7, A2, and A6. Agglomeration curve obtained in A10 test lies in between the curves of A7 and A2 tests being slightly closer to A2. This behavior agrees well with both melt superheat (A10 - 150°C, A7 - 200°C and A2 - 110°C) and jet diameter (A10 – 20 mm, A7 – 25 mm and A2 – 20 mm). Despite the fact that A11 test has larger jet free fall and thus higher jet velocity at the entrance into the water the data agrees well with A2, A6 tests with similar melt superheat. In terms of water subcooling and jet diameter at the water level, the closest to the A11 test is A6. It has slightly higher agglomeration on the top catcher which can be attributed to the higher melt superheat and experimental uncertainty due to proximity of the first catcher to the inherently instable jet leading edge. From the above considerations we can conclude that behavior of the new simulant material in terms of agglomeration agrees well with the results from the previous DEFOR-A tests series.

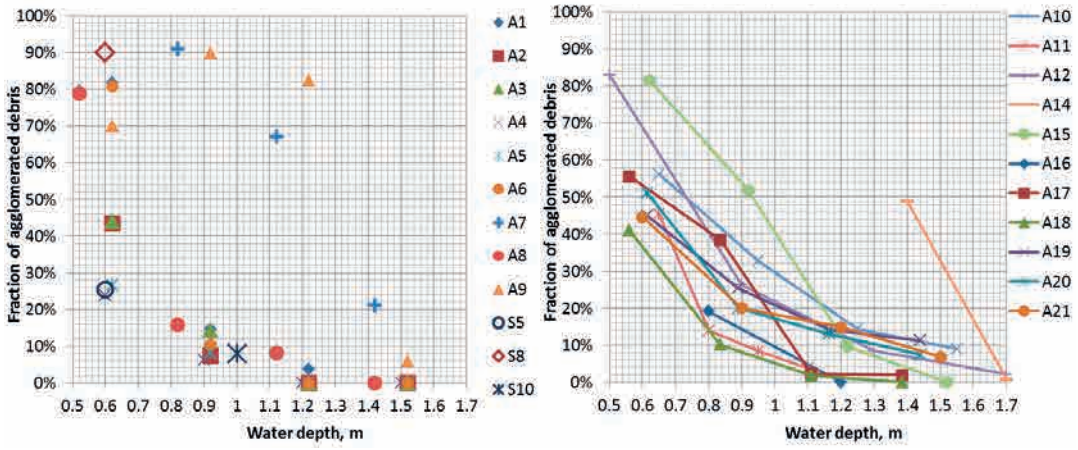

a) b)

Figure 3.41. Debris bed agglomeration fraction as function of water pool depth for A1-A9, S8, S10 (a) and A10-A21 (b) tests.

The particle size distributions (Figure 3.42) were obtained by sieving the debris. For comparison, the previously obtained result from DEFOR-A1-A9 test series [26] is provided in Figure 3.42a. Distributions from the tests with higher melt superheat are located slightly below the average, corresponding to larger particles. Some variations in the data due to the inherent uncertainties in high temperature melt-coolant interaction experiments can be expected. The data from A10-A21 tests (Figure 3.42b) show on average larger particles obtained with ZrO_2-WO_3 in comparison with the previous tests with Bi_2O_3-WO_3. Both series are within the ranges of FARO [43] data.

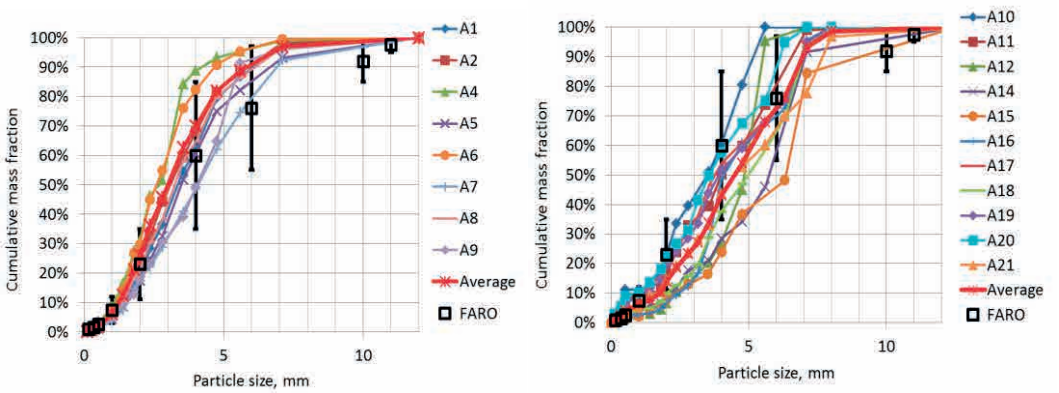

a) b)

Figure 3.42. Cumulative mass fraction for the debris in DEFOR-A1-A9 (a) and DEOFR-A10-A21 (b) tests. For comparison, the data from FARO tests and averaged DEFOR curves for corresponding series of tests are provided.

3.4.5. Small Scale DEFOR experiments

The small scale DEFOR project is motivated by the insights from larger scale (DEFOR-S and DEFOR-A) tests about the influence of water subcooling on particle morphology [28]. The changes of particle morphology from mostly round shape to a fractured products at relatively small changes of water subcooling (~10-20 K) were explained in [29] by the effect of particle cooling rate change at transition from film to nucleate boiling on the thermal stress of crystallized material. Experimental observations [28] and predictions [29] also suggested that smaller particles (below 1 mm) would have higher chances to avoid fracturing.

The main objective of the present work is to accomplish a detailed parametric study to address the effects of water subcooling, jet parameters and melt material on debris particle size distribution and morphology. The experiments (Table 3.5) were conducted at the MISTEE (Micro Interactions in STeam Explosion Energetic) small scale facility without steam explosion triggering. For a detailed description of the facility see [44]. The first series of experiments were performed with WO_3-Bi_2O_3 in eutectic composition (74:27 mol%, T_{liq}=870°C) with an initial melt superheat (ΔT_{sup}) of ~130°C. The second series of experiments were performed with WO_3-ZrO_2 in eutectic composition (73:26 mol%, T_{liq}=1231°C) with an initial melt superheat (ΔT_{sup}) of ~130 to 160°C. A set of 3 experiments were performed for each water subcooling (at equal intervals of ~10k) for confirmation of data repeatability. Post experiment, debris particles are carefully collected through a guide tube in the bottom hole of the test section for further analysis. Both inert and oxidizing (in order to avoid metallic phase formation due to thermal dissociation of Bi_2O_3 [17]) atmosphere was used in melt preparation.

Table 3.5: Experimental conditions.

Parameter	***Test series 1***	***Test series 2***
Component 1	Bi_2O_3	WO_3
Component 1 molar fraction (%)	27	74
Component 2	WO_3	ZrO_2
Component 2 molar fraction (%)	73	26
Composition (-)	Eutectic	Eutectic
Density of the melt (ρ) g/cm^3	~6	~5

Surface tension of the melt (σ) (mJ/m^2)	~126.8258	~196.07
Melt mass (charge) (g)	~20	~20
Melting temperature (T_{liq}) (°C)	870	1231
Melt temperature before melt discharge (°C)	~1000	~1390
Water temperature before melt discharge (°C)	20,30,40,50,60,70,80	20,30,40,50,60,70,80
Nozzle diameter (mm)	5,10	7

Experimental observations confirm that at high subcooling, the solidification is faster compared to low subcooling of water. Film boiling conditions (highly dependent on water temperature) dictates the fragmentation process. A morphological transition i.e. from round shapes (smooth) to rock like shape with sharp edges is observed, especially for the WO_3-Bi_2O_3. The mass fraction of fractured particles increases with increased water subcooling, see Figure 3.43. Moreover, a sharp transition in debris particle size distribution is observed at ~ 50 K water subcooling for WO_3-Bi_2O_3 and ~ 60 to 70 K water subcooling for WO_3-ZrO_2, see Figure 3.44. It is instructive to note that that the average particle size of WO_3- ZrO_2 is predominantly larger, where at high subcooling conditions ~ 60 to 70% of the debris particles were above 3 mm and at low subcooling conditions ~ 90% of the debris particles were above 3 mm. Additionally WO_3- ZrO_2 consistently produced mostly round shaped particles at even high subcooling conditions. This can be clearly seen in Figure 3.43 and Figure 3.44. One important observation is the brittle characteristic of WO_3-Bi_2O_3 debris particles compared to WO_3- ZrO_2 which can be explained by the differences in material properties.

Water Subcooling: 80 K Water Subcooling: 50 K Water Subcooling: 30 K

(a) WO_3-Bi_2O_3 debris particles.

Water Subcooling: 80 K Water Subcooling: 50 K Water Subcooling: 30 K

(b) WO_3- ZrO_2 debris particles.

Figure 3.43. Debris particles formed at varied water subcooling.

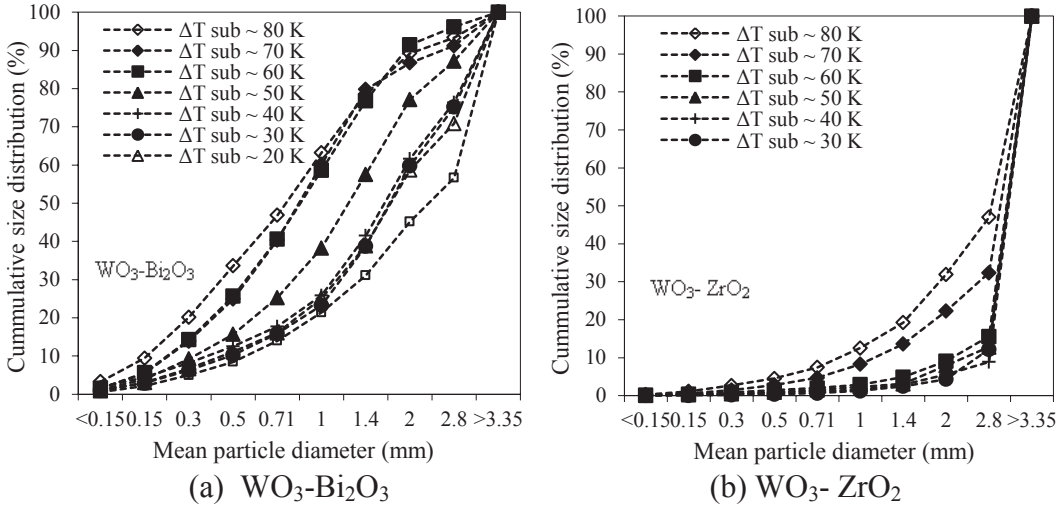

Figure 3.44. Average cumulative size distributions at varied water subcooling.

Experimental series 1 involving WO_3-Bi_2O_3 was performed with a 5mm nozzle diameter while experimental series 2 involving WO_3- ZrO_2 was performed with a 7mm nozzle diameter. Generally an increased jet diameter would result in larger sized particles. To assess the effects of variation in the nozzle diameter, a set of experiments involving WO_3-Bi_2O_3 were conducted with a 10 mm nozzle diameter. Post experimental analysis revealed no apparent dissimilarities in size distribution. Although slight variations are noticed the results are within the experimental deviations, see Figure 3.45. The observations on debris morphology and size distribution agree well with the mechanism explained in [29]. It is also observed that the smaller particles below a specific diameter (~0.3 mm) survive solid fracture even at high water subcooling conditions, see Figure 3.45d as it was predicted in [29].

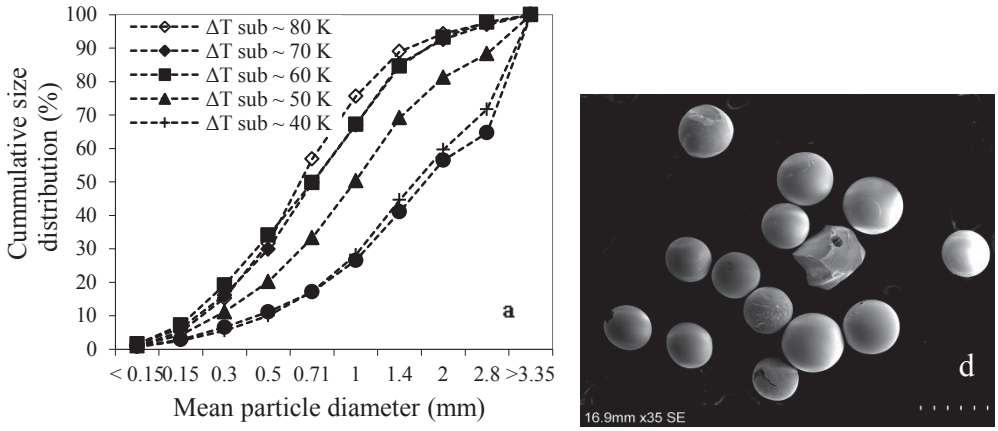

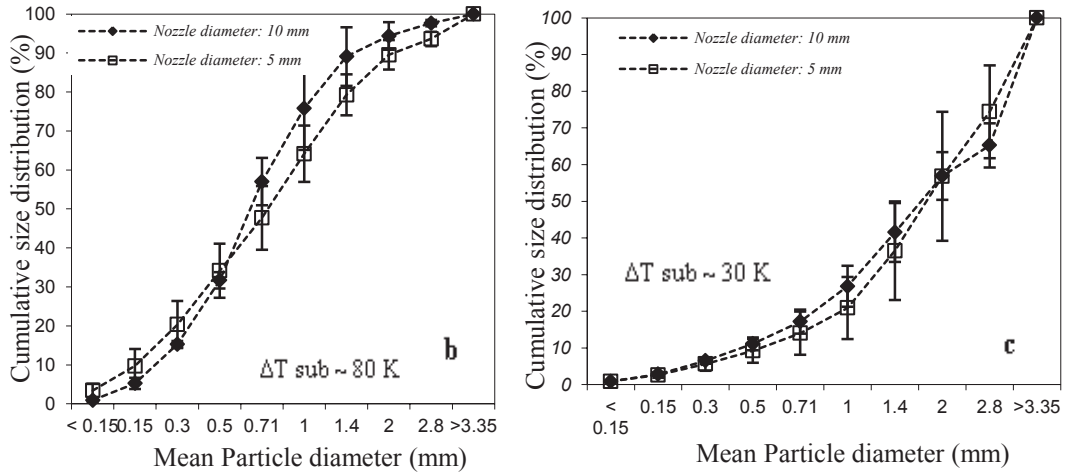

Figure 3.45. Average cumulative size distribution of WO_3-Bi_2O_3 particles at varied subcooling (a) with 10 mm nozzle diameter; nozzle diameter 5 and 10 mm at water subcooling (b) 80 K and (c) 30 K; (d) SEM image of WO_3-Bi_2O_3 particles lesser than ~ 0.3 mm diameter.

3.4.6. Particulate Debris Spreading

The debris bed height is one of the most important factors for coolability. A tall, mound shape debris bed can hardly be coolable, while the same debris can be easily cooled if the bed is spread uniformly over the area of the reactor cavity [74]. Boiling and two-phase flow inside the bed is a source of mechanical energy which can move the particles thus changing the shape of the bed. The process is called "self-leveling" [78], [79], [5], [6]. To be effective in providing a coolable geometrical configuration, the characteristic self-leveling time scale has to be smaller than the time scale for drying out and onset of re-melting of the bed.

The goal of this work is to develop predictive capabilities to assess characteristic time scale of the self-leveling process. In order to achieve the goal a tightly coupled analytical and experimental efforts have been undertaken. The experimental data are required for validation of the models. Model sensitivity and uncertainty analyses provide information on the most influential parameters that can be obtained from the experiments. In order to achieve the goal following tasks are addressed: (i) separate effect systematic experimental studies to quantify particulate debris flux at different test conditions including granular materials with different properties, morphology and size distributions; (ii) detailed analysis of the experimental data, generalization of the observed dependencies in non-dimensional variables using scaling approach; (iii) development of the model and code, extensive sensitivity and uncertainties analyses. The latter is required in order to identify the most influential parameters (such as material properties and SA conditions) and estimation of the accuracy of the modeling at reactor scale.

Experimental approach

The phenomenon of particle self-leveling is determined by the interactions between particles (solid phase), steam bubbles (gas phase) and water (liquid phase). The forces that drive a particle motion can be seen in Figure 3.46. Several PDS (particulate debris spreading) facilities were designed and built in order to study spreading phenomena. It has been demonstrated in previous PDS experiments that local parti-

cle flow rate depends on the local slope angle of the debris bed and local gas velocity, while the bulk volume of the debris bed is immobile (Figure 3.46). The particles are moving only in the topmost layer of the bed having a thickness of few particle diameters. Such behavior was insensitive to the facility scale, mass of the debris, and gas flux up to the point where the whole bed becomes fluidized. The local nature of the gas-coolant-particle interactions and the fact that only a thin top layer of particles is responsible for the spreading suggests that experiments in reduced size laboratory facilities can capture key physical phenomena. In this work we also show that the data produced in such tests is in principle scalable to the prototypic accident conditions. PDS-C (closure) facility was designed to carry out experiments with up to 40 kg or 8 liters of the granular material [2][19][18]. The steam production of the debris bed is simulated by the bottom injection of the compressed air with flow rate of up to 70 L/s.

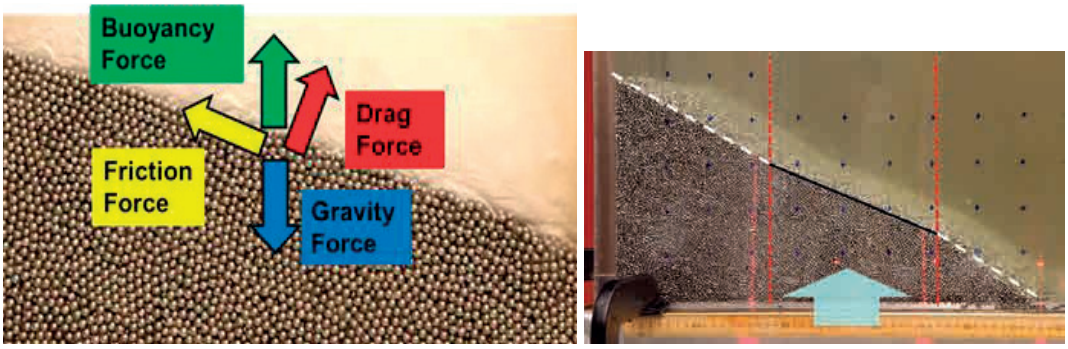

a) b)

Figure 3.46. (a) Schematic of the forces acting on particles near the top bed surface; (b) shape of the bed when gas is injected only under one section of the bed.

We developed an approach to evaluation of the debris bed slope $\theta(t)$ angle and particle flow rate $Q_p(t)$ as function of time t using image processing and edge recognition (Figure 3.47). The resulting $Q_p = Q_p(Q_g, \theta)$ *closure* dependence is a simple representation of the complex process. Hundreds of the tests in PDS-C facility have been carried out with different particles at different gas injection flow rates Q_g. The database of the dependencies $Q_p = Q_p(Q_g, \theta)$ has been analyzed and used for development of the generalized scaling approach allowing application of the self-leveling model to reactor scale. A model based on the closures was developed. The first results on experimental approach and successful model validation are reported in [18].

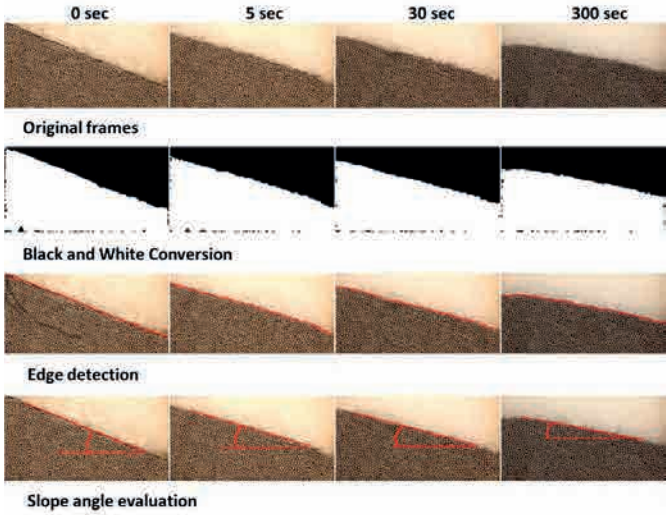

Figure 3.47. Image post-processing technique applied to the video recorded experiment on particle self-leveling carried out in PDS-C facility.

The database of experiments is also used to develop a *scaling* approach where the closures are expressed using non-dimensional variables, universal for particles of different shapes, sizes and materials. Such universal closure can be used even for corium particles for which there is no data from PDS-C type experiments. Scaling approach is based on the fact that particle flow rate can be expressed as a function of the main forces (i) buoyancy (F_B), (ii) aerodynamic drag (F_D), (iii) gravity (F_G), and (iv) inter-particle friction (F_{Fr}), and parameters which determine the forces:

$$Q_p = f(F_D, F_B, F_{Fr}, F_G), \tag{5}$$

$$Q_p = f\left(d_p, U_g, Q_g, \rho_p, \rho_l, \rho_g, \mu_g, g, \phi, k_{Fr}\right), \tag{6}$$

where $k_{Fr} = \tan\theta_{rep}\left(Q_g\right)$ is the friction coefficient which is a function of gas flow rate and for the coarse, cohesion-less materials is equal to the tangent of the repose angle. Since the rate of particulate debris spreading is determined by the local gas flow rate Q_g and slope angle ϕ of the bed following formula was proposed [2]

$$Q_p^*(\Phi) = \frac{Q_p\left(Q_g, \phi\right) \cdot Ar_{lg}}{\rho_p \cdot U_g \cdot d_p \cdot \dfrac{\tan\theta_{rep}(Q_g)}{\tan\theta_{rep}^0}} \tag{7}$$

where Q_p^* is a normalized non-dimension particle spreading rate (to be determined based on the PDS-C data), $\theta_{rep}^0 = \theta_{rep}(0)$ corresponds to critical repose angle of a particle heap at $U_g = 0$, and $\Phi = \tan\phi\,/\tan\theta_{rep}(Q_g)$, Ar_{lg} is the gas phase Archimedes number with liquid-buoyed solids. The first results on the development of such closures are illustrated in Figure 3.48, further details can be found in [2].

The universal closure (Figure 3.48) needed to be further validated against tests performed with different types and properties of the particles as well as their mixtures. The proposed modeling approach [18] on particulate debris self-leveling has been improved in terms of computational efficacy and, besides planar spreading, extended to the axisymmetric geometry of the debris bed spreading [3]. Model sensitivity analysis was used to identify the most influencing input parameters such as proper-

ties of the debris and SA conditions in application to prototypic accident conditions. The important findings in this work are: (i) the uncertainty in the terminal debris bed height (one of output of the model) reduces with time; (ii) the particulate debris spreading process is mostly effective in the first 30 minutes. These findings are illustrated graphically in Figure 3.49. Details on the analytical and numerical approaches are reported in [3].

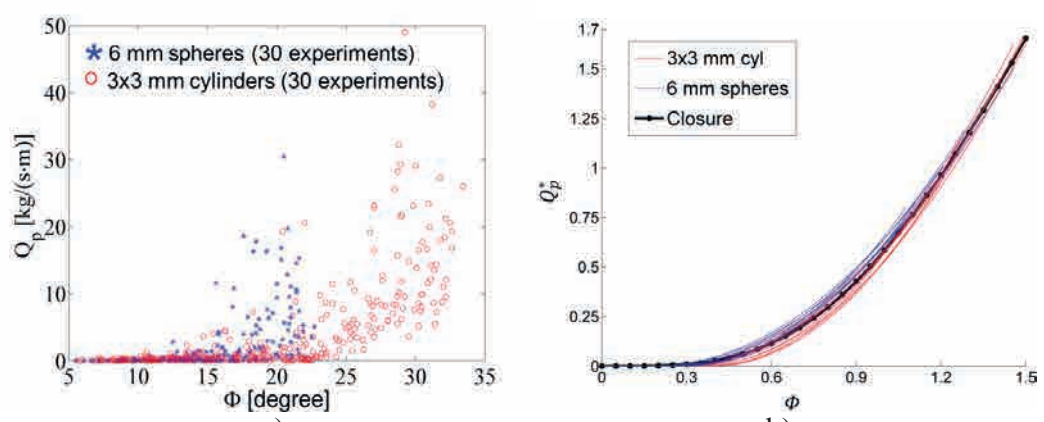

a) b)

Figure 3.48. Data in dimensional variables and non-dimensional representation of experimental closure curves.

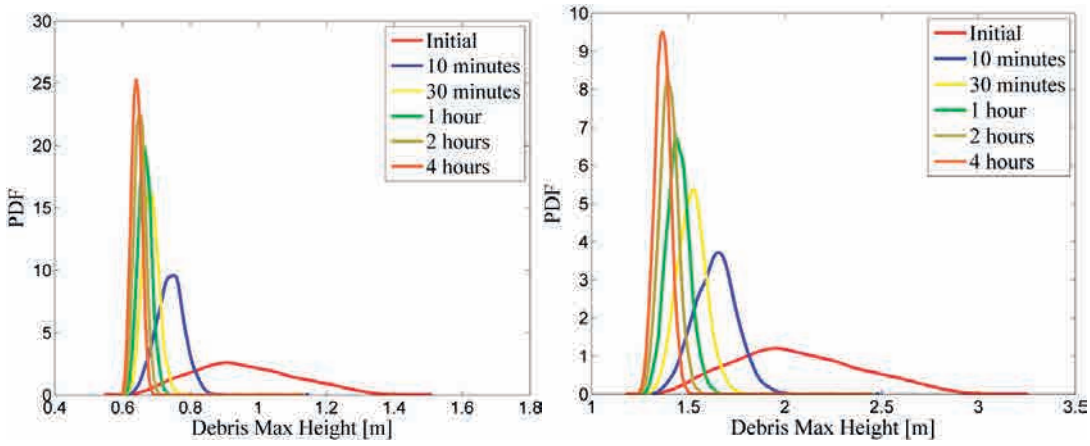

a) b)

Figure 3.49. Probability density functions of the maximal bed's height for scenarios with 20 tons (a) and 200 tons (b) of the particulate corium debris.

3.4.7. Debris Coolability: POMECO experiments

Motivated by reducing the uncertainties in coolability assessment of debris beds a series of tests were performed previously to investigate the effective particle diameters and dryout heat flux in the one-dimensional homogenous beds [32]-[38]. This is a follow-on work with the purposes to address coolability of non-homogeneous and multi-dimensional debris beds. The work also includes the study of coolability enhancement measures viz. bottom-fed (forced bottom injection of coolant) and use of downcomer (natural convection driven coolability). POMECO-FL and POMECO-HT facilities were employed to investigate frictional drags of adiabatic single/two-phase flow in porous media and dryout heat flux of a volumetrically heated particulate bed, respectively. Detail data about POMECO-FL facility can be found in [32].

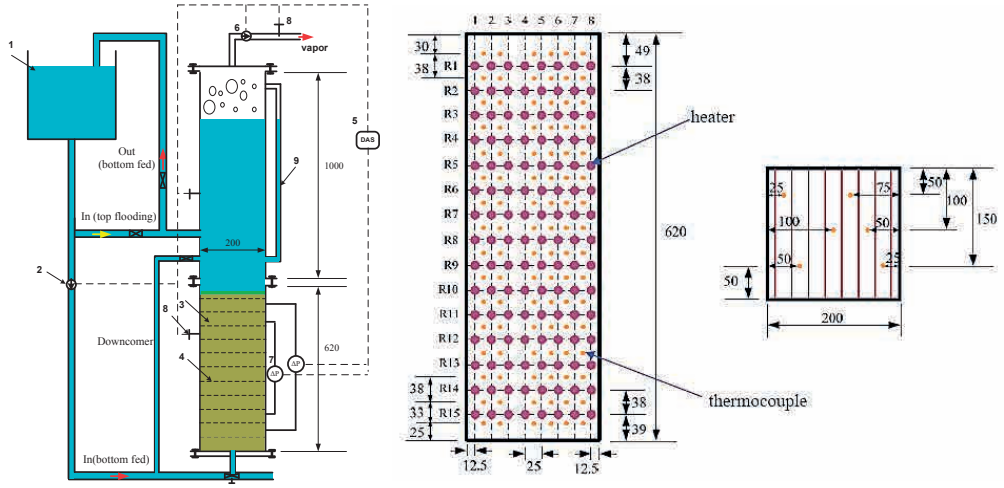

(a) the schematic (b) the side view and top view

(1-water tank, 2-water flowmeter, 3-particle bed, 4-heaters, 5-data acquisition system, 6-steam flowmeter, 7-pressure transducer, 8-thermocouples, 9-water level gauge)

Figure 3.50. a) Schematic of POMECO-HT facility; b) Distribution of heaters and thermocouples.

The POMECO-HT facility features a high heat flux up to 2.1 MW/m^2, to reach dryout condition for both top-flooding and bottom-fed cooling cases. The schematic of the POMECO-HT facility is shown in Figure 3.50a. The system is operating under atmospheric pressure. Total maximum power of the heaters is 84 kW. The heaters and thermocouples occupy about 0.7% in volume of the test section. Further details of the facility design can be found in [35], [38].

In the present study, six test beds are investigated (Figure 3.51). Figure 3.51c shows the bed packed with a radially stratified configuration of stainless steel spheres, constructed by packing 1.5 mm spheres in the middle part of the test section while putting 3 mm spheres at the periphery. The porosity of middle part is 0.363 while the porosity of outside part is about 0.367. Figure 3.51d represents a triangular bed packed with the stainless steel spheres of 1.5 mm, details of which are provided in Table 3.6. The total volume of triangular bed is about 13.2 liters and the porosity is around 0.37. The triangular bed is embedded with 72 pcs heaters (maximum power 50.4 kW). The remaining 48 heaters existing in the bed packed with 3 mm spheres are disconnected from the power source.

Table 3.6: Details of different bed configurations.

Bed	**Type of bed**	**Particles size** (mm)	**Porosity**
Bed-1	Homogeneous	1.5	0.363
Bed-2	Homogeneous	3	0.367
Bed-3	Radially stratified	1.5/3	0.363/0.367
Bed-4	Triangular	1.5	0.37
Bed-5	Multi-stratified	1.5/3	
Bed-6	Axially stratified	1.5/3	

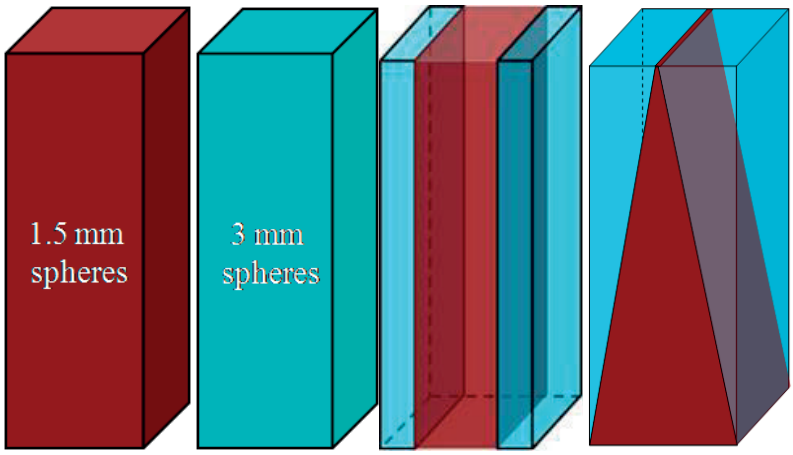

Figure 3.51. Schematic of various test beds.

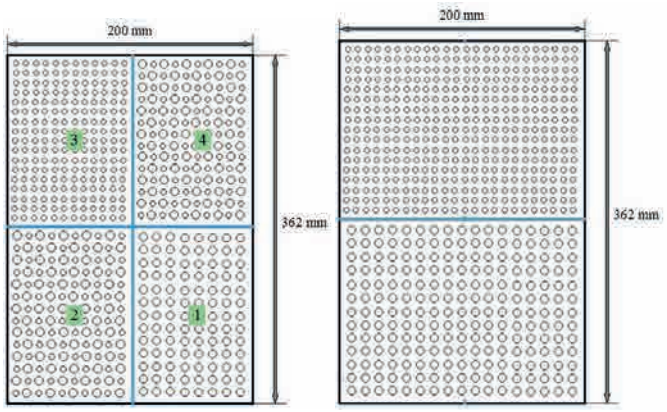

Figure 3.52. Schematic of multi-stratified bed and axially stratified bed.

Figure 3.52 shows the two other types of stratified beds, denoted as Bed-5 and Bed-6. Bed-5 is prepared with four zones of different size particles in the test section (Figure 3.52a). Zone 1 (porosity 0.398) and Zone 3 (porosity 0.439) are filled with 3 mm and 1.5 mm uniform size stainless steel particles, respectively, whereas Zone 2 (porosity 0.406) and Zone 4 (porosity 0.366) are consisting of uniform mixture of 1.5 and 3 mm size particles. Bed-6 is prepared with an axial stratification, upper-half and lower-half being of 1.5 mm and 3 mm size particles, respectively (Figure 3.52b). The porosity of the 1.5 mm particle layer is 0.387 and the 3 mm particle layer is 0.393.

For all the beds, the tests started with preheating the bed to fully saturated condition, and afterwards the power is increased in small steps to maintain the undisturbed flow regime in the bed. A dryout is considered to be occurred at the location where the temperature sensor shows a rise of 10^{o}C higher than the saturation temperature. The dryout power is further confirmed if the dryout disappears after slightly reducing the power and waiting for a longer time.

The dryout heat flux is 350 kW/m^2 for Bed-1 under top-flooding condition is closer to that predicted by Reed model (cf. Figure 3.53). The dryout determined by the counter-current flow limit (CCFL) occurred near the bottom of test section. Using

the 8-mm-diameter downcomer, the dryout heat flux increased by 19%, and by 34% using 12 mm downcomer size.

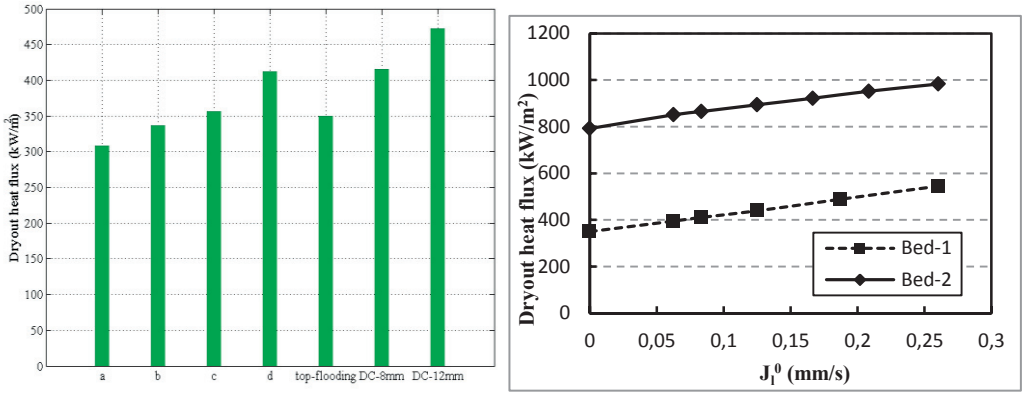

(a) (b)

Figure 3.53. a) Dryout heat flux in Bed-1 with 1.5 mm sphere particles (Models: a- Hu & Theofanous, b- Schulenberg & Műller, c- Reed, d- Lipinski); b) Variation of dryout heat flux with bottom injection water velocity.

Figure 3.53b illustrates that the dryout heat flux rises almost linearly with an increase in the bottom injection flow rate. The percentage of rise in the dryout heat flux for Bed-1 from zero bottom injection till 0.625 mm/s is around 82%, whereas, for Bed-2 it is 34%. Comparing the dryout heat fluxes in Figure 3.53a-b, it can be concluded that the 8-mm and 12-mm downcomers approximately create bottom injection flowrates of 0.08 mm/s and 0.16 mm/s, respectively, for both the beds.

The dryout heat flux found in the radially stratified bed is much higher (212%) than the bed packed with smaller size particles (Bed-1) and slightly smaller (93%) than the Bed-2 consisting of bigger size particles. We found that the downcomer and bottom injection significantly increases the DHF in a similar fashion if compared with the homogeneous beds (Bed-1 and Bed-2).

Figure 3.54 demonstrates that the dryout power densities of the triangular shape bed (Bed-4) are much higher than that of its equivalent 1D homogeneous bed (Bed-1C) for both top-flooding and bottom-fed cases, which means that the heap-like debris bed is more coolable than the 1D homogenous bed which has the same volume and bottom cross- section. According to Table 3.7, 23% of gain in dryout power density is found using 12-mm diameter downcomer and Bed-4 in comparison with the top flooding case. A comparison of data presented in Table 3.7 suggest that a downcomer is more effective for one-dimensional homogenous bed than for a triangular one.

Table 3.7: Details of the compared beds.

	Bed-1	Bed-1C	Bed-4
Bed configuration	See Table 3.7	as Bed-1	See Table 3.7
Volume of bed (*liters*)	24.4	13.2	13.2
Bed height (m)	0.61	0.33	0.61
Dryout power density (MW/m^3)	0.574	1.06	1.788 (2.2 with 12mm downcomer)

Figure 3.55a shows the dryout heat flux in the multi-stratified bed (Bed-5, Figure 3.52a) is between those of Bed-1 and Bed-2 (1.5 mm and 3 mm homogeneous particulate beds). However, it is lower than those of radially and triangularly stratified beds (Bed-3 and Bed-4). For Bed-5 with a 12-mm-ID downcomer, Figure 3.55b shows the 12% rise in the dryout heat flux, as compared to the top-flooding conditions

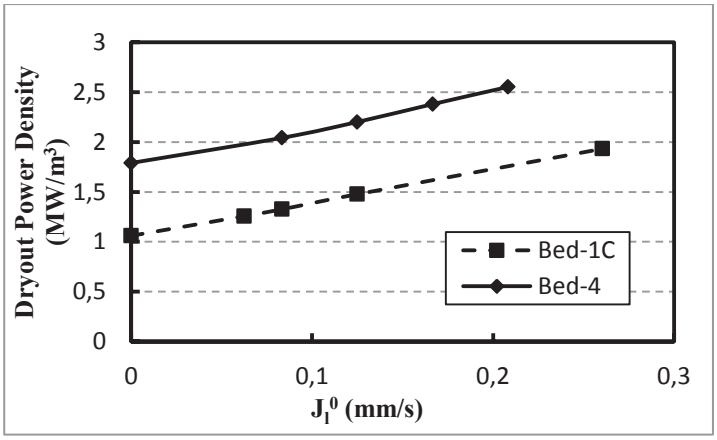

Figure 3.54. Dryout power density of Bed-1C and Bed-4 at different bottom injections.

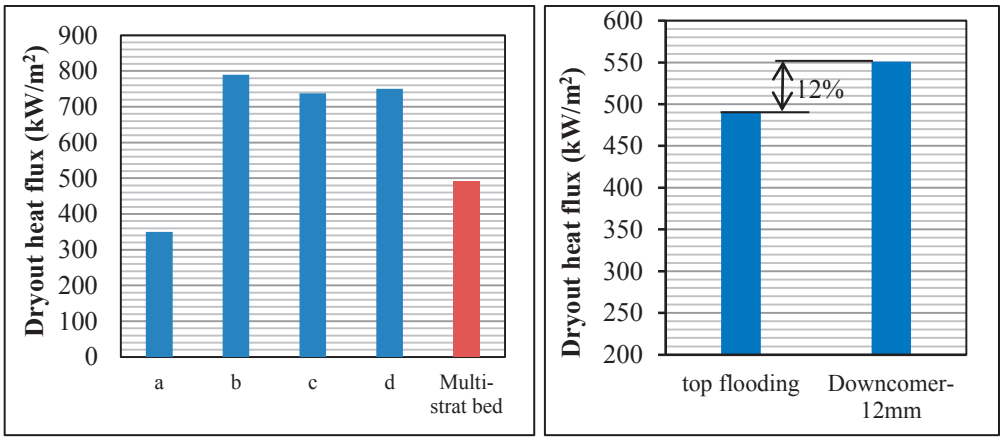

Figure 3.55. a) Dryout heat flux of various beds under top-flooding conditions (a- 1.5 mm homogeneous, b- 3 mm homogeneous, c- radially stratified, d- triangular); b) Effect of downcomer on dryout heat flux for the multi-stratified bed.

The axially stratified bed (Bed-6, shown in Figure 3.52b) is prepared with an upper layer of 1.5 mm particles and a lower layer of 3 mm size particles. The dryout heat flux of the bed under top-flooding condition is found 306 kW/m^2. The location of dryout is in the upper (small particles) region. The dryout heat flux found in the axially stratified bed is much lower than that of the homogeneous bed with 3 mm particles and other stratified beds. It is comparable with that of the homogeneous bed with 1.5 mm particles. The use of the 12-mm-ID downcomer shows the 39% rise in the dryout heat flux as compared to the top-flooding conditions, while it was 34% for the homogenous bed packed with 1.5 mm size particles.

In a cooperative research activity with VTT in Finland, two kinds of particulate beds packed with alumina gravels and multi-size zirconium silicate beads were investigated on the POMECO-FL and POMECO-HT facilities to identify their effective particle diameters and dryout heat fluxes, respectively. The alumina gravels

have the sizes from 0.25-10 mm and density of 3900 kg/m^3, packed bed has the porosity of 0.408. The zirconium silicate beads have the sizes of 0.8-1 mm and density of 4230 kg/m^3. The porosity of packed beds is 0.399. The effective particle diameter of the particles is calculated using frictional pressure gradients obtained from experiment and the Ergun equation [38]. Given the pressure gradients measured on the POMECO-FL test facility, the effective particle diameters (d_e) deduced from Ergun equation are 0.65 mm and 0.8 mm for the beds packed with alumina gravels and zirconium silicate beads, respectively.

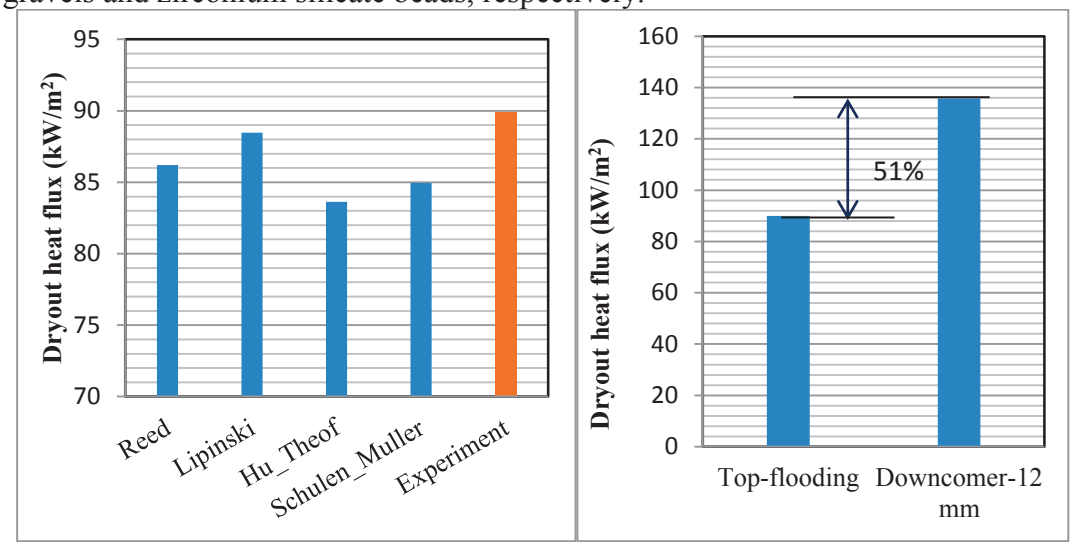

(a) (b)

Figure 3.56. a) Comparison of the measured dryout heat flux with predictions of various models under top-flooding conditions; b) Effect of downcomer on dryout heat flux in the bed packed with the alumina gravels.

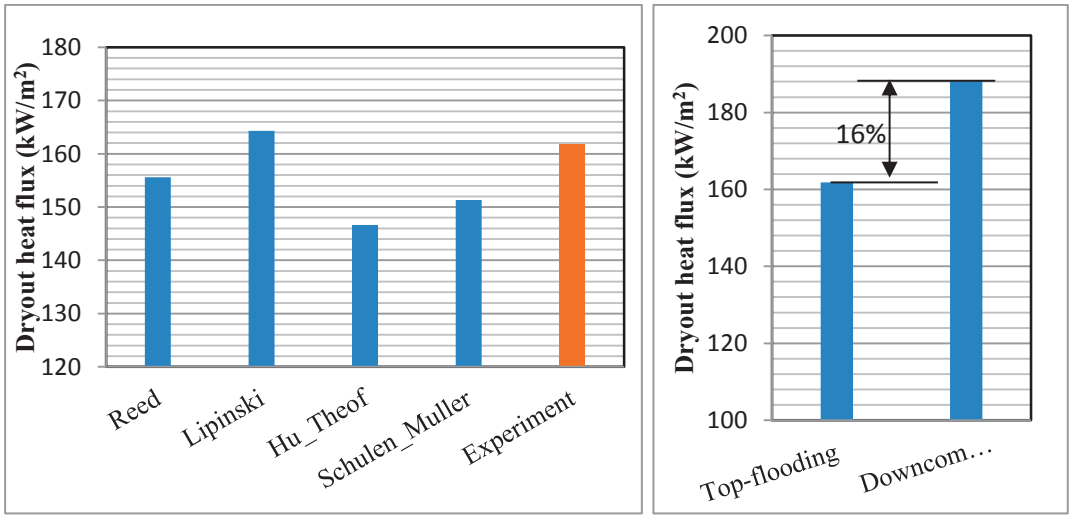

(a) (b)

Figure 3.57. a) Comparison of the measured dryout heat flux with predictions of various models under top-flooding conditions; b) Effect of downcomer on dryout heat flux in in the bed packed with zirconium silicate beads.

Based on the experiment on the POMECO-HT facility, the one-dimensional homogenous beds packed with alumina gravels and zirconium silicate beads have the dryout heat fluxes of 89.9 kW/m^2 and 161.8 kW/m^2, respectively. Figure 3.56a and Figure 3.57a show the comparisons of the measured dryout heat fluxes with those

predicted by different models. One can see that the dryout heat fluxes are better predicted by the Lipinski model. If the 12-mm downcomer is installed in the tests, it is found that the dryout heat fluxes are increased by 51% (see Figure 3.56b) and 16% (see Figure 3.57b) for the beds packed with alumina gravels and zirconium silicate beads, respectively.

3.4.8. DECO: Summary and Outlook

Significant progress has been achieved towards the main goal of DECO activity, i.e. development of the debris bed formation and coolability map. DECOSIM (Debris Coolability SIMulator) code capabilities were extended to solve energy equations for the liquid, gas, and solid phases in order to simulate (i) debris bed coolability in subcooled pool, taking into hydrostatic water head on the saturation temperature in the pool, (ii) post-dryout coolability of the debris bed. However, no melt pool formation model is implemented yet. A model for particulate debris bed spreading derived from the PDS-C experiments has been implemented in DECOSIM. Two computationally efficient surrogate models have been developed and validated against DECOSIM (full model) predictions. Namely a surrogate model (SM) for prediction of the dryout in a non-flat debris bed, and a model for prediction of the maximum temperature in a bed with a dry zone.

The model for prediction of dryout has been used in extensive sensitivity, uncertainty and risk analysis by evaluating the conditional dryout probabilities. The uncertainties in the ranges for (i) particle size and (ii) the slope angle of the debris bed are deemed to be the most important contributors to the uncertainty of the risk. Therefore, the most effective way to reduce the uncertainty in debris coolability would be research on the clarification of possible ranges of the slope angle and particle sizes and consideration of correlations between small particle diameters and high slope angles which can results in an unacceptable 27% probability of dryout. Experiments and numerical simulations performed in this project indicate that small particles are prone to spreading over the pool basemat by several physical mechanisms, including interaction with the large-scale circulation flows in the pool, and self-leveling of debris bed due to boiling and vapor release in the bulk of porous layer. This means that the probability of having a small particle diameter and a steep slope angle simultaneously would be less than that of having a tall bed with large particles, or a flat bed with small particles, limiting thus the probability of dryout occurrence. Further quantification of such correlations should be addressed in the future work.

Analysis of post dryout debris coolability with DECOSIM suggest that in all the cases with particle diameters of 3 mm, temperature stabilization occurred, while for the smallest particles (1 mm) steady temperature rise is observed at a rate proportional to specific power W. Preliminary DECOSIM simulations have been carried in order to investigate the effect of lateral debris bed spreading on coolability. It has been shown that (i) for 1 mm particles, debris bed remains non-coolable, temperature escalation is observed with or without particle spreading; (ii) for 1.5 mm particles temperature stabilization is observed, for spreading debris bed; (iii) for 2 mm particles, debris bed is coolable, regardless of particle spreading. Further studies are necessary in order to quantify the effect of the uncertainties in the particle spreading model and the effect of the dry zone on debris bed spreading and coolability.

Agglomeration surrogate model has been developed and validated against VAPEX-P full model results. The model is based on decomposition of initial tightly coupled problem into a set of loosely coupled ones (i.e. jet breakup, particle sedimentation, cooling and solidification, agglomeration) that can be linked together through initial and boundary conditions. Several parameters in the SM model are calibrated, using analytical assessments and data from the full model in order to take into account phenomena and dependencies, which are not modeled explicitly in the SM. Comparison of the results predicted with the full and calibrated SM suggest that SM provides acceptable accuracy obtained with about hundred times smaller computational effort.

A series of confirmatory DEFOR-A experiments has been carried out with ZrO_2-WO_3 simulant material in order to investigate debris formation and agglomeration phenomena and to produce data for development and validation of the models. The data on particle size distribution, debris bed porosity and agglomeration is in good agreement with the previous DEFOR-S, DEFOR-A and FARO tests. On average, larger particles were obtained with ZrO_2-WO_3 melt than with Bi_2O_3-WO_3, size distributions for both melt simulant materials are within the ranges of size distributions observed in FARO tests. The difference between particle sizes in the tests with free falling jets was found to be insignificant. There is a tendency to form slightly larger particles only in the tests with submerged nozzles where melt is released under water with initially small jet velocity. Initial jet velocity also seems to have no visible effect on the fraction of agglomerated debris.

Small-scale DEFOR experiments were carried out for clarification and confirmation of previous DEFOR-S data, analytical results hypotheses. The tests were performed with different water subcooling, jet diameter and melt composition have confirmed a profound effect of water subcooling on the particle size distribution and morphology. A sharp transition in size distribution and morphology between low and high subcooling conditions is observed at ~ 50 K water subcooling for WO_3-Bi_2O_3 and ~ 60 to 70 K water subcooling for WO_3-ZrO_2. Similar to DEFOR-A large scale tests, the average debris particle size of WO_3- ZrO_2 is predominantly larger than that of WO_3-Bi_2O_3; moreover WO_3- ZrO_2 consistently produced mostly round shaped particles at even high subcooling conditions pointing out the significant effect of material thermo-mechanical properties. It was also found that variation in jet diameter between 5 and 10 mm did not have an impact on the debris properties. In general, results of this experimental program are in good agreement with the results from DEFOR-S and DEFOR-A programs. Results with melt material WO_3-Bi_2O_3 is consistent with the particle fragmentation map predicted in [29] where particles below a certain diameter escape fracture and settle in smooth round shapes.

Particulate debris spreading that drive self-levelling of the debris bed has been investigated both experimentally and analytically in order to develop understanding of key physical processes and predictive capabilities for analysis of reactor accident progression. PDS-C (closures) experimental database obtained in separate effect tests was generalized and a universal non-dimensional closure has been proposed for determining particle flux as a function of the local slope angle and gas velocity. Developed closure has been used in a standalone 1D code for modeling of debris bed self-levelling in plant accident conditions and also implemented in DECOSIM code. The 1D debris spreading model has been used for extensive sensitivity and

uncertainty analysis. Further reduction of uncertainty in extrapolation to prototypic accident conditions requires extension of the PDS-C database to particles of different properties, morphologies and size distributions.

POMECO-FL and POMECO-HT tests have been carried out to investigate adiabatic single/two-phase flow in porous media and dryout heat flux of a volumetrically heated particulate bed. The study was motivated by the aim to obtain the coolability of debris beds with non-homogeneous and multi-dimensional characteristics, and to examine the effects of various stratifications of debris beds on coolability. Comparison of dryout heat flux of stratified bed with that of homogeneous configuration shows the additional effects such as, side ingression of coolant and effect of bigger size particle layer which then helps to enhance the dryout heat flux of the bed. These results can be used for validation of debris bed coolability analysis codes.

3.5 Steam Explosion Impact Map (SEIM)

Steam explosion in a deep pool is a credible threat to containment integrity potentially leading to large early release of radioactive products to the environment. Recent experiments carried out at KTH suggest that the risk of steam explosion in a relatively shallow pool might also need to be revisited [25]. The goal of this work is to develop ex-vessel Steam Explosion Impact Map (SEIM) framework to connect melt ejection mode with steam explosion loads on the containment structures to estimate containment failure probability. General approach to the development of the SEIM SM is illustrated in Figure 3.58. In order to achieve the goal the following tasks are addressed: (i) develop a well-posed full model (FM) taking into account melt ejection mode, pool conditions (accident scenarios and operator actions) and code modelling uncertainty; (ii) develop a computationally efficient surrogate model (SM) for prediction of ex-vessel steam explosion impulse; (iii) establish connection between predicted steam explosion impulse, containment fragility and risk of containment failure. Development of the SM relies on a database of solutions generated by a 1D FCI code TEXAS-V. Application of 1D code requires an additional method for calculating loads on 3D containment structures. There is also a need to resolve the link between ex-vessel coolability and steam explosion. Even a mild steam explosion might lead to degradation of debris bed cooling function, e.g. by destroying protective covers for cable penetrations and exposing them to hot debris, creating a leak of coolant from the lower drywell, etc. It is not clear at the moment if spreading of debris by a steam explosion can be effective.

Steam explosion models are physically ill-posed as they demonstrate high sensitivity of explosion energetics to the triggering time (depending on the triggering time steam explosion impulse can take values between 0 to 1.5 MPa) [13]. In order to make the model well-posed for a meaningful sensitivity analysis we introduce an *integral response function* (IRF). The IRF is the explosion impulse obtained with fixed initial and boundary conditions and statistical averaged for different triggering time. We use the IRF for both the sensitivity study and for the SM development. A comprehensive sensitivity study has been carried out. In total TEXAS-V input file contains more than 200 parameters for premixing and explosion modules. After consideration of dependencies between parameters we selected 23 physically meaningful parameters (see Table 3.8). These parameters represent both aleatory uncertainty in melt release scenarios and water pool conditions, and epistemic uncertainty

in modeling. Ranges of the parameters are selected based on the available information about prototypic severe accident conditions. Mesh cell height (dxi) has been set constant to 0.5 m. Statistical study has demonstrated that with parameter increase from 0.2 to 0.6 m the IRF increase will be insignificant. Other parameters were set either in according to the TEXAS-V manual [7] or based on other data [50], [51], [45], [42].

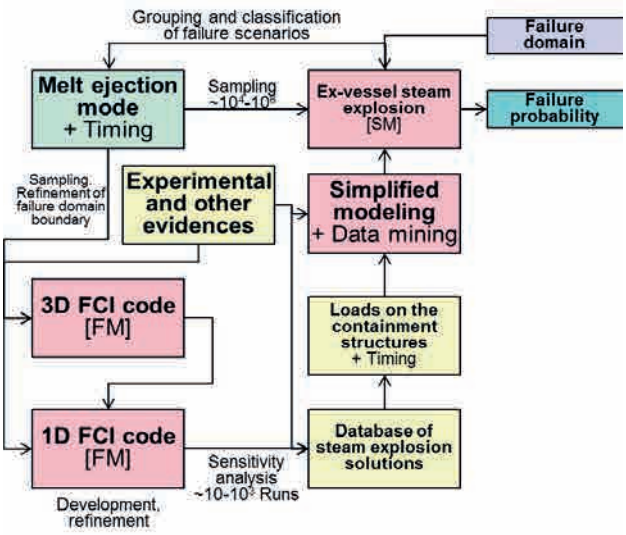

Figure 3.58. Ex-vessel steam explosion surrogate model.

Table 3.8: List of TEXAS-V parameters used in the study.

Parameter	Units	Range	Description
			Scenario parameters
Po	kPa	100-400	Initial pressure
Tlo	K	288-366	Water temperature
xpw	m	3.2-8.2	Water level in the containment
tgo	K	tlo	Cover gas temperature
two	K	tlo	Wall temperature
			Input modelled parameters
RPARN	m	0.07	Fuel injection radius
		0.15	
CP	J/kg·K	400-570	Fuel capacity
RHOP	kg/m3	7600-8600	Fuel density
PHEAT	kJ/kg	260-360	Fuel latent heat
TMELT	K	2850	Fuel melting temperature
TPIN	K	2850-3150	Fuel injection temperature
UPIN	m/sec	1.5-3.3	Fuel injection velocity
KFUEL	W/m·K	2-11	Fuel thermal conductivity
C(32)	J/m2	0.4-0.6	Fuel surface tension
C(18)	-	0.78	Fuel emissivity
			Deterministic modelling parameters
dxi	m	0.5	Cell height
ariy	m^2	0.7-1.8	Cell cross-section area
		4-8	
TMAX	sec	-	Premixing time
cfr	-	0.002-0.0027	constant for rate of fuel fine fragmentation
rfrag	m	0.0001	Initial size of fragmented particles
pold	Pa	2xPO	Threshold pressure for film collapse
tfraglimt	s	0.0005-0.003	Fuel fragmentation time interval
ptrig	kPa	300	Trigger pressure

In the scope of the study two scenarios of oxidic melt release relevant for the reference Nordic BWR were considered: (i) 140 mm jet diameter (CRGT failure with no ablation); (ii) 300 mm jet diameter (CRGT failure with ablation or vessel wall failure). IGT failure (70 mm jet diameter) is not included since preliminary calculations demonstrated rather weak explosions. The sensitivity study uses Morris method [48]. DAKOTA [1] code is applied to generate input dataset. For every scenario 3 sensitivity studies have been performed, the obtained averaged measures and respective ranges are demonstrated in Figure 3.59 - Figure 3.60.

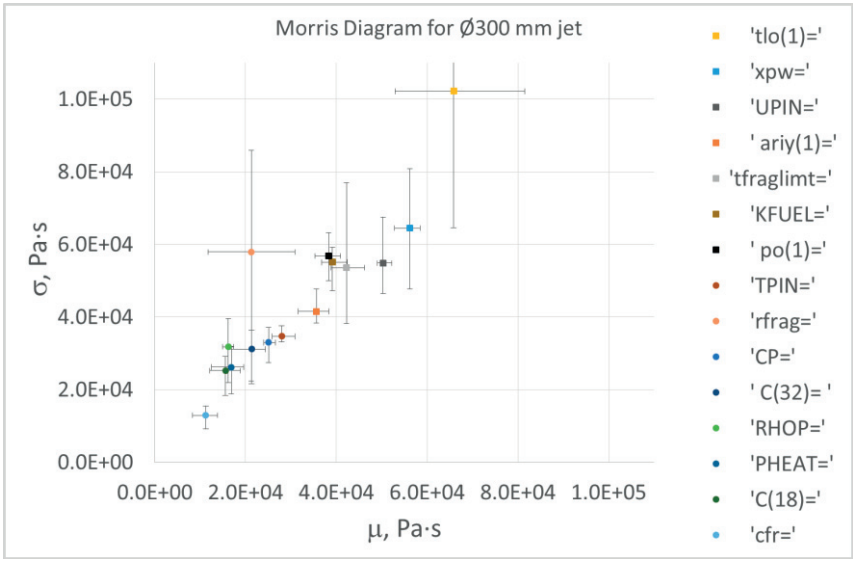

Figure 3.59. Morris diagram for the mean integral response function (jet Ø300 mm).

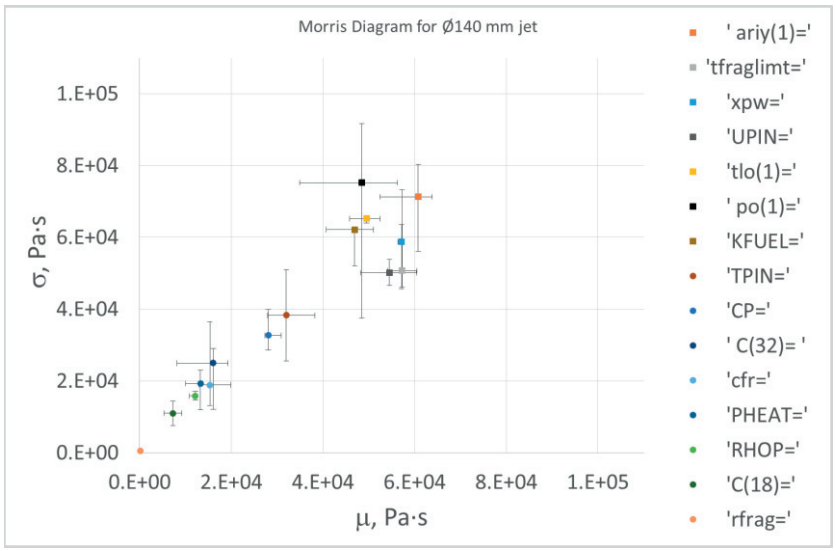

Figure 3.60. Morris diagram for the mean integral response function (jet Ø140 mm).

The cross comparison of the scenarios indicate some minor differences. However the list of 9 most influential parameters remains the same:
Water level: With decrease of water level steam explosion energetics decreases. System confinement and availability of volatile liquid are prerequisites for energetic steam explosion.

Water temperature: The explosion impulse is rising with increase of water temperature until saturation point, where high steam generation suppresses fine fragmentation and explosion propagation.
Initial melt velocity: The higher the initial velocity the higher is the explosion impulse. Amount of fragmented liquid melt in the premixture available for energetic interaction is driven by primary and secondary fragmentations rates. Both are proportional to the melt relative velocity.
System pressure: Affects water saturation point, steam density and thus volumetric steam generation rate.
Melt thermal conductivity: With increase of thermal conductivity explosion impulse decreases. The parameter drives melt solidification dynamics.
Melt initial temperature: Increases explosion impulse. Defines total amount of liquid melt available for fine fragmentation.
Fine fragmentation time: Sets the time of melt fine fragmentation during explosion phase limiting total amount of released thermal energy.
Cell cross-section area: In 1D code defines the total amount of water in the FCI zone. This has implications on the steam generation during premixing, water temperature at triggering time and respectively steam explosion energetics.
Other parameter: have demonstrated weak influence and have been excluded from future sensitivity / uncertainty study.

Impulse cumulative distributions from two scenarios obtained from TEXAS-V generated data is presented in the Figure 3.61. Notice that results are very close, though the scenario with smaller jet demonstrated on average slightly higher impulses. This effect will be investigated.

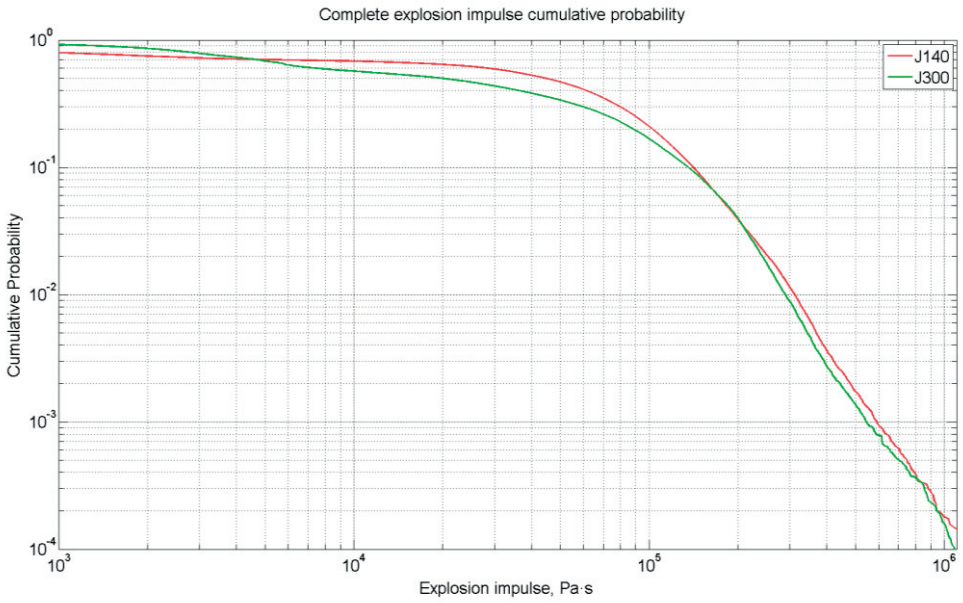

Figure 3.61. Explosion impulse cumulative distribution (50 000 samples).

3.5.1. SEIM: Surrogate Model Development

The computational cost of TEXAS-V code run is too high for direct use in the SEIM framework. Therefore, a computationally efficient SM is developed to reliably approximate TEXAS-V predictions. An iterative approach to the SM development is presented in Figure 3.62. First, an initial list of input parameters is defined

based on the actual variables in the TEXAS-V input file. Ranges for the parameters are defined based on the state-of-the-art knowledge and MC3D calculations. The obtained dataset is then provided to the dedicated sampling, optimization and post-processing algorithms that creates a database of predicted TEXAS steam explosion impulses per area and maximum dynamic pressures. This database is used for the sensitivity study (Morris sampling method) and for the training of Artificial Neural Networks (Sobol or Halton sampling method).

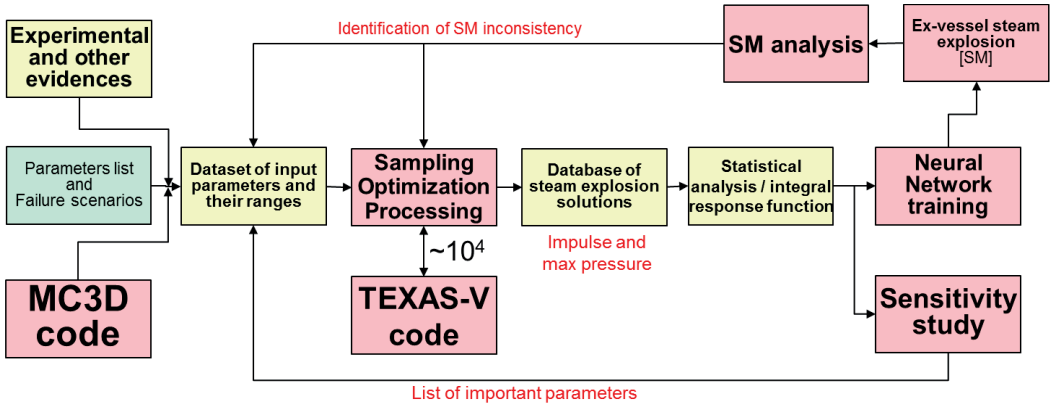

Figure 3.62. SM development methodology.

The results of the sensitivity study are used to reduce the number of input parameters and / or adjust input parameters ranges. In addition SM undergoes extensive numerical validation and, in case of inconsistent results, modifications to the sampling and optimization module are applied. With new dataset and processing module a new sensitivity study and new surrogate model are obtained. With such process of sampling and sensitivity, the SM development is repeated iteratively until consistent and physically sensible results are obtained. Note that ANN is trained to predict the IRF.

3.5.2. An Estimate of Steam Explosion Load using MC3D Code

The main goal of the study is the assessment of the steam explosion loading on the containment walls using MC3D, a multiphase FCI CFD code. A sensitivity analysis of the parameters in modeling of fuel coolant interactions is also performed. The geometry of the domain is as shown Figure 3.63a. The 2D problem is formulated using axisymmetric conditions. The melt droplet diameter of 2.5 mm is provided as an input to the CONST jet fragmentation model in MC3D.

The calculations time for the full domain is longer, even using a coarser mesh size (especially when jet interacts with a water pool). Therefore, the domain was restricted to 12 m height from the bottom. The new modified domain is as shown in Figure 3.63b. The calculations using a full geometry are then carried out, only to calculate the actual jet diameter and velocity at 12 m height, to be used in the further analysis. The constant pressure is specified at the upper boundary of the modified domain. The mesh (161×81) is refined near the center area and the bottom, where there is maximum jet coolant interaction. The premixing and explosion phase calculations are carried out for all the cases.

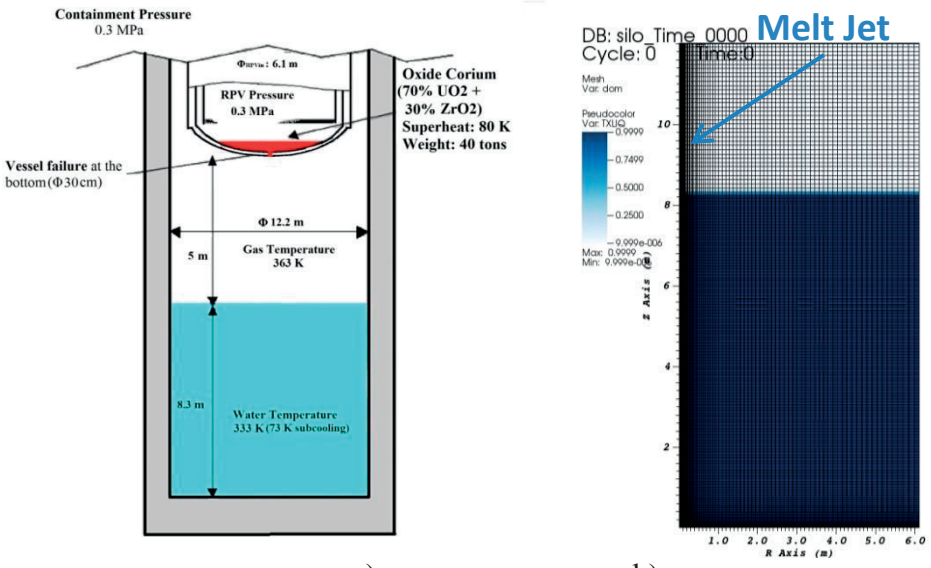

a) b)

Figure 3.63. a) Geometry of the cavity; b) Modified domain for calculations.

Load on Cavity Walls for a Basic Case

Initially, the base case calculations are carried out, for a jet diameter of 30 cm. Figure 3.64 shows the contour plots illustrating the flow patterns of jet in the water pool. It shows the fragmentation enhances when the jet enters into the pool. The area around the jet contains more void due to rapid evaporation of the coolant at the jet-coolant interface and also from the fragmented droplets. There is a highly wavy pocket of vapor around the jet. From the results, it is clear that the jet reaches the bottom with incomplete breakup. The time required for the jet to reach the bottom from the 12 m height is 1.45 s and the total time required from the RPV bottom is 1.97 s.

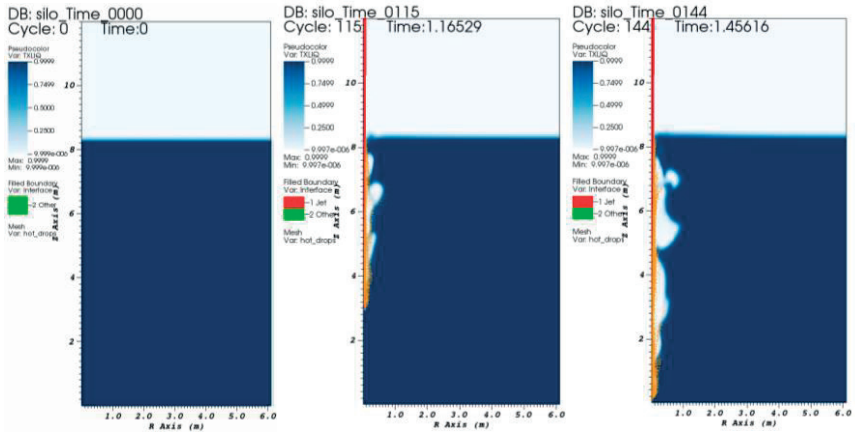

(a) 0s (b) 1.165s (c) 1.456s

Figure 3.64. Flow patterns in the domain at different time intervals.

The droplet mass in contact with water is decisive in the steam explosion energetics. It is seen from the results that, up to about 0.8 s, the fragmented drops are in liquid state and, since the amount of void is less, almost all the droplets are in contact with the coolant. Afterwards, the total droplet mass increases with the same rate, but the liquid droplet mass in water (void<0.6) reaches its peak and starts to decrease gradually. This may be because most of the fragmented liquid droplets are in high void

region. Therefore, it can be deduced that the optimal conditions for strong explosion can be achieved even before the jet reaches the bottom.

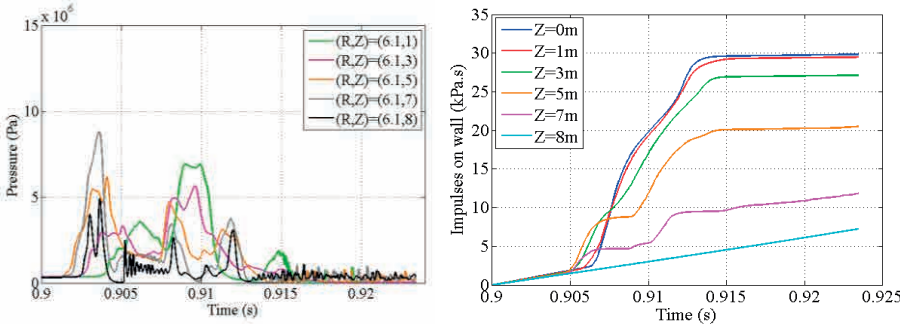

(a) (b)

Figure 3.65. a) Pressure attained at different locations in the cavity; b) Impulses on side wall.

The triggering for the explosion phase is initiated at the time when the total mass of liquid droplets in water (void<0.6) reaches its maximum. Figure 3.65a and b show the pressure and impulses respectively achieved at different locations at the side wall. It can be clearly seen that the higher impulses strike on the bottom side of the wall. The highest impulse on the wall is 30 kPa.s while at the bottom floor the impulse is slightly higher than that on the side wall.

Sensitivity Analysis: Effect of jet diameter

In the present study the smaller jet diameters 14 cm and 7 cm are considered according to CRGT and IGT failure scenarios, respectively. Similar to the results with larger break, the maximum pressure buildup and the maximum impulses are at the bottom of the side wall were obtained. The maximum impulse is around 17 kPa.s for the CRGT failure case (Figure 3.66a) and around 12 kPa.s for the IGT failure case (Figure 3.66b). Comparing the basic case above, the mass of liquid droplets in water in the case of 30-cm-diameter jet is 3 and 10 times more than those in the 14- and 7-cm-diameter jets, respectively. This is why the impulse on the wall for the 30-cm-diameter jet is 2 times and 2.5 times higher than 14- and 7-cm-diameter jets, respectively. In addition to liquid droplets mass, there may be other factors responsible for the intensity of steam explosion.

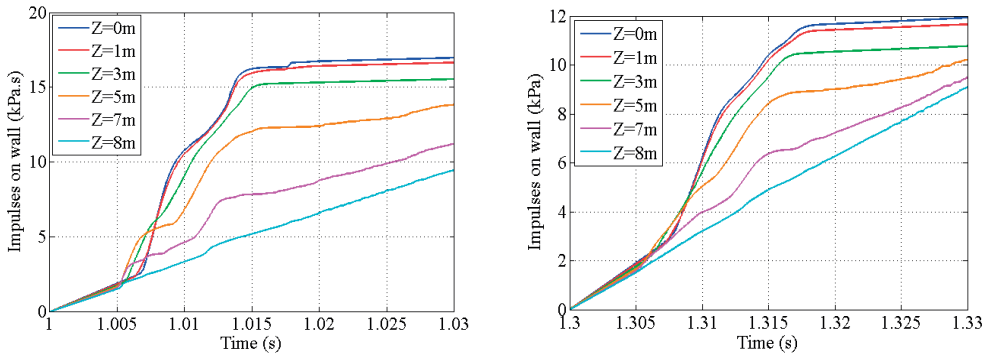

(a) CRGT failure case (b) IGT failure case

Figure 3.66. Maximum impulse on wall (CRGT case).

Effect of jet velocity: Three different velocities ranging from 5 to 7 m/s have been used in the calculations. The jet diameter of 14 cm is used for these calculations. Figure 3.67a shows the liquid droplets mass in contact with water which illustrates that the fragmentation rate increases with the jet velocity, resulting in a larger liquid droplets mass for a higher jet velocity. Thus, a higher jet velocity may enhance the conditions for steam explosion and its intensity. Figure 3.67b shows the maximum impulses on the wall, indicating that the impulses are higher for higher jet velocities.

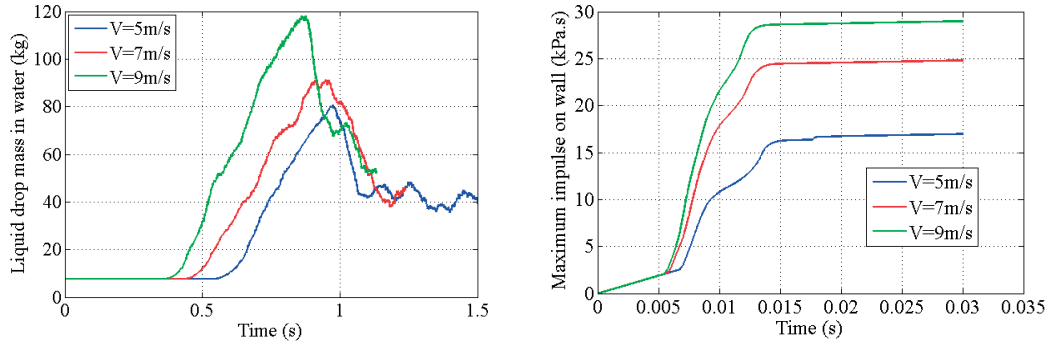

(a) (b)

Figure 3.67. a) Droplets mass for different jet velocities; b) Maximum impulses on the wall.

Effect of subcooling: the maximum impulses on wall are higher for the higher subcooling cases (Figure 3.68a). This is due to the fact that vapor generation is comparatively smaller in case of higher subcooling. Most of the heat from the melt primarily goes into heating the coolant till saturation and therefore the overall void generation is less. The effect of condensation is also higher in case of high subcooling. As a result, most of the liquid melt droplets are in low void region in case of higher subcooling, and therefore high intensity impulses are created.

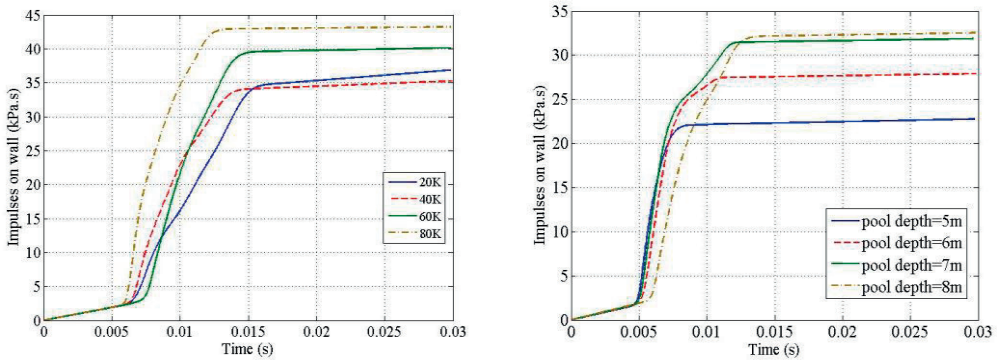

(a) (b)

Figure 3.68. a) Maximum impulses on the wall, for different subcooling; b) Maximum impulses on the wall, for different water pool depths.

Effect of water pool depth: Figure 3.68b shows the impulses on the wall for the cases with different water pool depths (5~8 *m*) in the flooded cavity. It illustrates that at a smaller pool depth the pressure peak near the wall is higher but at a larger pool depth there is additional reflections of the waves from the side walls and bottom which augment the area under the pressure curve. Thus, the case with a higher pool depth gives rise to a higher impulse which is the integration of pressure with time.

SEIM: Summary and outlook

The ex-vessel steam explosion impact map (SEIM) framework has been developed in order to connect melt ejection mode and pool parameters with steam explosion loads on the containment structures. Development of the SM relies on a database of solutions generated by a 1D FCI code TEXAS. Multidimensional fuel-coolant-interaction (FCI) codes are used to identify information which is missing in 1D FCI codes. However, 3D, 2D and even 1D FCI codes are too computationally expensive given large number of uncertain scenario and modeling parameters for direct application in the SEIM framework for uncertainty and risk analysis. Sensitivity study is used to identify the list of the influential input parameters that should be used in surrogate model development. A methodology for SM development has been proposed and applied. The ongoing work now concentrates on integration of the SM into the top level of the ROAAM+ framework. Application of 1D code requires an additional method for calculating loads on containment structures. There is also a need to resolve the link between ex-vessel coolability and steam explosion. Even a mild steam explosion might lead to degradation of debris bed cooling function. However, small size particles generated in steam explosion have little chance to settle on the bed as long as there is intensive coolant circulation in the pool.

The premixing and explosion calculations are carried out using the MC3D code, for the reference Nordic BWR. The main results show the higher energetics of steam explosion triggered before jet reaches half of a water pool. In the explosion phase, maximum pressure is attained at the bottom and the maximum impulse is at the bottom of the wall. Moreover, a parametric study is carried out using different jet diameters, jet velocity, subcoolings and water pool depth. From the results it is clear that these parameters have significant effect on the steam explosion loads on the cavity walls. As a next step, this work is being extended to a sensitivity analysis using additional parameters. Considering the most sensitive and eliminating the least sensitive parameters, an uncertainty study can be carried out to get the best estimate of the steam explosion loads on the cavity walls of the BWR plant.

3.6 Infrastructure development for high-temperature melt experiments

3.6.1. Motivation and approach

Phenomenologically, a steam explosion is associated with the fine fragmentation of the fuel which dramatically increases the fuel-coolant contact area. Rapid heat transfer between the two liquids then leads to the explosive vaporization of the coolant. The intense interaction occurs in such a short time-scale that pressure relief is unfeasible. As a result, the high pressure buildup generates a shock wave that imposes dynamic loading on the pool's surrounding structures. Experiments on steam explosions were performed at different scales, with varied fuel mass and coolant conditions. The large scale FCI experiments, including those using prototypic corium melts, were carried out in several laboratories worldwide to study the phenomena in FCI, namely pre-mixing and propagation. Although analysis and mechanistic modeling were attempted, and a basic understanding exists on FCI's premixing and propagation, diverse complex limiting mechanisms remains elusive.

While the large scale experiments provide an integrated picture of all phases of the explosion, the MISTEE was focused on the micro interactions in steam explosion energetics, which aims to characterize the fuel coolant interactions at micro-scale. Specifically, the MISTEE facility features a visualization system which enables a simultaneous high-speed photography and radiography, and thus provides vapor film dynamics as well as the melt fragmentation dynamics, which is vital to understand the governing mechanisms for steam explosions [15]. The MISTEE approach is suitable to address separate effects of the phenomena in order to elucidate the large-scale experimental results (such as the material effect). Nevertheless, the orientation would be mainly to consider limiting mechanisms rather than all possible effects.

Previously, the MISTEE experiments were carried out for corium simulant whose melting temperature is less than 1200 ^{o}C. To reduce the gap between the temperatures of the simulant and corium, the present work pertains to the development of experimental methodologies/infrastructure for fundamental research on steam explosion for a new corium simulant at high melting point, ultimately towards using prototypical corium in tests.

3.6.2. Infrastructure development

For the purpose of operation at high temperature, various designs of the facility (called MISTEE-HT) and feasibility studies of prototypes have been conducted for high-temperature melt preparation and molten droplet delivery. After a series of testing, qualification/calibration of the designs and prototypes which were necessary to develop the infrastructure with good instrumentation, the old furnace developed and utilized in the previous MISTEE experiments is replaced a completely new design made of concentric tubes.

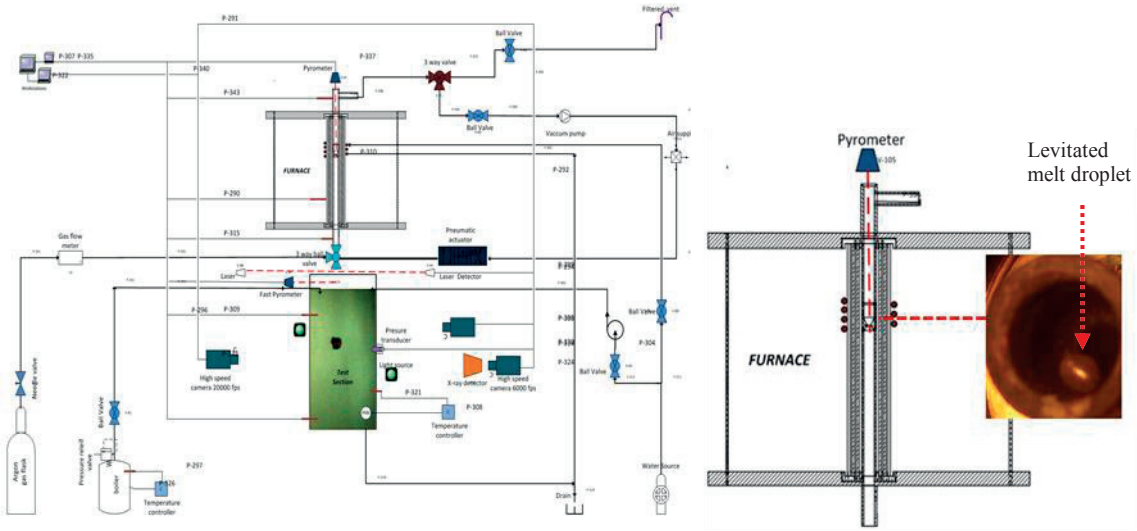

Figure 3.69. Schematic of the MISTEE-HT facility.

The new furnace consists of inductively heated tungsten crucible placed inside of multiple concentric zirconia tubes as thermal screens and hermetic quartz chamber blown by an inert gas. The set-up is designed to allow well-controlled high-temperature melt preparation, single-drop delivery at high temperature and precise

measurements. The schematic of the MISTEE-HT facility is shown in Figure 3.69. The molten mixture is levitated inside the crucible by exerting a force through upward inert gas stream to oppose the gravity. The melt retention (through the aerodynamic levitation) and discharge (by cutting off inert gas stream) is controlled by a quick-acting pneumatically controlled 3-way valve which is installed under the bottom of the crucible. So far the new design has enabled an operating temperature more than 2200 ^{o}C, and more improvement is under consideration towards elevated temperatures.

3.7 Preliminary Analysis Results using ROAAM+ Framework

3.7.1. Motivation Goals and Tasks

The goal is to illustrate comprehensive uncertainty analysis for identification and clarification of (i) main contributors to the uncertainty and risk; (ii) importance of the dependencies between different accident stages in different accident progression scenarios; (iii) the needs for further refinement of the knowledge and tools (models, experimental data, etc.)

We discuss key elements of the reverse analysis with the failure domain (FD) identification and forward analysis with estimation of failure probability (FP) for ex-vessel steam explosion and coolability.

3.7.2. Description of the framework

The surrogate models implemented in the framework and their role is detailed in the Table 3-9. Four techniques were used for implementation of the SMs: (i) mapping (based on mapping of the FM solution to a grid in the space of the input parameters); (ii) polynomial (scaling analysis and data fitting); (iii) physics based uses simplified modelling of the phenomena; (iv) Artificial Neural Networks (ANN is based on complex regression analysis). Failure criteria are determined for SEIM and DECO.

Table 3-9: Surrogate models of the ROAAM+ framework

SM	Type	Role
CORE	Mapping	Given timings of ADS and ECCS recovery provides time, composition and mass of core relocation and conditions in the lower drywall: pressure, pool temperature and depth
Vessel failure	Polynomial	Given mass and composition of the debris in the lower head computes timings of the IGT, CRGT and vessel failures and corresponding mass and composition of liquid melt available for release
Melt release	Physics based	Given timings and mode of lower head failure computes conditions of melt release, i.e. ablation of the breach, rate and duration of the release, thermal properties of the melt
SEIM	ANN	Given conditions of melt release and LDW characteristics, returns three explosion impulses and three values of containment capacity

DECO	Physics based	Given conditions of melt release and LDW characteristics, returns dryout heat flux and max debris bed heat flux

At given melt release conditions SEIM surrogate model estimates characterizes loads by mean and standard deviation of the explosion impulses predicted by TEXAS-V for different triggering times. Different confidence levels are used: mean value (in ~50% cases the impulse will be lower); mean plus standard deviation (in ~84% cases the impulse will be lower); mean plus two standard deviations (in ~98% cases the impulse will be lower). The SEIM failure domain is determined for three fragility limits: 20, 50 and 80 kPa·s. These roughly correspond to the order of magnitudes of fragility limits for non-reinforced hatch door, reinforced hatch door and reactor vessel pedestal respectively.

Current implementation of DECO is a combination of two surrogate models: (i) spreading of particles during sedimentation in the pool which estimates the slope angle of the formed debris bed; (ii) debris bed coolability (returning actual and critical heat flux for given debris bed configuration).

Forward and reverse analysis is currently performed by considering two distributions (optimistic and pessimistic) for the intangible parameters. Optimistic distribution is determined such that it decreases the probability of high loads. Pessimistic distribution decreases probability of low loads.

The failure domain is constructed in the space of the input parameters (input space) partitioned into a finite number of cells. Every cell is characterized by a unique combination of the input parameters ranges. The output of the SM is sampled in each cell (by varying deterministic and intangible parameters). The framework compares loads against capacity and renders every computed case to a failure or success. The number of "fail" and "success" cases is counted in each cell, weighted by corresponding probability density functions of deterministic and intangible parameters and normalized to provide conditional failure probability which is compared to the screening probability. The cells where conditional failure probability exceed screening level are grouped into a "failure domain" indicating conditions at which the mitigation strategy fails. For visualization green color identifies "safe" domain and red signifies the opposite. Note that all data presented here is obtained assuming 0.001 as the screening probability unless otherwise is explicitly stated.

3.7.3. Reverse Analysis for Steam Explosion using SEIM Surrogate Model

Three scenarios of melt release have been considered: 70, 140 and 300 mm jet diameters. System pressure was fixed to 3.5 bar. The failure domain is determined in the space of the SEIM input parameters: xlo – water pool depth, UPIN – melt jet release velocity; tlo – water pool temperature. The results for 70 mm jet diameter suggest that reaching to 50 kPa·s load, equivalent to failure of the reinforced hatch door and stronger containment structures is physically unreasonable with ~98% confidence regardless of the choice of the intangible parameters distributions. The failure domain for 20 kPa·s (non-reinforced hatch door) constitutes around 5-50% of the input space depending on the pessimistic/optimistic distributions of the intangible parameters (Figure 3.70).

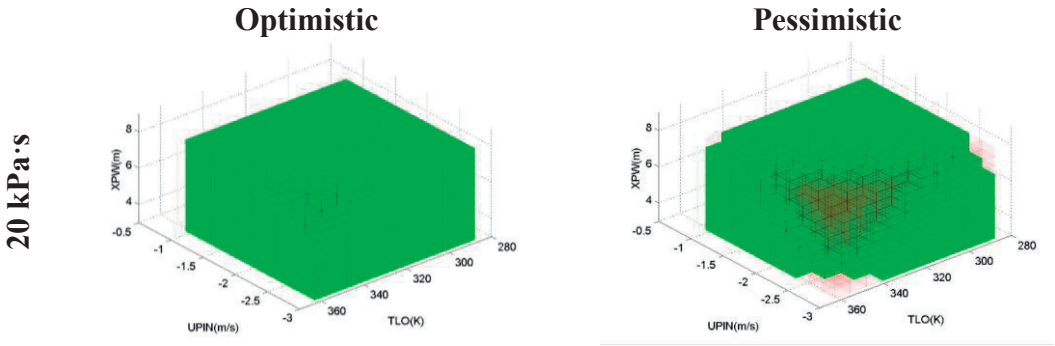

Figure 3.70. Failure domain for 20 kPa·s in the SEIM input space parameters. Jet diameter 70 mm; confidence 98%; screening probability 0.001.

Failure domains for 140 mm jet diameter are presented in Figure 3.71. The results are provided for ~98% confidence level and suggest that only in case of optimistic assumptions there is a small fraction of the input space (<10%) where probability of failure at 20 kPa·s is below physically unreasonable level. In case of pessimistic assumptions, this fraction is zero. The failure domain for 50 kPa·s criterion (reinforced door) occupies around 30-60% of the input space depending on the distributions of the intangible parameters. This indicates that transition form 70 to 140 mm jets is more important for the failure probability than different distributions of the intangible parameters. The failure domain at 80 kPa·s (pedestal) is more sensitive to the distribution of the intangible parameters (optimistic/pessimistic) and can change from almost 0 to about 20%. Thus obtaining knowledge on the distributions of the intangible parameters can help to reduce uncertainty in the pedestal failure in scenarios with 140 mm diameter jet. It is instructive to note that for 0.99 screening probability (almost imminent failure) the failure domain of the reinforced hatch door (Figure 3.72) still occupies about 20% of the input space.

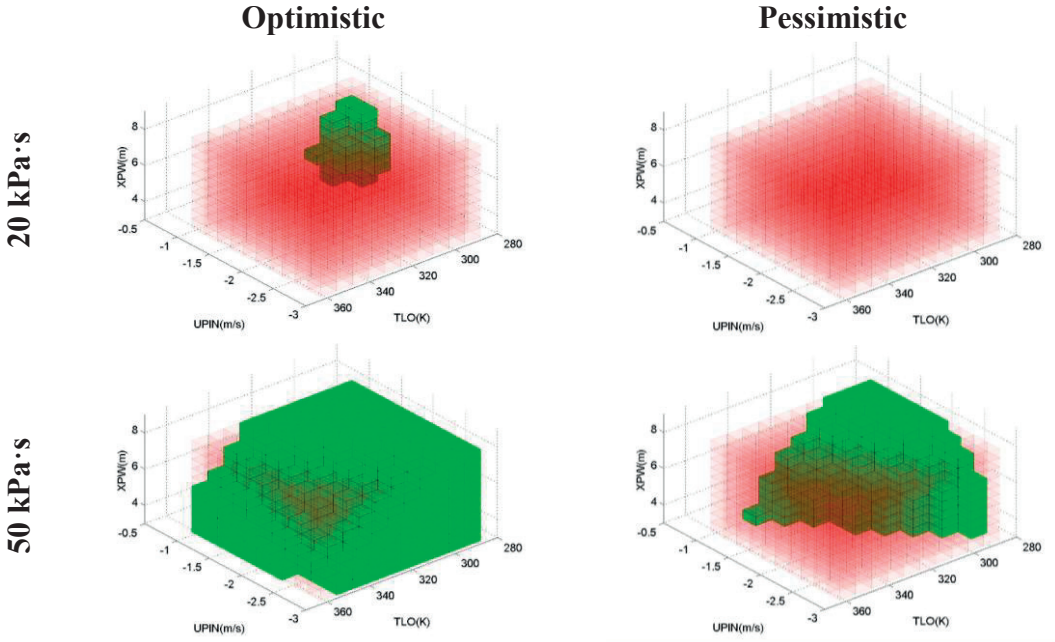

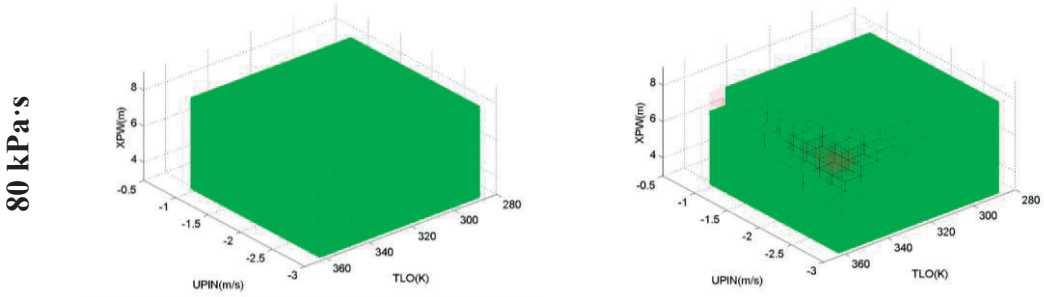

Figure 3.71. Failure domain in the SEIM input parameter space. Jet diameter 140 mm; confidence level 98%; screening probability 0.001.

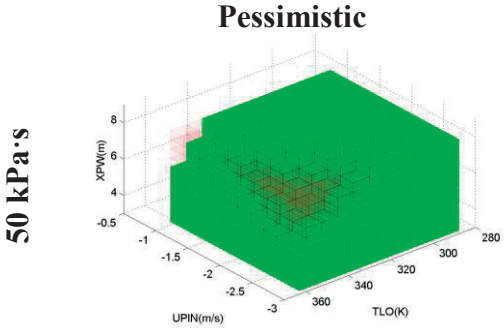

Figure 3.72. SEIM failure domain in terms of SEIM input space parameters. Jet diameter 140 mm; confidence level 98%; screening probability 0.99.

For 300 mm jet diameter, the failure of the pedestal is imminent for the major part of the input space regardless of the assumptions about distributions for the intangible parameters even with decreased (~84%) confidence level (Figure 3.73). This means that forward analysis using complete framework is necessary in order to assess whether such scenarios of melt release are possible.

In general the failure domain is growing if the jet diameter, water pool depth, or water temperature or the jet release velocity are increased. The major effect is still due to the jet diameter.

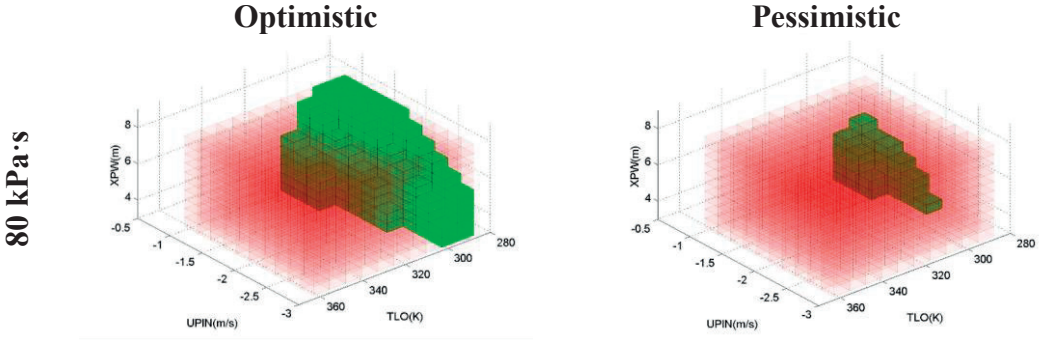

Figure 3.73. SEIM failure domain in terms of SEIM input space parameters. Jet diameter 300 mm; confidence level 84%; screening probability 0.99.

3.7.4. Reverse Analysis for Steam Explosion using the Whole Framework

The failure domain was determined in the space of CORE SM input parameters, i.e. ADS and ECCS activation times. The results are provided in the Figure 3.74.

Optimistic **Pessimistic**

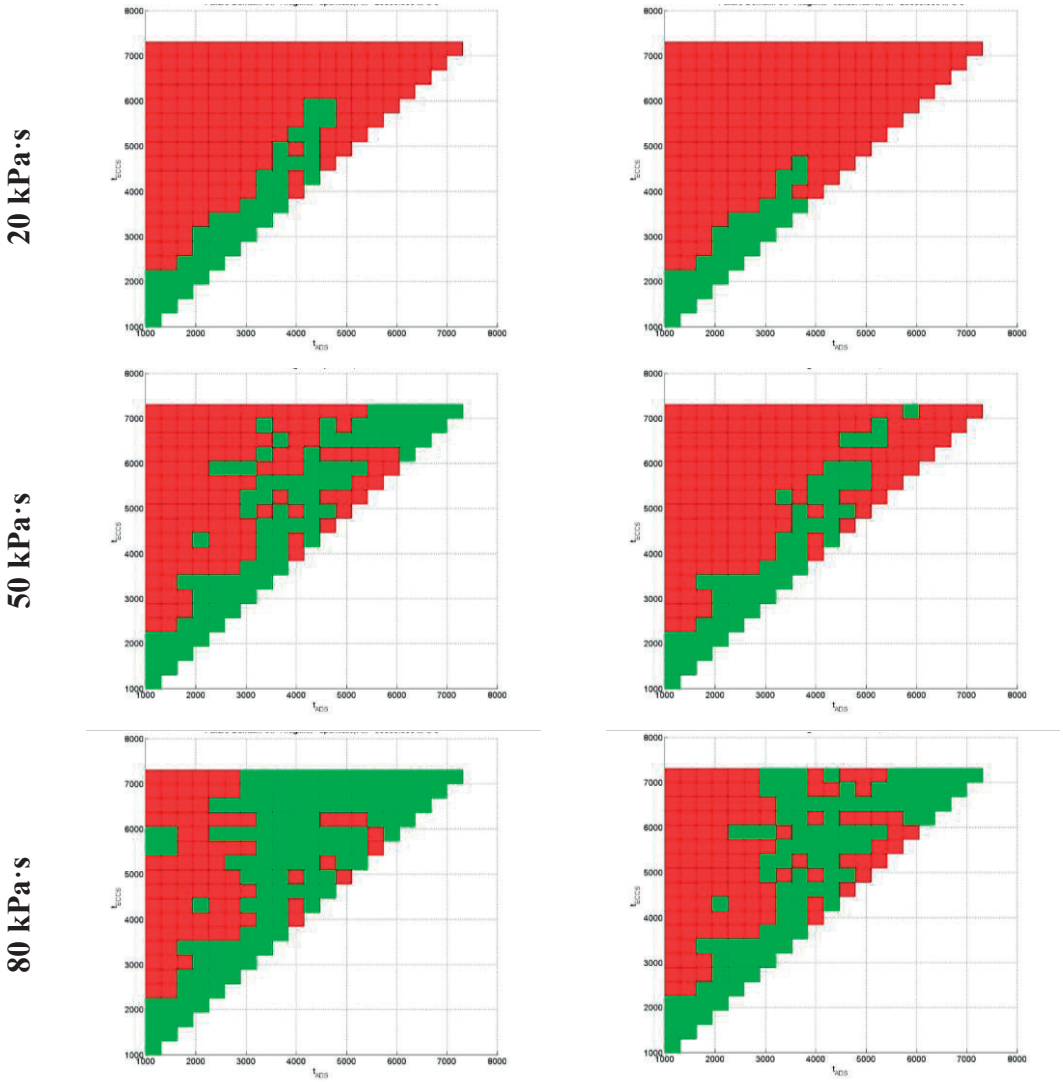

Figure 3.74. SEIM failure domain in terms of CORE input space parameters. Confidence level 98%; screening probability 0.001.

Clearly the failure domain is large and only a small safety domain exists. The first reason is that LDW conditions are dominated by deep (>6.6 m) water pools (see Figure 3.75). The water pool depth can be changed in the mitigation strategy. However, reduction of the pool depth will lead to increased risk of agglomeration. The second reason is scenarios of melt release are dominated by cases with melt velocities exceeding 5 m/s. This shifts the input space of SEIM parameters towards SEIM failure domain leaving only jet diameter as a parameter that defines the failure domain in the input space of CORE SM (Figure 3.76).

Water level, m Water temperature, K LDW pressure, Bar

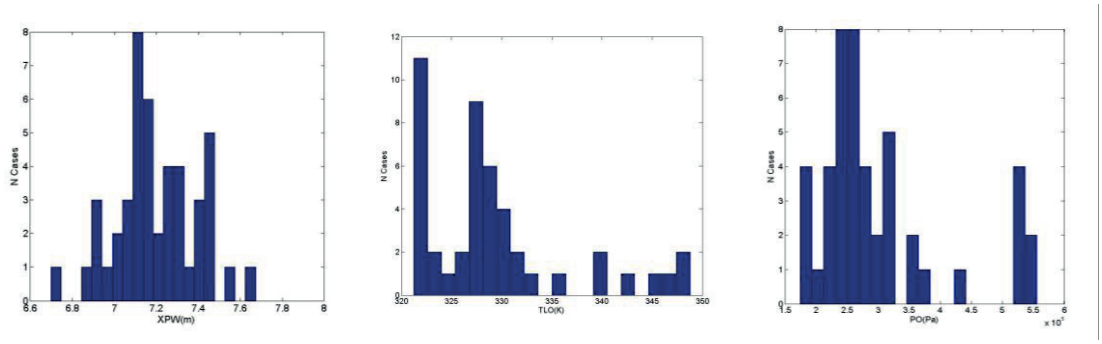

Figure 3.75. LDW characteristics.

Jet radius, m

Melt release velocity, m/s

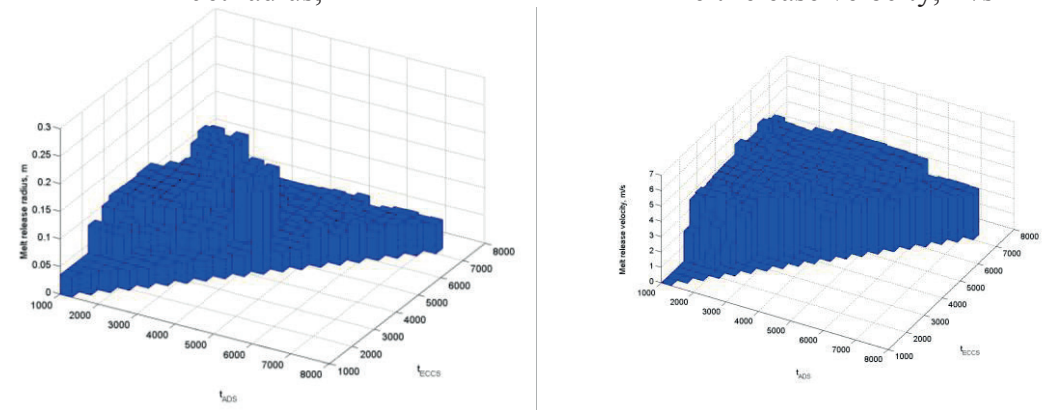

Figure 3.76. Melt jet release characteristics.

3.7.5. Revere and Forward analysis for Debris Bed Coolability with and without Consideration of the Particle Spreading in the Pool

The DECO failure probability was determined using following assumptions: constant debris bed porosity 40%; two distributions for the debris bed particles: "pessimistic" (1-1.5 mm) and optimistic (1-3 mm); and two ranges with uniform distribution of the initial debris bed angle: 0-35º, 0-20º. It was identified that failure domain is sensitive to the debris bed angle and particle size distribution (Figure 3.77).

A surrogate model for debris bed formation in the gradual melt release mode was developed and verified against DECOSIM simulations. Significant (1-2 order of magnitude) reduction in dryout probability was demonstrated (see Table 3-10 and Figure 3.77) when particle spreading in the process of debris bed formation is taken into account. Reason for that is demonstrated in Figure 3.78. Specifically, tall debris beds cannot be formed with small particles. DECO SM with integrated model of particle spreading predicts very small failure domain and failure probabilities. Further validation of particle spreading model is necessary against PDS-P experiments and DECOSIM simulations. In addition, extension of the debris bed formation model to subcooled water pool (delayed onset of boiling, less efficient particle spreading) and massive releases (short interaction time, collective effects due to high concentration of particles) are necessary.

Spreading **No Spreading**

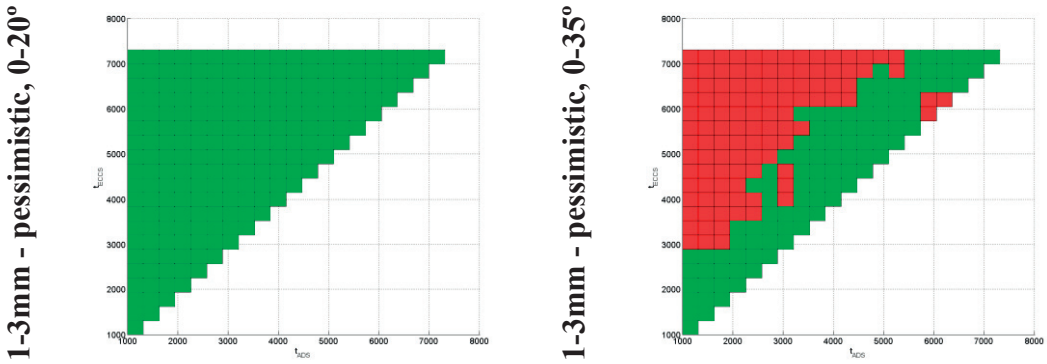

Figure 3.77. DECO failure domain in terms of CORE input space parameters. screening probability 0.001.

Table 3-10: Effect of particle convective spreading on the dryout probability

Slope angle distribution	Pool depth, [m]	Conditional dryout probability, [%]
Uniform, 0^o-35^o	8	19.3
Surrogate model	8	0.13
Uniform, 0^o-20^o	5	7.1
Surrogate model	5	0.33

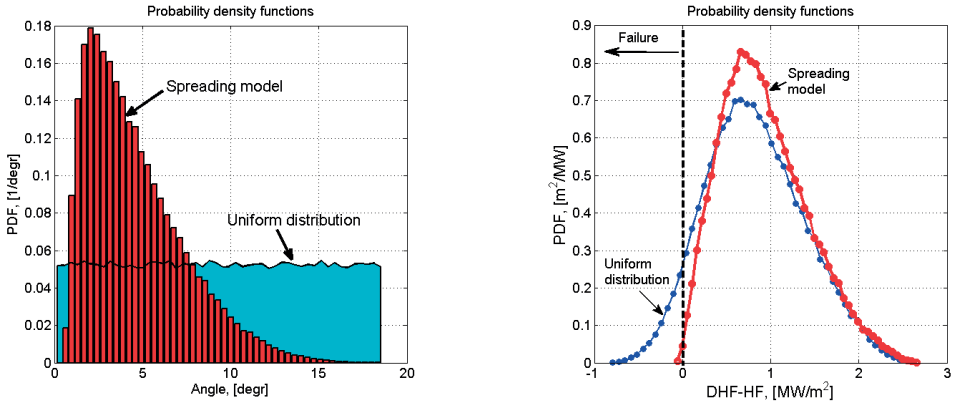

a b

Figure 3.78. Probability density functions of the debris slope angle (a) and capacity minus load for debris coolability (b).

3.7.6. Summary of the Preliminary Risk Analysis Results

The main purpose of the preliminary results is to demonstrate how ROAAM+ approach can help to understand the importance of different factors based on simultaneous consideration of scenario (aleatory) and epistemic (modeling) uncertainties. ROAAM+ framework can clarify importance of different (optimistic/pessimistic) assumptions and models from risk perspective and suggest areas were research efforts would provide most effective reduction of the uncertainty. For instance, steam explosion failure domain is determined mostly by two parameters of melt release: jet diameter and initial velocity. This means that a better knowledge is necessary for the vessel failure and melt release phenomena, such as remelting of multi-

component debris, filtration of liquid melt through porous debris bed and ablation/plugging of the vessel breach.

Debris bed coolability analysis demonstrated that convective spreading of particles in the pool is one of the most influential limiting mechanisms against formation of a tall non-coolable debris bed. Therefore, improved modelling of convective particle spreading in the pool is necessary to carry out robust risk analysis. Another important issue of the debris bed coolability, yet, to be included in the framework is debris agglomeration.

Current version of the surrogate models (SM) have different degrees of maturity, need further verification and validation based on the in-depth evaluation of the preliminary results. Quantitative preliminary data might change in the iterative process of model refinement. Further development of ROAAM+ framework and tools for post-processing and presenting results of the risk analysis are necessary.

3.8 Conclusions

This report presents research progress in APRI-8 towards the main goal of the APRI-KTH project, namely development of risk oriented accident analysis frameworks for quantifying conditional threats to containment integrity for a reference plant design of Nordic type BWRs.

Significant efforts have been undertaken in the Risk Evaluation and Synthesis (RES) task in order to develop deterministic and probabilistic elements of the Risk Oriented Accident Analysis Methodology (ROAAM) frameworks, which connect initial plant damage states and respective containment failure modes. We found that the challenges presented by the SAM strategy of the reference plant require further development of ROAAM. Therefore an extension of the original methodology called ROAAM+ was developed. The key element of ROAAM+ is a two-level coarse-fine adaptive iterative refinement process of the development of risk assessment framework and necessary knowledge. The top level of the risk assessment framework is based on computationally efficient surrogate models (SMs) that can be used for extensive sensitivity and uncertainty analysis in order to guide identification of the main sources of uncertainty, failure domains in the space of uncertain scenarios and modeling parameters, and ultimate risk assessment. The bottom layer of the framework consists of detailed computationally expensive full models (FMs) and databases of their solutions as well as experimental data and evidences, which are used in the development of the SMs.

Deterministic tools (experiments, full and surrogate models) have been developed for analysis of core degradation, vessel-failure and melt release modes, debris bed formation and coolability, ex-vessel steam explosion in order to enable accident progression analysis for the quantification of loads, fragilities and ultimately containment failure risks in different accident scenarios.

As a part of the Melt Ejection Mode (MEM) task, significant reduction of the uncertainty has been achieved in understanding of the potential impact of the accident scenarios and core degradation and relocation processes on the in-vessel accident progression and melt release modes. Further study is necessary for (i) completeness

of the database of the full model (MELCOR) analyses; and (ii) development and validation of the core degradation SM with respect to the relocated debris mass, composition and properties.

Vessel failure and melt ejection modes have been studied extensively in MEM with full models (PECM/ANSYS and DECOSIM) showing importance of the in-vessel debris bed properties and spatial configuration. The databases of the FMs solutions are currently processed in order to develop adequate SMs. Melt ejection mode requires further development of the full and surrogate models as well as experimental data on the phenomena of vessel breach ablation and plugging.

Debris bed formation and coolability map (DECO) task has provided the state-of-the-art knowledge and data by (i) development of the DECOSIM code for prediction of post-dryout coolability, subcooled water conditions, particulate debris spreading model; validation against COOLOCE test; (ii) development of surrogate models for prediction of non-flat debris bed dryout and maximum temperature in the dry zone; (iii) experimental and analytical investigation of the debris formation and agglomeration phenomena in large and small scale DEFOR tests, with full (VAPEX) and surrogate models; (iv) experimental (PDS-C tests) and analytical activities on particulate debris bed spreading and self-leveling phenomena; (v) experimental investigation of coolability in debris beds with different configurations in POMECO-FL and POMECO-HT facilities. Further work is necessary on development and validation of fully coupled debris bed formation and coolability map that will combine currently standalone surrogate models.

Significant progress has been achieved in steam explosion impact map (SEIM) in application to the plant accident analysis with FMs (1D TEXAS and 3D MC3D codes). Extensive sensitivity and uncertainty analysis has been carried out and key important parameters have been identified. The first version of a surrogate model is under development. Further detailed analysis is necessary in order to reduce uncertainties in the SM predictions.

Preliminary results obtained with ROAAM+ approach are instrumental for understand the importance of different factors based on simultaneous consideration of scenario (aleatory) and epistemic (modeling) uncertainties and using different (optimistic/pessimistic) assumptions. The results suggest areas were research efforts would provide most effective reduction of the uncertainty. For instance, steam explosion failure domain is determined mostly by two parameters of melt release: jet diameter and initial velocity. Debris bed coolability analysis demonstrated that convective spreading of particles in the pool is one of the most influential limiting mechanisms against formation of a tall non-coolable debris bed. Remaining work on development and validation of the ROAAM+ frameworks and models as well as experiments and application of the ROAAM+ to risk analysis of the reference plant is planned to be accomplished in APRI-9.

The experimental infrastructure project is focused on the development of the MISTEE-HT facility which can be used to perform fundamental investigation on steam explosion energetics of corium simulant with high melting temperature or prototypical corium. By testing various designs through proof of concept prototypes, a new furnace has been developed with a capability to melt metallic/oxidic

material whose melting point is 2200 ^{o}C and above, as well as good instrumentation and well-controlled mechanisms for melt preparation, and droplet levitation and delivery.

The unique experimental infrastructure and the team of reactor safety experts developed with APRI project support contributes to the retention and development of national expertise in analysis of severe accident phenomena and complex reactor safety issues specific to the Nordic plants. KTH participation in the international activities (EU, OECD, NKS, etc.) related to severe accident analysis brings the international efforts and knowledge to Nordic context.

3.9 References

[1] B.M. Adams, et al., "Dakota, a Multilevel Parallel Object-Oriented Framework for Design Optimization, Parameter Estimation, Uncertainty Quantification, and Sensitivity Analysis: Version 6.0 Reference Manual". Sandia National Laboratories, 2014.

[2] S. Basso, A. Konovalenko and P. Kudinov, "Development of scalable empirical closures for self-leveling of particulate debris bed," In Proceedings of ICAPP-2014, Charlotte NC, USA, April 6-9, Paper 14330, 2014.

[3] S. Basso, A. Konovalenko and P. Kudinov, "Sensitivity and Uncertainty Analysis for Predication of Particulate Debris Bed Self-Leveling in Prototypic SA conditions", In Proceedings of ICAPP-2014, Charlotte NC, USA, April 6-9, paper 14329, 2014.

[4] V. A. Bui and T.-N. Dinh, "Modeling of Heat Transfer in Heated-Generating Liquid Pools by an Effective Diffusivity-Convectivity Approach", Proceedings of 2nd European Thermal-Sciences Conference, Rome, Italy, 1365-1372, 1996.

[5] S. Cheng, H. Tagami, H. Yamano, T. Suzuki, Y. Tobita, B. Zhang, T. Marsumoto and K. Morita, "Evaluation of debris bed self-leveling behavior: A simple empirical approach and its validations", Annals of Nuclear Energy, vol. 63, 188, 2014.

[6] S. Cheng, H. Yamano, T. Suzuki, Y. Tobita, Y. Gonda, Y. Nakamura, B. Zhang, T. Matsumoto and K. Morita "An experimental investigation on self-leveling behavior of debris beds using gas-injection", Experimental Thermal and Fluid Science, vol. 48, 110, 2013.

[7] M.L. Corradini, "Users' manual for Texas-V: One dimensional transient fluid model for fuel-coolant interaction analysis", University of Wisconsin-Madison: Madison WI 53706, 2002.

[8] T.-N. Dinh, "Validation Data to Support Advanced Code Development", 15th International Topical Meeting on Nuclear Reactor Thermal Hydraulics, NURETH-14, paper 676, Pisa, Italy, May 2013.

[9] L. Fausett, "Fundamentals of neural networks architectures, algorithms, and applications." Prentice Hall International editions, Englewood Cliffs, NJ: Prentice Hall Internat. XVI, 461 S., 1994.

[10] S. Galushin, P. Kudinov, "An Approach to Grouping and Classification of Scenarios in Integrated Deterministic-Probabilistic Safety Analysis", PSAM12, Honolulu, USA, June 22-27, 2014

[11] I. Gallego-Marcos, W. Villanueva, P. Kudinov, "Possibility of Air Ingress into a BWR Containment during a LOCA in case of Activation of Contain-

ment Venting System," The 10th International Topical Meeting on Nuclear Thermal-Hydraulics, Operation and Safety (NUTHOS-10), Okinawa, Japan, December 14-18, Paper 1292, 2014.
[12] R.O. Gauntt, et al., MELCOR Computer Code Manuals. NUREG/CR-6119/SAND 2005-5713, US Nuclear Regulatory Commission, Washington, DC., 2014.
[13] D. Grishchenko, S. Basso, P. Kudinov, and S. Bechta, "Sensitivity Study of Steam Explosion Characteristics to Uncertain Input Parameters Using TEXAS-V Code," The 10th International Topical Meeting on Nuclear Thermal-Hydraulics, Operation and Safety (NUTHOS-10), Okinawa, Japan, December 14-18, Paper 1293, 2014.
[14] A. Goronovski, W. Villanueva, C.-T. Tran, P. Kudinov, "The Effect of Internal Pressure and Debris Bed Thermal Properties on BWR Vessel Lower Head Failure and Timing," Proceedings of the 15th International Topical Meeting on Nuclear Reactor Thermal Hydraulics (NURETH-15), Pisa, Italy, paper NURETH15-500, 2013.
[15] R. C. Hansson, L. Manickam, T. N. Dinh, "The effect of binary oxide materials on a single droplet vapor explosion triggering", 14th International Topical Meeting on Nuclear Reactor Thermalhydraulics, NURETH-14, Toronto, Canada, Sep 25-29, 2011.
[16] S. Kaplan and B. J. Garrick, "On the Quantitative Definition of Risk," Risk Analysis, 1: pp.11–27, 1981.
[17] L.A. Klinkova, V.I. Nikolaichik, N.V. Barkovskii and V.K. Fedotov, "Thermal Stability of Bi2O3", Russian journal of inorganic chemistry, vol 52, no:12, pp.1822-1829, 2007.
[18] A. Konovalenko, S. Basso and P. Kudinov, "Experimental and Analytical Study of the Particulate Debris Bed Self-leveling", The 9th International Topical Meeting on Nuclear Thermal-Hydraulics, Operation and Safety (NUTHOS-9), Paper N9P0305, Kaohsiung, Taiwan, September 9-13, 2012.
[19] A. Konovalenko, S. Basso, and P. Kudinov "Experiments and Characterization of the Two-Phase Flow Driven Particulate Debris Spreading in the Pool," The 10th International Topical Meeting on Nuclear Thermal-Hydraulics, Operation and Safety (NUTHOS-10), Okinawa, Japan, December 14-18, Paper 1257, 2014.
[20] P. Kudinov and M.V. Davydov, "Development and validation of conservative-mechanistic and best estimate approaches to quantifying mass fractions of agglomerated debris," Nuclear Engineering and Design, 262, pp. 452-461, 2013.
[21] P. Kudinov and M. Davydov, "Development of Surrogate Model for Prediction of Corium Debris Agglomeration," In Proceedings of ICAPP-2014, Charlotte, USA, April 6-9, Paper 14366, 2014.
[22] P. Kudinov, M. Davydov, G. Pohlner, M. Bürger, M. Buck, R. Meignen, "Validation of the FCI codes against DEFOR-A data on the mass fraction of agglomerated debris," 5th European Review Meeting on Severe Accident Research (ERMSAR-2012) Cologne (Germany), March 21-23, paper 2.09, 2012.
[23] P. Kudinov, S. Galushin, S. Yakush, W. Villanueva, V.-A. Phung, D. Grishchenko, N. Dinh, "A Framework for Assessment of Severe Accident Management Effectiveness in Nordic BWR Plants," Probabilistic Safety Assessment and Management PSAM 12, June, Honolulu, Hawaii, Paper 154, 2014.

[24] P. Kudinov, S. Galushin, A. Goronovski, and W. Villanueva, "RES1: Definition of a Reference Nordic BWR Plant Design and Plant Damage States for Application of ROAAM to Resolution of Severe Accident Issues," Research Report, The Eighth Framework of Accident Phenomena of Risk Importance (APRI-8), Division of Nuclear Power Safety, Royal Institute of Technology (KTH), Stockholm, Sweden, April 04, 2014.
[25] P. Kudinov, D. Grishchenko, A. Konovalenko, A. Karbojian, S. Bechta, "Investigation of Steam Explosion in Stratified Melt-Coolant Configuration," The 10th International Topical Meeting on Nuclear Thermal-Hydraulics, Operation and Safety (NUTHOS-10), Okinawa, Japan, December 14-18, Paper 1316, 2014.
[26] P. Kudinov, A. Karbojian, C.-T. Tran, W. Villanueva, "Experimental Data on Fraction of Agglomerated Debris Obtained in the DEFOR-A Melt-Coolant Interaction Tests with High Melting Temperature Simulant Materials," Nuclear Engineering and Design, 263, Pages 284-295, 2013.
[27] P. Kudinov, A. Karbojian, C.-T. Tran, W. Villanueva, "The DEFOR-A Experiment on Fraction of Agglomerated Debris as a Function of Water Pool Depth," The 8th International Topical Meeting on Nuclear Thermal-Hydraulics, Operation and Safety (NUTHOS-8), Shanghai, China, October 10-14, N8P0296, 2010.
[28] P. Kudinov, A. Karbojian, W. Ma, and T.-N. Dinh, "The DEFOR-S Experimental Study of Debris Formation with Corium Simulant Materials," Nuclear Technology, 170(1), pp. 219-230, 2010.
[29] P. Kudinov and V. Kudinova, "Cavity Formation in Particles Obtained from a High Temperature Oxidic Melt Jet Disintegration in Water," 7th International Conference on Multiphase Flow ICMF, Tampa, FL USA, May 30-June 4, 2010.
[30] P. Kudinov, Y. Vorobyev, M. Sánchez-Perea, C. Queral, G. Jiménez Varas, M. J. Rebollo, L. Mena, J. Gómez-Magán, "Integrated Deterministic-Probabilistic Safety Assessment Methodologies", Nuclear España, 347, Enero, pp.32-38, 2014.
[31] L. Li, A. Karbojian, P. Kudinov, W. Ma, "An Experimental Study on Dryout Heat Flux of Particulate Beds Packed with Irregular Particles," Proceedings of ICAPP 2011, Nice, France, May 2-5, Paper 11185, 2011.
[32] L.X. Li and W.M. Ma, "Experimental characterization of effective particle diameter of a packed bed with multi-diameter spheres", Nuclear Engineering and Design, 241: 1736-1745, 2011.
[33] L.X. Li and W.M. Ma, "Experimental investigations on friction laws and dryout heat flux of particulate bed packed with multi-size spheres or irregular particles", Proc. of ICONE19, May 16-19, Chiba, Japan, 2011.
[34] L.X. Li and W.M. Ma, "An experimental study on the effective particle diameter of a packed bed with non-spherical particles", Transport in Porous Media, 89: 35-48, 2011.
[35] L.X. Li, S. Thakre and W.M. Ma, "An experimental study on two-phase flow and coolability of particulate beds packed with multi-size particles", Proc. of NURETH-14, Toronto, Canada, September 25-29, 2011.
[36] L.X. Li, S.J. Gong and W.M. Ma, "An experimental study on two-phase flow regime and pressure drop in a particulate bed packed with multi-diameter particles", Nuclear Technology, 177(1), pp 107-118, 2012.

[37] L.X. Li and W.M. Ma, “Toward quantification of debris bed coolability in corium risk assessment”, Transactions of ANS Winter Meeting, Washington DC, Oct. 30-Nov. 3, 2011.
[38] L.X. Li, W. M. Ma, S. Thakre, “An experimental study on pressure drop and dryout heat flux of two-phase flow in packed beds of multi-sized and irregular particles”, Nuclear Engineering and Design, 242: 369-378, 2012.
[39] W.-K. Liao, Y. Liu, and A. Choudhary, “A Grid-based Clustering Algorithm using Adaptive Mesh Refinement,” In proceedings of the 7thWorkshop on Mining Scientific and Engineering Datasets, 2004.
[40] W.M. Ma, “Prediction of dryout heat flux of volumetrically heated particulate beds packed with multi-size particles”, Proc. NURETH-14, Toronto, Canada, September 25-29, 2011.
[41] W.M. Ma, L.X. Li and A. Karbojian, “An experimental study on coolability of volumetrically heated particulate beds of prototypical characteristics”, Proc. of NUTHOS-8, Shanghai, China, October 10-14, 2010.
[42] D. Magallon, “SERENA Programme Reactor exercise: Synthesis of calculations”. 20p., 2012.
[43] D. Magallon and I. Huhtiniemi, Corium melt quenching tests at low pressure and subcooled water in FARO. Nuclear Engineering and Design, vol. 204, pp. 369-376, 2001.
[44] L. Manickam, P. Kudinov, and Bechta, S., “On the influence of water subcooling and melt jet parameters on debris formation,” 15th International Topical Meeting on Nuclear Reactor Thermalhydraulics, NURETH-15, Pisa, Italy, May 12-15, 2013.
[45] R. Meignen, and S. Picchi, “MC3D V3.7p1 User’s guide”, IRSN. 139 p., 2012.
[46] J. L. Rempe, S. A. Chavez, G. L. Thinnes, C. M. Allison, G. E. Korth, R. J. Witt, J. J. Sienicki, S. K. Wang, L. A. Stickler, C. H. Heath, and S. D. Snow, Light Water Reactor Lower Head Failure, Report NUREG/CR-5642, Idaho Falls, 1993.
[47] C.J. Roy, W.L. Oberkampf, “A comprehensive framework for verification, validation, and uncertainty quantification in scientific computing”. Computer Methods in Applied Mechanics and Engineering, 200(25–28), pp.2131-2144, 2011.
[48] A. Saltelli, et al., “Sensitivity analysis in practice: a guide to assessing scientific models,” John Wiley & Sons Inc. 219p., 2004.
[49] W. Schmidt, “Interfacial drag of two-phase flow in porous media,” Int. J. Multiphase Flow, 33, pp. 638-657, 2007.
[50] B.R. Sehgal, A. Jasiulevicius, and M. Konovalikhin, “Investigation of the potential for in-Vessel melt retention in the lower head of a BWR by cooling through the control rod guide tubes”. 2004, SKI. p. 45.
[51] J.H. Song, et al., “The effect of corium composition and interaction vessel geometry on the prototypic steam explosion”. Annals of Nuclear Energy, 33(17–18): p. 1437-1451, 2006.
[52] U. Steinberner and H. H. Reineke, “Turbulent Buoyancy Convection Heat Transfer with Internal Heat Sources,” Proceedings of the 6th International Heat Transfer Conference, Toronto, Canada, 2, 305-310, 1978.

[53] Strålsäkerhetsmyndigheten, “APRI-7 Accident Phenomena of Risk Importance”, En lägesrapport om forskningen inom svåra havarier under åren 2009-2011, rapportnummer 2012:12, ISSN:2000-0456, 2012.
[54] E. Takasuo, S. Holmström, T. Kinnunen, and P.H. Pankakoski, “The COOLOCE experiments investigating the dryout power in debris beds of heap-like and cylindrical geometries,” Nuclear Engineering and Design 250, p. 687-700, 2012.
[55] E. Takasuo, T. Kinnunen, T. Lehtikuusi, and S. Holmström, “COOLOCE coolability experiments with a cylindrical debris bed and lateral flooding: COOLOCE-10,” Research Report VTT-R-00463-13. Espoo, 19 p., 2013.
[56] E. Takasuo, T. Kinnunen, T. Lehtikuusi, and S. Holmström, “COOLOCE-12 debris bed coolability experiment: cone on a cylindrical base,” Research Report VTT-R-07967-13. Espoo, 21 p., 2013.
[57] T.G. Theofanous, “On Proper Formulation of Safety Goals and Assessment of Safety Margins for Rare and High-Consequence Hazards,” Reliability Engineering and System Safety, 54, pp.243-257, 1996.
[58] T.G. Theofanous and T.-N. Dinh, “Integration of multiphase Science and Technology with Risk management In Nuclear Power reactors: Application of the Risk-Oriented Accident Analysis Methodology to the Economic, Simplified Boiling Water Reactor Design,” Multiphase Science and Technology, V20(2), pp.81-211, 2008.
[59] C.T. Tran, P. Kudinov, and T. N. Dinh, “An approach to numerical simulation and analysis of molten corium coolability in a BWR lower head,” Nuclear Engineering and Design, 240, 2148–2159, 2010.
[60] C.-T. Tran and T.-N. Dinh, “The Effective Convectivity Model for Simulation of Melt Pool Heat Transfer in a Light Water Reactor Pressure Vessel Lower Head. Part I: Physical Processes, Modeling and Model Implementation,” Progress in Nuclear Energy, 51, pp. 849-859, 2009.
[61] C.-T. Tran and T.-N. Dinh, “The effective convectivity model for simulation of melt pool heat transfer in a light water reactor lower head. Part II: Model assessment and application”, J. Progress in Nuclear Energy, 51, 860-871, 2009.
[62] V. X. Tung, V. K. Dhir, “A hydrodynamic model for two-phase flow through porous media,” Int. J. Multiphase Flow, 14(1), pp. 47–65, 1988.
[63] User’s Manual ANSYS 12.1, ANSYS®, Inc., 2009.
[64] W. Villanueva, C. T. Tran, and P. Kudinov, “Coupled thermo-mechanical creep analysis for boiling water reactor pressure vessel lower head,” Nuclear Engineering and Design, 240, 146-153, 2012.
[65] Y. Vorobyov and T.N. Dinh. A Genetic Algorithm-Based Approach to Dynamic PRA Simulation. in ANS PSA Topical Meeting - Challenges to PSA during the nuclear renaissance. Knoxville, Tennessee: American Nuclear Society, LaGrange Park, IL, 2008.
[66] Yu.B. Vorobyev, P. Kudinov, M. Jeltsov, K. Kööp, T.V.K. Nhat, “Application of information technologies (genetic algorithms, neural networks, parallel calculations) in safety analysis of Nuclear Power Plants,” Proceedings of the Institute for System Programming of RAS, 26(2), pp.137-158, 2014.
[67] Y. Vorobyev, P. Kudinov, “Development of Methodology for Identification of Failure Domains with GA-DPSA,” 11th International Probabilistic Safety Assessment and Management Conference (PSAM) and The Annual European

Safety and Reliability (ERSEL) Conference, Scandic Marina Congress Center, Helsinki, Finland, 25–29 June, 2012.
[68] S.E. Yakush and P. Kudinov, "A Model for Prediction of Maximum Post-Dryout Temperature in Decay-Heated Debris Bed," Proceedings of the 22nd International Conference on Nuclear Engineering, ICONE22, July 7-11, Prague, Czech Republic, ICONE22-31214, 2014.
[69] S. Yakush, P. Kudinov, "Effects of water pool subcooling on the debris bed spreading by coolant flow", Proceedings of the 11th International Conference on Advanced Nuclear Power Plants (ICAPP 2011), Nice, France, paper 11416, 14 pp., 2011.
[70] S.E. Yakush and P. Kudinov, "A Model for Prediction of Maximum Post-Dryout Temperature in Decay-Heated Debris Bed," Proceedings of the 2014 22nd International Conference on Nuclear Engineering, ICONE22, July 7-11, Prague, Czech Republic, ICONE22-31214, 2014.
[71] S. Yakush and P. Kudinov, "Simulation of Ex-Vessel Debris Bed Formation and Coolability in a LWR Severe Accident," Proceedings of ISAMM-2009, Böttstein, Switzerland, October 26 - 28, 2009.
[72] S.E. Yakush, P. Kudinov, T.-N. Dinh, "Multiscale simulations of self-organization in the formation and coolability of corium debris bed", Proceedings of the 13th International Topical Meeting on Nuclear Reactor Thermal-Hydraulics (NURETH-13), Kanazawa City, Japan, paper N13P1143, 13 pp., 2009.
[73] S.E. Yakush, P. Kudinov, W. Villanueva, S. Basso, "In-Vessel Debris Bed Coolability and its Influence on the Vessel Failure" Proceedings of the 15th International Topical Meeting on Nuclear Reactor Thermal Hydraulics (NURETH-15), Pisa, Italy, paper NURETH15-464, 2013.
[74] S. Yakush, N. Lubchenko, and P. Kudinov, "Risk-Informed Approach to Debris Bed Coolability Issue", Proceedings of the 20th International Conference on Nuclear Engineering (ICONE-20), Anaheim, CA, USA, July 30 - August 3, Paper 55186, 2012.
[75] S.E. Yakush, N.T. Lubchenko, and P. Kudinov, "Surrogate Models for Debris Bed Dryout," 15th International Topical Meeting on Nuclear Reactor Thermal Hydraulics, NURETH 15, May 12 - 17, Pisa, Italy, Paper 278, 2013.
[76] S.E. Yakush, N.T. Lubchenko, and P. Kudinov, "Risk and Uncertainty Quantification in Debris Bed Coolability," 15th International Topical Meeting on Nuclear Reactor Thermal Hydraulics, NURETH 15, May 12 - 17, Pisa, Italy, Paper 283, 2013.
[77] S. E. Yakush, W. Villanueva, S. Basso and Kudinov P., "Simulation of In-vessel Debris Bed Coolability and Remelting," The 10th International Topical Meeting on Nuclear Thermal-Hydraulics, Operation and Safety (NUTHOS-10), Okinawa, Japan, December 14-18, Paper 1281, 2014.
[78] B. Zhang, T. Harada., D. Hirahara, T. Matsumoto, K. Morita., K. Fukuda, H. Yamano, T. Suzuki, Y. Tobita, "Self-Leveling Onset Criteria in Debris Beds", J. Nuclear Science and Technology, 47(4), pp.384-395, 2010.
[79] B. Zhang, T. Harada., D. Hirahara, T. Matsumoto, K. Morita., K. Fukuda, H. Yamano, T. Suzuki, Y. Tobita, "Experimental investigation on self-leveling behavior in debris beds", Nuclear Engineering and Design, vol. 241(1), pp.366-377, 2011.

4. CHALMERS RESEARCH ON SEVERE NUCLEAR ACCIDENTS

4.1 Iodine chemistry

4.1.1. Background

The release of volatile iodine species such as elemental iodine is a major concern in case of the occurrence of a nuclear accident. Iodine is a biological active compound that gets concentrated in the thyroid gland which takes part in the regulation of the metabolism. Therefore, a main goal in severe accident management is to limit the releases in order to reduce the risk to health. Iodine has a rather high fission yield from the fuel. The fission yield for iodine from uranium dioxide fuel reaches from 0.1233 % (A = 127) to 6.751 % (A = 138) for thermal neutron induced fission [1]. The fission products with the highest yield in the fission of U-235 are the iodine isotopes I-132 to I-141 (Fig. 4.1). I-131 is produced with a yield of 2.368 %, I-129 with a yield of 0.74 %. I-127, I-129 and I-131 occur with an isotopic ratio of 6.06 for I-129/I-127 and 3.82 for I-131/I-129 [1].

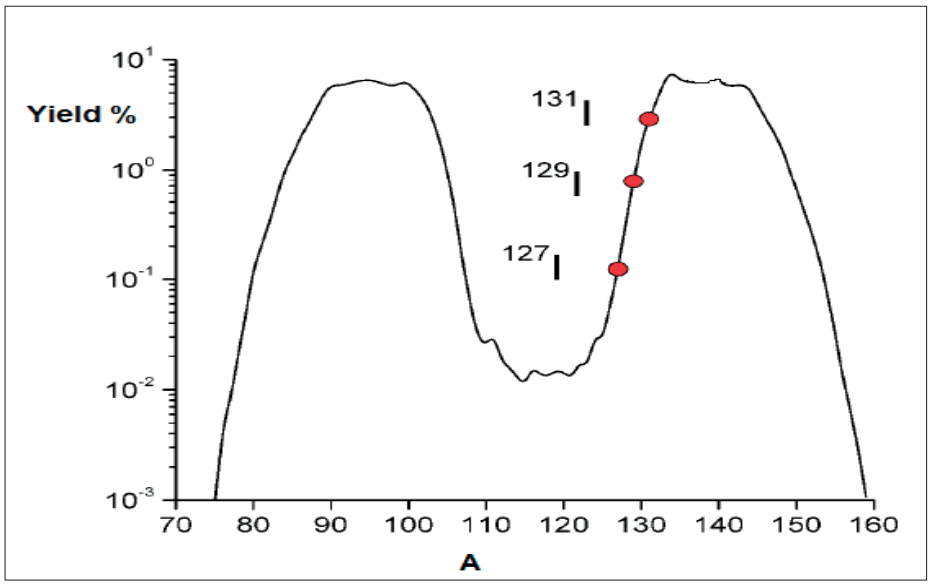

Fig. 4.1: Fission yields of iodine isotopes from U-235 fission with thermal neutrons [1].

Most of the generated iodine isotopes have a very short half-life and are of interest short after an occurred nuclear accident and are therefore mainly relevant for the worker on-site (Table 4.1).One important task in severe accident management on the volatile iodine source term is to delay the release of volatile iodine species to avoid the release of the short-lived isotopes ($T_{1/2}$ < 24 hours) which are generated with a high yield. The shorter lived iodine isotopes have in addition higher β-energies and thus have a higher potential to cause harm to the small thyroid gland (see Table 4.1). The iodine isotope considered to be most harmful after a severe accident is I-131 with its half-life of 8.04 days [3]. Its half-life is short enough to have a high specific activity and long enough to persist for a significant time after a severe accident [3].

Table 4.1. Half-lifes and β - energies of selected iodine isotopes [2].

Nuclide	Half-life	β - energy [keV]
I-127	Stable	-
I-128	25.0 min	2119.0
I-129	$1.57 \cdot 10^7$ years	193.8
I-130m	9.0 min	2989.0
I-130	12.36 h	2949.0
I-131	8.02 days	970.8
I-132	2.3 h	3577.0
I-133	20.8 h	1770.6
I-134	52.5 min	4170.0
I-135	6.57 h	2648.1
I-136	83.4 s	6930.0
I-137	24.5 s	5880.0
I-138	6.49 s	7820.0
I-139	2.28 s	6806.0
I-140	0.86 s	8760.0
I-141	0.43 s	7800.0

Iodine is a very reactive element with many available oxidation states and therefore the chemistry of it is very complex. The processes include the partitioning of multiple chemical forms of iodine between the aqueous and gaseous phase, chemical reactions in each phase, radiolysis and hydrolysis behavior, as well as interactions with surfaces. In both the aqueous and gaseous phase cesium iodide aerosols and elemental iodine that have been released from uranium dioxide fuel can be converted into different inorganic and organic compounds of iodine. These new compounds may have different transport properties to the forms of iodine which were originally released from the fuel. Such substances are iodine oxide aerosols and organic iodides. In the containments of nuclear power plants (NPP) several sources of large amounts of organic materials that can contribute to the formation of organic iodides can be found. Most of the concrete and metal surfaces in the containment of a NPP are protected with an organic based paint coating or a zinc primer coating. Additionally a lot of cable materials are required for the operation of the technical and electronic equipment. Another significant organic source could be the leakage of pump oil from damaged equipment. Under the conditions of a severe accident those organic materials can decompose and react with e.g. elemental iodine to form organic iodides. Iodine oxide aerosols can be e.g. formed in gas phase reactions of elemental iodine and organic iodides with ozone [4-8].

There are different approaches to be considered to reduce the release of volatile iodine species into the environment once the species have entered the containment gas phase. The currently used approaches are solid absorbents (or filters) and/or

using a liquid filled (wet) scrubber to decontaminate the gases after they left the containment before they are released into the environment. Already many nuclear power plants have a cascade of charcoal filter materials installed to filter off volatile iodine species but their chemical composition is not suitable to sufficiently retain volatile organic iodides. Another approach is to modify currently used paint formulations with additives to retain volatile iodine species already in the containment. Some of the iodine will be in form of cesium iodide and therefore will cause a long time contamination of e.g. painted surfaces which needs to be taken care off in order to keep the radiation exposure in the containment low.

4.1.2. Aim

Within this research project attempts were made to identify the species of iodine that can be formed in a light water reactor (LWR) containment and to predict the relative amounts of different chemical forms of iodine that could be released into the environment. Elemental iodine, cesium iodide and iodine oxide aerosols, as well as organic iodides and their behavior in the containment were studied within the following projects:

1. Formation of organic iodides from organic materials in the containment
2. Experimental investigation and mathematical modeling of the partitioning and hydrolysis behavior of organic iodides between the gaseous and aqueous phase in the containment
3. Interactions of gaseous iodine species with paint coatings in comparison to metal surfaces
4. The effects of impurities, radiolysis products and other fission products on the volatile iodine source term
5. Development of modified paint formulations to reduce the volatile iodine source term
6. Investigation of solid-bed and wet-filter systems to improve the retention of organic iodides
7. Methods to chemically clean-up contaminated surfaces, soil and waste water considering the effects of sea water

The performed work is/will be published in scientific journals. The projects will be summarized in a dissertation which will be a follow up of the Licentiate thesis (Sept. 2012) [8] and be presented in April 2015 at Chalmers University of Technology.

4.1.3. Methodology

1. Formation of organic iodides from organic materials in the containment

Different types of paint products used in Swedish and foreign nuclear installations have been studied with respect to their composition and degradation behavior under the conditions of a severe nuclear accident within APRI 7. The main focus during APRI-7 was on bisphenol-A based Teknopox Aqua VA ^{TM} epoxy paint and the zinc primer Interzinc 315^{TM} [9]. Samples of other floor and wall paints were provided from Ringhals NPP. Paint films from Barsebäck NPP were also discussed in APRI-

7 [9]. Due to the participation in the Behavior of Iodine Projects BIP-1 and BIP-2 additionally paint samples of the in German nuclear installations used GEHOPON EW 10 epoxy paint [9] could be studied within APRI-8. The studied paint coupons are the same as used in the German iodine test facility called THAI. The paint was provided by GRS and AREVA located in Germany. Cable materials were provided from Ringhals NPP, Barsebäck NPP and Forsmark NPP. PVC, Hypalon ™ /Lipalon™, Rockbestos™ and Eupen™ cable coatings were characterized in the studies both within APRI-7 and APRI-8. Samples of new and used pump oil (Q8 Verdi 46) were provided by the Ringhals NPP and were analyzed within APRI-8.

I-131 for radioactive experiments was obtained from Sahlgrenska University hospital in Göteborg.

The newly obtained paint and cable plastics were first characterized as described in APRI-7 using (pyro-) infrared (IR), pyro- /headspace – gas chromatography mass spectroscopy (GC-MS), single electron microscopy coupled with energy dispersive X-ray spectroscopy (SEM-EDX) and thermo gravimetric analysis (TGA) on both non-irradiated and irradiated samples. Furthermore the degradation behavior of the polymer in Teknopox Aqua VA paint was investigated using viscosity measurements of the irradiated and then in tetrahydrofuran (THF) dissolved polymer and gel permeation chromatography (GPC). Pyrolysis GC-MS was performed at Manchester University (UK). The GPC studies were performed at Reading University (UK).

Selected organics identified in the newly studied organic materials were mixed with stable elemental iodine and the formation of organic iodides was studied under gamma irradiation with head-space GC-MS alike performed in APRI 7 [10, 11]. The experiments have been extended for oil, n-hexene and the plasticizer dibutyl phthalate and dioctyl phthalate. For comparison high linear energy transfer (LET) radiation experiments using alpha radiation at the University of California – Irvine are currently performed. The solvent samples containing elemental iodine were sealed both under anaerobic and aerobic conditions in Quartz ampoules with a B-10 containing compound as alpha source and were irradiated in the UC Irvine 250 kW TRIGA Mark I reactor. The type and amount of organic iodides formed are measured as previously described using GC-MS.

2. *Experimental investigation and mathematical modeling of the partitioning and hydrolysis behavior of organic iodides between the gaseous and aqueous phase in the containment*

The work on the partitioning and hydrolysis behavior of methyl iodide and other selected organic iodides which was performed within APRI-7 using the FOMICAG (Facility for Online Measurements of I-131 labelled species Concentrations in Aqueous and Gaseous Phase) facility [12] was continued and extended within APRI-8 using other organic iodides than methyl iodide. I-131 labelled ethyl, isopropyl, butyl, allyl, benzyl iodide, as well as iodoanisol and chloroiodomethane were studied at pH 4, 7, 10 and at room temperature (21 ± 0.5 °C), 50 °C, 70 °C, 150 °C. The organic iodides were synthesized as described earlier [13]. The effects of gamma irradiation on the speciation of iodine were investigated using solvent extraction experiments [14]. In the solvent extraction experiments the hydrolysis behavior of different organic iodides and their degradation to form elemental iodine was studied. In the first step of the solvent extraction procedure the organic phase of

a 1 ml aliquot was extracted with 1 ml of octane to separate all organic iodides and elemental iodine from other inorganic aqueous species such as iodide ions. In the second step the organic phase was extracted with a 1 M KI solution to separate all elemental iodine from the organic phase. Each phase was measured using liquid scintillation counting (LSC). Furthermore the hydrolysis of organic iodides was studied in non-radioactive experiments using on-line pH measurements and measurements with an iodide selective electrode. The behavior of the organic iodides in distilled water, lake and sea water was studied for comparison.

Attempts are currently made to model the experimental data involving gamma irradiation and compare the obtained partitioning coefficient for organic iodides such as methyl iodide with the ones obtained without presence of gamma irradiation and therefore without consideration of the elemental iodine formation.

3. *Interactions of gaseous iodine species with paint coatings in comparison to metal surfaces*

The studies on the sorption behavior of gaseous iodine species on dry surfaces reported in APRI-7 were continued. The gas phase absorption of iodine oxide and cesium iodide aerosols was studied in collaboration with VTT Technical Research Centre of Finland [4, 5] mainly within APRI 7. The sorption of different I-131 radiolabelled organic iodide model substances representing different classes of organic iodides that could be formed were primarily investigated within APRI-8. Methyl, ethyl, ispopropyl, butyl, allyl and benzyl iodide, as well as chloroiodomethane and iodoanisol were compared. In the studies the ageing effects of heat and irradiation on the paint films was compared for different paint products. The radiolysis of gaseous organic iodides was studied for different dose rates. The conversion yield of the organic iodides into elemental iodine was monitored by the measurement of the amount of iodine that reacted with a copper wire present in the vial containing the organic iodide.

The sorption in gaseous phase was performed by gaseous exposure of the species on paint films. All species have a high enough vapor pressure that they distribute and transfer at room temperature into gaseous phase. The gaseous loading and revaporisation was monitored using a high purity germanium (HPGe) detector. The released amounts of elemental iodine were collected on a copper wire which selectively reacts with elemental iodine. The wire was also measured with the HPGe detector. The speciation of iodine on the paint surfaces was compared to the speciation on metal surfaces using X-ray photoelectron spectroscopy (XPS) measurements.

4. *The effects of impurities, radiolysis products and other fission products on the volatile iodine source term*

The effects of pre-exposure of paint surfaces with ozone, chlorine and hydrogen chloride were investigated, as well as the effects of those gases and carbon monoxide and nitrogen dioxide on the revaporisation rate after exposure to the iodine species. Furthermore the effects of ruthenium tetroxide deposition were evaluated under both heat and gamma irradiation exposure. Ozone, chlorine and nitrogen chloride from commercial gas cylinders from Air Liquid were used. Ozone was made from an oxygen cylinder and an ozone generator. Ruthenium tetroxide was prepared in an oxidation reaction from a mixture of ruthenium chloride, potassium carbonate,

potassium persulphate and a Ru-103 radiotracer [15]. All depositions were performed with gaseous species. To determine the relevance of carbon monoxide and gaseous chlorine species released from cable and paint materials pyrolysis-FTIR measurements were performed at Manchester University (UK).

In the aqueous loading experiments the effects of pH and chlorine content, as well as other anions such as nitrate and sulphate ions were studied with and without presence of gamma irradiation. The change of the iodine concentration in aqueous phase was measured using LSC, whereas the uptake in the paint films was studied with an HPGe detector. The change of the iodine speciation was determined in non-radioactive experiments using either an iodide selective electrode or an ion chromatograph. In radioactive experiments solvent extraction experiments were used as described under 2.to determine the change of the iodine speciation under different conditions. The ability of organic impurities (paint solvents) in distilled and sea water to react with organic iodides and iodide ions was studied with and without presence of gamma irradiation. The change of the speciation of the added iodine species was determined using the solvent extraction procedure described under 2. [14].

5. *Development of modified paint formulations to reduce the volatile iodine source term*

Different paint formulations have been prepared using Teknopox Aqua VA epoxy paint as basis. The additives were selected based on their reported or in previous experiments tested ability to react with elemental iodine and or organic iodides. 1-10 mass % of the wet paint ingredients were immersed into the paint matrix before it was cured as usual. Then the dried and in some cases additionally thermally aged paint films were exposed to elemental iodine or organic iodides and compared to the loading of a regular paint without the additive and the zinc primer Interzinc 315^{TM}. One very promising approach was the addition of pyrene. Pyrene was in a synthesis linked to an amine group in order to make it bind to the resin and therefore less subjected to leaching processes. The exposed paint films were irradiated, heated and immersed in cold and hot water to test their retain ability for the iodine species under severe accident conditions. The change of iodine activity on the surfaces was measured with an HPGe detector and with an autoradiograph. The autoradiograph was used to determine in case of solid additives if they dissolved evenly in the paint matrix and if not if areas of higher absorption can be linked to the added absorber.

6. *Investigation of solid-bed and wet-filter systems to improve the retention of organic iodides*

Many of the currently used solid filters are non-treated or amine or silver impregnated charcoal filters. Many of the used filter materials have not been tested for organic iodides or organic iodides other than elemental iodine. In the different tests a range of different volatile organic iodides were found. Different solid absorber materials were compared for their applicability to retain those species. DABCO (1,4-diazabicyclo[2.2.2]octane) also known as triethylene diamine (TEDA) loaded charcoals containing different amounts of DABCO were synthesized and compared to silver, zinc, iron and copper loaded silica`s that were synthesized, as well as a silver loaded zeolite and different types of clays and pigments were tested. The ab-

sorbers were weight out and the microscopic surface area was measured with a BET (Brunauer-Emmett-Teller) surface absorption instrument. The different absorber materials were exposed to the gaseous iodine species and their reactivity was evaluated using an HPGe detector. Then the exposed absorber were heated, irradiated or exposed to humidity in order to determine the retainability under accident conditions. The measurements were repeated for irradiated absorber materials and compared to the same materials which were exposed to elemental iodine.

A range of different organic additives, from a diverse range of classes of organic compounds, were screened for use in the wet-scrubber systems which is currently used in Sweden during APRI-7. A promising approach using trialkyl phosphines (triibutyl, trihexyl and trioctyl phosphine) as additives was successfully tested in solvent extraction experiments and experiments in the FOMICAG facility [12] to remove a range of organic iodides identified in the paint and cable degradation studies. In the FOMICAG facility the contact area between the gaseous and aqeous phase is more or less in steady state. In flow-through experiments the removal of gaseous organic iodides was studied under conditions similar to a Venturi scrubber. Gaseous organic iodides were carried by an nitrogen or air gas stream (2 l/min) through gas-wash bottles (200 ml) containing the conventional thiosulfate solution and/or the trialkyl phosphines. Cascades of several bottles were set up in order to determine the efficiency for a short residence time. Methyl, ethyl, isopropyl, butyl, benzyl, allyl iodide and chloroiodomethane were compared with elemental iodine. In solvent extraction experiments the liquid alkyl iodides were added to the trialkyl phosphine layer and extracted with water containing different impurities or the inorganic scrubbing solution (0.015 M $Na_2S_2O_3$). The amount of I-131 was recorded in aqueous and organic phase using LSC measurements. The irradiation and oxygen stability of the phosphines has been investigated using GC-MS. Surface tension between water-air, thiosulfate-air and the interfacial tension between phosphine-air was measured with the Du Nouy ring method.

The phosphines required are freely available as semi bulk chemicals from CYTEC. The trialkyl phosphines are already used in industry for the synthesis of ionic liquids and used as part of a catalytic system used for hydroformylation (reaction of alkenes {olefins} with hydrogen and carbon monoxide). The trialkyl phosphines can be supplied as liquids in metal cylinders under inert conditions. While organic phosphorus compounds have a reputation for being highly toxic, this reputation is undeserved. The trialkyl phosphines lack the structural features required to function as fast acting neurotoxins (acetylcholinase inhibitors). It is noteworthy that the fact that a substance is a neurotoxin does not render it a particularly bad poison, ethanol (ordinary alcohol) is an example of a neurotoxin.

7. Methods to chemically clean-up contaminated surfaces, soil and waste water considering the effects of sea water

Iodine is not a big concern in terms of long-lived contamination issues on surfaces as most of the iodine will be released as short-lived radioisotopes. However, a fraction will be released as cesium iodide. Different approaches to reduce contaminated waste water were investigated to decontaminate e.g. CsI contaminated surfaces. Conventional detergents like water, oxalic acid, citric acid, sodium hydroxide were compared to the use of an ionic liquid [16]. An highly water soluble ionic liquid

consisting of a deep eutectic of magnesium chloride and choline chloride was synthesized.

On fresh and aged paint films and zinc primer surfaces was I-131 in form of I^- and Cs-137 as Cs^+ applied as liquids to the surfaces. The surfaces were dried and then either immersed in the conventional cleaning solutions or a thin film of the ionic liquid was applied. The used ionic liquid was that viscous that it was like a gel on the paint surfaces. After different time intervals the ionic liquid was washed off with water and the remaining cesium and iodine activity on the surfaces was determined using an HPGe detector. The results were compared to the cleaning effect in the same time interval of the conventional solutions. The experiments were repeated for surfaces exposed to gaseous iodine species. In separate experiments the sorption behavior of I, Cs, Sr, Co and Eu ions from different aqueous phases (distilled water, lake water, sea water) was studied on different types of clay, soil, paint and pigments [16]. The change of the aqueous nuclide activity was followed by LSC measurements of the liquid phase.

4.1.4. Results

The results section contains selected and as most relevant considered results of the experiments described in 4.1.3.

1. Formation of organic iodides from organic materials in the containment

The measurements revealed that both paints and cable plastics not only consist of a polymer that contains functional groups that could react with iodine, but also volatile solvents similar to those that can be found in oil. It was proven that the solvents, as well as the plasticizer in cable materials (dibutyl phthalate, dioctyl phthalate) can form significant amounts of organic iodides whereas the pure polymers formed both less amounts but also a smaller variety of organic iodides. Aliphatic double bonds like those found in hexene showed to consume elemental iodine. It was also found that the organic iodides formed were not limited to be methyl iodide. Other organic iodides such as volatile ethyl-, isopropyl- and butyl- iodide were also found to be formed in large quantities. Longer chained organic iodides were detected as well but in lower amounts.

When organic materials are subjected to very high irradiation doses (1 MGy) in addition aromatic organic iodides such as iodo-benzene were found. The studies of paint samples aged under real and simulated conditions showed that the formation of organic iodides was lower from the thermally aged samples. However, even after aging for twenty years under real reactor conditions the paint film from the Barsebäck NPP still contained detectable amounts of residual solvents that could form organic iodides during an accident. Organic iodide formation was also observed in both the aqueous and the gaseous phase. Irradiation studies of a bisphenol-A based polymer used in epoxy paints such as Teknopox Aqua VA™ revealed that the polymer is predominantly shortened when the polymer receives a dose of 100 kGy or more. Polymers have a good thermal stability as they formed no organic iodides below 400 °C. Therefore, it is assumed that the polymers are not the main sources of organic iodides, rather the paint solvents as those are much more mobile and radiation sensitive.

2. *Experimental investigation and mathematical modeling of the partitioning and hydrolysis behavior of organic iodides between the gaseous and aqueous phase*

It was found that in aqueous phases of low pH (pH < 2) very low amounts of elemental iodine are formed without gamma irradiation present during the hydrolysis of organic iodides. However, in presence of gamma irradiation also in distilled water significant amounts of aqueous elemental iodine were formed and some elemental iodine became airborne. This was detected after exposure to a low dose as of 100 Gy (Fig. 4.2).

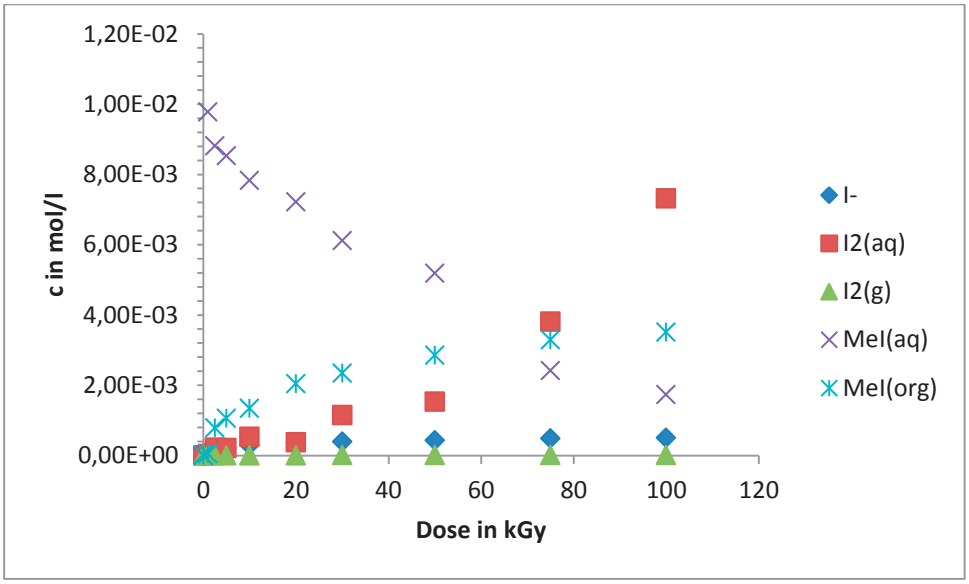

Fig.4.2: Hydrolysis of 10^{-2} M methyl iodide (MeI(org)) at 43 °C in distilled water (dose rate = 10 kGy/h).

In sea water the formation of elemental iodine was found to be much larger under the same conditions. The formation of elemental iodine for a low pH region and under gamma irradiation has been implemented into the mathematic model that has been presented previously [8]. The basic OIPHA model (**O**rganic **i**odide **p**artitioning and **h**ydrolysis **a**nalysis model) contains the partitioning of gaseous organic iodides between aqueous and gaseous phase (1), as well as the hydrolysis of the organic iodides into iodide ions (2).

$$MI(g) \underset{k_2}{\overset{k_1}{\leftrightarrow}} MI(aq) \qquad (1)$$

$$MI(aq) \xrightarrow{k_h} MOH + I^- + H^+ \qquad (2)$$

For hydrolysis reactions in acidic media the oxidation of iodide ions needs to be taken into consideration (3) in the extended model, while under gamma irradiation additionally radical reactions that can lead to the formation of elemental iodine have to be considered, (4) and (5).

$$4H^+ + 4\,I^- + O_2 \rightarrow 2\,H_2O + 2I_2 \qquad (3)$$

$$HO\cdot + I^- \rightarrow HOI^- \rightarrow OH^- + I\cdot \quad (4)$$

$$2\,I\cdot \rightarrow I_2 \quad (5)$$

These reactions have been summarized in the following set of chemical equations (6) to be considered for the determination of the partitioning coefficient for organic iodides.

$$2RI(g) \underset{k_1}{\overset{k2}{\leftrightarrow}} 2RI(aq) + 2H_2O(aq) \overset{k_h}{\rightarrow} 2ROH(aq) + 2I^-(aq) + 2H^+(aq) \underset{k_3}{\overset{k_4}{\leftrightarrow}}$$
$$I_2(aq) + 2H^+(aq) + 2ROH(aq) \underset{k_5}{\overset{k_6}{\leftrightarrow}} I_2(g) + 2H^+(aq) + 2ROH(aq) \quad (6)$$

Furthermore in order to make a realistic estimate of the gaseous organic iodide concentration it would need to be furthermore implemented the radiolysis of organic iodides in gaseous phase and the interactions on metallic and organic surfaces, as well as the impact of impurities like chlorine in aqueous phase.

3. *Interactions of gaseous iodine species with paint coatings in comparison to metal surfaces*

Gamma irradiation at different dose rates revealed that gamma irradiation leads to the radiolysis of the organic iodides. As a result of the radiolysis the organic iodides are rather quickly converted into elemental iodine (Fig. 4.3). In absence of light or gamma irradiation no elemental iodine was found to be formed and no decomposition of the organic iodide was observed.

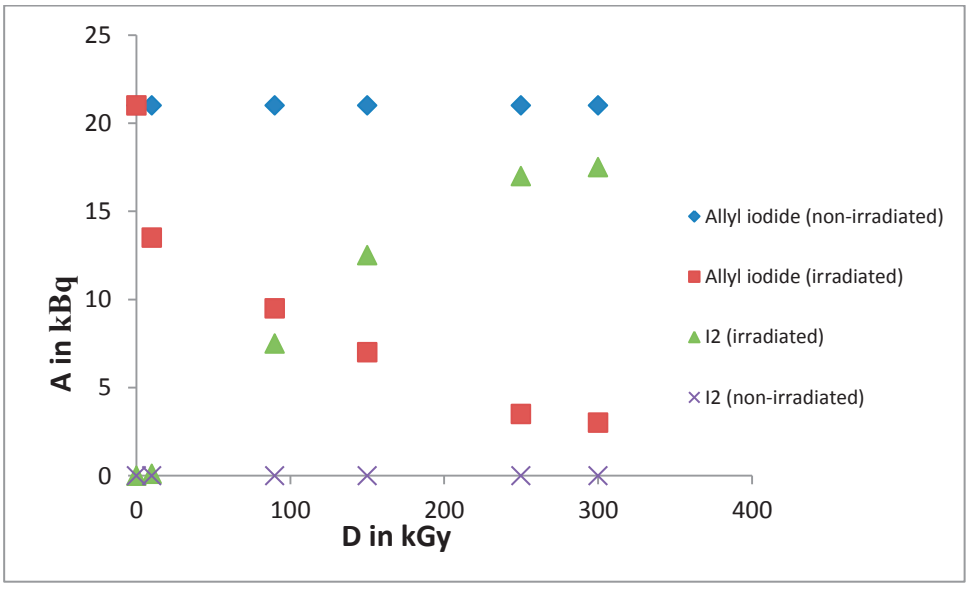

Fig. 4.3: Radiolysis of organic iodides (here: allyl iodide; dose rate 3 kGy/h, 43 °C) (In the non-irradiated case the D value corresponds to the time interval the sample would have been exposed to irradiation at the gamma cell temperature T = 43 °C).

The absorption behavior for organic iodides was found to be different to the one of elemental iodine. While the elemental iodine loading was found to be steadily increasing until reaching saturation in the paint film (Fig. 4.4), the methyl iodide

amount on the surface reached a maximum and then decreased again indicating that the chemical conversion and uptake of the organic iodides is slower than the revaporisation of physisorbed species (Fig. 4.5). As the amounts decrease over time decomposition of the organic iodide on the surface or revaporisation is assumed.

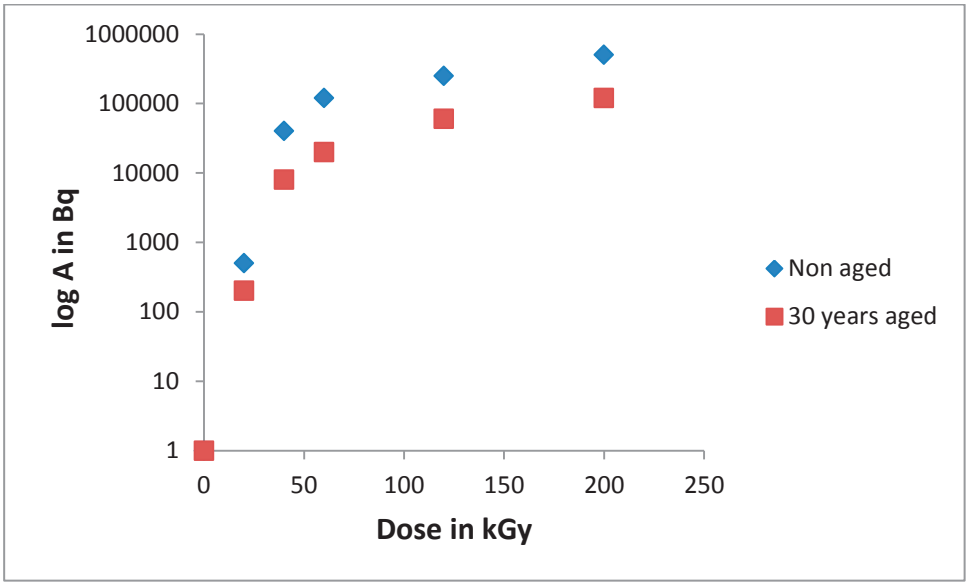

Fig. 4.4: Elemental iodine loading in dependence of the paint age (Teknopox Aqua VA epoxy paint).

The loading behavior of any gaseous iodine species was found to depend on the age of paint, the temperature and in presence of gamma irradiation on the dose rate (Fig.4.4-6) [17, 18]. In all cases the chemisorption of iodine oxides was found to be significantly lower than the sorption of organic iodides.

The iodine loading ability of a non-aged paint film was found to be higher than from a thermally aged paint film supporting the theory that the paint solvents play a main role in the iodine uptake ability. SEM-EDX measurements confirmed these results (Table 2). With increasing ageing the carbon content on the paint surface degraded.

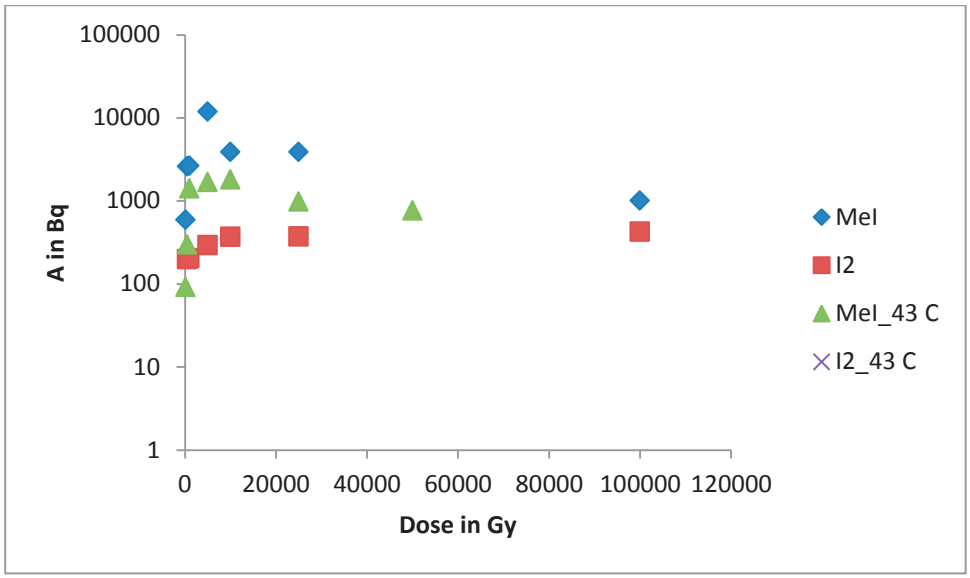

Fig. 4.5: MeI loading with and without gamma irradiation and the corresponding elemental iodine formation on non-aged Teknopox Aqua VA epoxy paint films. (In the non-irradiated case the dose value corresponds to the time interval the sample would have been exposed to irradiation at the gamma cell temperature T = 43 °C).

Table 4.3: SEM-EDX comparison of the main composition of non-aged, irradiation aged paint (dose rate = 10 kGy/h) and heat treated Teknopox Aqua VA epoxy paint.

w %	Non-aged	Irr. (50°C, 7200 kGy)	Heat aged (1 month, 100 °C)
C	66.6	60.6	55.4
O	28.6	35.2	40.5
Ti	3.8	4.2	4.7

The presence of gamma irradiation during the iodine loading process showed to decrease the absorption rate on the paint surface (Fig. 4.6).

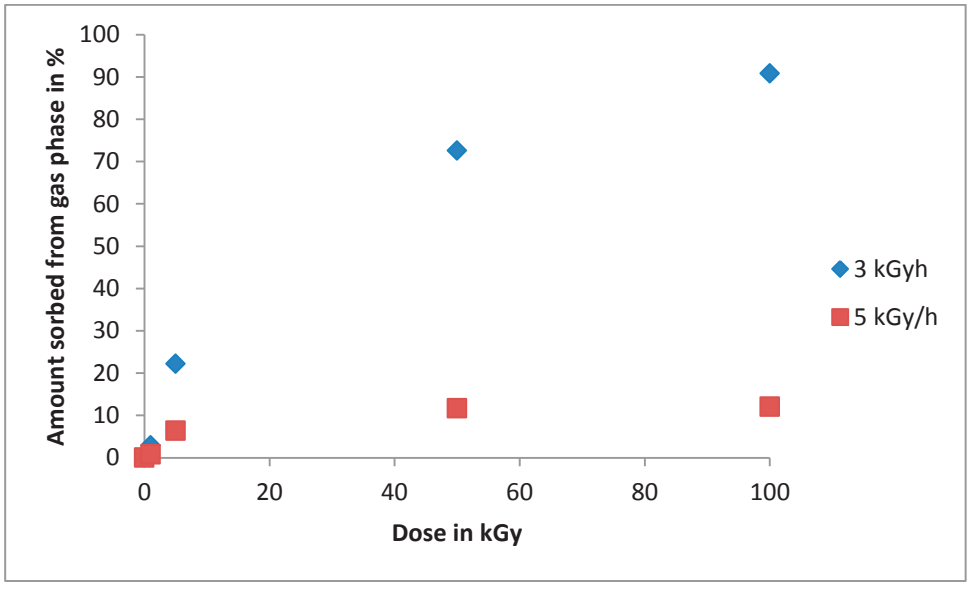

Fig. 4.6: Dose rate effect on the elemental iodine loading non-aged Teknopox Aqua VA epoxy paint.

The speciation of the iodine species on paint films is difficult to determine with XPS. An attempt to measure iodine species with EXAFS (Extended X-ray Absorption Fine Structure) at Stanford University failed. While the speciation of elemental iodine on metal surfaces was easily determined to be metal iodides or metal hydroxides, a range of iodooxy anions were determined on painted surfaces, as well as elemental iodine in the performed XPS measurements. The paint samples which had been aged for a long time, which have low water content, showed that a large fraction of the iodine which was exposed as organic iodine was in fact on the surface found to be converted into elemental iodine. The humidity causes the hydrolysis of especially the aerosols leading to the formation of iodine containing acids.

The revaporisation studies revealed that the age of the paint film effects the revaporisation of all studied volatile iodine species [17, 18]. With increasing thermal treatment the retention ability of the paint films decreased (Fig. 4.7). The release of the iodine species was found to be mainly dominated from the temperature effect but an additional dose effect could be determined (Fig. 4.8). The Gehopon paint coupons showed a slightly higher release of organics compared to Teknopox paint under absence of gamma irradiation. However, when gamma irradiation was present the releases are similar indicating that the Teknopox paint could contain more radiation sensitive functional groups. At higher dose rates the release rates were found to be increased (Fig. 4.8).

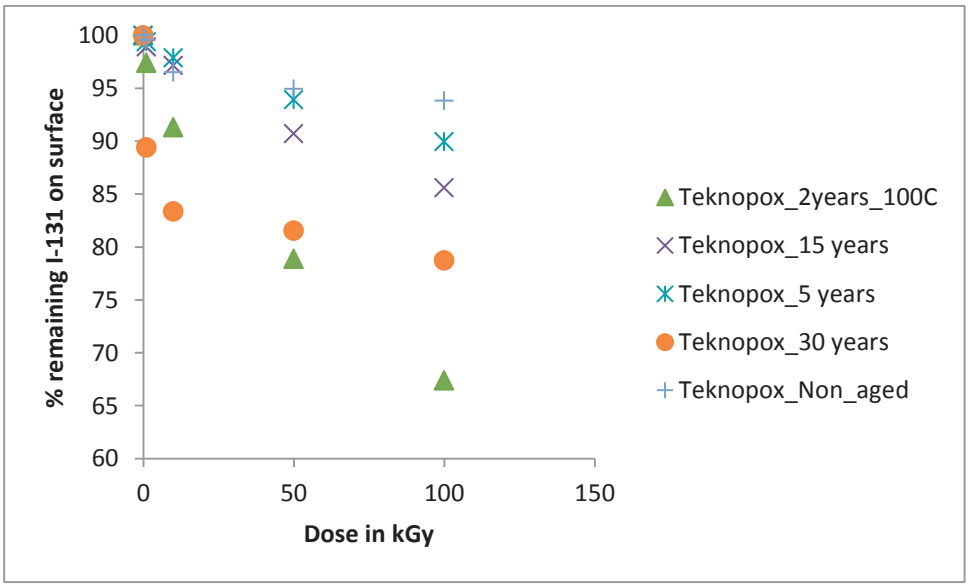

Fig. 4.7: Paint age effect and presence of gamma irradiation on the revaporisation of elemental iodine.

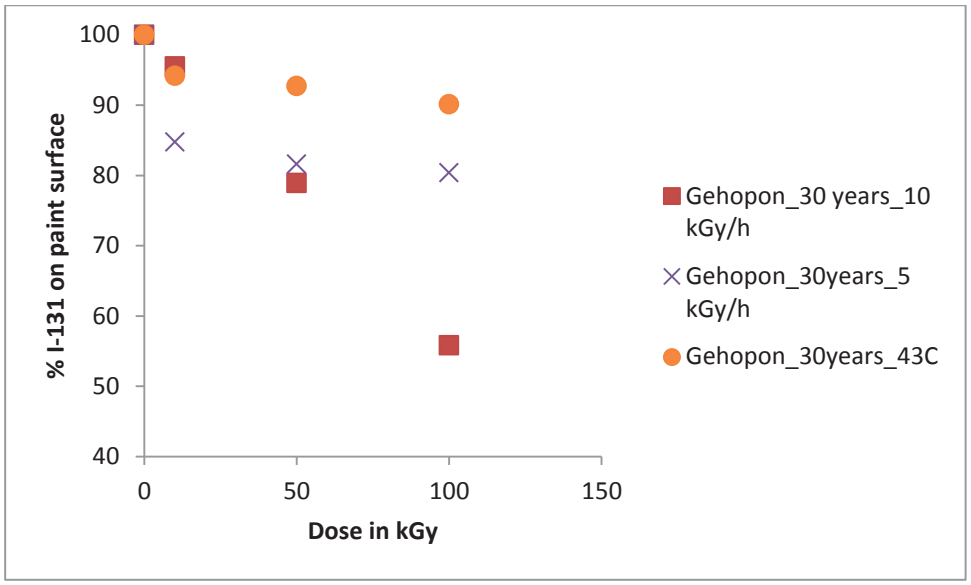

Fig. 4.8: Dose rate effect on the revaporisation of elemental iodine.

Organic iodides such as methyl iodide showed to bond more weakly to the surface and are thus easier to revaporise than elemental iodine both with and without gamma irradiation (Fig. 4.9). In presence of gamma irradiation elemental iodine was formed from methyl iodide exposed paint films. The performed tests showed that the revaporisation rate is temperature and dose rate dependent as was previously found for elemental iodine.

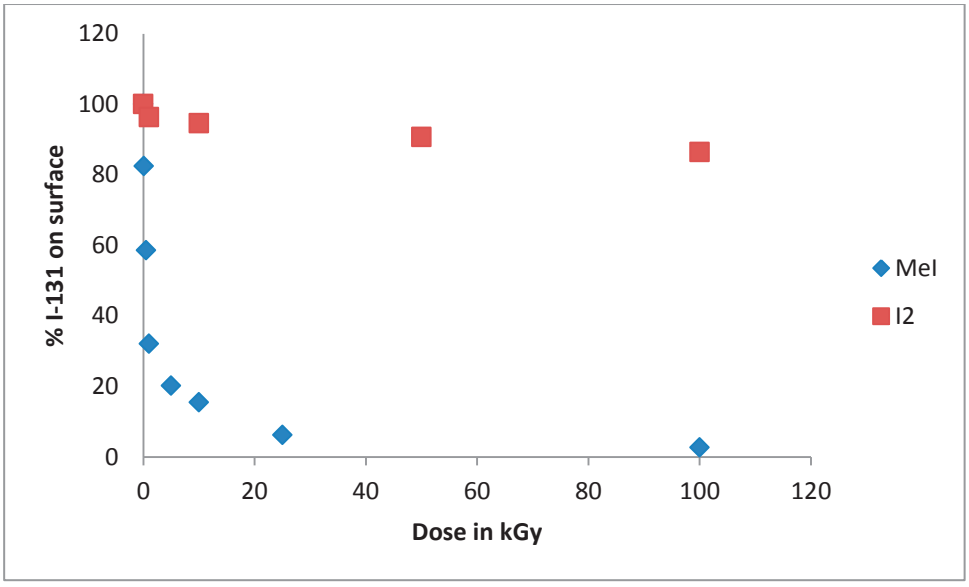

Fig. 4. 9: Comparison of the revaporisation of MeI and I_2 from Gehopon paint 5 years aged under gamma irradiation.

4. *The effects of impurities, radiolysis products and other fission products on the volatile iodine source term*

The radiolysis products such as carbon monoxide, ozone and nitrogen dioxide showed to have minor effects compared to the effect of temperature on the revapor-

isation behavior. However, the presence of chlorine species on paint surfaces prior to the exposure to iodine species showed to reduce the loading capacity and to increase the revaporisation rate for the iodine species. Pyrolysis-FTIR measurements revealed that both temperature and irradiation will affect the release of chlorine species from cable plastics (Fig. 4.10). It was found that the HCl release and hydrocarbon release was significantly higher for irradiated samples. In case of Hypalon^{TM} it was also found that HCl is released in two temperature steps (Fig. 10)

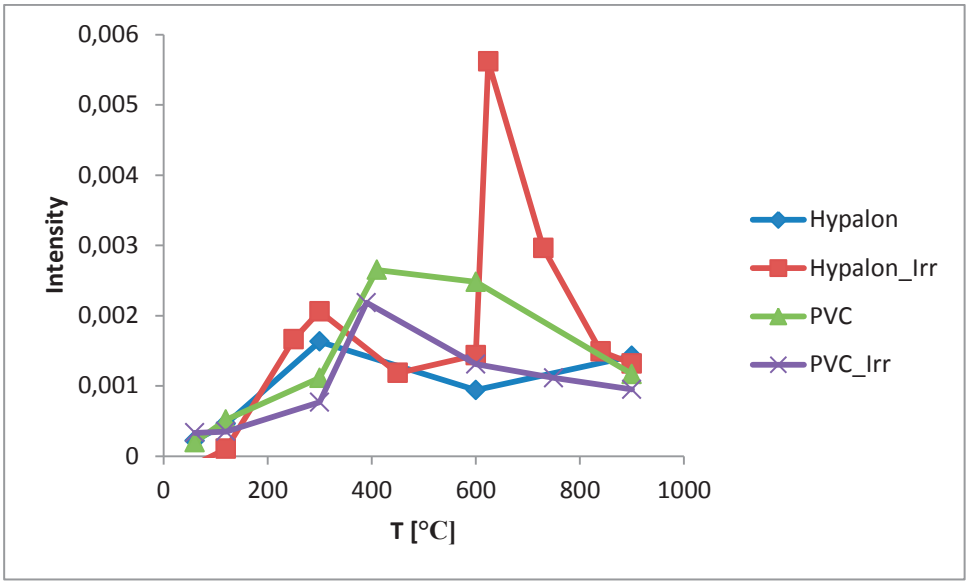

Fig. 4.10: Release of HCl from non- and pre-irraditated (1 MGy) HypalonTM organic cable coatings.

The exposure of paint films to ruthenium tetroxide was found to reduce the revaporisation and leaching ability of already absorbed iodine species and also reduced the ability of further iodine species to be taken up in the paint matrix.

The aqueous phase loading of iodine species was found to be dependent on the temperature, pH, irradiation and paint age, as well as on additives present in aqueous phase. The uptake into the aged paint was significantly slower and smaller than the uptake in the non-aged paint film (Fig. 4.11). Previous reported experiments showed that the uptake occurs more quickly at higher temperatures. Without radiation present the paint coupon remained unchanged in terms of its color. However, when the same experiment was performed with gamma irradiation both the aqueous solutions as well as the sample turned rapidly yellow/orange caused by the radiolysis of methyl iodide generating elemental iodine. The uptake of elemental iodine and inorganic iodide (I^-) present in the same amount was significantly faster compared to that of methyl iodide.

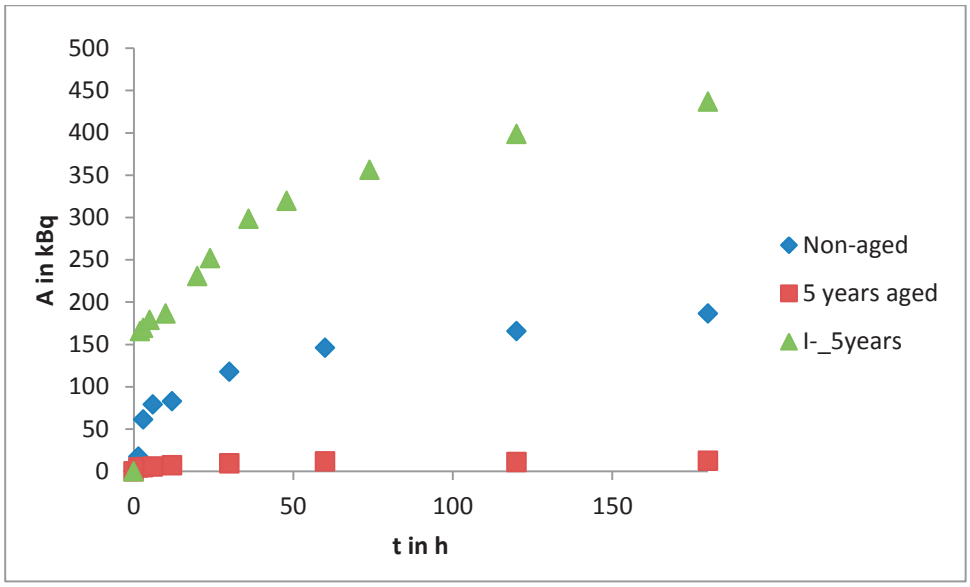

Fig. 4.11: Aqueous loading of MeI and I⁻ at 43 °C

The effects of impurities and pH on the leaching of sorbed iodine species into water pools was reported within APRI-7. A low pH, a high dose rate, high temperatures and a high anionic strength increase the kinetics of the leaching or iodine species from paint films. Once iodine species were leached into aqueous phase their ability was significantly reduced to be reabsorbed into a paint film or onto an organic impurity in a chlorine rich media [14]. Instead in chlorine rich media a higher rate of elemental iodine formation was found. A high chloride content in the water under gamma irradiation can lead to the formation of chlorine radicals that can oxidize iodide ions to form elemental iodine, (7) – (9).

$$CI^- + OH\cdot \rightarrow Cl\cdot + OH^- \quad (7)$$

$$Cl\cdot + I^- \rightarrow I\cdot + CI^- \quad (8)$$

$$2\,I\cdot \rightarrow I_2 \quad (9)$$

In a simplified version of the same experiments using one organic solvent like texanol ester instead of the entire paint film, it was confirmed that the addition of 1 vol% of an organic solvent showed a significant consumption of both organic iodide, elemental iodine and iodide ions [14]. However, in salt water systems the conversion rate of inorganic species into the organic layer was lower and formation of elemental iodine was dominating. When the solvents were pre-irradiated before the experiment, lower yields of organic iodide formation were measured. This indicated that the content of paint solvents the paint films determines the reactivity with iodine species. The water phases which were subjected to the highest radiation doses had the lowest organic content. This suggests that the radiation decomposed the organic matter into inorganic species. Inorganic carbon species are not converted into organic iodides.

5. *Development of modified paint formulations to reduce the volatile iodine source term*

Different paint formulations have been prepared using Teknopox Aqua VA epoxy paint as base. The commercial zinc primer showed to be by far the most efficient elemental iodine catcher. However, the retention of organic iodides was found to be low. DABCO (triethylene diamine) which is used in commercial available filters was also able to retain sufficient amounts of organic iodides. However, due to the water solubility of DABCO iodine washed out of the paint matrix when being exposed to humidity or immersed in water. A significantly increased and permanent retention of elemental iodine and organic iodides could be obtained when anthracene was incorporated into the resin of Teknopox Aqua VA epoxy paint. Due to the aromatic structure of anthracene (Fig. 4.12) the molecule becomes very radiation stable. After a dose of 1 MGy the paint showed the same retainability for iodine than without exposure to radiation whereas the amounts sorbed on DABCO loaded charcoal were lower after irradiation. In agreement with that the measured release rates of iodine were found to be lower than from non-aromatic organic additives. The losses due to leaching and irradiation could be reduced when anthracene was cured as an amine with the paint resin.

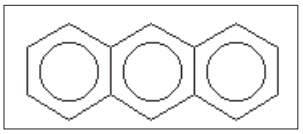

Fig. 4.12: Anthracene

6. *Investigation of solid-bed and wet-filter systems to improve the retention of organic iodides*

Tests on different solid filter materials revealed that conventional and DABCO loaded charcoals are not able to retain organic iodides sufficiently in comparison to elemental iodine. The yields for increasing molecule size were decreasing. The retention of isopropyl iodide was found to be the lowest of the studied organic iodides. The conventional coals showed to also fail to retain chlorine containing species. Silver loaded zeolites were found to be the best alternative to water sensitive DABCO filter to retain methyl iodide. The silver loaded silica showed to be a better alternative for longer chained organic iodides.

The remaining gaseous organic forms of iodine should be removed from vented gases during a severe nuclear accident requiring a venting of the containment. The approach studied at Chalmers uses an organic nucleophile, more specifically a trialkyl phosphine. Such compounds have been shown to remove and retain all organic iodides tested with a high efficiency. In experiments using the FOMICAG experimental rig which is a system where the liquid and gaseous phase do not mix it was found that after the addition of a trialkyl phosphine to the system (after an alkyl iodide {such as methyl iodide} had been introduced into the gaseous phase) that within seconds (typically ten) it is impossible to detect the radioactive alkyl iodide in the gaseous phase. Such a rapid removal of from air is too fast to be measured reliably and accurately by this experimental rig. In the more realistic flow experiments with a violent mixing of the gas and liquid phase, in none of the performed experiments any iodine was detected in the second or third gas wash bottle

when the first bottle contained a thin film of the trialkyl phosphines. Also in the experiments with air flow the trialkyl phosphines did not decompose to such an extent that the removal efficiency was reduced. On the other hand nearly no iodine was retained when the first bottle contained water or the inorganic scrubber solution indicating that the contact time was too low to hydrolyze the methyl iodide. A very thin layer of the tributyl phosphine (100 µl on top of 10 ml of distilled water) in this test was able to remove 23 µl of methyl iodide which corresponds to 94 ± 2 % of the organic iodide initially injected. However, as no iodine was detected in the second and third bottle containing as well phoshines it is assumed that possibly some iodine was not revaporised from the injection flask.

The mechanism of the reaction of trialkyl and triaryl phosphines with alkyl iodides (such as methyl iodide) is well known to be an example of the S_N2 reaction. The S_N2 reaction is a second order reaction between a nucleophile (such as a hydroxide anion) and an unhindered electrophile (such as methyl iodide) which occurs according to the following equation, (10).

$$OH^- + CH_3I \rightarrow CH_3OH + I^- \quad (10)$$

In the case of tributyl phosphine as an example of a trialkyl phosphine and methyl iodide the reaction mechanism is as in equation (11). One molecule of organic iodide (methyl iodide) can be removed by one molecule of the tributyl phosphines.

$$Bu_3P + CH_3I \rightarrow [Bu_3PCH_3]^+ + I^- \quad (11)$$

The rate of the reaction can be described by the following mathematical equation:

$$-d[CH_3I]/dt = k[CH_3I][Bu_3P] \quad (12)$$

The nucleophilic attack of phosphines on alkyl iodides was reported early in the 20th century [15]. The reaction of undiluted methyl iodide with trialkyl phosphines is so rapid that it is impossible to measure in nuclear chemistry at Chalmers. Even dilute solutions of a less nucleophilic phosphine (triphenyl phosphine) in toluene react within seconds with methyl iodide [16]. It is also possible to remove elemental iodine using the same reagents.

The transfer of the radioactive iodide ions from an organic layer to a water layer was very fast. Typically after one single shaking (rapidly displacing the vial once in a direction perpendicular to the surface at the bottom of a flat bottomed cylindrical vial before bringing it to rest thus subjecting the mixture to an acceleration) that the vast majority of the radioactive iodine (> 99 %) was transferred to the aqueous phase. The rate of such a rapid transfer of iodine radioactivity between phases is impossible to measure at Chalmers.

Both the kinetics and thermodynamics of the transfer of radioactive iodide ions from the organic phase to the aqueous phase were found to be unaffected by changes in acidity / alkalinity (pH) or by the presence of the potassium (or sodium) salts of thiosulfate, nitrate, chloride or sulfate. When the experiment was repeated with radioactive cesium (Cs-137) after shaking the cesium was only present in the aqueous layer. It was impossible to measure the cesium radioactivity in the organic lay-

er. This failure to detect cesium in the organic phase coupled with the fact that the cesium activity of the water remained constant suggests that the separation of the two layers is exceptionally good. If the two layers had formed a stable emulsion similar to milk then cesium would have been detected in the organic phase.

The reaction of iodine with a phosphine will occur according to equation (13). One molecule of iodine can be removed by one molecule of the phosphines. In common with the reaction of methyl iodide with phosphines this reaction is exceptionally fast, in the organophosphorus community it is common to decontaminate glass equipment which has been used with phosphines using a dilute solution of iodine in ethanol. This reaction is so fast that the brown color of the iodine solution is decolorized within a few seconds when the iodine solution is added to a typical phosphine.

$$Bu_3P + I_2 \rightarrow Bu_3PI_2 \quad (13)$$

The phosphorus (V) species formed from the iodine (Bu_3PI_2) reacts with water to form a phosphine oxide according to the following reaction equation, (14).

$$Bu_3PI_2 + H_2O \rightarrow 2HI + Bu_3P = O \quad (14)$$

The removal efficiency is not dependent on the length of the alkyl chain bonded to the phosphorus atom but will affect the surface tension. Measurements of the surface tension (interfacial tension) between air / thiosulfate solutions, air / phosphines and phosphines / thiosulfate suggest that it is thermodynamically favorable for the inner surface of a bubble of gas in a mixture of a trialkyl phosphine and water to be covered with a layer of the phosphine rather than a layer of water. This fact will contribute to bringing the air into intimate contact with the phosphine.

The oxidation of the trialyl phosphines into phosphine oxide by the oxygen of the air needs to be taken into consideration additionally to the consumption by the organic iodides for the dosing recommendation for the installation in combination with a non-inert containment. In a gas chromatography experiment it was found that exposure of a tributyl phosphine to 1 MGy of Co-60 gamma rays under anaerobic conditions did not cause the appearance of any impurity in the sample whereas the reaction caused the formation of phosphine oxide.

A patent application on the subject of this scrubber chemistry has been applied for with Westinghouse.

7. Methods to chemically clean-up contaminated surfaces, soil and waste water considering the effects of sea water

Cesium iodide was found in sorption studies to bind similar to strontium and cobalt to the inorganic pigment of the paint. Iodine species bind preferably to the organic part of paint and also to soil. The tested approach to decontaminate cesium contaminated surfaces with a eutectic solution of magnesium chloride and choline chloride showed to be efficient and to require significant lower amounts of chemicals and water [17]. This could be a valuable advantage during a clean-up after an accident,

as the production of secondary waste will be minimized. Especially on paint surfaces that had been aged before contamination the cesium will bind tightly as more of the pigment will be on the paint film surface. Fig. 4.13 shows the improved removal efficiency using the eutectic in comparison to two conventional cleaning detergents. The detergent was found to be suitable also to remove Co. Sr and I can be removed but with lower yields.

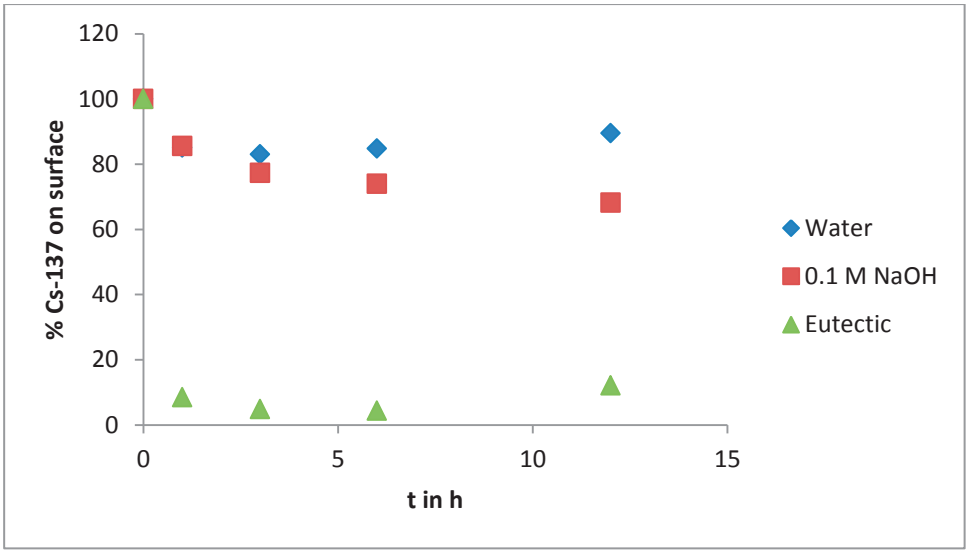

Fig. 4.13: Cs removal from a 2 years at 100 °C aged paint film

4.1.5. Comparison of results obtained at Chalmers and within BIP

Experiments on a series of epoxy paint films including Ripolin, Amerlock and Gehopon paints revealed that significant higher amounts of elemental iodine absorption onto Gehopon and Teknopox Aqua VA epoxy paint films occurs. The iodine loading ability on Gehopon which has a similar chemical composition as Teknopox Aqua VA paint was slightly higher. These paints which absorbed larger amounts of elemental iodine were able to release larger amounts of organic iodine than the other paints. The Gehopon paint tended to release more aromatic organic iodides than the Teknopox Aqua VA paint which only formed and released small amounts of aromatic organic iodides when subjected to higher radiation doses. These aromatic iodine compounds could be formed from the benzyl alcohol in the paint, as well as from the degradation of the bisphenol-A (epoxy) resin. In agreement with the BIP results, significantly lower amounts of iodine chemically bond to the paint films was found on paint films that have been exposed to iodine oxide aerosols. No detectable effects on the iodine absorption (20 Gy/h) were found in the tests at AECL but significant effects were detected with the high dose rates studied at Chalmers. AECL did not detect any other organic iodide formation than methyl iodide. It is suspected that the failure to observe organic iodine compounds other than methyl iodide during the work at AECL may be due to their choice of conditions and equipment used for the gas chromatographic experiments.

In the Chalmers studies it was found that the majority of the organic iodides were formed from the paint solvents. The fraction of the organic iodine decreased with

increasing doses. Experiments including nitrogen dioxide, hydrochloric acid and chlorine gas were performed only very initial and prior to the iodine exposure at AECL as there was at the time no knowledge of how much of the impurities to study. The amounts studies were found lateron to be far too low and no control was given on to how much of the species the actual sample was exposed to. This could be a reason why within BIP no measureable effects of those species were determined, while in case of chlorine in the Chalmers studies significant effects on the iodine chemistry were determined.

4.1.6. Summary

The conducted experiments revealed that a range of organic iodides can be formed from organic materials. Paint plastics, cable plastics and oil contain solvents, plasticizer and polymers that can react either instantly with iodine or under the influence of gamma irradiation in radical reactions. The most commonly detected volatile organic iodides were methyl iodide, ethyl iodide, isopropyl iodide, butyl iodide, iodo-benzene and iodohexane. The range of organic iodides formed is strongly dependent on the composition of the organic materials that was found to vary greatly between different paint and cable products. As the organics are subjected to heat and irradiation induced ageing the yield of organic iodide formation was found to be decreasing with increasing age and increasing with increasing dose rates, increasing obtained dose and for increasing temperatures. Both the presence of oxygen and pre-irradiation reduced the yield of organic iodides. The formation of organic iodides in aqueous phase, as well as the release of elemental iodine was found to be pH, temperature, irradiation and chlorine content dependent. Acidic conditions, high temperatures, high chlorine contents and high irradiation doses were shown to increase the elemental iodine formation and the hydrolysis of organic iodides.

With increasing chain length organic iodides become more hydrophobic and are therefore less able to remain in the containment gas phase. Exposure to gamma irradiation however causes decomposition of organic iodides and generates elemental iodine which partitions faster to the water pools.

Elemental iodine and organic iodides can react with the radiolysis product ozone to form iodine oxide aerosols. These as well as cesium iodide aerosols, elemental iodine and organic iodides were found to be able to deposit on paint films and to be partially absorbed into the paint matrix and transformed into new iodine species. These can be either less mobile or more mobile than the original species. The sorption of elemental iodine was found to be very high on zinc primer surfaces. The absorption of organic iodides and iodine aerosols was found to be much lower on metal surfaces than on organic materials. The possible release of hydrochloric acid and the possibility to generate chlorine alters the chemistry greatly as chlorine has a similar behavior to iodine. Chlorine exposed surfaces absorb less iodine in the form of elemental iodine or an alkyl iodide. Some chlorine species can undergo halogen exchange reactions with iodine species. Exposure to ruthenium tetroxide prevents further uptake of iodine species into organic materials, as well as reduces the revaporisation and leaching rate of iodine species from organic materials.

Particularly paint films were found to be sinks for both aqueous and gaseous iodine species. However, under the conditions in the containment the species can be re-

released from the paint films and possibly be revolatilized. Aromatic paint additives that can be linked to the paint resin such as anthracene were found to be suitable additives to permanently retain iodine species and therefore to reduce the amount of gaseous iodine species already in the containment.

As organic iodides other than methyl iodide were found to be formed in relevant amounts both solid and wet filter systems need to be reassessed. Conventional filter systems showed to have a lower decontamination factor for organic iodides. Silver loaded zeolites and silicates were found to be suitable and less humidity dependent solid absorber for organic iodides than charcoal filter. The ability of wet-scrubber systems to retain alkyl iodides (methyl iodide) could be optimized with a trialkyl phosphine additive. The additive is able to also react with elemental iodine.

Cesium iodide contaminated surfaces were found to be more efficiently decontaminated and to generate less waste water using a highly viscous deep eutectic instead of an aqueous complexing solution.

4.2 Ruthenium chemistry in a severe nuclear accident

4.2.1. Ruthenium chemistry in water phase

Theory

During a severe nuclear accident where the hot fuel has been exposed to air, it is possible to form volatile ruthenium tetroxide (RuO_4). This is a reactive and toxic gas which is able to form deposits on surfaces inside the plant and also form hot particles [19]. Additionally ruthenium relatively long lived radioisotopes ^{103}Ru and ^{106}Ru make gaseous ruthenium important from the radiological point of view. It is likely that the pyrolysis of chlorine containing plastics, such as cable insulation, during an accident will form hydrochloric acid. It is well known in platinum group chemistry that ruthenium tetroxide can be trapped in hydrochloric acid as "ruthenium trichloride". It is therefore likely that the interaction with chlorine compounds may alter the reaction of ruthenium tetroxide and water. Ruthenium tetroxide is known to react with hydrochloric acid; the products of this reaction include Ru(IV) and Ru(III) complexes. In dilute hydrochloric acid, ruthenium complexes ranging from $[RuCl(H_2O)_5]^{2+}$ to $[RuCl_4(H_2O)_2]^{3-}$ have been observed [20]. It is possible that some of the fission ruthenium may become immobilized as chloride complexes on the surfaces inside the containment. Additionally a part of ruthenium could be re-vaporized from the solution due to formation of oxidative species by radiolysis of water. The radiolysis of water yields formation of several oxidative and reducing species. The most oxidizing product of water radiolysis is hydroxyl radical $OH^{\cdot}$ with high reduction potential for the pair $OH^{\cdot}/H_2O$ with value 2.8 V. Another specie possibly causing re-vaporization of ruthenium from the aqueous solution could be H_2O_2. Therefore, effect of gamma radiation on aqueous chloride-ruthenium solutions was examined with focus on possibility to re-vaporize ruthenium into the gaseous specie presumably in form of RuO_4. On the other hand, the reducing species originating from water radiolysis can cause precipitation of the ruthenium from the solution in form of very insoluble ruthenium dioxide or as amorphous ruthenium hydroxides.

Method

Experiments regarding possible re-vaporization of ruthenium-chloride complexes were done with use of aqueous ruthenium solutions. Working solutions of ruthenium chloride complexes were prepared by boiling commercial ruthenium trichloride in hydrochloric acid of different concentrations. On these solutions the effect of irradiation was investigated. Both inactive and radioactive experiments using a ^{103}Ru tracer were performed to track ruthenium distribution between liquid and gas phase and to eventually quantify precipitate induced by irradiation.

Irradiations were performed with use of the gamma source at Chalmers (Gammacell 220) with the dose rate of 14kGy per hour. This is a realistic dose rate in the case of a severe nuclear accident and induces relevant insight into behavior of radionuclides [21]. Temperature in the irradiation chamber during experiments was 317 ± 1K. Gas phase over the aqueous solutions was air.

Results

Results of performed irradiations are summed up in the table 4.4. As can be seen, the fractions of re-vaporized ruthenium are under the uncertainty limits of measurements within the whole range of chloride concentration in the solutions.

Table 4.4: Re-vaporized fraction of the ruthenium from chloride solutions

Concentration of chloride in the solution (Mol/liter)	Received dose (kGy)	Fraction of re-vaporized ruthenium from solution (%)
0,1	336kGy	0,3±3
0,5	336kGy	-1±3
1	336kGy	1,5±3
5	336kGy	0,8±3
13	336kGy	0,2±3

Based on the obtained results, it was concluded that re-vaporization of ruthenium from chloride solution into the gas phase does not occur when the solution is irradiated by gamma radiation. Additionally no precipitation of ruthenium in solutions was observed during experiments. This leads to conclusion that solutions of ruthenium chlorides are stable under the gamma radiation with respect to the ruthenium content.

4.2.2. Interaction of ruthenium with surfaces in the containment of nuclear power plant

Background

At the conditions expected in the containment building during an accident, the most relevant gaseous species is considered to be RuO_4. Ruthenium tetroxide is known as

a reactive substance with reported affinity to various kinds of surfaces. It is a strong oxidizing agent that readily reacts with organic compounds, like epoxy paint in the containment. The ability of ruthenium to react with different metals or epoxy has also been reported previously [22, 23]. The surfaces in the nuclear power plant containment are mostly covered by epoxy paint. Furthermore non-negligible amounts of different metals are present in the containment of the nuclear power plants [24].

Therefore interaction of RuO_4 with epoxy paint and reactive metals will be prominent in the containment. As shown previously, reaction of RuO_4 with different surfaces leads to the formation of dark ruthenium-rich deposits [22, 23]. The chemical characterization of these deposits has previously been widely discussed. For the characterization of these deposits in the past, mainly the XPS technique was used [23, 25]. Regarding the interaction of RuO_4 with metal surfaces, many authors agree that ruthenium rich deposits consist of RuO_2 as a product of RuO_4 reduction, according to the reaction 1.

$$RuO_{4(g)} \rightarrow RuO_{2(s)} + O_2 \quad (1)$$

Kim and Winogradov identified that a layer of RuO_3 is deposited on the layer of RuO_2 [26] But this explanation seems improbable due to the instability of RuO_3 in temperatures below 1273K [27] B. Eichler et al. obtained the same results in their experiments [28] T. Sakurai observed a layer of RuO_4 with peroxide bonds between ruthenium atoms in the deposits [25]. Deposits were then characterized as a polymerized form of RuO_4 condensed on the surface after deposition of RuO_4 vapors. In the work of C. Mun deposits were characterized as a hydrolyzed form of hydrated RuO_2. The proposed hydrolysis product of RuO_2 was oxo-hydroxide species or ruthenium in the oxidation state IV, probably in form of $RuO(OH)_2$ [23]. These different chemical speciations would eventually lead to different chemical behavior of ruthenium deposits in the severe accident conditions. Therefore, further examination of deposits composition seemed necessary. As an addition, during experiments the distribution of RuO_4 among different metals was examined.

Method

Experiments conducted at Chalmers were focused on the interaction of ruthenium tetroxide with epoxy paint and reactive metals (copper, zinc, aluminum), which can be observed in the containment building. Epoxy paint samples were prepared by applying a film of paint on the glass coupons that were left to dry for a month to evaporate excessive solvents. Metals were in form of coupons and were cleaned with use of acetone and Milli-Q water prior depositions, to avoid organic impurities on the surface. The chemical form of ruthenium deposits was examined with use of SEM/EDX, XPS and EXAFS techniques. Due to the instability of RuO_4, it was prepared in house before the depositions according to Krtil and Mencl [29].

With use of ruthenium radiotracer ^{103}Ru, distribution ratio among metals could be obtained. Surface area of metal samples available for the absorption process was established with use of BET measurements. Experiments regarding distribution ratio among reactive metals were conducted in both dry atmosphere with <3% humidity and humid atmosphere where humidity was as high as 99%.

Results

With use of scanning electron microscopy (SEM), microscopic structure of deposited ruthenium layer was revealed. EDX analysis showed elemental composition of the samples and indicated concentration of ruthenium in the deposits on different spots.

SEM/EDX analysis showed variations of physical nature of the deposits on different materials. Aluminum and zinc samples showed uneven distribution of the ruthenium on the surface with formation of ruthenium rich grains. In case of copper and paint samples, ruthenium was distributed evenly over the surface of samples and fully covered the surface of samples as can be seen in the Fig 4.14.

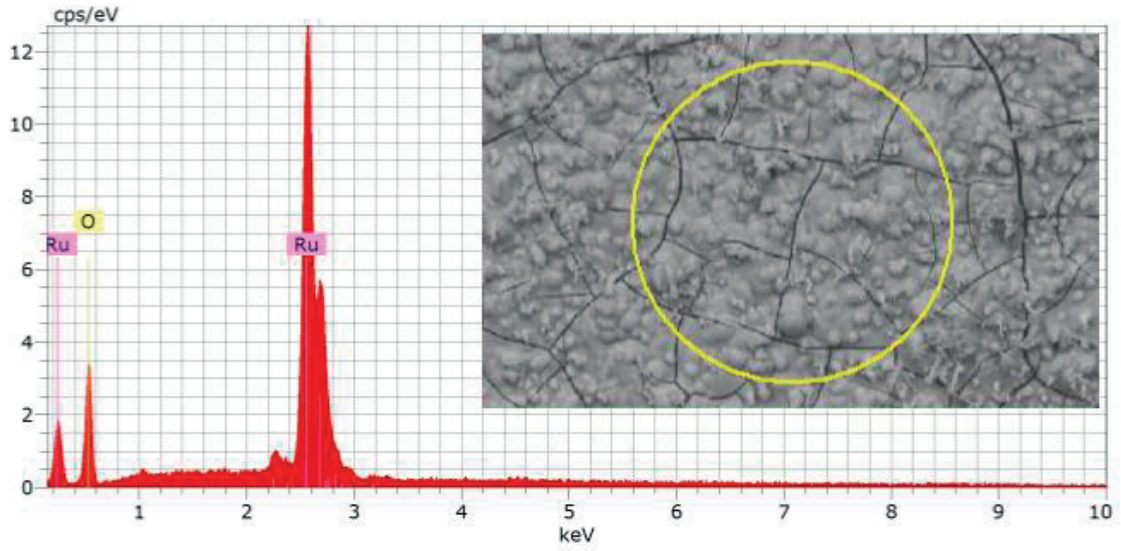

Fig. 4.14. SEM photo with EDX analysis of ruthenium deposited paint coupon

XPS analysis revealed that ruthenium deposits have the same chemical composition regardless deposited material. Deposit formed by interaction of RuO_4 with metals and paint was identified to be hydrated form of ruthenium dioxide with ruthenium in the oxidation state IV. However, during the analysis of oxygen speciation on the surfaces, strong hydroxylation in oxygen peak was observed. This can be attributed to the natural behavior of oxides in the humid environment where water reacts with the surfaces of metals oxides creating a thin layer of OH groups on the surface. This explanation is strengthened by the fact that RuO_2 is known to be a hygroscopic oxide.

Crystal structures of deposits were analyzed by *EXAFS* technique that indicated the crystal structure of deposit to be very similar to the structure obtained by measurements of commercially supplied $RuO_2.xH_2O$. *EXAFS* measurements revealed also higher hydration of ruthenium deposit on the painted surfaces when compared to the metal samples.

After introducing fumes of RuO_4 into the deposition glass vessel, it interacted with different materials and revealed its distribution to the metals based on their reactivity towards ruthenium tetroxide. The weight of deposited ruthenium per square centimeter of the sample is summed up in the Table 4.5. for humid atmosphere (99% of

humidity) and the Table 4.6. for the dry atmosphere (<3% humidity). Interestingly, BET measurements of the metals surface area revealed much higher surface than would be obtained by simple geometrical measurements of the sample.

Table 4.5. Distribution of ruthenium on the different metals in the humid atmosphere

Sample type	Zinc	Copper	Aluminum
Ru/sample ($\mu g/cm^2$)	15.3 ± 0.3	18.0 ± 0.3	31.6 ± 0.6
Ru/sample ($\mu g/cm^2$)	13.2 ± 0.2	12.1 ± 0.2	24.8 ± 0.5
Ru/sample ($\mu g/cm^2$)	18.5 ± 0.3	19.2 ± 0.4	38.9 ± 0.7

Table 4.6. Distribution of ruthenium on the different metals in the dry atmosphere

Sample type	Zinc	Copper	Aluminum
Ru/sample ($\mu g/cm^2$)	2.73 ± 0.5	9.42 ± 0.2	103.29 ± 0.7
Ru/sample ($\mu g/cm^2$)	0.76 ± 0.02	0.39 ± 0.1	86.78 ± 0.6
Ru/sample ($\mu g/cm^2$)	2.23 ± 0.4	2.45 ± 0.5	98.35 ± 0.7

The attraction of RuO_4 to the different metals seems to be quite variable. A proposed explanation for this is the difference between the properties of oxide films formed on the metal surfaces by atmospheric oxidation. The different conductivity of these oxides leads to increased or decreased attraction of RuO_4. As water plays a role as an electrons conductor, electrochemical reduction of RuO_4 can proceed on the zinc and copper surfaces during the deposition in the humid atmosphere. The standard redox potential of the reaction RuO_4/RuO_2 was stated to be 1.4 V in a neutral solution [30]. The standard redox potential for the couple Zn/Zn^{2+} is -0.7618 V and for the couple Cu/Cu^{2+} is -0.337 V [31]. This leads to the possibility of electrochemical oxidation of zinc and copper metal through the water layer, due to the potential difference.

During dry atmosphere deposition, no water layer is formed on the samples. The loss of the water layer as an electrolyte prohibits the electrochemical reduction of RuO_4 on the zinc and copper samples and leads to the lower adsorption of ruthenium on these samples.

Aluminum samples demonstrated exceptional ability to trap ruthenium among the metals used in the experiments. The effect of high oxygen site density on the aluminum surface is the proposed explanation. As oxygen groups are presenting formal negative charge, transfer of electrons will lead to reduction of ruthenium tetroxide on the surface of aluminum oxide. As aluminum cannot be further oxidized from the form of Al_2O_3, it most probably works as a catalyst of the ruthenium reduction process. Illustration of the ruthenium reduction is shown in the Figure 4.15.

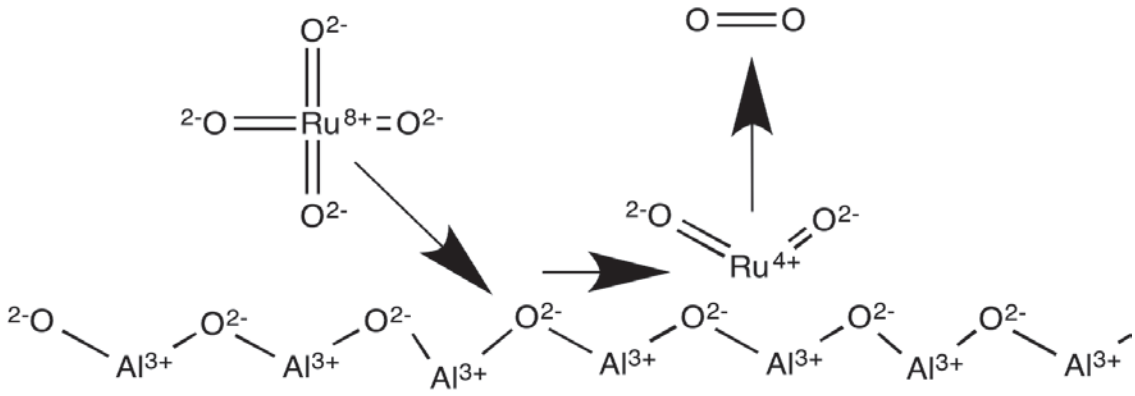

Fig. 4.15. Reduction of RuO_4 on the surface layer of Al_2O_3

The difference between wet and humid depositions can be explained by hydroxylation of surface oxygen atoms by water in case of humid atmosphere, thus lowering the reactivity of surface. This leads to the lower attraction of ruthenium to the aluminum surface during the humid atmosphere deposition experiments.

4.2.3. Possible re-vaporization of ruthenium in the containment

Background

Due to a high radiation field in the containment during a severe accident, there will be continuous formation of oxidation agents like ozone via the radiolysis of air. These oxidation agents may react with ruthenium deposits on the surfaces in the containment and reproduce volatile ruthenium species, which can be released from the containment. The aim of this part is to investigate the re-vaporization of deposited ruthenium on aluminum, copper, zinc and paint surfaces due to exposure to gamma radiation. These metals and painted surfaces are present in significant amounts in a BWR containment [32]. If ruthenium could be released from these surfaces in form of ruthenium tetroxide, this would contribute to formation of additional volatile source term. Therefore, quantification of possible ruthenium re-vaporized fraction to the gas phase is important information during a severe nuclear accident.

Method

Metal and paint samples covered with ruthenium deposits were exposed to the gamma radiation (gamma cell 220, ~14kGy/h). Temperature during experiments was 317 ± 1K because of the extensive thermal effect caused by the decay heat of cobalt in the gamma cell and consequent heating of the lead shielding. In case of experiments with ruthenium deposits on paint, time of irradiation and humidity of atmosphere were parameters to change. In case of metal samples experiments were conducted in the humid atmosphere. Evaluation of re-vaporized ruthenium fraction was done with use of radiotracer ^{103}Ru. The release of the ruthenium from surface of samples was quantified with use of HPGe detector.

Results

Dependence of ruthenium re-vaporized fraction from the paint coupons on the received dose in the dry atmosphere is shown in the Figure 4.16. In the dry air atmosphere, detected amounts of released ruthenium were actually lower than the uncer-

tainty of measurements. That leads to the conclusion that no re-vaporization of ruthenium was detected up to the received dose of 264 kGy. This indicates that the amount of oxidizing agents created by radiolysis of air was not sufficient for the re-vaporization of ruthenium from the samples. Interestingly, it was proved before, that ozone has ability to oxidize ruthenium from oxidation state IV to VIII leading to formation of volatile RuO_4 [33]. Explanation can be proposed that the amount of ozone, that is the prominent oxidizing agent in the dry air, was not sufficient to efficiently react with ruthenium deposits.

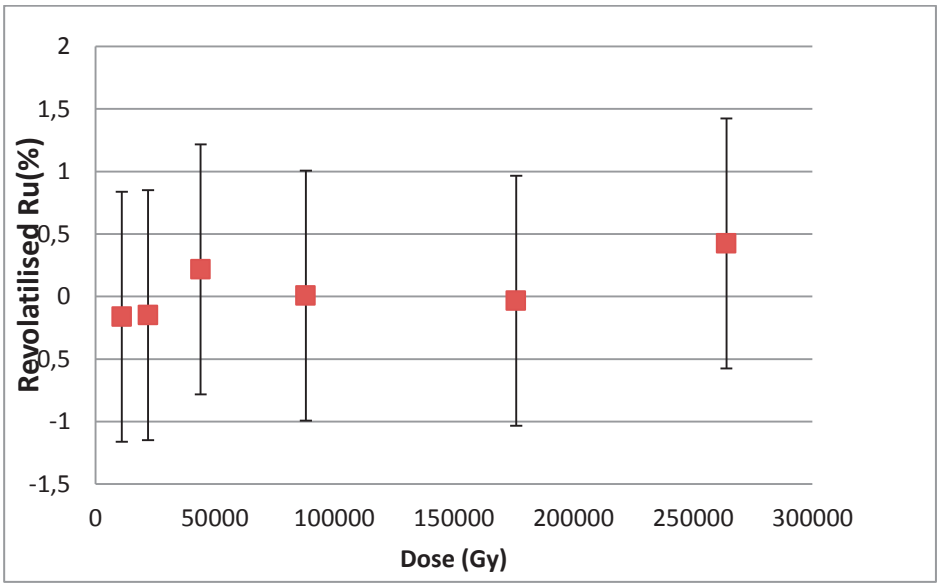

Fig. 4.16. Re-vaporized fraction of ruthenium in the dry atmosphere

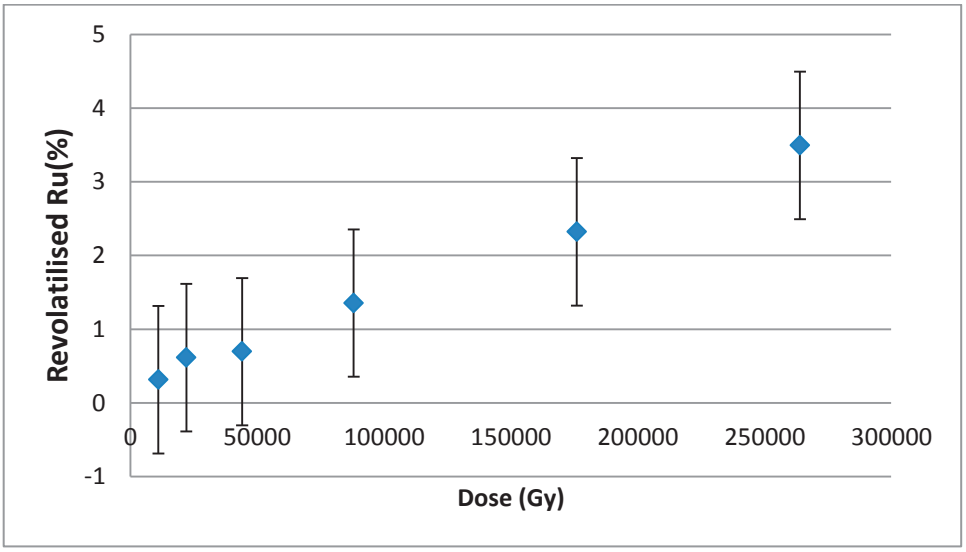

Fig. 4.17. Re-vaporized fraction of ruthenium in the humid atmosphere

Results of ruthenium re-vaporization experiments in the humid atmosphere are summed up in Fig. 4.17. The fraction of re-vaporized ruthenium in the humid atmosphere is significantly higher when compared to the virtually non-existing volatilization of ruthenium in the dry atmosphere experiments. The amount of re-

vaporized ruthenium was linearly increasing over the whole received dose interval up to 264kGy. The distinction between re-vaporized ruthenium fractions in the case of the dry and humid atmospheres can be explained by production of the hydroxyl radical by radiolysis of water in the humid atmosphere. Hydroxyl radical, which is a very strong oxidizing agent, provides the ability to oxidize ruthenium from the oxidation state +IV to +VIII. This is because of the high electrochemical reduction potential of the pair $OH^{\cdot}/H_2O$ with value 2.8 V [31]. Re-vaporization of ruthenium deposits occurred probably according to the reaction 2.

$$RuO_x(OH)_{2(2-X)} + 4OH. \rightarrow RuO_{4(g)} + (x + (4 - 2x))H_2O \quad (2)$$

where X=1,2

In comparison, standard electrochemical potential of the pair RuO_2/RuO_4 is -0,58 V indicates that the oxidation of ruthenium deposits by $OH^{\cdot}$ is possible. Due to the linearity of re-vaporized fraction, it was calculated that for the re-vaporization of 1% of the ruthenium fraction dose of roughly 79.5 kGy was needed.

Experiments with metal samples irradiation showed significantly different behavior of ruthenium deposits when compared to the paint. After the irradiation, noteworthy corrosion of samples was observed. This was resulting to the physical fall of ruthenium deposits from the samples with parts of metal substrate. Corrosion behavior was mostly prominent in the case of zinc samples, where corrosion of the substrate metal was quite significant. In case of aluminum samples color change of the deposited ruthenium layer occurred, although chemical speciation of ruthenium deposit remained the same. Photographs of the samples before and after the irradiation can be seen in the Fig. 4.18.

(a)

(b)

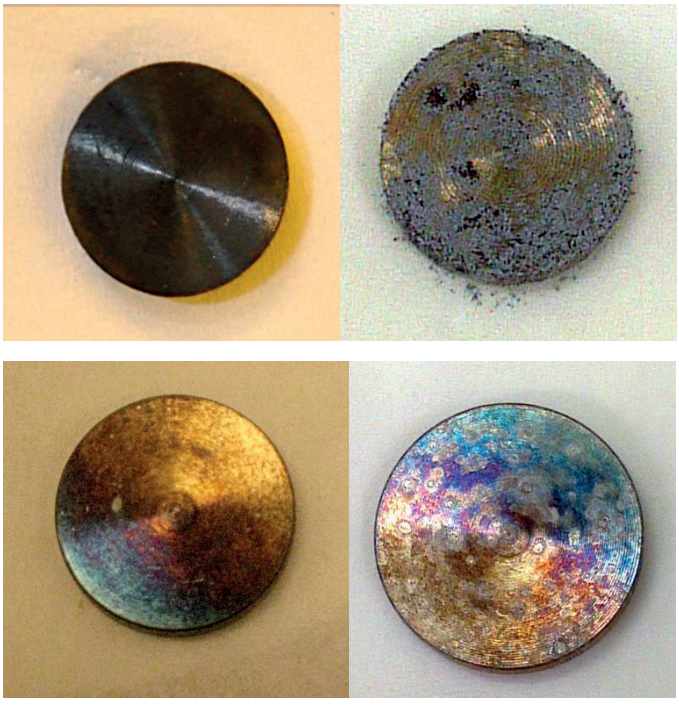

Fig. 4.18. Zinc (a) and Aluminum (b) samples before and after the irradiation

Release of ruthenium from the samples varied between different metals, as can be seen in the Table 4.7.

Table 4.7. Loss fractions of ruthenium from metal samples after dose of 264kGy

Sample type	Aluminum	Copper	Zinc
Re-vaporized fraction (%)	4,67±1,3	3,66 ±1,37	19,03±4,24

The most prominent loss of ruthenium occurred in case of zinc sample. However, due to the physical fall of the ruthenium deposits from the samples, it was impossible to distinguish between the re-vaporized fraction of ruthenium and part of ruthenium that physically fell off the samples. Assumption is that the oxidative species created by the radiolysis of the air, promoted corrosion of substrate metals leading to extensive loss of deposited ruthenium.

4.2.4. Interaction of iodine and ruthenium in severe accident conditions

Background

During a hypothetical severe accident both iodine and ruthenium can be released from the fuel due to their volatile and semi-volatile properties. It is expected that iodine will be released in the beginning of accident as its release is governed mostly by diffusion of gaseous iodine through the fuel. As a prerequisite for ruthenium oxidation to volatile state, a disintegration of the fuel pins and presence of oxygen is necessary. This leads to later release of ruthenium from the nuclear fuel. As a consequence in time of ruthenium release, surfaces in nuclear power plant had already been exposed to the volatile iodine, which leads to formation of perspective metal iodides or organic iodides in case of the paint. Therefore, chemical interaction between ruthenium tetroxide and iodide covered surfaces can effect chemistry inside the containment. As ruthenium tetroxide is strong oxidizing agent it can possibly interact with iodides on the surfaces causing re-volatilization of iodine to the gas phase.

Method

In this part of the project elemental iodine (I_2) was deposited on aluminum, copper, zinc and epoxy paint in form of chemical vapors. These materials have shown ability to trap iodine and form metal iodide [32]. The metal surfaces were thereafter exposed to vapors of RuO_4 to see if the oxidation of I^- to I_2 on the surfaces is possible. Quantification of adsorbed iodine and ruthenium was performed with use of radiotracers ^{131}I and ^{103}Ru. Quantitative measurements were done on HPGe detector. Chemical speciation of iodine and ruthenium species formed on the samples was performed by SEM/EDX and then by XPS technique.

Results

SEM/EDX analysis performed on the samples revealed the physical nature of the deposits. Reactions of iodides with RuO_4 lead to the significant physical changes in the microscopic scale. Cracking of the deposited layer were formed as can be seen

in Fig. 4.19. This behavior was dominant mainly in case of zinc and aluminum. Copper and paint showed more evenly distributed deposits without major cracks of deposits.

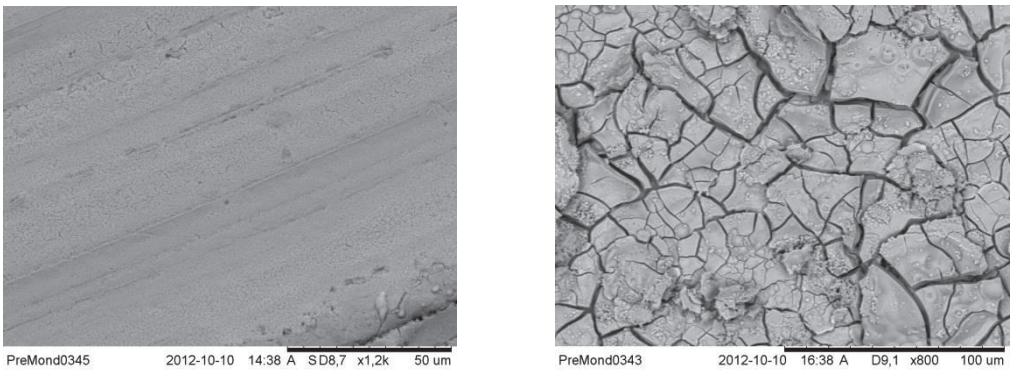

(a) (b)

Fig. 4.19 Zinc surface deposited with iodine (a) and afterwards with ruthenium (b)

XPS analysis showed different iodine species before and after the interaction with ruthenium tetroxide vapors. After deposition of I_2 onto metal samples respective metal iodides were formed. Interaction with RuO_4 with metal samples caused oxidation of iodide to iodine (I_2) that stayed partly on the sample in case of zinc. Differentiation of iodine species before and after the deposition of RuO_4 is illustrated in Fig. 4.20. Doubling and shift of the I 3d5/2 peak was observed. The higher binding energy was then attributed to the formation of gaseous I_2 that stayed in sample. Aluminum sample did not show change in the chemical speciation of iodine absorbed on the sample.

In case of paint and copper samples, iodide was oxidized to the higher oxidation states leading to formation of iodine oxides IOx thus creating new chemical speciation of iodine trapped in the samples. This is illustrated in Fig. 4.21. From the figure it is obvious that after deposition of RuO_4 new peak for binding energy of I 3d5/2 with the value of 624 eV appeared in the measured spectra. This energy was attributed to the formation of IOx species on the sample.

Additionally the release of iodine from the samples was observed due to volatilization of iodide to iodine (I_2) and consequent escaping samples into the gas phase. Revolatilization of iodine was most significant on aluminum and zinc samples where up to 20% of iodine was released. This is due to the proposed reactions (3), (4). The XPS evaluation revealed that a part of formed I_2 stayed on the surface of zinc sample. Proposed explanation is that encapsulation of I_2 under the layer of ruthenium deposits occurred. In case of aluminum sample this behavior was not detected with XPS measurements. Fractions of re-vaporized iodine from the samples are summed up in the Table 4.8.

$$RuO_{4(g)} + 2ZnI_2 \rightarrow RuO_{2(s)} + 2I_{2(g)} + 2ZnO \quad (3)$$

$$3RuO_{4(g)} + 4AlI_3 \rightarrow 3RuO_{2(s)} + 6I_{2(g)} + 2Al_2O_3 \quad (4)$$

Table 4.8. Fractions of re-vaporized iodine from the samples after the interaction with RuO_4

Sample type	Al	Cu	Zn	paint
Revap. fraction (%)	21,9±1,08	1,5±1,73	29,3±2,08	0,43±1,67

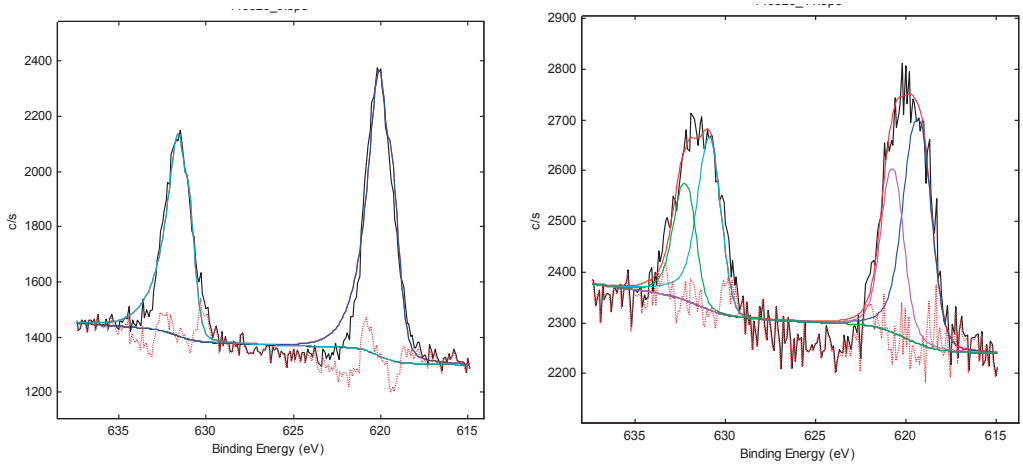

Fig. 4.20. XPS spectras of iodine species on zinc sample before (a) and after (b) the interaction with RuO_4. Where black lined curves represent obtained spectra from the XPS measurements and colored lines are resulting from performed curve fitting.

As can be seen there was no loss of iodine from the paint and copper samples. Different behavior of these samples can be explained by oxidation of iodine to higher oxidation states as was shown in XPS data. Preference of formation of IOx over I_2 can be caused by stronger chemical bonding of iodides in these samples leading to decreased volatility.

4.2.5. Conclusions

Experiments regarding the possible re-vaporization of ruthenium from chloride solutions did not show release of ruthenium from the samples after gamma irradiation. Neither the precipitation of ruthenium from the solutions was detected. Based on these observations it can be concluded that aqueous ruthenium chloride solutions are stable under the gamma radiation

The EXAFS and XPS techniques revealed the chemical characterization of the ruthenium deposits on different metals and on epoxy paint. Measurements showed that the substrate material has no effect on the chemical speciation of deposit. Identification of the oxygen species in XPS measurements showed strong hydroxylation of the oxygen on the surface of samples. Ruthenium dioxide is known as a hygroscopic oxide, which leads to its hydration during deposition in high humidity conditions. Observance of the water in the sample can lead then to the hydrolysis of deposit upper layers. The process of hydration of the RuO_2 deposits on the samples and further hydrolysis leads to the formation of ruthenium oxo-hydroxide species with the ruthenium in a formal oxidation state +IV on the surface of deposits. The

evaluation of the EXAFS data showed that the crystal structure of deposits on all samples was very similar to the structure of RuO_2.

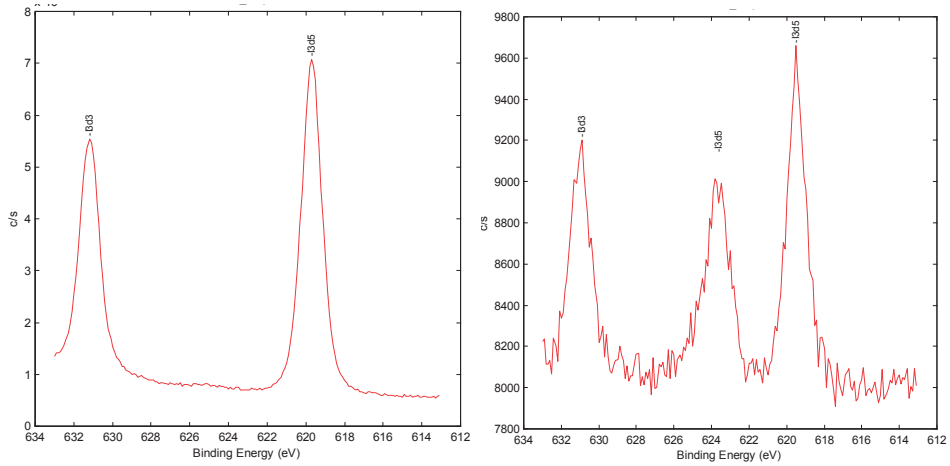

Fig. 4.21. XPS spectras of iodine species on copper sample before (a) and after (b) the interaction with RuO_4.

Based on comparison of EXAFS and ESCA results it can be concluded, that upper layers of deposits are strongly hydrolyzed, whether bulk of the deposit had structure of hydrated RuO_2. This reveals different chemical speciation of the outer and deeper layers of deposits on the samples.

The attraction of RuO_4 to the different metals seems to be quite variable. A proposed explanation for this is the difference between the properties of oxide films formed on the metal surfaces by atmospheric oxidation. Aluminum samples demonstrated exceptionally ability to trap ruthenium among the metals used in the experiments. The high oxygen site density on the aluminum surface leading to the higher attraction of aluminum for the ruthenium tetroxide is the proposed explanation.

Due to the virtually non-existing re-vaporization of the ruthenium from the deposits in the dry atmosphere, it can be assumed that ozone and nitrogen oxide species, created by the radiolysis of air, had only minor effect on the re-vaporization of ruthenium from the samples. During the irradiation experiments in humid atmosphere, a strong dependence of re-vaporized ruthenium fraction on the humidity in atmosphere was found. The hydroxyl radical seems to be the main oxidative species produced by radiolysis of air responsible for the re-oxidation of ruthenium to the volatile state. In case of experiments with the different metals, significant corrosion of the samples occurred under the irradiation. As a consequence high amounts of ruthenium were released specially from zinc samples.

Iodine and ruthenium interaction experiments showed ability of RuO_4 to change the chemical speciation of iodine on the samples. Deposition of RuO_4 onto copper and paint samples lead to oxidation of iodides to higher oxidation states and creation of iodine oxides (IOx). In the case of zinc sample a formation of I_2 that stayed partly on the sample was detected by XPS. Adittionally RuO_4 showed ability to re-volatilize metal iodides from the aluminum and zinc samples in significant amounts.

This iodine release can lead to the creation of adittional volatile source term in the containment.

4.3 References

[1] R. Michel, K. Klipsch, Th. Ernst, M. Gorny, D. Jakob, J. Vahlbruch, H.-A. Synal, C. Schnabel, Ableitung von radioökologischen Parametern aus dem langfristigen Eintrag von Iod-129, Schriftenreihe Reaktorsicherheit und Strahlenschutz, BMU – 2004 – 650 (2004).

[2] Korea Atomic Energy Research Institute, Table of Nuclides, http://atom.kaeri.re.kr/ (2000).

[3] R. Zilliacus, P. Koukkar, T. Karjunen, H. Sjövall, Formation and behaviour of organic iodine, NKS-42 (2002)

[4] S. Tietze, T. Kärkelä, M.R.StJ. Foreman, C. Ekberg, A. Auvinen, U. Tapper, S. Lamminmäki, J. Jokiniemi, , Adsorption and revaporisation studies on iodine oxide aerosols deposited on containment surface materials in LWR, NKS-R, NKS- 272, ISBN 978-87-7893-345-4 (2012).

[5] S. Tietze, T. Kärkelä, C. Ekberg, A. Auvinen, U. Tapper, J. Jokiniemi, Adsorption and revaporisation studies of thin iodine oxide and CsI aerosol deposits from containment surface materials in LWRs, NKS-R, NKS-285, ISBN 978-87-7893-360-7 (2013).

[6] A. Auvinen, Y. Ammar, L. Bosland, B. Clément, S. Dickinson, F. Funke, G. Glowa, T. Karkela, D A Powers, M. Reeks, S. Tietze, G. Weber, Experimental and modelling studies of iodine oxide formation and aerosol behaviour relevant to nuclear reactor accidents, 6th European Review Meeting on Severe Accident Research (ERMSAR-2013), Avignon (France), Palais des Papes, 2-4 October, 2013 (2013).

[7] S. Dickinson, A. Auvinen, Y. Ammar, L. Bosland, B. Clément, F. Funke, G. Glowa, T. Kärkelä, S. Tietze, G. Weber, S. Zhang, Experimental and modelling studies of iodine oxide formation and aerosol behaviour relevant to nuclear reactor accidents, Annals of Nuclear Energy, 74, 200-207 (12/2014)DOI: 10.1016/j.anucene.2014.05.012, 2014 (2014).

[8] S.Tietze, Formation, partitioning and interactions of organic iodides under severe nuclear accident conditions in LWR containments, Thesis for the Degree of Licentitate of Engineering, Nuclear Chemistry, Department of Chemical and Biological Engineering, Chalmers University of Technology, (March 2012).

[9] S. Tietze, M. R. St. Foreman, C. Ekberg, B. van Dongen, Identification of the chemical inventory of different paint types applied in nuclear facilities, J. Radioanal. Nucl. Chem., 3, 1981-1999 (2013).

[10] S. Tietze, M. R. St. Foreman, C. Ekberg, Formation of organic iodides from containment paint ingredients caused by gamma irradiation, Journal of Nuclear Science and Technology, 50 (7), 689-694 (2012).

[11] E. Aneheim, M. R. St. Foreman, S. Tietze, An organic experiment on the subject of S_N2 chemistry which uses a radioisotope which is used in nuclear medicine and is relevant to nuclear accidents, Journal of Nuclear Energy Science and Power Generation Technology, 3(3), in press (2014).

[12] H. Glänneskog, Y. Albinsson, J.O. Liljenzin, G. Skarnemark, Apparatus for on-line measurements of iodine species concentration in aqueous and gaseous phases, Nucl. Instrum. Meth. Phys. Res., 498, 517-521 (2003).

[13] S. Tietze, M.R.St. Foreman, C. Ekberg, Synthesis of I-131 labeled iodine species relevant during severe nuclear accidents in light water reactors, Radiochimica Acta, 101 (10) 675–680 (2013).

[14] S. Tietze, M. R. St. Foreman, Aqueous organic iodide and elemental iodine formation and the resulting impact on the containment chemistry during a severe nuclear accident**,** 7th European R**e**view Meeting on Severe Accident Research (ERMSAR 2014), Marseille (France), 24 - 26 March, 2015 (2015).

[15] I. Kajan, RuO_4 interaction with surfaces in the containment of nuclear power plant, Thesis for the Degree of Licentitate of Engineering, Nuclear Chemistry, Department of Chemical and Biological Engineering, Chalmers University of Technology, (February 2014).

[16] S. Tietze, M. R. St. Foreman, Post-Severe Nuclear Accident Chemical Water And Surface Clean-up Methods For LWRs To Reduce The Amounts Of Highly Contaminated Waste Water, Proceedings Nuclear Plant Chemistry Conference (NPC 2014), Sapporo, October 26-31, Japan, 2014 (2014).

[17] A. Auvinen, L. Bosland, S. Dickinson, G.A. Glowa, L.E. Herranz, H.C. Kim, S. Lamminmäki, T. Kärkelä, D.A. Powers, M. Salay, S. Tietze, Iodine-Paint Interactions, 6th European Review Meeting on Severe Accident Research (ERMSAR-2013), Avignon (France), Palais des Papes, 2-4 October, 2013 (2013).

[18] L. Bosland, S. Dickinson, G.A. Glowa, L.E. Herranz, H.C. Kim, D.A. Powers, M. Saley, S. Tietze, Iodine-paint interactions during nuclear reactor severe accidents, Annals of Nuclear Energy, 184–199, 12/2014, 2014.07.016

[19] V.A. Kashparov, et al., Formation of hot particles during the Chernobyl nuclear power plant accident. Nuclear Technology, 1996. 114(2), 246-25 (1996).

[20] M.M., Taqui Khan, G. Ramachandraiah, and A.P. Rao, Ruthenium(III) chloride in aqueous solution: electrochemical and spectral studies. Inorganic Chemistry, 25(5), 665-670 (1986).

[21] N. Könönen, K. Penttilä, The formation of nitric acid inside BWR containment after severe accident, VTT, Helsinki (2012).

[22] J. Holm, H. Glanneskog, and C. Ekberg, Deposition of RuO4 on various surfaces in a nuclear reactor containment. Journal of Nuclear Materials, 392(1), 55-62 (2009).

[23] C. Mun, et al., XPS investigations of ruthenium deposited onto representative inner surfaces of nuclear reactor containment buildings. Applied Surface Science, 253(18), 7613-7621 (2007).

[24] H. Glänneskog, Interactions of I_2 and CH_3I with reactive metals under BWR severe-accident conditions. Nuclear Engineering and Design, 227(3), 323-329 (2004).

[25] T. Sakurai, A. Takahashi, and G. Fujisawa, Interaction of Ruthenium Tetroxide with Stainless-Steel. Journal of Nuclear Science and Technology, 20(1), 81-83 (1983).

[26] K.S. Kim, N. Winograd, X-Ray Photoelectron Spectroscopic Studies of Ruthenium-Oxygen Surfaces. Journal of Catalysis, 35(1), 66-72 (1974).

[27] C. Mun, L. Cantrel, and C. Madic, Review of literature on ruthenium behavior in nuclear power plant severe accidents. Nuclear Technology, 156(3), 332-346 (2006).

[28] B. Eichler, et al., Volatilization and Deposition of Ruthenium Oxides in a Temperature-Gradient Tube. Radiochimica Acta, 56(3), 133-140 (1992).

[29] J. Krtil, J. Mencl, Radiochem. Radioanal lett., 7, 175-180 (1971).

[30] C. Mun, L. Cantrel, and C. Madic, Radiolytic Oxidation of Ruthenium Oxide Deposits. Nuclear Technology, 164(2), 245-254 (2008).

[31] W. M. Latimer, Oxidation Potentials, Prentice-Hall (1952).

[32] H. Glänneskog, Iodine-Metal surface interactions under severe accident conditions in a nuclear power plant, Chalmers university of technology: Göteborg (2005).

[33] C. Mun, L. Cantrel, and C. Madic, Oxidation of ruthenium oxide deposits by ozone. Radiochimica Acta, 96(6), 375-384 (2008).

5. SLUTSATSER OCH REKOMMENDATIONER

5.1 Sammanfattning av projektet

APRI 8 har följt den internationella forskningen och utvärderat resultaten. Det fortsatta stödet till KTH har gett ökad kunskap om möjligheten att kyla den smälta härden i reaktortanken och om processer i samband med kylbarheten i inneslutningen samt vid ångexplosioner. Stödet till Chalmers har gett ökad kunskap om haverikemi, främst jods uppförande i inneslutningen efter ett haveri.

5.1.1. Internationella forskningsprojekt

Deltagande i CSARP ger tillgång till en mängd information om olika fenomen av betydelse för händelseförlopp vid svåra haverier som kommer fram från internationell forskning. Informationsutbytet sker huvudsakligen vid en årlig konferens. Deltagandet ger också tillgång till beräkningskoder utfärdade av NRC, varav MELCOR används i flera projekt.

SARNET utgör en viktig plattform för forskningen inom svåra haverier och främjar utbyte av kunskap och erfarenheter. De forskningsprojekt som stöds av APRI ingår i SARNET. I gengäld får APRI och forskningsinstitutionerna tillgång till de forskningsresultat som genereras i de övriga deltagarländerna. I APRI 8-projektet har forskningsinstitutionerna KTH och Chalmers varit aktiva i SARNET.

Forskningsprogrammet ISTP (International Source Term Project) har studerat jodkemi vid temperaturer som råder i primärsystemet under ett svårt haveri. Avancerade experiment har visat att med god tillgång på syre kan jod fortsätta existera som elementär jod (I_2) istället för att reagera med cesium och bilda cesiumjodid. Orsaken är att molybden under dessa förhållanden effektivt konsumerar all cesium. Det har också lagts fram starka bevis för att den termodynamiska miljön i primärsystemet förändras så snabbt att den kemiska sammansättningen ”fryser” i vissa lägen. Därigenom förhindras kemiska reaktioner vilket i förlängningen gör elementär till en dominerande jodform. Experiment har också visat att cesium börjar frigöras från bränslekutsar redan vid ~1200°C och att halvflyktiga ämnen som barium och molybden frigörs i nästan lika stor omfattning som flyktiga ämnen när bränslet upphettas till ~2000°C. Resultat ifrån ISTP kommer att i möjligaste mån implementeras i haverikoder som MAAP, MELCOR och ASTEC. Erfarenheter från Phebus har infogats i MAAP. Exempelvis har en förfinad modell för fissionsprodukter införts. Tidigare 12 grupper med fissionsprodukter har nu utvecklats till 18 grupper bl.a. har CsMo införts.

OECD-projektet THAI2 har syftat till att studera frågeställningar kring vätgas, jod och aerosoler och de fenomen som dessa kan ge upphov till vid svåra haverier. Förståelsen för de processer som kan uppstå är central för utvärdering av hot mot inneslutningens integritet och för bestämning av mängden luftburen radioaktivitet vid bränsleskador. Beträffande vätgas har fokus legat på inneslutningssprinklingens påverkan på deflagration och passiva katalytiska rekombinatorers effektivitet vid låga syrgasnivåer. Vad gäller fissionsprodukter har man huvudsakligen studerat jodfrigörelse från en flashande jetstråle och deposition av gasformig jod på aerosoler med hänsyn även tagen till samtidig reaktion mellan dessa. Projektet har levere-

rat värdefulla och högkvalitativa data för validering av koder och förbättrad förståelse av haverifenomen rörande jod, vätgas och aerosoler.

OECD-projektet BIP 2 har syftat till studier av jodkemin inom följande områden: a) Ökad förståelse av jod aborption, b) förståelse av hur organiskt jod bildas och c) Jämförelse av resultat från BIP 1 och EPICUR. Projekt har givit ökad kunskap om hur jod absorberas på olika typer av färgytor samt hur organiskt jod bildas. BIP 2 är nu avslutat och resultaten kommer att publiceras i under år 2015.

5.1.2. Uppfölning av Fukushima olyckan

APRI:s uppföljning har fokuserat på de fenomen och händelser som i huvudsak uppträdde i tidsrymden efter tsunamin och som ledde fram till härdsmältorna. Utgångspunkten för APRI:s uppföljning har varit att få en bättre förståelse av de riskdominerande händelser och fenomen som inträffade under kärnkraftsolyckan i Fukushima-Daiichi med fokus på de tekniska faktorer som kan ha bidragit till härdsmältorna. I slutändan är målet att identifiera möjliga faktorer som kunde ha stoppat kärnkraftsolyckan eller begränsat konsekvenserna. Erhållna kunskaper kan bidra till underlag för översyn av om sådana faktorer även är tillämpliga för säkerheten i svenska reaktorer.

Det som är intressant att notera är de stora skillnaderna i förlopp mellan reaktorerna beroende på tillgången till el-kraft. Det verkar som om komponentskydden kan ha spelat mycket betydande roll. Noterbart är att i de reaktorer som hade viss tillgång till elkraft, och där komponentskydden därför åtminstone delvis var aktiva, inträffade härdsmältorna snabbare än i de reaktorer som inte hade tillgång till el.

Det visade sig att strategin att använda brandutrustning för haveribekämpning innebar olika typer av problem. När inpumpningen kom igång kom endast en mindre del av vattnet dit det skulle. I stället fanns det alternativa flödesvägar på grund av felmonterade eller läckande ventiler. Ett annat problem med brandvattnet var att trycket inte var tillräckligt för att pumpa in. En lärdom kan därför vara att det som inte provas, kommer heller inte att fungera.

5.1.3. ROAAM-projektet

ROAAM-projektet, som syftar till att kvantifiera den betingade sannolikheten för brott på inneslutningens integritet för en Nordisk referens-BWR, har under APRI 8 nått ett flertal viktiga delmål. Mot bakgrund av de utmaningar som den svenska haverihanteringsstrategin har ställt på ROAAM har KTH utvecklat ROAAM+. Ett av huvuddragen i ROAAM+ är en iterativ beräkningsprocess som är uppdelad i två nivåer och som med en adaptiv metod förfinar nödvändiga beräkningsresultat. Den ena beräkningsnivån kallas surrogatmodeller och är beräkningsmässigt effektiva och kan användas för uttömmande känslighets- och osäkerhetsstudier. Den andra beräkningsnivån kallas fullmodeller och utgörs av detaljerade beräkningar med system- och integralkoder. Beräkningsresultaten från fullmodellerna bygger upp en databas som tillsammans med experimentella data används för att utveckla surrogatmodellerna.

Deterministiska beräkningsverktyg, både surrogat- och fullmodeller, har utvecklats för att kunna analysera förloppen:

- Nedsmältning av härden
- Tankgenomträngning med olika genomsmältningsmoder
- Formering och kylbarhet av härdrester i både reaktortank och nedre primärutrymme
- Ångexplosioner med tillhörande laster och impulser i nedre primärutrymme

För alla förlopp har känslighets- och osäkerhetsanalyser med den beskrivna metodiken utförts och preliminära resultat har producerats. I det fortsatta arbetet ska resultaten analyseras och ytterligare beräkningar genomföras baserat på en adaptiv metod som indikerar var utökade beräkningar är nödvändiga för att uppnå efterfrågade beräkningsresultat. En viktig iakttagelse under utvecklingen av ROAAM+ har varit tydliggörandet att förloppen tidigt i ett haveri har avgörande betydelse för fortsättningen i senare skeden.

5.1.4. Jodkemi vid svåra haverier

Ett stort antal organiska jodider kan bildas i reaktorinneslutningen genom reaktion mellan jod, färg, kablage och oljor. Det är både lösningsmedel, polymerer och mjukgörare i dessa material som reagerar med jod och bildar flyktiga organiska föreningar.

Både elementär jod och organiska jodider kan via strålning bilda aerosoler av jodoxider. Jodoxiderna, såväl som elementär jod och organisk jod, kan deponera på färgytor, absorberas i färgmatrisen och förvandlas till nya sorters jodföreningar. Härigenom skapas ett dynamiskt förlopp där källtermen av jod kontinuerligt förändras beroende på miljömässiga faktorer såsom strålning, temperatur, syretillgång och tid.

Det finns möjligheter att utnyttja färgytorna i inneslutningen som jodfällor. Genom att tillsätta aromatiska föreningar i den färg som sedan appliceras på inneslutningsytor kan en förmåga att permanent fånga in jodföreningar skapas.

Dagens torr- och våtfilter kan effektivt fånga elementär jod i den gas som strömmar igenom dem. Chalmers forskning visar att en effektiv infångning kan ske också av organiska jodider ifall torrfilter innehållande zeoliter eller silikater belagda med silver används. Genom tillsats av organiska fosfiner till våtfiltren kan dessas förmåga att fånga organisk jod förbättras väsentligt.

5.1.5. Ruteniumkemi vis svåra haverier

Den flyktigaste formen av rutenium utgörs av ruteniumtetroxid som bildas ifall syretillgången är god under ett svårt haveri. När ruteniumtetroxid sedan reagerar med färg- och metallytor i inneslutningen blir slutprodukten en hydratiserad ruteniumdioxid.

Förmågan att absorbera rutenium skiljer sig åt för koppar, zink och aluminium. Aluminium har störst benägenhet att fånga ruteniumtetroxid och förklaringen står att finna i en hög koncentration av syremolekyler i ytskiktet.

En inneslutningsyta som i ett tidigt skede i haveriet har blivit täckt av jod kan komma att påverkas av ruteniumtetroxid i ett senare skede. Jod oxideras då av ru-

teniumtetroxid till elementär jod eller jodoxider. Denna mekanism kan potentiellt leda till en fördröjd källterm av jod.

5.2 Slutsatser

Från projektet APRI 8 kan följande slutsatser dras:

- Deltagande i CSARP har ökat kunskapen om svåra haverier genom utbyte av forskningsresultat och givit tillgång till haverianalyskoden MELCOR.
- Deltagande i SARNET är viktigt för att samordna forskning med andra länder och få tillgång till andra länders forskningsresultat.
- PHEBUS/ ISTP -projekten har satt kemi och aerosolbeteende inom svåra haverier i fokus.
- Uppföljning av Fukushimahändelsen har inte uppdagat några nya fenomen som skulle påverka den svenska startegin för haverihantering.
- Genom ökad tillförsel av medel till KTH och Chalmers från SSM och industrin har kontinuiteten avseende forskning om svåra haverier kunnat säkras.
- Tillämpningen av ROAAM och utvecklingen av ROAAM+ vid KTH har bidragit till en ökad förståelse och ökade möjligheter att analysera fenomenen och förloppen under ett svårt haveri.
- Forskningen på Chalmers har resulterat i ökade kunskaper om jod interagerar med olika färger och andra material i inneslutningen. Det har också visats att infångningen av organisk jod i skrubbern kan ökas genom att tillsätta organiska fosfiner.

5.3 Rekommendationer

Följande rekommendationer lämnas inför fortsättningen av APRI-projektet:

- Fortsatt deltagande i internationella projekt som CSARP, SARNET, THAI 3, och BIP 3.
- Fortsatt uppföljning av haveriet i Fukushima.
- Fortsatt utveckling ROAAM+-metodiken
- Fortsatta studier av smältans kylbarhet i reaktortankens botten.
- Fortsatta studier av smältans kylbarhet i reaktorinneslutningen.
- Fortsatta studier av de mekanismer som styr ångexplosioner.
- Fortsatta studier av haverikemi i inneslutningen andra fissionsprodukter är jod.

6. FÖRKORTNINGSLISTA

AECL	Atomic Energy of Canada Limited
ANL	Argonne National Laboratory
APRI	Accident Phenomena of Risk Importance
ASTEC	Accident Source Term Evaluation Code
BET	Brunauer-Emmett-Teller theory
BIP	Behaviour of Iodine Project
BWR	boiling water reactor
CCI	Core-Concrete Interaction
CFD	computational fluid dynamics
CHF	critical heat flux
CRGT	control rod guide tube
CSARP	Cooperative Severe Accident Research Program
DABCO	1,4-diazabicyclo [2.2.2] octane (also known as triethylene diamine (TEDA))
DCH	Direct Containment Heating
DECOSIM	code for debris bed coolability simulation
DEFOR	debris bed formation
DEM	discrete element method
DHF	dryout heat flux
LIVE	Late In-Vessel Phase Experiments
LP	Lumped Parameter
LWR	light water reactor
EC	European Commission
ECM	effective convectivity model
EDF	Electricité de France
EOP	Emergency Operating Procedures
ERMSAR	European Review Meetings on Severe Accident Research
EXAFS	Extended X-ray Absorption Fine Structure analysis
FCI	fuel coolant interaction
FM	Full Model
FOMICAG	Facility for Online Measurements of I-131 labelled species Concentrations in Aqeous and Gaseous Phase
HPGe	High Purity Germanium detector
FP	framework programme
FPT	Fission Product Test
GC-MS	Gas Chromatography – Mass Spectroscopy
IGT	instrumentation guide tube
INCO	in-vessel coolability
IRSN	Institut de Radioprotection et de Sûrité Nucléaire
ISTP	International Source Term Project
IVR	in-vessel retention
KROTOS	a small-scale test facility for FCI (steam explosion) study at CEA
KTH	Royal Institute of Technology
LSC	Liquid Scintillation Counting
LET	Linear Energy Transfer
LOCA	loss of coolant accident
LWR	Light Water Reactor
MCCI	Melt Corium Concrete Interaction
MET	Melt Eruption Test
MELCOR	code for integral simulation of severe accident developed by USNRC
MISTEE	micro interactions of steam explosion energetics
MSWI	melt structure water interactions
NCG	non-condensable gas

NPP	nuclear power plant
NRC	Nuclear Regulatory Commission
NROI	Nordic Research on Radiolytic Oxidation of Iodine
OECD	Organisation for Economic Co-operation and Development
OIPHA	Organic Iodide Partitioning and Hydrolysis Analysis model
PDS	Particulate debris spreading
PECM	phase-change ECM
Pyro-IR	Pyrolysis – Infrared
POMECO	porous media coolability
PSA	probabilistic safety analysis
PWR	pressurized water reactor
ROAAM	risk oriented accident analysis methodology
RPV	reactor pressure vessel
RTF	Radioiodine Test Facility
SAID	severe accident information distillation
SA	severe accident
SAM	severe accident management
SAMG	Severe Accident Management Procedures
SARNET	severe accident research network of excellence
SBO	station blackout
SEE	steam explosion energetics
SEM-EDX	Single Electron Miscroscopy – Energy Dispersive X-ray spectroscopy
SERENA	Steam Explosion REsolution for Nuclear Applications
TEDA	TriEthylene DiAmine
TGA	Thermo Gravimetric Analysis
XPS	X-ray Photoelectron Spectroscopy

2015:27

Strålsäkerhetsmyndigheten har ett samlat ansvar för att samhället är strålsäkert. Vi arbetar för att uppnå strålsäkerhet inom en rad områden: kärnkraft, sjukvård samt kommersiella produkter och tjänster. Dessutom arbetar vi med skydd mot naturlig strålning och för att höja strålsäkerheten internationellt.

Myndigheten verkar pådrivande och förebyggande för att skydda människor och miljö från oönskade effekter av strålning, nu och i framtiden. Vi ger ut föreskrifter och kontrollerar genom tillsyn att de efterlevs, vi stödjer forskning, utbildar, informerar och ger råd. Verksamheter med strålning kräver i många fall tillstånd från myndigheten. Vi har krisberedskap dygnet runt för att kunna begränsa effekterna av olyckor med strålning och av avsiktlig spridning av radioaktiva ämnen. Vi deltar i internationella samarbeten för att öka strålsäkerheten och finansierar projekt som syftar till att höja strålsäkerheten i vissa östeuropeiska länder.

Strålsäkerhetsmyndigheten sorterar under Miljödepartementet. Hos oss arbetar drygt 300 personer med kompetens inom teknik, naturvetenskap, beteendevetenskap, juridik, ekonomi och kommunikation. Myndigheten är certifierad inom kvalitet, miljö och arbetsmiljö.

Strålsäkerhetsmyndigheten
Swedish Radiation Safety Authority

SE-171 16 Stockholm
Solna strandväg 96

Tel: +46 8 799 40 00
Fax: +46 8 799 40 10

E-mail: registrator@ssm.se
Web: stralsakerhetsmyndigheten.se